Inelastic Neutron and Resonant Elastic X-Ray Scattering Studies of Honeycomb Quantum Magnets



Miska Elliot
Lincoln College
University of Oxford

A thesis submitted for the degree of
Doctor of Philosophy

Trinity 2022

Inelastic Neutron and Resonant Elastic X-Ray Scattering Studies of Honeycomb Quantum Magnets

Miska Elliot, Lincoln College

Thesis submitted for the Degree of Doctor of Philosophy, Trinity 2022

This thesis presents results from inelastic neutron scattering experiments on the magnetically ordered phases of the stacked honeycomb quantum magnets $CoTiO_3$ and $FeTiO_3$. The two materials are isostructural with ferromagnetic alignment within the honeycomb layers, and antiferromagnetic alignment between neighbouring honeycomb layers. In $CoTiO_3$, the magnetic moments have an easy-plane anisotropy and high resolution inelastic neutron scattering measurements reveal the presence of a finite energy gap. Such a gap implies the existence of bond-dependent anisotropic couplings and a quantum order-by-disorder mechanism. Furthermore, the inelastic scattering measurements reveal a winding of the scattering intensity at linear crossing points in the vicinity of the corners of the two-dimensional Brillouin zone. On the other hand, the magnetic moments of $FeTiO_3$ possess an easy-axis anisotropy with doubly degenerate magnetic modes. This degeneracy is lifted under the application of an external magnetic field, and if this magnetic field exceeds a critical value of 8 T the magnetic structure transitions from an antiferromagnetic phase to a spin-polarised phase. The magnon dispersions in $FeTiO_3$ have a small avoided crossing at the corners of the two-dimensional Brillouin zone, and such a gap arises due to the presence of an antisymmetric Dzyaloshinskii-Moriya exchange interaction. Nonetheless, the azimuthal dependence of the inelastic neutron scattering intensity around these avoided crossing points was found to have a similar profile to that observed in $CoTiO_3$. This periodicity appears to be a universal feature of magnetic excitations supported by the honeycomb lattice and was found in both low energy magnons and higher energy spin-orbit excitons in $CoTiO_3$, and in the magnon excitations of $FeTiO_3$ in both the antiferromagnetic and spin-polarised magnetic phases. Finally, results of elastic x-ray scattering experiments measuring the structural and magnetic properties of crystalline samples of lithium substituted Na_2IrO_3 are presented. Such systems have previously been found to exhibit anisotropic Kitaev exchange between the Ir^{4+} moments, which may stabilise exotic magnetic phases. Studies of the structural order of these samples reveal stacking faults and rotational twins. Resonant elastic x-ray scattering studies allow the magnetic structure of a 5% Li-substituted sample of Na_2IrO_3 to be determined as a zigzag ordered magnetic state, which implies the presence of both isotropic Heisenberg and anisotropic Kitaev exchange interactions.

Acknowledgements

I would like to thank everybody who contributed towards the work presented in this thesis. First and foremost, I'd like to thank my supervisor Radu Coldea whose insight into condensed matter physics has helped direct the approach taken, and vastly contributed to the work I have achieved over the last four years. I'd also like the thank him for his patient guidance in teaching me about and introducing me to the wonderful research field of neutron scattering and quantum magnetism. Additionally, I'd like to thank Roger Johnson for teaching me about the resonant elastic x-ray scattering technique and about the use of x-ray diffractometers. I'd also like to thank him for useful discussions and about each of the materials presented in this thesis. Thanks also go to Paul McClarty for his contributions to the $CoTiO_3$ project and to many insightful discussions about magnetic excitation spectra.

A vital part of any condensed matter experiment is sample growth, for which I'd like to thank Dharmalingham Prabhakaran for synthesis of the ilmenites $CoTiO_3$ and $FeTiO_3$, and also the Philipp Gegenwart group at Augsburg for synthesis of the iridate samples. I'm grateful for the help of the instrument scientists, without whom data could not have been taken - Robert Bewley, David Voneshen, Helen Walker, and Ross Stewart at the ISIS Neutron and Muon Source; Alessandro Bombardi, Gareth Nisbet, and Anuradha Vibhakar at the Diamond Light Source; and Sonia Francoual at PETRA III. I'd also like to thank Alex Buts for his informative discussions about parallel processing.

I'd like to thank the many people I've worked with at the Clarendon Laboratory over the last four years, including the workshop team for assisting with the design and manufacturing of the sample mounts; and the outreach team for providing me with many opportunities to present demonstrations highlighting quantum properties of materials to younger audiences. I'd like to thank everyone I have worked with in office 105 over the last four years, helping to provide a fun and productive environment to do research, in addition to a wide variety of discussions of technical physics problems. In particular I'd like to thank my 'physics rival' Matthew Steggles with whom I came up to Oxford eight years ago, his friendship has proven invaluable to me throughout our time training as physicists.

Finally, I'd like to thank my family - in particular my parents, siblings, grandmas, and Isabelle. I dedicate this thesis to their unconditional love and support.

Contents

1 Introduction **1**

2 Introduction to Quantum Magnetism **5**

2.1 Magnetic Moments 5

2.2 Magnetic Exchange and Magnetic Order 9

2.3 Magnetic Excitations: Linear Spinwave Theory 13

2.4 Nodal Lines in the Honeycomb Quantum Magnets $CoTiO_3$ and $FeTiO_3$ . . 16

2.5 Kitaev Physics in the Honeycomb Iridates $\mathcal{A}_2IrO_3$ 18

References 21

3 Experimental Techniques **22**

3.1 Neutron Scattering Cross Section 23

3.1.1 Nuclear Scattering 25

3.1.2 Magnetic Scattering 28

3.2 Time of Flight Spectrometry 32

3.3 Elastic and Resonant Elastic X-Ray Scattering 37

3.3.1 Elastic X-Ray Scattering Amplitude 37

3.3.2 Resonant Elastic X-Ray Scattering Amplitude 39

3.4 X-Ray Scattering Instrumentation 43

3.4.1 Lab-based Diffractometers 43

3.4.2 Synchrotron Diffractometers 46

References 47

4 Order by Disorder, Bond Dependent Exchange, and Nodal Quasiparticles in $CoTiO_3$ **48**

4.1 Crystal and Magnetic Structure 49

4.1.1 Structural and Magnetic Unit Cells 49

4.1.2 Structural Domains 52

4.2 Neutron Scattering Results 56

4.3 Single Ion Physics . . . 61
4.4 XXZ Easy-Plane Spin Wave Model for Magnons . . . 70
4.5 Spectral Gap and Fitting of XXZΔ Model . . . 79
4.6 Bond Dependent Exchange . . . 87
4.7 Quantum Order by Disorder . . . 93
4.8 Nodal Lines and Isospin Winding . . . 98
4.8.1 Nodal Line Fine Structure . . . 99
4.8.2 Isospin Winding . . . 105
4.9 Tight Binding Model for Spin-Orbit Excitons . . . 109
4.10 Conclusions . . . 113
References . . . 113

5 Isospin Winding, Crystal Field Excitations, and Spin-Flip Transition in the Easy-Axis Honeycomb Quantum Magnet $FeTiO_3$ 115
5.1 Crystal and Magnetic Structure . . . 116
5.2 Inelastic Neutron Scattering Results . . . 120
5.3 Single Ion Physics and Crystal Field Excitations . . . 124
5.3.1 Single Ion Physics . . . 124
5.3.2 Dispersive Single Ion Excitations . . . 128
5.4 Easy-Axis Spin Wave Models for Magnons . . . 135
5.4.1 Spin Wave Model in Zero Field . . . 135
5.4.2 Spin Wave Model in Intermediate Field . . . 145
5.4.3 Spin Wave Model in the Polarised Phase . . . 149
5.5 Gapped Nodal Lines and Isospin Winding . . . 158
5.5.1 Zero Field Nodal Lines . . . 158
5.5.2 High Field Nodal Lines . . . 161
5.5.3 Isospin Winding . . . 164
5.6 Further Refinement of the Modelling of Magnon Dispersions . . . 169
5.6.1 Dispersions in the Polarised Phase . . . 169
5.6.2 Dispersions in Zero Field . . . 176
5.6.3 Dispersions in Intermediate Field . . . 182
5.7 Conclusions . . . 185
References . . . 185

6 Zigzag Magnetic Structure in Isoelectronically Doped $(Na_{1-x}Li_x)_2IrO_3$ 186
6.1 Structual Analysis of Honeycomb Iridate Samples 186
6.2 Resonant X-Ray Scattering Experimental Details 199
6.3 Structure Factor Analysis 204
6.4 Azimuthal Dependence of Scattering Intensity 207
6.5 Fitted Magnetic Structure 213
6.6 Conclusions 215
References 215

7 Concluding Remarks 216
References 218

List of Figures

2.1 Magnetically ordered phases of the Heisenberg-Kitaev model on the honeycomb lattice . . . 12
2.2 Visualisation of the magnon band structure of a two dimensional honeycomb lattice with nearest neighbour ferromagnetic Heisenberg couplings . . . 16
2.3 Visualisation of the azimuthal profile of the dynamical correlations near the K point of a two dimensional honeycomb Heisenberg ferromagnet . . . 17
2.4 Single ion spectrum for Ir^{4+} ions in a strong octahedral crystal field and spin-orbit coupling . . . 19
2.5 Bond geometry for the ideal honeycomb lattice with edge sharing octahedra 20

3.1 Scattering geometry for a neutron scattering experiment . . . 24
3.2 Schematic diagrams of the LET and MERLIN time-of-flight-spectrometers . 35
3.3 Scattering geometry for a resonant elastic x-ray scattering experiment . . . 42
3.4 Depiction of the Oxford Diffraction Supernova x-ray scattering instrument . 44
3.5 Depiction of the Rigaku Smartlab x-ray scattering instrument . . . 46
3.6 Photographs of the I16 and P09 x-ray diffractometers . . . 47

4.1 Models of the crystallographic unit cell, magnetic unit cell, and magnetic structure of $CoTiO_3$ . . . 50
4.2 Structural domains of $CoTiO_3$ . . . 54
4.3 Determination of the structural domain of a $CoTiO_3$ sample measured using x-ray diffraction . . . 55
4.4 Measurement and calculation of the $hk1$ and $hk\bar{1}$ planes on the elastic line in INS measurements on $CoTiO_3$ . . . 56
4.5 Coaligned single crystal samples of $CoTiO_3$ mounted on an aluminium sample holder with crystallographic axes labelled . . . 57
4.6 INS energy scan in $CoTiO_3$ for $E_i = 81.5$ meV . . . 58
4.7 Constant energy slices through unsymmetrised and symmetrised data sets in $CoTiO_3$ . . . 58

4.8 INS data in $CoTiO_3$ at 8 K for $E_i = 45$, 18, and 9.6 meV 59
4.9 Neutron powder diffraction data in $CoTiO_3$ 61
4.10 Single-ion spectrum within the lowest $l = 1$, $\mathsf{S} = 3/2$ sector for a Co^{2+} ion in an octahedral crystal field 67
4.11 Anisotropic g-factors along and perpendicular to the trigonal axis for Co^{2+} ions as a function δ/λ 68
4.12 Ground state moment and energy levels for Co^{2+} ions as a function of the in-plane mean field 70
4.13 Comparison of dispersions and dynamical correlations of the analytical expressions from the XXZ model with the numerical values calculated from a SpinW model 79
4.14 INS intensity along orthogonal wavevector directions through the $(1, 1, 3/2)$ magnetic Bragg peak 81
4.15 Plot of observed and calculated magnon energies in $CoTiO_3$ 84
4.16 Energy scan above the $(1, 1, 3/2)$ magnetic Bragg peak 85
4.17 INS data observing the magnon dispersions along high-symmetry directions compared with the XXZΔ model 86
4.18 Structural and magnetic Brillouin zones for $CoTiO_3$ 91
4.19 INS scans near K points indicative of bond dependent exchange in $CoTiO_3$ 92
4.20 Parametrisation of quantum zero-point energy in $CoTiO_3$ 96
4.21 Nodal lines along L for Heisenberg and XXZ interlayer couplings in $CoTiO_3$ 103
4.22 Shift of the Dirac nodal points in momentum space for bond dependent exchange in a honeycomb layer 105
4.23 INS data through the $(2/3, 2/3)$ K point along orthogonal in-plane directions in $CoTiO_3$ 106
4.24 Momentum intensity maps above and below the Dirac node energy in $CoTiO_3$ compared between experimental data and the XXZη model 107
4.25 Azimuthal intensity dependence around $(2/3, 2/3)$ K point for differing L values in $CoTiO_3$ 109
4.26 INS data observing the dispersions of the first excited crystal field level along high-symmetry directions compared with the tight-binding model 112
4.27 INS data observing the dispersions and azimuthal intensity profile for the dispersive first excited crystal field level around the K points 114

5.1 Models of the crystallographic and magnetic unit cells of $FeTiO_3$ 117

5.2 Isothermal magnetization curves in $FeTiO_3$ at 4.2 K with an external magnetic field applied parallel and perpendicular to the hexagonal $\mathbf{c}_h$ axis . . . 118
5.3 X-ray powder diffraction data in $FeTiO_3$ collected at 300 K compared to the fit from structural refinement . . . 118
5.4 Coaligned single crystal samples of $FeTiO_3$ mounted on an aluminium sample holder with crystallographic axes labelled . . . 120
5.5 INS data in $FeTiO_3$ taken in externally applied magnetic fields of 8.75 T, 7 T, 4 T, and 0 T . . . 122
5.6 Cut in energy taken from INS data in $FeTiO_3$ with incident neutron energies of 36 meV, revealing the presence of excited crystal field levels . . . 123
5.7 Single-ion spectrum within the lowest $l = 1$, $\mathsf{S} = 2$ sector for a Fe^{2+} ion in a trigonally distorted octahedral crystal field in the presence of spin-orbit coupling . . . 128
5.8 Calculated INS intensities for a nearest neighbour exchange model over the spectrum of excited Fe^{2+} single-ion states . . . 133
5.9 Ground state magnetic moment and g-factor for an exchange model over the spectrum of excited Fe^{2+} single-ion states . . . 134
5.10 Slice taken through the zero field INS data in $FeTiO_3$ compared to modelled dispersions from a Heisenberg exchange model with an easy-axis single ion anisotropy . . . 141
5.11 Slice taken through K points in zero field INS data in $FeTiO_3$ compared to modelled dispersions from a model including Heisenberg exchange, single-ion easy-axis anisotropy, and a Dzyaloshinskii–Moriya interaction . . . 144
5.12 Comparison of dispersions and dynamical correlations of the analytical expressions from the Heisenberg exchange model, including an easy-axis single-ion anisotropy, and a Dzyaloshinskii–Moriya interaction on a buckled honeycomb lattice with the numerical values calculated from a SpinW model . . . 145
5.13 Cut through the $(\frac{1}{2}, 1, 0)$ position taken through the zero field, 4 T, and 7 T data set to show the splitting of the magnon modes under an applied magnetic field. Plotting the energies of the fitted peaks shows a linear dependence of the splitting on the applied magnetic field. . . . 146
5.14 INS data comparing the observed zero field magnon dispersions against dispersions of easy-axis ordered moments calculated using a model including Heisenberg exchange, single-ion easy-axis anisotropy, and a Dzyaloshinskii–Moriya interaction . . . 147

5.15 INS data comparing the observed 4 T magnon dispersions against dispersions of easy-axis ordered moments calculated using a model including Heisenberg exchange, single-ion easy-axis anisotropy, a Dzyaloshinskii–Moriya interaction, and a Zeeman interaction 148
5.16 INS data comparing the observed 7 T magnon dispersions against dispersions of easy-axis ordered moments calculated using a model including Heisenberg exchange, single-ion easy-axis anisotropy, a Dzyaloshinskii–Moriya interaction, and a Zeeman interaction 148
5.17 Phase diagram depicting antiferromagnetic, spin-flop, and polarised magnetic ground states that are stabilised by competition between single-ion anisotropy and the external magnetic field in the presence of interlayer Heisenberg exchange couplings 150
5.18 Slices through the INS data sets at 0 T, 7 T, and 8.75 T with dispersion points mapped from symmetry equivalent (hkl) values overplotted, and a scatter plot showing the energy of experimentally observed dispersion points plotted against their calculated values using the easy-axis ordered Heisenberg exchange model including an easy-axis single-ion anisotropy, DM interaction, and g factor. 154
5.19 INS data comparing the observed 8.75 T magnon dispersions against dispersions calculated using a LSWT model with parameters simultaneously fitted to the zero field, 4 T, 7 T and 8.75 T INS data sets. 155
5.20 INS data comparing the observed 7 T and 4 T magnon dispersions against dispersions in the antiferromagnetic phase calculated using a LSWT model with parameters simultaneously fitted to the zero field, 4 T, 7 T and 8.75 T INS data sets. 156
5.21 INS data comparing the observed magnon dispersions in zero field against dispersions in the antiferromagnetic phase calculated using a LSWT model with parameters simultaneously fitted to the zero field, 4 T, 7 T and 8.75 T INS data sets. 157
5.22 Energy scan through the $(2/3, 2/3)$ K point of the zero field INS data for $FeTiO_3$. The energy scan has a two peak profile that is accounted for by the inclusion of a Dzyaloshinskii-Moriya interaction to the LSWT model for the magnon dispersions. 160
5.23 Calculated magnon dispersions in zero field in the vicinity of a K point. The inclusion of the Dzyaloshinskii-Moriya exchange coupling term gaps out the nodal line. 160

5.24 Nodal lines along L under the inclusion of the second nearest neighbour (J_2) exchange coupling in the high field exchange model 162
5.25 Calculated magnon dispersions in the high field phase in the vicinity of the K point. The inclusion of second nearest neighbour exchange or Dzyaloshinskii-Moriya interactions shifts or gaps out the nodal lines 163
5.26 Energy scans through the $(2/3, 2/3)$ K point of the high field INS data for $FeTiO_3$. The energy scan has a two peak profile that is accounted for by the inclusion of a Dzyaloshinskii-Moriya interaction, and a second nearest neighbour Heisenberg coupling set to 0 meV to the LSWT model for the magnon dispersions. 164
5.27 Azimuthal intensity dependence around the $(2/3, 2/3)$ K point for differing L values in the zero and high field INS data of $FeTiO_3$ 167
5.28 Momentum intensity maps above and below the nominal Dirac node energy in the zero and high field INS data for $FeTiO_3$ compared with calculations using exchange models 168
5.29 Modelled dispersions of an acoustic magnon, a hypothetical mode $\tilde{\omega}$, and the two modes resulting from their hybridisation 172
5.30 Comparison of slices through the high field INS data against the same slices modelled with easy-axis ordered moments coupled with an acoustic $\tilde{\omega}$ mode 174
5.31 Plot of the energy dependence of the mixing mode coupling constant 175
5.32 Scatter plot showing the energy of over 3900 experimentally observed dispersion points in the high field data set compared to the energy of the same points as calculated in the model. 176
5.33 Modelled dispersions of the acoustic magnon mode, a pair of mixing modes $\tilde{\omega}_1$ and $\tilde{\omega}_2$, and the three modes resulting from their hybridisation 178
5.34 Scatter plot showing the energy of over 7000 experimentally observed dispersion points in the zero field data set compared to the energy of the same points as calculated in the model. 179
5.35 Comparison of slices through the zero field INS data against the same slices modelled with magnons coupled with acoustic mixing modes 180
5.36 Modelled dispersions of a pair of acoustic magnon modes split by an applied magnetic field, a pair of acoustic mixing modes, and the six modes - $\lambda_n^{\pm}$ - resulting from their hybridisation 183
5.37 Scatter plot showing the energy of over 2500 experimentally extracted dispersion points in the 7 T data set compared to the energy of the same points as calculated in the intermediate field model. 183

5.38 Comparison of slices through the 4 T and 7 T INS data against the same slices modelled with easy-axis ordered moments coupled with acoustic $\tilde{\omega}_{1,2}$ modes 184

6.1 Unit cells of Na_2IrO_3, $Na_3LiIr_2O_6$, and $\alpha - Li_2IrO_3$ 189
6.2 Comparison of the diffraction pattern in the $hk0$ hexagonal plane data versus calculations including rotational twins about the $\mathbf{c}^*$ axis. 192
6.3 Comparison of the $0kl$, $hk1$, and $hk\bar{1}$ planes in diffraction data versus calculated planes displaying rotational twins about the $\mathbf{c}^*$ axis, and a rotational twin about the monoclinic $\mathbf{a}$ axis. 193
6.4 Comparison of the diffraction pattern in the $0kl$, $hk1$, and $hk\bar{1}$ hexagonal planes (top row) versus calculations (bottom row), including rotational twins about the $\mathbf{c}^*$ axis, a rotational twin about the monoclinic $\mathbf{a}$ axis, and twins resulting from composite rotations about both the $\mathbf{a}$ and $\mathbf{c}^*$ axis. 195
6.5 Comparison of the diffraction pattern in the $hk2$, $2kl$, and $h2l$ planes in diffraction versus calculations, including many rotational twins about the $\mathbf{c}^*$ axis and stacking faults in streaks along the $(0, 0, L)$ direction. 196
6.6 X-ray diffraction measurements using a point source detector showing mosaicity and twinning in a single phase sample 199
6.7 Resonant elastic x-ray scans for the magnetic peak at $(0, -1, 6.5)_m$ 201
6.8 Raster map showing the intensity of the $(0, 0, 6)$ structural Bragg peak scanned across the surface sample. The rocking curve scans at the three brightest points show different peak positions in η indicating that the sample has a $0.5(1)^\circ$ mosaicity. 203
6.9 Integrated intensity of the $(0, -1, 6.5)_m$ magnetic Bragg peak as a function of the azimuthal angle ψ. Each point in the ψ scan is found by scanning along the $(0, 0, L)$ direction and attempting to fit a peak profile. The scattering geometry is shown inset. 204
6.10 $z = 0$ layer of the magnetic iridium ions with magnetic structures that transform according to single irreducible representations 205
6.11 Illustration of the xyz coordinate system defined in terms of the crystallographic lattice vectors, and the $u_1u_2u_3$ coordinate system defined in terms of the scattering geometry 209
6.12 Azimuthal scan about the $(0, -1, 6.5)_m$ magnetic Bragg peak with a fitted profile for magnetic moments constrained to the crystallographic ac plane and the moment direction subtending an angle μ from the $\mathbf{a}$ axis 211

6.13 Azimuthal scan about the $(0, -1, 6.5)_m$ magnetic Bragg peak with a fitted profile for magnetic moments tilted out of the *ac* plane and the moment direction subtending an angle $\delta\zeta$ from the $\mathbf{c}^*$ axis 213
6.14 Magnetic structure of 5% Li-doped $(Na_{1-x}Li_x)_2IrO_3$ viewed in the plane of, and perpendicular to, the honeycomb layers 215

List of Tables

4.1 Fractional coordinates and Wyckoff positions of constituent ions of $CoTiO_3$ extracted from room temperature single crystal x-ray diffraction data. . . . 52

4.2 Solutions for the fractional positions of the constituent atoms from single crystal x-ray diffraction of four samples of $CoTiO_3$ at room temperature . . 53

4.3 Refined 150 K crystal structure parameters of $CoTiO_3$ 62

4.4 Character table of the O_h point group 64

4.5 First order perturbation in energy of eigenstates of the spin-orbital Hamiltonian for Co^{2+} ions in a trigonally distorted octahedral crystal field of O^{2-} ions. 67

5.1 Refined 300 K crystal structure parameters of $FeTiO_3$ from analysis of powder x-ray diffraction data 119

5.2 Energy of eigenstates of the spin-orbital Hamiltonian for Fe^{2+} ions in an octahedral crystal field of O^{2-} ions to first order in the trigonal distortion parameter δ. 127

5.3 Fitted exchange parameters for the Heisenberg exchange model, with easy-axis single-ion anisotropy, a Dzyaloshinskii-Moriya interaction along the third nearest neighbour bond, and a Zeeman interaction. 153

5.4 Fitted parameters for the Heisenberg exchange model including single-ion anisotropy, Dzyaloshinskii-Moriya interaction, and a Zeeman interaction term, with additional mixing modes, and interactions between the acoustic magnon and mixing modes. The mixing parameters are denoted by the subscript (A) for the zero field, 4 T, and 7 T data sets, and by the subscript (P) for the spin-polarised 8.75 T data set. 181

6.1 Structural unit cell parameters of Na_2IrO_3 and α-Li_2IrO_3 187

6.2 Structural unit cell parameters of $(Na_{1-x}Li_x)_2IrO_3$ measured at $T = 300$ K using the Supernova diffractometer for $x = 0, 0.05, 0.06, 0.13, 0.25$ sample . . 188

6.3 Refined 300 K crystal structure parameters of $(Na_{1-x}Li_x)_2IrO_3$ for $x = 0.05$ 198

6.4 Character table of the $2/m$ (C_{2h}) point group 206

Chapter 1

Introduction

This thesis presents studies of quantum magnetic materials where the crystal structure contains magnetic ions that are arranged in a honeycomb. These systems were studied using the experimental techniques of x-ray and neutron scattering, revealing information about their magnetic structure and excitations. The subsequent chapter - Chapter 2 - will introduce key aspects of quantum magnetism such as how the electronic structure of an ion, in addition to the presence of a crystal field environment and spin-orbit coupling, can give rise to local magnetic moments, and how the local magnetic moments may interact to stabilise magnetic structures which can support magnetic excitations that propagate across the lattice. The model of magnetic moments on a two-dimensional honeycomb layer interacting via Heisenberg exchange is treated within the scope of linear spinwave theory (LSWT) and presented as an illustrative example. Such an illustration allows features of magnetic excitation spectra such as crossing points, nodal lines, and isospin texture to be presented, with such features observed in the results of inelastic neutron scattering experiments on the ilmenite materials $CoTiO_3$ and $FeTiO_3$. The final set of explored systems are honeycomb iridates which have a far stronger spin-orbit interaction and a strong Kitaev interaction than the ilmenites, and such interactions may give rise to key features of Kitaev physics on the honeycomb lattice such as spin liquid states and exotic magnetic ordering. The experimental techniques of inelastic neutron scattering and of both resonant and non-resonant x-ray scattering are presented in Chapter 3, with descriptions of their underlying theoretical principles, and the use of time-of-flight spectrometers and X-ray diffractometers

(both lab-based and synchrotron based) that were used in experimental work performed in this thesis.

Chapters 4 and 5 detail inelastic neutron scattering (INS) experiments on $CoTiO_3$ and $FeTiO_3$, respectively. Both chapters outline models for the excitation spectra in both materials. Three different calculational methods are used in order to model these excitation spectra, specifically a multilevel 'pseudoboson' approach is taken to attempt to model the entire spectrum of the magnetic excitations of $FeTiO_3$, linear spinwave theory is used to model the lowest energy magnon dynamics in both $CoTiO_3$ and $FeTiO_3$, and a tight-binding model is used to model the dispersion and INS intensity of a spin-orbit exciton. The pseudoboson approach involves expressing all relevant operators, such as the Hamiltonian and spin operators, in terms of raising and lowering operators for the multiple energy levels on each single-ion site. This method can model many different excitations within a single Hamiltonian, but due to the size of the matrix representation of each operator is a more difficult calculational method than LSWT or a tight-binding model. Instead, by projecting the multilevel expansion down to a subset of the levels, the LSWT and tight-binding model can be recovered, and - in the cases of $CoTiO_3$ and $FeTiO_3$ - such models allow the dispersions and INS intensities of the magnon modes and spin-orbit excitons to be written in closed form expressions. For $CoTiO_3$, INS revealed the presence of a previously predicted spectral gap. This spectral gap can be added phenomenologically to the LSWT model, and can be understood as a result of the breaking of the continuous $U(1)$ symmetry of the mean field ground state into the discrete $\bar{3}$ point-group symmetry of the lattice via a quantum 'order by disorder' (ObD) mechanism. The presence of ObD requires bond-dependent exchange, and evidence in the INS data for such an anisotropic exchange interaction is also presented. In addition to the low energy magnons, INS measurements on $CoTiO_3$ revealed a higher energy excitation which is interpreted to be a spin-orbit exciton. This feature is explained within the scope of the single-ion physics of the Co^{2+} ions and the dispersion of this excitation is modelled with a tight-binding model. Finally, the features of Dirac points in both the magnon and spin-orbit exciton are presented. The fitted exchange parameters for the LSWT model suggest a winding double-helix nodal line structure, and the angular dependence of the INS intensity of both the low energy magnons and high energy spin-orbit

exciton is presented and shown to have a cosinusoidal periodicity with the top and bottom bands out of phase with each other.

For $FeTiO_3$, INS experiments were performed in zero field in addition to applied fields of 4, 7, and 8.75 T. The zero field measurement was repeated at a far higher neutron incident energy in order to capture the crystal field dynamics. In order to describe the crystal field and spin-orbital physics and the magnetic excitations within a single model, a 'psuedoboson' model is constructed and provides a description of the dispersion and INS intensity of the low energy dispersive magnons in addition to the higher energy crystal field excitations within a single Hamiltonian. The inelastic neutron scattering experiments in applied field are consistent with a spin-flip transition previously measured at an applied field of 8 T, and a Hamiltonian that allows such a phase transition is presented. The magnetic excitations supported by this Hamiltonian are modelled using LSWT, however this Hamiltonian does not completely capture all observed features of the INS data - specifically additional low energy signals that form modes that appear to hybridise with the magnon dispersions. A phenomenological model that describes these additional low energy modes is constructed and fitted to INS data in both zero and applied fields. In addition to the coupling of these two sets of modes, the magnon modes in the vicinity of the corners of the two-dimensional Brillouin zone appear to be gapped and can be modelled by the addition of a non-zero Dzyaloshinskii-Moriya (DM) interaction. A consequence of the DM interaction is that the nodal lines are 'gapped out' in the direction normal to the honeycomb layers. Despite the nodal lines being gapped, the angular dependence of the INS intensity of the magnons observed in both the zero field and 8.75 T phases both exhibit the same cosinusoidal periodicity as shown in $CoTiO_3$.

Chapter 6 details lab based x-ray diffraction (XRD) and resonant elastic X-ray scattering (REXS) experiments on Li-substituted Na_2IrO_3. This chapter opens with results of characterisation of the quality of these samples using x-ray diffraction. Stacking faults and crystallographic twinning are shown to be ubiquitous features of these honeycomb iridates. The twinning schemes are characterised and XRD measurements allow a highest quality sample to be selected from a batch in preparation for a REXS experiment. The parent compound Na_2IrO_3 has been previously found to order into a 'zig-zag' magnetic structure

at low temperature and the $x = 1$ end-point $\alpha - Li_2IrO_3$ has been found to have an exotic counter-rotating spiral magnetic structure, both with magnetic ordering temperatures $T_N \approx 15$ K. Both of these magnetic structures are stabilised by competition between differing types of exchange, including Kitaev and Heisenberg exchange. The purpose of studying these Li-substituted iridates is to explore the dependence of the magnetic ordering temperature and the evolution of the magnetic structure as the Li-substitution varies. 25% and 26% Li-substituted samples were taken to the P09 beamline at PETRA III, DESY, yet no evidence of magnetic order was found. This is not evidence of an absence of low temperature magnetic order in these materials since the doping may suppress the magnetic ordering temperature, the cryostat may have not been able to cool the sample enough, and the poor structural quality of the samples may have lead to a 'smearing' of the magnetic Bragg peak intensity - rendering the intensity of the magnetic signal to be beyond the sensitivity of the instrument. A 5% Li-doped sample was taken to the I16 beamline at the Diamond Light Source, and a magnetic scattering signal was measured. This magnetic signal was localised as a series of peaks in reciprocal space, and the temperature and energy dependence of the scattering intensity of one of these peaks confirmed that the sample magnetically orders at low temperature. Polarisation analysis allowed the magnetic structure to be experimentally determined, and was found to be similar to the magnetic structure of the parent compound Na_2IrO_3. Furthermore, the observation of zig-zag ordering of the magnetic moments of the iridium sites is indicative of a Kitaev exchange interaction between the moments.

Chapter 2

Introduction to Quantum Magnetism

This thesis presents the study of magnetism in materials with periodic crystal structures that include transition metal ions that possess localised magnetic moments that undergo interactions which stabilise magnetic ground states and support magnetic excitations. In this chapter, details of magnetic interactions, structures, and excitations that are typical of honeycomb lattices of transition metal ions are introduced.

2.1 Magnetic Moments

Consider a free ion which possesses a magnetic moment originating from the constituent electrons. The electron has an angular momentum $\hbar\hat{\mathbf{s}}$ from the spin degree of freedom which has an associated magnetic moment $\hat{\boldsymbol{\mu}}_s = -g\mu_B\hat{\mathbf{s}}$, where the μ_B is Bohr magneton given by $\mu_B = e\hbar/2m_e = 0.0579\ \text{meV}\cdot\text{T}^{-1}$, e is the magnitude of the charge of the electron, m_e is the mass of the electron, and $\hbar$ is the reduced Planck constant. The value for g for a free electron is given by $g = 2(1 + \alpha/2\pi + \mathcal{O}(\alpha^2))$, where the $\mathcal{O}(\alpha)$ corrections are due to the interaction of the electron with the electromagnetic field as described by quantum electrodynamics [1]. The fine structure constant is given by $\alpha = e^2/4\pi\epsilon_0\hbar c \approx 1/137$. The electron also has a contribution to the magnetic moment from the orbital angular momentum $\hbar\hat{\mathbf{l}}$ given by $\hat{\boldsymbol{\mu}}_l = -\mu_B\hat{\mathbf{l}}$. The constituent electrons in the ion can then be considered as moving

in a spherically symmetric potential arising from the electrostatic attraction to the atomic nucleus and repulsion from other electrons. The wavefunction for an electron in the ions may be written as $\varphi_{nlm}(r,\theta,\phi) = R_{nl}(r)Y_{lm}(\theta,\phi)$, where the angular dependence - $Y_{lm}(\theta,\phi)$ - is a spherical harmonic. The wavefunction is described by three quantum numbers which take integer values: the principal quantum number n, the orbital angular momentum quantum number l ($0 < l < n$), and the magnetic quantum number m ($-l \leq m \leq l$). Since the electron is a spin-1/2 particle, the electron state can be doubly occupied - once by each spin state. The energy of each electron state will be dependent on the principal and orbital quantum numbers, but independent of the magnetic quantum number and the electron spin. Consequently, there will be $2(2l+1)$ degenerate states of energy E_{nl}, and each set of degenerate states is called a shell. The ground state electronic configuration of the ion will have shells in order of increasing energy occupied by electrons. The orbital and spin angular momenta of the electrons in a filled shell will sum to zero and will not contribute to the magnetic moment. Hence, only partially filled - or valence - shells will contribute to the electronic magnetic moment of the ion. The Coulomb interaction between the valence electrons commutes with the total orbital - $\hat{\mathbf{L}}$ - and total spin - $\hat{\mathbf{S}}$ - angular momentum operators defined by

$$\hat{\mathbf{L}} = \sum_i \hat{\mathbf{l}}_i, \qquad \hat{\mathbf{S}} = \sum_i \hat{\mathbf{s}}_i, \tag{2.1}$$

where the sums in each expression are over the electrons in the valence shell. Consequently the eigenvalues of the total orbital and total spin angular momentum will be good quantum numbers, denoted by L and S, respectively. Consequently, the valence shell will consist of multiplets with $(2L+1)(2S+1)$-fold degeneracy with the ground state multiplet having values of L and S that usually obey Hund's rules: the state that maximises L selected from the set of states that maximise S is the ground state multiplet.

The next order perturbation to the electronic ground state of a free-ion is a spin-orbit coupling arising from the magnetic interaction between the spin magnetic moment and the magnetic field induced by the orbital motion. An electron moving with velocity $\mathbf{v}$ in the

electric field $\mathbf{E}$ of the atomic nucleus experiences a magnetic field of

$$\mathbf{B} = \frac{\mathbf{v} \times \mathbf{E}}{c^2}.$$

The Hamiltonian describing the interaction of an electron spin with this magnetic field is then given by

$$\hat{H}_{so,i} = \zeta(r_i)\hat{\mathbf{l}}_i \cdot \hat{\mathbf{s}}_i, \tag{2.2}$$

where $\zeta(r_i)$ contains the functional dependence of the interaction strength as a function of the electronic radius r_i, and is strictly positive. This Hamiltonian describes an interaction between the spin and orbital components of the wavefunctions of a single electron in the valence shell of a free-ion. By application of Hund's rules, it can be noted that if the valence shell is less than half-occupied, then all spins are parallel; if the valence shell is more than half-occupied, then contributions from electrons with parallel orbital angular momenta and antiparallel spins will exactly cancel. Summation over all electrons in the valence shell can be performed by replacing $\hat{\mathbf{s}}_i$ by $\pm\hat{\mathbf{S}}/2S$ where the $+/-$ sign is used for a valence shell with less/more than half occupancy. Consequently the spin-orbit Hamiltonian for the Hund's rule ground state can be found by summing equation 2.2 over all electrons in the valence shell and is given by

$$\hat{H}_{so} = \lambda\hat{\mathbf{L}} \cdot \hat{\mathbf{S}}, \tag{2.3}$$

where the spin-orbit coupling parameter λ is positive for a valence shell with less than half occupancy, and negative for a valence shell with more than half occupancy. This Hamiltonian will break the degeneracy of the multiplet since $\hat{\mathbf{L}}$ and $\hat{\mathbf{S}}$ do not commute with the spin-orbit Hamiltonian. However, the total angular momentum $\hat{\mathbf{J}} = \hat{\mathbf{L}} + \hat{\mathbf{S}}$ does commute with the spin-orbit Hamiltonian, and so J is is a good quantum number which takes integer values from $|L - S|$ to $L + S$. The eigenvalues of the spin-orbit Hamiltonian are given by

$$E_{so} = \frac{\lambda}{2}\left[J(J+1) - L(L+1) - S(S+1)\right], \tag{2.4}$$

and so the ground state has a degeneracy of $2J+1$ with $J = |L-S|$ for $\lambda > 0$, and $J = L+S$ for $\lambda < 0$. The magnetic moment of the free ion is given by

$$\hat{\mathbf{M}} = -\mu_B(\hat{\mathbf{L}} + g\hat{\mathbf{S}}). \tag{2.5}$$

Which does not commute with the spin-orbit Hamiltonian, but via the Wigner-Eckart theorem may be written as to lie along the direction of $\hat{\mathbf{J}}$ up to some constant g_J. By assuming $g_S = 2$, the magnetic moment is given by $\hat{\mathbf{M}} = -g_J\mu_B\hat{\mathbf{J}}$ where

$$g_J = \frac{3}{2} + \frac{S(S+1) - L(L+1)}{2J(J+1)}. \tag{2.6}$$

This treatment holds for a free-ion with a valence shell that obeys Hund's rules and has a coupling between the total spin and total orbital angular momenta. However, the materials of interest in this thesis contain additional ions that surround the magnetic ions. In all three systems studied, the magnetic ions are surrounded by an octahedron of oxygen ions which will expose the magnetic ion to an inhomogeneous electric field and reduce the symmetry of the local environment from the spherical symmetry of the free-ion to a discrete rotational symmetry of the crystal field. In order to determine the effect of the crystal electric field on the state of the electronic valence shell of a magnetic ion, it is important to consider the hierarchy of energy scales: the interaction between the crystal field and valence electrons, the Coulomb repulsion of electrons in the free ion, and the spin-orbit coupling of the spin and orbital degrees of freedom. For two of the materials presented in this thesis - $CoTiO_3$ and $FeTiO_3$ - with a $3d$ valence shell, the dominant energy scale is the interelectronic Coulomb interaction, giving a ground state multiplet where L and S are good quantum numbers. The octahedral crystal field acts as a perturbation on the total orbital angular momentum states defined by the operator $\hat{\mathbf{L}}$. In both $CoTiO_3$ and $FeTiO_3$, as presented in further detail in sections 4.3 and 5.3, the ground state will be an effective total orbital angular momentum triplet. The next order perturbation is the spin-orbit coupling and trigonal distortion which

will act on the ground state defined by the total spin angular momentum and the effective total orbital angular momentum states.

On the other hand, the remaining material presented in this thesis has a $5d$ valence shell. Although the electronic wavefunctions in a free $5d$ ion has the same angular dependence as the wavefunction in a free $3d$ ion, the radial wavefunctions differ significantly such that the leading order energy scale upon the valence electrons in the honeycomb iridates - presented in Chapter 6 - is the crystal electric field from the surrounding octahedron of oxygen ions. The spherical symmetry of the free-ion is reduced to the octahedral symmetry of the crystal field, lifting the degeneracy of the five single electron orbital states into a ground state t_{2g} orbital triplet and an excited e_g orbital doublet [2]. The valence electrons of the Ir^{4+} ions occupy the t_{2g} orbital triplet to give an $l_{\text{eff}} = 1$ effective total orbital angular momentum state, and an $S = 1/2$ total spin angular momentum state upon which the spin-orbit interaction acts to give an effective $j_{\text{eff}} = 1/2$ state [3].

2.2 Magnetic Exchange and Magnetic Order

At low temperatures, ionic crystals containing magnetic ions may exhibit ordered states stabilised by interactions between the magnetic moments on each site of the lattice. The interaction between the spin degrees of freedom of two magnetic ions originating from the exchange term of the Coulomb interaction between d electrons on neighbouring ions can be written in the form [4]

$$\hat{H}_{i,j} = J_{i,j}\hat{\mathbf{S}}_i \cdot \hat{\mathbf{S}}_j, \tag{2.7}$$

where the indices i and j denote the positions of the magnetic moments, and $J_{i,j}$ is the exchange coupling between the two ions denotes by i and j. For $J_{i,j} < 0$, the energy of the exchange Hamiltonian is minimised if the pair of spins are aligned, giving a ferromagnetic coupling; for $J_{i,j} > 0$, the energy of the exchange Hamiltonian is minimised if the pair of spins are antiparallel, giving an antiferromagnetic coupling. For a many-body system with multiple differing Heisenberg interactions between the spin degrees of freedom, the generic form of the Heisenberg interaction takes the form

$$\hat{H}_{HB} = \sum_{i,j} J(\mathbf{r}_i - \mathbf{r}_j)\hat{\mathbf{S}}_i \cdot \hat{\mathbf{S}}_j. \tag{2.8}$$

Although the eigenvalues and eigenvectors of the Heisenberg Hamiltonian are difficult to find in general, the ground state of a Bravais lattice of spins may be solved by considering the spin degrees of freedom on each site as a classical vector. Provided the Heisenberg interaction is symmetric under the exchange of two sites, the ground state energy may be written in terms of Fourier components of the spin degrees of freedom - expressed as $\mathbf{S}_\mathbf{q} = \frac{1}{\sqrt{N}} \sum_j \mathbf{S}_j e^{i\mathbf{q}\cdot\mathbf{r}_j}$ - and exchange interaction in the form

$$E_{GS} = \sum_{\mathbf{q}} J(\mathbf{q})\mathbf{S}_\mathbf{q} \cdot \mathbf{S}_{-\mathbf{q}}, \tag{2.9}$$

which is minimised if $\mathbf{S}_\mathbf{q}$ vanishes except for $\mathbf{q} = \pm\mathbf{Q}$ where the Fourier components of the exchange interaction - $J(\mathbf{q})$ - are minimised. The general solution for the ground state orientation of the magnetic moments $\mathbf{S}_i$ in a single Bravais lattice - with one spin per primitive unit cell - is a helical spin structure [5, 6]. The $\mathbf{Q} = 0$ solution corresponds to ferromagnetic ordering, and antiferromagnetic ordering corresponds to $\mathbf{Q}$ being located on the Brillouin zone boundary.

The magnetic interaction described by the Heisenberg interaction is isotropic and symmetric under the exchange of the positions of the magnetic moments. In general, magnetic interactions may occur via higher order perturbative processes and lead to anisotropic exchange interactions such as XXZ exchange, Dzyaloshinskii-Moriya exchange, or Kitaev exchange. XXZ exchange interactions have differing strength couplings between components of spins parallel and perpendicular to a given axis and can be written in the form

$$\hat{H}_{XXZ} = \sum_{i,j} \left[J^{\perp}_{i,j} \left(\hat{S}^x_i \hat{S}^x_j + \hat{S}^y_i \hat{S}^y_j \right) + J^z_{i,j} \hat{S}^z_i \hat{S}^z_j \right]. \tag{2.10}$$

For an interaction between the spin degrees of freedom of two magnetic moments, easy-plane ordering where moments are confined to the xy plane are selected for $|J^{\perp}_{i,j}| > |J^z_{i,j}|$. Conversely, in the opposing limit, where $|J^{\perp}_{i,j}| < |J^z_{i,j}|$, the moments are confined to the z axis and are easy-axis ordered. In the limit $|J^{\perp}_{i,j}| = |J^z_{i,j}|$, the isotropic Heisenberg exchange

interaction is recovered.

Dzyaloshinskii-Moriya interactions may be considered on phenomenological grounds as an antisymmetric exchange interaction between two magnetic moments and hence takes the form [7]

$$\hat{H}_{DM} = \sum_{i,j} \mathbf{D}_{i,j} \cdot \left(\hat{\mathbf{S}}_i \times \hat{\mathbf{S}}_j \right). \tag{2.11}$$

The vector $\mathbf{D}_{i,j}$ must vanish if the bond connecting sites i and j has inversion symmetry at the midpoint of the bond. Similarly, there are a number of constraints placed upon the vector $\mathbf{D}_{i,j}$ based on the symmetry of the associated bond [8].

- For a mirror plane through the midpoint of the bond and perpendicular to the bond direction, $\mathbf{D}$ is perpendicular to the bond direction and contained in the mirror plane
- For a mirror plane containing the bond, $\mathbf{D}$ is perpendicular to the mirror plane
- For a two-fold rotation axis through the midpoint of the bond and perpendicular to the bond direction, $\mathbf{D}$ is perpendicular to the two-fold rotation axis
- For an n-fold rotation axis along the bond direction, $\mathbf{D}$ is parallel to the rotational axis

Magnetic systems with an antiferromagnetic easy plane anisotropic exchange interaction will consist of two magnetic sublattices aligned antiparallel with respect to each other. The inclusion of an additional small Dzyaloshinskii-Moriya coupling between sites of the two magnetic sublattices and oriented normal to the easy plane will cant the magnetic moments inside the easy plane by a small angle and provide a ferromagnetic component perpendicular to the direction of spin orientation and the Dzyaloshinskii-Moriya vector - an archetypical example of spin canting is the magnetic structure of $\alpha - Fe_2O_3$ [8].

Kitaev interactions are anisotropic exchange interactions where the direction of the nearest neighbour bond determines which component of the magnetic moments of neighbouring ions are coupled, and can expressed by the Hamiltonian

$$\hat{H}_K = K \sum_{\langle i,j \rangle_\gamma} \hat{S}_i^\gamma \hat{S}_j^\gamma. \tag{2.12}$$

On the honeycomb lattice, there are three distinct nearest neighbour bonds, and each bond may be assigned to couple mutually orthogonal components of the magnetic moments - this component is labelled by γ and is dependent on which bond connects sites i and j. Since the couplings are mutually orthogonal, the magnetic moments cannot simultaneously co-align along each axis, resulting in the full quantum solution of this model for $S = 1/2$ being a highly entangled state - a quantum spin liquid. This ground state is an exact solution for $S = 1/2$ and supports two sets of Majorana fermions, one set can propagate through the lattice, whereas the other set are static fluxes defined for each honeycomb plaquette. Although this model exhibits local magnetic order, there is no long range magnetic order [9]. A honeycomb system with magnetic interactions described by a combination of Heisenberg and Kitaev nearest neighbour exchange couplings may support a quantum spin liquid phase - without magnetic ordering - in the limit of large Kitaev exchange. A ferromagnetic state - where all spins are parallel - or Néel antiferromagnetic state - where neighbouring spins are antiparallel - will be exhibited in the limit of large Heisenberg exchange. More exotic phases such as stripy or zigzag ordered phases may be exhibited when the magnitude of the Heisenberg and Kitaev exchanges are comparable [3, 10, 11].

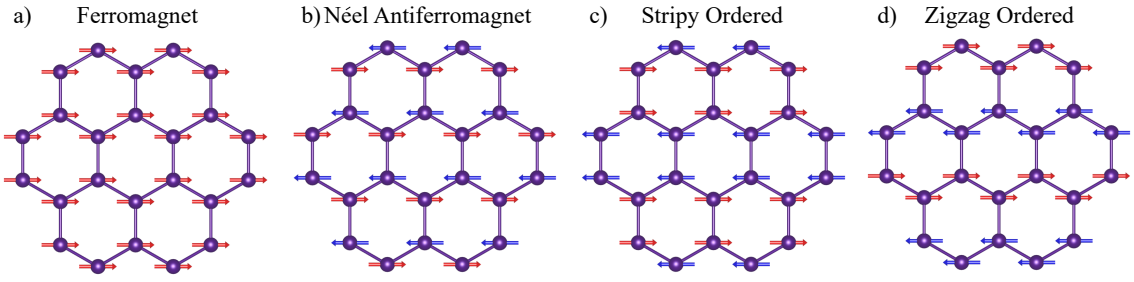

Figure 2.1: Magnetically ordered phases of the Heisenberg-Kitaev model on the honeycomb lattice showing a) ferromagnetic ordering, b) Néel ordering, c) stripy ordering, and d) zigzag ordering.

2.3 Magnetic Excitations: Linear Spinwave Theory

The low energy excitations of a magnetically ordered system can be considered as deviations from the ground state. In the case of a spin-1/2 Heisenberg ferromagnet, with a ground state configuration consisting of all spins aligned, a single spin flipped from the ferromagnetic ground state is an excited state. Such an excited state is not an eigenstate with the Heisenberg Hamiltonian in equation 2.8, but the eigenstate is a state that may be considered as a wave of spin flips that move across the lattice of ordered spins. These excitations are known as spinwaves, and are quantised as magnons - $S = 1$ quasiparticles - with a dispersion relation which may be modelled using linear spinwave theory.

In order to model the magnon dispersions of a Heisenberg ferromagnet on the honeycomb lattice, consider the Heisenberg Hamiltonian

$$\hat{H}_{HB} = J \sum_{\langle i,j \rangle} \hat{\mathbf{S}}_i^{\mathrm{A}} \cdot \hat{\mathbf{S}}_j^{\mathrm{B}} = J \sum_{\langle i,j \rangle} \left[\hat{S}_i^{\mathrm{A}z} \hat{S}_j^{\mathrm{B}z} + \frac{1}{2} \left(\hat{S}_i^{\mathrm{A}+} \hat{S}_j^{\mathrm{B}-} + \hat{S}_i^{\mathrm{A}-} \hat{S}_j^{\mathrm{B}+} \right) \right] \tag{2.13}$$

where the exchange parameter $J < 0$ stabilises a magnetic ground state with ferromagnetic ordering between spins of the two sublattices. The honeycomb lattice consists of two sublattices denoted by A and B, with spin-operators $\hat{\mathbf{S}}_i^A$ and $\hat{\mathbf{S}}_j^B$ on sites i and j defined on the A and B sublattice, respectively. The nearest neighbour bonds on the honeycomb layer connect A sublattice sites with B sublattice sites, and vice-versa. The sum is over pairs of sites connected by a nearest neighbour bond and is such that each bond is only counted once. Rather than considering the interaction of neighbouring spins, it is useful to transform to a Hamiltonian that describes spin flip bosons. In this case, the ground state of the ordered ferromagnet can be thought as a lattice of sites of unoccupied sites. A spin flip at a given site is equivalent to the creation of a boson at that site. The Heisenberg Hamiltonian describing spins on a lattice interacting via exchange can be mapped to a Hamiltonian describing the dynamics of spin-flip bosons using the Holstein-Primakoff transformation [12]

$$
\begin{aligned}
\hat{S}_i^{\mathrm{A}z} &= S - \hat{a}_i^\dagger \hat{a}_i, \\
\hat{S}_i^{\mathrm{A}+} &= \sqrt{2S}\sqrt{1 - \frac{\hat{a}_i^\dagger \hat{a}_i}{2S}}\hat{a}_i, \\
\hat{S}_i^{\mathrm{A}-} &= \sqrt{2S}\hat{a}_i^\dagger\sqrt{1 - \frac{\hat{a}_i^\dagger \hat{a}_i}{2S}}, \\
\hat{S}_i^{\mathrm{B}z} &= S - \hat{b}_i^\dagger \hat{b}_i, \\
\hat{S}_i^{\mathrm{B}+} &= \sqrt{2S}\sqrt{1 - \frac{\hat{b}_i^\dagger \hat{b}_i}{2S}}\hat{b}_i, \\
\hat{S}_i^{\mathrm{B}-} &= \sqrt{2S}\hat{b}_i^\dagger\sqrt{1 - \frac{\hat{b}_i^\dagger \hat{b}_i}{2S}}.
\end{aligned}
\tag{2.14}
$$

Where the direction of the ordered spin is taken to lie along the $\hat{\mathbf{z}}$ direction. Performing the Holstein-Primakoff transformation on the Hamiltonian in equation 2.13 requires an expansion in $1/S$. It is assumed that $1/S$ is a small parameter, but linear spinwave theory is also often used to extract functional forms of magnon dispersions in $S = 1/2$ systems. The expansion of the Heisenberg Hamiltonian will contain a term that is quadratic in bosonic operators which is of the form

$$
\hat{H}_{HB} = -JS\sum_{i\in\mathrm{A}}\sum_{\boldsymbol{\delta}_1}\left(\hat{a}_i^\dagger \hat{a}_i + \hat{b}_{i+\boldsymbol{\delta}_1}^\dagger \hat{b}_{i+\boldsymbol{\delta}_1} - \hat{a}_i \hat{b}_{i+\boldsymbol{\delta}_1}^\dagger - \hat{a}_i^\dagger \hat{b}_{i+\boldsymbol{\delta}_1}\right). \tag{2.15}
$$

This quadratic form contains a sum over sites i on the A sublattice, and another sum over the three nearest neighbour bonds that connect each A sublattice site to neighbouring B sublattice sites. The final two terms in the sum connect sites of differing sublattices and so the Hamiltonian is of the form of a coupled oscillator. The next step is to write the operators acting on lattice sites in terms of operators acting on Fourier modes, as defined by

$$\begin{aligned}
\hat{a}_{\mathbf{k}} &= \sqrt{\frac{2}{N}} \sum_{i \in A} e^{-i\mathbf{k}\cdot\mathbf{x}_i} \hat{a}_i, \\
\hat{a}^{\dagger}_{\mathbf{k}} &= \sqrt{\frac{2}{N}} \sum_{i \in A} e^{i\mathbf{k}\cdot\mathbf{x}_i} \hat{a}^{\dagger}_i, \\
\hat{b}_{\mathbf{k}} &= \sqrt{\frac{2}{N}} \sum_{i \in B} e^{-i\mathbf{k}\cdot\mathbf{x}_i} \hat{b}_i, \\
\hat{b}^{\dagger}_{\mathbf{k}} &= \sqrt{\frac{2}{N}} \sum_{i \in B} e^{i\mathbf{k}\cdot\mathbf{x}_i} \hat{b}^{\dagger}_i.
\end{aligned} \tag{2.16}$$

Consequently, the Hamiltonian in equation 2.15 can be written as

$$\hat{H}_{HB} = \sum_{\mathbf{k}} \begin{pmatrix} \hat{a}^{\dagger}_{\mathbf{k}} & \hat{b}^{\dagger}_{\mathbf{k}} \end{pmatrix} \begin{pmatrix} -3JS & JS\gamma_{1\mathbf{k}} \\ JS\gamma^{*}_{1\mathbf{k}} & -3JS \end{pmatrix} \begin{pmatrix} \hat{a}_{\mathbf{k}} \\ \hat{b}_{\mathbf{k}} \end{pmatrix}, \tag{2.17}$$

where the term $\gamma_{1\mathbf{k}} = \sum_{\boldsymbol{\delta}_1} e^{i\mathbf{k}\cdot\boldsymbol{\delta}_1}$ is defined in terms of the first nearest neighbour bonds. The dispersions and dynamical correlations - which are proportional to the inelastic neutron scattering intensity - can be calculated by diagonalising the Hamiltonian in equation 2.17. There will be two modes with dispersions $\omega_{\pm}(\mathbf{k})$ and dynamical correlations $S^{xx}(\mathbf{k}, \omega)$ given by

$$\begin{aligned}
\omega_{\pm}(\mathbf{k}) &= |J|\, S\left(3 \pm |\gamma_{1\mathbf{k}}|\right), \\
S^{xx}(\mathbf{k}, \omega) &= S \sin^2 \frac{\phi}{2} \times \delta\left(\omega - \omega_{+}(\mathbf{k})\right) + S \cos^2 \frac{\phi}{2} \times \delta\left(\omega - \omega_{-}(\mathbf{k})\right),
\end{aligned} \tag{2.18}$$

where the angle ϕ is the phase of the complex number $\gamma_{1\mathbf{k}}$. The magnon band structure calculated using linear spin wave theory is plotted in figure 2.2 and shows two bands with a crossing point at the corners of the Brillouin zone - denoted by K and K' - with a linear dispersion $\omega(\mathbf{k}) = v|\mathbf{k}|$.

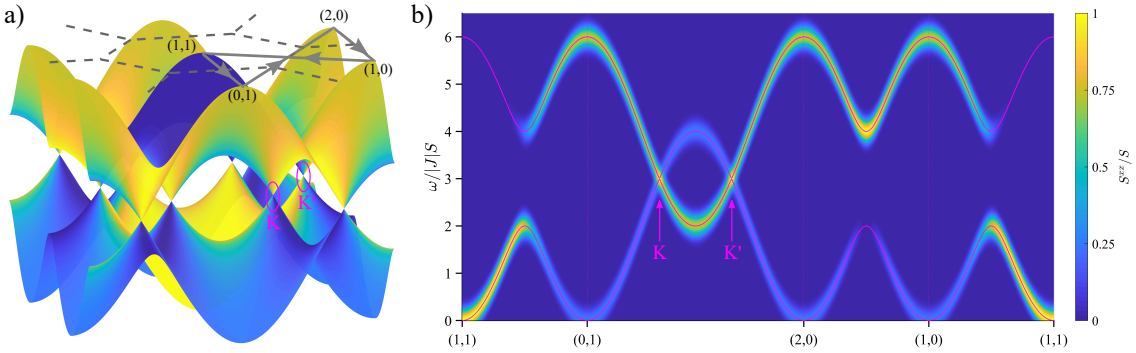

Figure 2.2: Visualisation of the magnon band structure of a two dimensional honeycomb lattice with nearest neighbour ferromagnetic Heisenberg couplings. a) Surface plot of magnon dispersions. The linear crossing points at the corners of the Brillouin zone are indicated by the magenta ellipses and labelled by K and K'. The grey dashed line plotted above the band structure denotes the Brillouin zone. b) A two-dimensional slice can be taken through the magnon band structure along the path through reciprocal space denoted by the lighter grey solid lines in (a). The magenta lines denote the dispersions ω plotted as a function of momentum. The colour of the band structure in both (a) and (b) denotes the value of the dynamical correlation S^{xx} in units of the spin S.

2.4 Nodal Lines in the Honeycomb Quantum Magnets $CoTiO_3$ and $FeTiO_3$

By expanding the Hamiltonian in equation 2.17 around the linear crossing points at K, the effective Hamiltonian takes the form $\hat{H}_{\text{eff}} = v\,(k_x\hat{\sigma}_x + k_y\hat{\sigma}_y)$. The Dirac velocity v is given by $\sqrt{3}|J|Sa/2$. The two indices of the operators $\hat{\sigma}_x$ and $\hat{\sigma}_y$ correspond to the two sublattices of the honeycomb layer. This effective Hamiltonian is the massless Dirac equation [13], and so the linear touching points have been named Dirac points. Such physics has been previously studied for the electronic band structure in graphene [14], where the touching point is at the Fermi surface of undoped graphene. Conversely for magnon dispersions there is no Fermi surface associated with the bosonic quasiparticles and the touching point is at finite energy $\omega_0 = 3|J|S$.

$CoTiO_3$ and $FeTiO_3$ are isostructural materials which contain transition metal ions with a $3d$ valence shell that possess a magnetic moment and form honeycomb layers that are stacked in three dimensions. In three dimensional materials with stacked honeycomb layers, the Dirac point extends in reciprocal space to form a Dirac nodal line [15]. In contrast to fermionic electrons hopping on the honeycomb lattice of graphene, the magnetic excitations

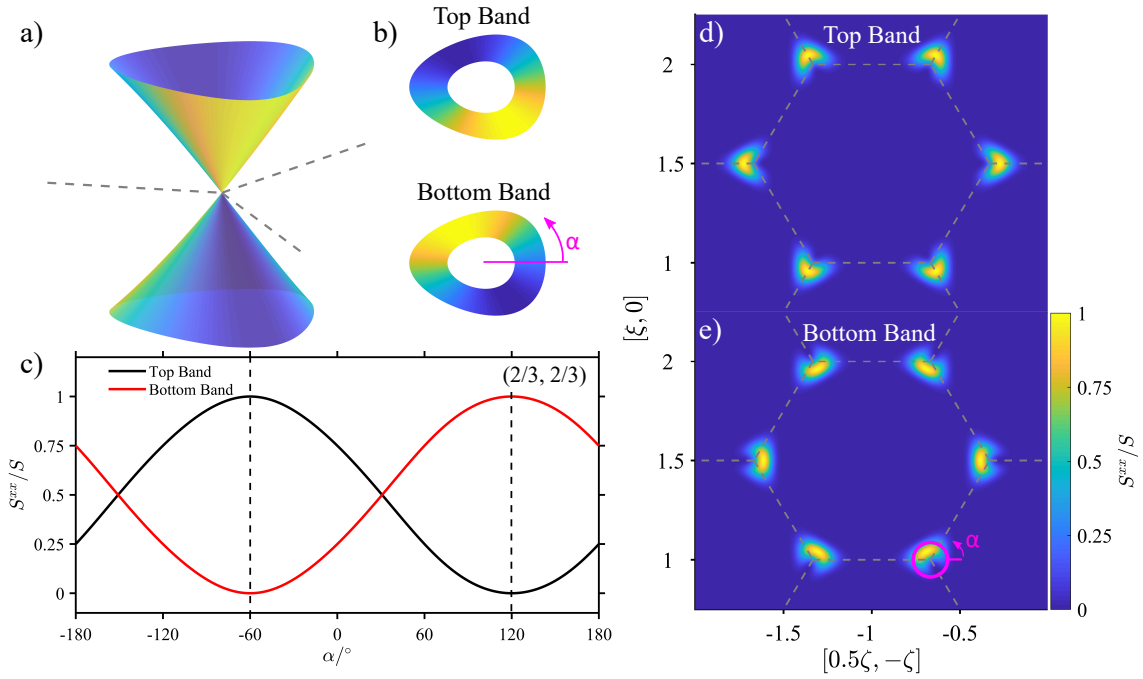

Figure 2.3: Visualisation of the azimuthal profile of the dynamical correlations at the K point of a two dimensional honeycomb Heisenberg ferromagnet. a) Conical dispersion at a Dirac nodal point. b) Winding pattern of the dynamical correlations for the top and bottom bands. c) Azimuthal cuts at constant energy of the dynamical correlation S^{xx} around the $(2/3, 2/3)$ nodal point. The dashed vertical lines denote the azimuthal angles $\alpha = -60°$ and $120°$ where the dynamical correlations take their extremal values. These values of azimuth correspond to the angle subtended from the centre of the Brillouin zone to the Dirac nodal point, and vice-versa. The azimuthal winding takes a two-fold periodicity with the top and bottom bands 180° out of phase. d/e) Constant energy slices of the hk plane above/below the crossing point of the magnon bands at the nodal points. The dashed grey lines outline the edges of the Brillouin zone. The upper band has a concentration of the dynamical correlations outside the Brillouin zone, whereas the lower band has a concentration of the dynamical correlations mostly inside the Brillouin zone. The magenta circle in (e) highlights the $(2/3, 2/3)$ nodal point with the curly arrow denoting the direction of α as plotted in (c).

- magnons - which are supported by the stacked honeycomb lattices of $CoTiO_3$ and $FeTiO_3$ are bosonic quasiparticles. Signatures of Dirac physics in a two dimensional Heisenberg ferromagnet are linear crossing points in the magnon dispersions ω and a winding of the dynamical correlation S^{xx} around the corners of the Brillouin zone, as presented in figure 2.3. As presented subsequently in section 3.1, the inelastic neutron scattering intensity is proportional to the dynamical correlation, and so inelastic neutron scattering provides an ideal technique to measure and experimentally observe bosonic Dirac quasiparticles, and

explore their behaviour in three dimensional systems.

2.5 Kitaev Physics in the Honeycomb Iridates $\mathcal{A}_2\mathrm{IrO}_3$

For honeycomb materials where the magnetic ion is a transition metal ion with a $5d$ valence shell, the energy scale of the spin-orbit coupling becomes comparable to the crystal field splitting. Strong spin orbit coupling can give rise to novel phases such as quantum spin liquids exhibiting excitations with fractional statistics, topological insulators with symmetry protected surface states, and magnetic states with unconventional ordering [11]. Such unconventional magnetic states may contain a bond dependent anisotropic interaction which will become frustrated on a honeycomb lattice. Honeycomb iridates of the form $\mathcal{A}_2\mathrm{IrO}_3$ where $\mathcal{A} = \mathrm{Li}, \mathrm{Na}$ contain Ir^{4+} ions with the electronic configuration [Xe] $4f^{14}$ $5d^5$, which possess a magnetic moment. These ions experience a strong crystal field splitting from the surrounding octahedron of O^{2-} ions leading to the fivefold degeneracy of the free d-ions splitting into a ground state t_{2g} triplet and an excited e_g doublet. The d^5 electronic configuration populate the t_{2g} triplet with a total spin angular momentum of $S = 1/2$, which can alternatively be considered as a single hole in an effective $l = 1$ state with wavefunctions

$$\begin{aligned} |l^z = 1\rangle &= -i\,|-1\rangle\,, \\ |l^z = 0\rangle &= \frac{-i}{\sqrt{2}}\left(|2\rangle - |-2\rangle\right), \\ |l^z = -1\rangle &= i\,|1\rangle\,, \end{aligned} \tag{2.19}$$

defined in terms of the $|L_z\rangle$ states of the atomic d levels. The angular momentum operator of the atomic levels - $\hat{\mathbf{L}}$ - is equivalent to $-\hat{\mathbf{l}}$.

The spin-orbit coupling $\hat{H}_{SO} = \lambda\hat{\mathbf{l}}\cdot\hat{\mathbf{S}}$ with $\lambda > 0$ acts on the single hole in the t_{2g} level. By defining an effective angular momentum $\hat{\mathbf{J}}_{\text{eff}} = \hat{\mathbf{l}} + \hat{\mathbf{S}}$ where J_{eff} is a good quantum number of the eigenstates of the spin-orbit Hamiltonian, the hole in the t_{2g} level has a ground state $J_{\text{eff}} = 1/2$ doublet and an excited $J_{\text{eff}} = 3/2$ quadruplet with wavefunctions

$$
\begin{aligned}
|J_{\text{eff}} = 3/2, J^z_{\text{eff}} = \pm 3/2\rangle &= |\pm 1, \pm 1/2\rangle \\
|J_{\text{eff}} = 3/2, J^z_{\text{eff}} = \pm 1/2\rangle &= \frac{1}{\sqrt{3}} |\pm 1, \mp 1/2\rangle + \sqrt{\frac{2}{3}} |0, \pm 1/2\rangle \\
|J_{\text{eff}} = 1/2, J^z_{\text{eff}} = \pm 1/2\rangle &= \pm\sqrt{\frac{2}{3}} |\pm 1, \mp 1/2\rangle \mp \frac{1}{\sqrt{3}} |0, \pm 1/2\rangle
\end{aligned}
\tag{2.20}
$$

defined in the $|l_z, S_z\rangle$ basis.

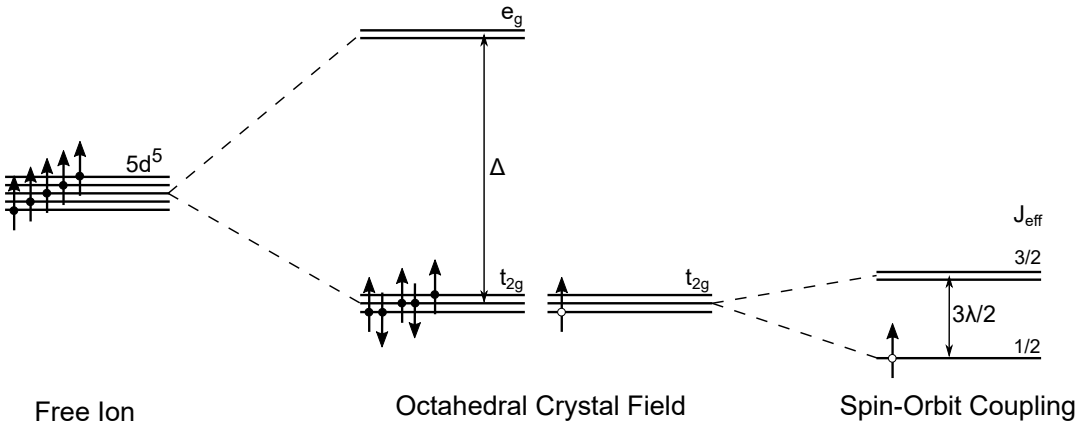

Figure 2.4: Single ion spectrum for Ir^{4+} ions. The octahedral crystal field splits the five-fold degenerate $5d^5$ orbitals into a triplet - labeled by t_{2g} - and a doublet - labeled by e_g. The large crystal field splitting, Δ, results in a low spin state, where the electrons only occupy the t_{2g} level. The are five electrons, or equivalently a single hole, occupying the t_{2g} orbital. Due to spin-orbit coupling, the hole in the t_{2g} manifold gives rise to a $J_{\text{eff}} = 1/2$ Kramer's doublet.

It can be shown that the isotropic components of the exchange interaction between neighbouring Ir^{4+} ions exactly cancel in an idealised honeycomb lattice of edge sharing octahedra with Ir-O-Ir bond angles of exactly 90° [3]. Instead, the exchange between neighbouring ions is anisotropic and dependent on the bond direction, with the direction of spin coupling normal to the plane containing the two Ir-O-Ir bonds. This can be expressed with the Kitaev Hamiltonian in equation 2.12

Na_2IrO_3 and α-Li_2IrO_3 are isostructural honeycomb iridates containing edge sharing IrO_3 octahedra slightly distorted such that the Ir-O-Ir bond angles deviate from the ideal 90° angle by around 10°. As a consequence, the low energy physics of these magnetic systems will have isotropic exchange in addition to anisotropic couplings, including Kitaev

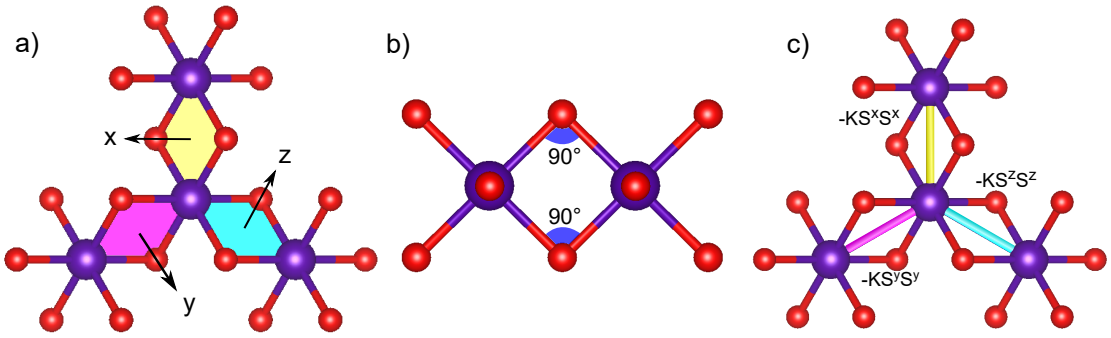

Figure 2.5: Bond geometry for the ideal honeycomb lattice with edge sharing octahedra. a) The magnetic ions in a honeycomb lattice have three nearest neighbours, and each pair of neighbours shares two Ir-O-Ir exchange paths which defines a plane - highlighted in yellow, magenta, and cyan. A Cartesian coordinate system x, y, and z can be defined using the unit vectors normal to each plane. b) The Ir-O-Ir bond angle for the ideal honeycomb lattice is 90° which leads to a vanishing isotropic exchange between neighbouring ions. c) The exchange between ions is anisotropic and dependent on the bond direction, with the easy axis along the normal of the Ir-O_2-Ir planes. Since these axes are all mutually perpendicular the energy of each bond cannot be simultaneously minimized, leading to frustration.

coupling [10]

$$\hat{H} = \sum_{\substack{<ij>\in\gamma \\ \alpha\neq\beta\neq\gamma}} \left[J\hat{\mathbf{S}}_i \cdot \hat{\mathbf{S}}_j + K\hat{S}_i^{\gamma}\hat{S}_j^{\gamma} + \Gamma\left(\hat{S}_i^{\alpha}\hat{S}_j^{\beta} + \hat{S}_i^{\beta}\hat{S}_j^{\alpha}\right)\right]. \tag{2.21}$$

Theoretical calculations show that inclusion of an isotropic Heisenberg interaction, J, and an anisotropic pseudo-dipolar interaction, Γ, may stabilise magnetic phases such as conventional ferromagnetic and antiferromagnetic phases, in addition to exotic phases - such as stripy, zig-zag, and spiral ordering - and suppress the quantum spin liquid phase [10].

Magnetic resonant X-ray diffraction experiments performed on α-Li_2IrO_3 reveal a counter-rotating spiral order [16]; inelastic neutron scattering on powdered Na_2IrO_3 reveal zig-zag ordering [17]. Both counter-rotating spiral and zig-zag order are key signatures of Kitaev exchange, but since these materials exhibit magnetic ordering, they are not quantum spin liquids. This theoretical treatment can be extended to the hyperhoneycomb and harmonic honeycomb lattices [18], where symmetry allowed non-Kitaev couplings can suppress the quantum spin liquid phase and stabilise exotic magnetic phases. The magnetic structures of the $\beta-$ and $\gamma-$polytypes of Li_2IrO_3 have been measured experimentally using magnetic

resonant X-ray diffraction and were found, like the $\alpha-$polytype, to exhibit counter-rotating spiral ordering [19] [20].

Honeycomb iridates can be isoelectronically doped from Na_2IrO_3 to α-Li_2IrO_3 as $(Na_{1-x}Li_x)_2IrO_3$. It has been proposed that the Néel temperature will be suppressed upon doping [11] since the exchange parameters in the Hamiltonian for the honeycomb iridates - and hence their magnetic ground states - are sensitive to electronic doping from Na and Li ions. Such honeycomb iridate samples can be synthesised for $0 < x < 0.25$ [21], and so the effect of electronic doping upon the magnetic ground states of these materials can be investigated. Chapter 6 presents an investigation of the structural and magnetic properties of such materials using X-ray diffraction techniques.

References

1. Peskin, M. E. & Schroeder, D. V. *An Introduction to Quantum Field Theory* (Addison-Wesley, 1995).

2. Abragam, A. & Bleaney, B. *Electron Paramagnetic Resonance of Transition Ions* (Oxford University Press, 1970).

3. Jackeli, G. & Khaliullin, G. Mott Insulators in the Strong Spin-Orbit Coupling Limit: From Heisenberg to a Quantum Compass and Kitaev Models. *Phys. Rev. Lett.* **102,** 017205 (2009).

4. Heisenberg, W. Mehrkörperproblem und Resonanz in der Quantenmechanik. *Z. Phys.* **38** (1926).

5. Luttinger, J. M. & Tisza, L. Theory of Dipole Interaction in Crystals. *Phys. Rev.* **70,** 954–964 (11-12 Dec. 1946).

6. Lyons, D. H. & Kaplan, T. A. Method for Determining Ground-State Spin Configurations. *Phys. Rev.* **120,** 1580–1585 (1960).

7. Dzyaloshinskii, I. A thermodynamic theory of "weak" ferromagnetism of antiferromagnetics. *Journal of Physics and Chemistry of Solids* **4,** 241–255 (1958).

8. Moriya, T. Anisotropic Superexchange Interaction and Weak Ferromagnetism. *Phys. Rev.* **120,** 91–98 (1960).

9. Kitaev, A. Anyons in an exactly solved model and beyond. *Ann. Phys.* **321,** 2 (2006).

10. Rau, J. G., Lee, E. K.-H. & Kee, H.-Y. Generic Spin Model for the Honeycomb Iridates beyond the Kitaev Limit. *Phys. Rev. Lett.* **112,** 077204 (2014).

11. Rau, J. G., Lee, E. K.-H. & Kee, H.-Y. Spin-Orbit Physics Giving Rise to Novel Phases in Correlated Systems: Iridates and Related Materials. *Annual Review of Condensed Matter Physics,* 195–221 (2016).

12. Holstein, T. & Primakoff, H. Field Dependence of the Intrinsic Domain Magnetization of a Ferromagnet. *Phys. Rev.* **58,** 1098–1113 (1940).

13. Dirac, P. A. M. The Quantum Theory of the Electron. *Proceedings of the Royal Society of London* **117,** 610–624 (1928).

14. Castro Neto, A. H., Guinea, F., Peres, N. M. R., Novoselov, K. S. & Geim, A. K. The electronic properties of graphene. *Rev. Mod. Phys.* **81,** 109–162 (2009).

15. Pershoguba, S. S. *et al.* Dirac Magnons in Honeycomb Ferromagnets. *Phys. Rev. X* **8** (2018).

16. Williams, S. C. *et al.* Incommensurate counterrotating magnetic order stabilized by Kitaev interactions in the layered honeycomb $\alpha-Li_2IrO_3$. *Phys. Rev. B* **93,** 195158 (2016).

17. Choi, S. K. *et al.* Spin Waves and Revised Crystal Structure of Honeycomb Iridate Na_2IrO_3. *Phys. Rev. Lett.* **108,** 127204 (2012).

18. Lee, E. K.-H. & Kim, Y. B. Theory of magnetic phase diagrams in hyperhoneycomb and harmonic-honeycomb iridates. *Phys. Rev. B* **91,** 064407 (2015).

19. Biffin, A. *et al.* Unconventional magnetic order on the hyperhoneycomb Kitaev lattice in $\beta-Li_2IrO_3$: Full solution via magnetic resonant x-ray diffraction. *Phys. Rev. B* **90,** 205116 (2014).

20. Biffin, A. *et al.* Noncoplanar and Counterrotating Incommensurate Magnetic Order Stabilized by Kitaev Interactions in $\gamma-Li_2IrO_3$. *Phys. Rev. Lett.* **113,** 197201 (2014).

21. Manni, S. *et al.* Effect of isoelectronic doping on the honeycomb-lattice iridate A_2IrO_3. *Phys. Rev. B* **89,** 245113 (2014).

22. Yosida, K. *Theory of Magnetism* (Springer, 1996).

Chapter 3

Experimental Techniques

In this chapter, the experimental techniques of neutron and X-ray scattering will be introduced. Neutron scattering is a useful technique for probing the structural and magnetic properties of condensed matter systems, and there are many textbooks which provide excellent accounts of the physical principles behind behind this technique, namely those written by Squires [1], Boothroyd [2], and Lovesey [3]. The de Broglie wavelength of a thermal neutron is on the order of interatomic distances in solids and so interference effects due to thermal neutron scattering will be dependent on the structure of the material involved in scattering. Additionally, the kinetic energy of a thermal neutron is on the order of the milli-electron volt, which is comparable to the energy of the typical excitations of interest in condensed matter systems. Although electrically neutral, neutrons carry a magnetic moment, allowing for the neutron to penetrate the scattering system and measure the nuclear and magnetic properties in the bulk of the sample. Because of this feature, it is a requirement for almost all users of neutron scattering to use a sufficiently bulky sample as the scattering system. As a result, nuclear scattering can be used to determine information about the atomic structure, and magnetic scattering can be used to determine information about the magnetic properties of the scattering system in bulk. Elastic scattering - where the neutron is diffracted by the scattering system, transferring momentum without transferring energy - is used to measure properties of the atomic and magnetic structure of the sample; inelastic scattering - where both energy and momentum are transferred to the scattering system - can be used to measure the dynamics of structural and magnetic

excitations supported by the sample. Time-of-flight spectroscopy will also be presented along with details of the LET and MERLIN spectrometers - located at the ISIS Neutron and Muon Source - that were used for the undertaking of work presented in this thesis.

X-ray scattering is a complimentary technique to neutron scattering. Away from resonance, incident x-rays are sensitive to the charge distribution in a material, and so elastic x-ray scattering can be used to determine the structural order, and consequently also identify the lattice vectors of a crystalline sample. When the energy of an incident x-ray is tuned to resonance - where a core electron in one of the constituent ions can be excited to the valence shell - the x-ray scattering intensity is dependent on the direction of the magnetic moment of the scattering material. Consequently, resonant elastic x-ray scattering (REXS) can be used to experimentally determine the magnetic structure in magnetic materials. As lab based sources of x-rays - such as the Oxford Diffraction Supernova and Rigaku Smartlab diffractometers - are more readily available, with their operation detailed in this chapter, it is useful to use x-ray diffraction to characterise the crystal structure of a material in preparation for a neutron or resonant x-ray scattering experiment. Furthermore, details of the I16 and P09 diffractometers based at the Diamond Light Source and PETRA III synchrotrons are presented.

3.1 Neutron Scattering Cross Section

In a neutron scattering experiment a neutron beam of flux Φ, initial wavevector $\mathbf{k}$, and initial energy E is incident upon the sample. Some of these neutrons will be scattered by the sample and as a result have wavevector $\mathbf{k}'$ and energy E'. The rate of neutrons detected by the detector subtending a solid angle $\Delta\Omega$ with some energy resolution $\Delta E'$ and efficiency η will is given by

$$I = \eta\Phi\frac{d^2\sigma}{d\Omega dE'}\Delta\Omega\Delta E', \tag{3.1}$$

where $d^2\sigma/d\Omega dE'$ is the partial differential cross section, which is the quantity measured experimentally in a scattering experiment that can be related to theoretical models. The scattering geometry is depicted in figure 3.1.

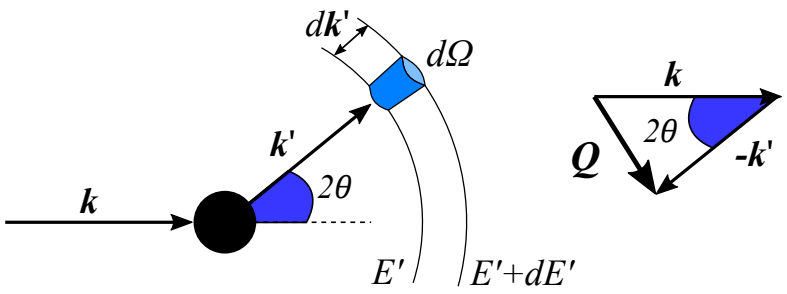

Figure 3.1: Left: Scattering geometry for a neutron scattering experiment. A neutron with incident wavevector $\mathbf{k}$ is scattered into a small volume $k'^2 dk' d\Omega$. Right: The scattering triangle depicting the definition of the scattered wavevector $\mathbf{Q} = \mathbf{k} - \mathbf{k}'$ and the scattering angle 2θ.

Suppose a neutron with momentum $\mathbf{k}$ and spin state σ is incident upon a scattering system with state λ. The neutron may interact with some interaction potential $\hat{V}$, scatter with final momentum $\mathbf{k}'$ and spin state σ', and transition the scattering system into a state λ'. Treating this process as a first-order perturbation, the transition rate is obtained using the Fermi Golden Rule

$$\Gamma_{\mathbf{k}\sigma\lambda\to\mathbf{k}'\sigma'\lambda'} = \frac{2\pi}{\hbar} |\langle \mathbf{k}'\sigma'\lambda'|\hat{V}|\mathbf{k}\sigma\lambda\rangle|^2 \rho(\mathbf{k}'), \tag{3.2}$$

where $\rho(\mathbf{k}')$ is the number of states of momentum $\mathbf{k}'$ per solid angle per unit energy. The partial differential cross section for transitions from state λ to λ' can be written as

$$\begin{aligned}\left(\frac{d^2\sigma}{d\Omega dE'}\right)_{\mathbf{k}\sigma\lambda\to\mathbf{k}'\sigma'\lambda'} &= \frac{1}{\Phi}\frac{1}{\Delta\Omega}\Gamma_{\mathbf{k}\sigma\lambda\to\mathbf{k}'\sigma'\lambda'}\delta\left(E - E' + E_\lambda - E'_\lambda\right), \\ &= \left(\frac{m}{2\pi\hbar^2}\right)^2 \frac{k'}{k}\left|\langle \mathbf{k}'\sigma'\lambda'|\hat{V}|\mathbf{k}\sigma\lambda\rangle\right|^2 \delta\left(E - E' + E_\lambda - E'_\lambda\right).\end{aligned} \tag{3.3}$$

Upon scattering the neutron will transfer energy $E - E'$ into the crystal, creating an excitation in the sample with energy given by $E'_\lambda - E_\lambda = \hbar\omega$. In order to conserve energy, the excitation energy $\hbar\omega$ must equal the energy $E - E'$ transferred into the sample. By assuming that the incident and scattered neutron wavefunctions are plane waves, the matrix element $\langle \mathbf{k}'\sigma'\lambda'|\hat{V}(\mathbf{r})|\mathbf{k}\sigma\lambda\rangle$ can be written in terms of the Fourier transform of the scattering potential $\langle \sigma'\lambda'|\hat{V}(\mathbf{Q})|\sigma\lambda\rangle$, where $\mathbf{Q} = \mathbf{k} - \mathbf{k}'$ is the scattering wavevector and $\hat{V}(\mathbf{Q})$ is given

by

$$\hat{V}(\mathbf{Q}) = \int \hat{V}(\mathbf{r}) e^{i\mathbf{Q}\cdot\mathbf{r}} d^3\mathbf{r}, \tag{3.4}$$

where $\mathbf{r}$ is the position of the neutron. In general, the scattering system may exist in one of a variety of different initial states λ, with a statistical distribution with probability p_λ of the system having the initial state λ. Similarly, the scattering experiment will excite the system to one of multiple scattered states λ', and so a sum over scattered states λ' and an average over initial states λ is taken to find the partial differential scattering cross section for all allowed processes. Similarly, for experiments with unpolarised neutrons, a sum over the final spin states σ' and an average over the initial spin states σ must be taken. As a result, the partial differential cross section takes the form

$$\left(\frac{d^2\sigma}{d\Omega dE'}\right) = \frac{k'}{k}\left(\frac{m}{2\pi\hbar^2}\right)^2 \sum_{\lambda,\lambda'} p_\lambda \sum_{\sigma,\sigma'} p_\sigma \left|\langle\sigma'\lambda'|\hat{V}(\mathbf{Q})|\sigma\lambda\rangle\right|^2 \delta\left(\hbar\omega + E_\lambda - E'_\lambda\right). \tag{3.5}$$

3.1.1 Nuclear Scattering

Now consider the scattering of neutrons by the atomic nuclei of the scattering system. The scattering potential experienced by a neutron in the presence of a single nucleus is very short range and so can be written in the form of the Fermi pseudopotential

$$\hat{V}(\mathbf{r}) = \frac{2\pi\hbar^2}{m} b\delta(\mathbf{r}), \tag{3.6}$$

where b is the scattering length of the nuclear interaction. The magnitude of b is a measure of the interaction strength, with $b > 0$ for a repulsive interaction, and $b < 0$ for an attractive interaction. For a collection of scattering sites with scattering length b_j at position $\mathbf{R}_j$, then the potential experienced by the neutron is

$$\hat{V}(\mathbf{r}) = \tfrac{2\pi\hbar^2}{m}\textstyle\sum_j b_j \delta(\mathbf{r} - \mathbf{R}_j), \quad \hat{V}(\mathbf{Q}) = \tfrac{2\pi\hbar^2}{m}\textstyle\sum_j b_j e^{i\mathbf{Q}\cdot\mathbf{R}_j}, \tag{3.7}$$

where $\hat{V}(\mathbf{Q})$ was obtained by equation 3.4. This potential has no spin dependence and

so holds in the case where the nucleus has no spin, or where the incoming neutrons are unpolarised. Since $\hat{V}(\mathbf{Q})$ is independent of the initial and final spin state of the scattering system, the partial differential cross section due to nuclear scattering takes the form

$$\left(\frac{d^2\sigma}{d\Omega dE'}\right)_{\text{nuc.}} = \frac{k'}{k}\sum_{\lambda,\lambda'} p_\lambda \left|\sum_j b_j \langle\lambda'|e^{i\mathbf{Q}\cdot\mathbf{R}_j}|\lambda\rangle\right|^2 \delta\left(\hbar\omega + E_\lambda - E'_\lambda\right). \tag{3.8}$$

The Dirac delta function can be represented as an integral over the time domain, in which case the partial differential cross section becomes

$$\left(\frac{d^2\sigma}{d\Omega dE'}\right)_{\text{nuc.}} = \frac{1}{2\pi\hbar}\frac{k'}{k}\sum_{j,j'} b_j b_{j'} \int_{-\infty}^{+\infty} \langle e^{-i\mathbf{Q}\cdot\mathbf{R}_{j'}(0)} e^{+i\mathbf{Q}\cdot\mathbf{R}_j(t)}\rangle\, e^{-i\omega t} dt, \tag{3.9}$$

where $\hbar\omega$ is the energy transferred by the neutron. The angled brackets in the equation above denote an average of the operator over all initial states λ, i.e. $\langle\hat{A}\rangle = \sum_\lambda \langle\lambda|\hat{A}|\lambda\rangle$. In a scattering system consisting of many nuclei, there will be a distribution of scattering lengths such that a nucleus with scattering length b_j will be present in the sample with frequency f_j. Consequently, averages of the scattering length and its square for each nuclear site can be defined as follows

$$\textstyle\sum_j f_j = 1, \quad \bar{b} = \sum_j f_j b_j, \quad \bar{b^2} = \sum_j f_j b_j^2. \tag{3.10}$$

The cross section averaged over all possible arrangements of scattering lengths is then given by

$$\left(\frac{d^2\sigma}{d\Omega dE'}\right)_{\text{nuc.}} = \left(\frac{d^2\sigma}{d\Omega dE'}\right)_{\text{coh.}} + \left(\frac{d^2\sigma}{d\Omega dE'}\right)_{\text{inc.}}, \tag{3.11}$$

where the first term is the coherent scattering cross section, and the second term is the incoherent scattering cross section. These terms take the following forms

$$\begin{aligned}\left(\frac{d^2\sigma}{d\Omega dE'}\right)_{\text{coh.}} &= \frac{\sigma_{\text{coh.}}}{4\pi}\frac{1}{2\pi\hbar}\frac{k'}{k}\int_{-\infty}^{+\infty}\sum_{j,j'}\langle e^{-i\mathbf{Q}\cdot\mathbf{R}_{j'}(0)}e^{+i\mathbf{Q}\cdot\mathbf{R}_j(t)}\rangle\, e^{-i\omega t}dt,\\ \left(\frac{d^2\sigma}{d\Omega dE'}\right)_{\text{inc.}} &= \frac{\sigma_{\text{inc.}}}{4\pi}\frac{1}{2\pi\hbar}\frac{k'}{k}\int_{-\infty}^{+\infty}\sum_{j}\langle e^{-i\mathbf{Q}\cdot\mathbf{R}_{j}(0)}e^{+i\mathbf{Q}\cdot\mathbf{R}_j(t)}\rangle\, e^{-i\omega t}dt,\end{aligned} \tag{3.12}$$

where $\sigma_{\text{coh.}} = 4\pi\bar{b^2}$ and $\sigma_{\text{inc.}} = 4\pi\left(\bar{b^2} - \bar{b}^2\right)$. The coherent scattering term is dependent on correlations between nuclei at different sites and therefore will lead to interference effects. This term is furthermore identical if all scattering lengths b_j were replaced by their mean. The incoherent scattering term is dependent only on the correlation of the position of the same nucleus and is proportional to the variance of the scattering lengths of all nuclei in the sample.

Now it is assumed that the scattering system is crystalline. In the case of a Bravais lattice where each site is static - i.e. without thermal fluctuations - the correlation terms can be easily evaluated

$$\begin{aligned}\sum_{j,j'}\langle e^{-i\mathbf{Q}\cdot\mathbf{R}_{j'}(0)}e^{+i\mathbf{Q}\cdot\mathbf{R}_j(t)}\rangle &= \sum_{j,j'}\langle e^{i\mathbf{Q}\cdot(\mathbf{R}_j-\mathbf{R}_{j'})}\rangle\delta(t),\\ &= \frac{(2\pi)^3 N}{v_0}\sum_{\boldsymbol{\tau}}\delta(\mathbf{Q}-\boldsymbol{\tau})\delta(t),\\ \sum_{j}\langle e^{-i\mathbf{Q}\cdot\mathbf{R}_{j}(0)}e^{+i\mathbf{Q}\cdot\mathbf{R}_j(t)}\rangle &= N\delta(t),\end{aligned} \tag{3.13}$$

where N is the number of unit cells in the sample, v_0 is the volume of the unit cell. $\boldsymbol{\tau}$ is a reciprocal lattice vector. The partial scattering cross sections for coherent and incoherent scattering in equation 3.12 become

$$\begin{aligned}\left(\frac{d\sigma}{d\Omega}\right)_{\text{coh.el.}} &= \frac{(2\pi)^3 N}{v_0}\frac{\sigma_{\text{coh.}}}{4\pi}\sum_{\boldsymbol{\tau}}\delta(\mathbf{Q}-\boldsymbol{\tau}),\\ \left(\frac{d\sigma}{d\Omega}\right)_{\text{inc.el.}} &= N\frac{\sigma_{\text{inc.}}}{4\pi}.\end{aligned} \tag{3.14}$$

Note that the energy dependence has been integrated out and both cross sections provide

scattering intensity in elastic nuclear scattering. The coherent elastic scattering term will provide sharp features corresponding to when the momentum transfer $\mathbf{Q}$ is equal to a reciprocal lattice vector $\boldsymbol{\tau}$ - this is precisely the Laue condition for elastic scattering, and these features are structural Bragg peaks. Conversely, the incoherent scattering will be featureless and provide a constant background in elastic scattering.

There will also be a contribution to the nuclear scattering cross section corresponding to oscillations of the nuclei about their equilibrium positions. Such oscillations will alter the elastic scattering terms in equations 3.14, multiplying them by e^{-2W}, where W is known as the Debye-Waller factor, and is temperature dependent. In inelastic scattering, this contribution can be considered as a neutron transferring energy into the crystal scattering system and exciting a vibrational mode. These quantised vibrational modes are also known as phonons. Phonons can be thermally excited in a crystal material, with the number of excited phonons being temperature dependent according to Bose-Einstein statistics. There will be an inelastic scattering contribution due to the excitation of a single phonon in a scattering event. The inelastic coherent scattering will provide sharp phonon modes, with a diffuse background due to inelastic scattering.

3.1.2 Magnetic Scattering

This section will extend the previously presented ideas and techniques to consider the interaction between neutrons and unpaired atomic electrons in the scattering system. The neutron and atomic electrons both carry magnetic dipole moments, allowing for a magnetic interaction between the two particles. Following the convention of Squires [1], the magnetic dipole moment of the neutron is given by

$$\hat{\boldsymbol{\mu}}_n = -\gamma \mu_N \hat{\boldsymbol{\sigma}}, \tag{3.15}$$

where $\mu_N = e\hbar/2m_p$ is the nuclear magneton (with e and m_p denoting the magnitude of the electron charge and the proton mass, respectively) and γ is the gyromagnetic ratio of the neutron, with the value 1.913. $\boldsymbol{\sigma}$ is the Pauli operator for the spin of the neutron and has eigenvalues of each component are ± 1. The electron has an intrinsic angular momentum $\hbar\mathbf{s}$

due to the spin degree of freedom, where the eigenvalues of each component of $\mathbf{s}$ are $\pm 1/2$. This intrinsic angular momentum has an associated magnetic moment

$$\hat{\boldsymbol{\mu}}_e = -g\mu_B \hat{\mathbf{s}}, \tag{3.16}$$

where $\mu_B = e\hbar/2m_e$ is the Bohr magneton and $g \approx 2$. The potential arising due to a magnetic interaction between a neutron and a single electron with position operator $\hat{\mathbf{R}}$ and momentum operator $\hat{\mathbf{p}}$ is given by

$$\hat{V}_{\text{mag.}} = -\frac{\mu_0}{4\pi} g\gamma\mu_N\mu_B \hat{\boldsymbol{\sigma}} \cdot \left[\boldsymbol{\nabla} \times \left(\frac{\hat{\mathbf{s}} \times \hat{\mathbf{R}}}{R^3} \right) + \frac{\hat{\mathbf{p}} \times \hat{\mathbf{R}}}{\hbar R^2} \right], \tag{3.17}$$

where the two terms in the square brackets correspond to the interaction of the neutron spin with the magnetic moments arising from the electron spin and the electron orbital angular momentum, respectively. The partial differential cross section can be found by evaluating equation 3.5 which is significantly more difficult for magnetic scattering than for nuclear scattering since the magnetic interaction is neither short range nor a central force, instead depending on multiple vector quantities. A detailed derivation is provided in Squires [1]. The partial differential cross section due to magnetic scattering takes the form

$$\left(\frac{d^2\sigma}{d\Omega dE'} \right)_{\text{mag.}} = N(\gamma r_0)^2 \frac{k'}{k} \left(\frac{1}{2} g F(\mathbf{Q}) \right)^2 e^{-2W} \sum_{\alpha,\beta} \left(\delta_{\alpha\beta} - \frac{Q_\alpha Q_\beta}{Q^2} \right) S^{\alpha\beta}(\mathbf{Q}, \omega), \tag{3.18}$$

where r_0 is the classical radius of the electron. Although a complicated expression, equation 3.18 can be thought of as a combination of different effects. Although the scattering potential in equation 3.17 described the magnetic interaction between a neutron and a single electron, this may be generalised to an atom with mutliple electrons in the valence shell, with a Landè g-factor g, and a magnetic form factor $F(\mathbf{Q})$, which captures the $\mathbf{Q}$ dependence of the magnetisation of the unpaired valence electrons [2]. W is the Debye-Waller factor which provides a temperature-dependent correction to the magnetic scattering cross section due to the oscillation of atoms in the scattering system about their equilibrium position. The sum over α and β is over spatial coordinates x, y, z. This sum includes

the polarisation factor $\left(\delta_{\alpha\beta} - \frac{Q_\alpha Q_\beta}{Q^2}\right)$, which arises due to the fact that magnetic neutron scattering is sensitive only to the component of the magnetic moment perpendicular to the scattering vector $\mathbf{Q}$. The final term is the dynamical structure factor $S^{\alpha\beta}(\mathbf{Q},\omega)$ which itself is given by

$$S^{\alpha\beta}(\mathbf{Q},\omega) = \frac{1}{N}\sum_{j,j'} e^{i\mathbf{Q}\cdot(\mathbf{R}_j - \mathbf{R}_{j'})} \times \frac{1}{2\pi\hbar}\int_{-\infty}^{\infty} \langle \hat{S}_j^\alpha(0)\hat{S}_{j'}^\beta(t)\rangle\, e^{-i\omega t} dt. \tag{3.19}$$

The dynamical structure factor contains a dynamical correlator $\langle \hat{S}_j^\alpha(0)\hat{S}_{j'}^\beta(t)\rangle$ which captures the correlation of the components of magnetic moments between different sites j and j' as a function of time t. This term captures the key physics describing the response of a magnetically ordered crystal in neutron scattering.

In order to illustrate how the magnetic scattering contribution to the partial differential cross section depends on the dynamical correlator, consider a paramagnetic material in the absence of an externally applied magnetic field. In this case, the components of the magnetic moments between different sites on the lattice are uncorrelated in time and so $\langle \hat{S}_j^\alpha(0)\hat{S}_{j'}^\beta(t)\rangle = \frac{1}{3}S(S+1)\delta^{\alpha\beta}\delta_{j,j'}$. Now the elastic contribution to the dynamical structure as defined in equation 3.19 takes the form

$$S^{\alpha\beta}(\mathbf{Q},\omega=0) = \frac{1}{3}S(S+1)\delta^{\alpha\beta}, \tag{3.20}$$

and consequently the elastic scattering cross section due to magnetic scattering from a paramagnet is given by

$$\left(\frac{d\sigma}{d\Omega}\right)_{\text{PM,el.}} = \frac{2}{3}NS(S+1)(\gamma r_0)^2 \left(\frac{1}{2}gF(\mathbf{Q})\right)^2 e^{-2W}. \tag{3.21}$$

Although this cross section has $\mathbf{Q}$ dependence in the form of the magnetic form factor $F(\mathbf{Q})$, the magnetic contribution to the neutron scattering signal will be a diffuse band of scattering along the elastic line.

Now consider a system that is ferromagnetically ordered, and all magnetic moments are aligned along the $\mathbf{z}$ axis. In this case, the dynamical correlator considered in the limit $t \to \infty$, corresponding to the case of elastic scattering, is given by $\langle \hat{S}_j^\alpha(0)\hat{S}_{j'}^\beta(t)\rangle = \langle S^z\rangle^2 \delta^{\alpha z}\delta^{\beta z}$,

which can be substituted into equation 3.19 to give the dynamical structure factor

$$S^{\alpha\beta}(\mathbf{Q},\omega=0) = \langle \hat{S}^z \rangle^2 \delta^{\alpha z}\delta^{\beta z}\frac{(2\pi)^3}{v_0}\sum_{\boldsymbol{\tau}}\delta(\mathbf{Q}-\boldsymbol{\tau}), \tag{3.22}$$

and by substitution into 3.18, the elastic scattering cross section due to magnetic scattering from a ferromagnet is given by

$$\left(\frac{d\sigma}{d\Omega}\right)_{\text{FM,el.}} = N(\gamma r_0)^2 \langle \hat{S}^z \rangle^2 \frac{(2\pi)^3}{v_0} e^{-2W}\sum_{\boldsymbol{\tau}}\left(\frac{1}{2}gF(\boldsymbol{\tau})\right)^2\left(1-\frac{\tau_z^2}{\tau^2}\right)\delta(\mathbf{Q}-\boldsymbol{\tau}). \tag{3.23}$$

Therefore, the elastic scattering cross section for magnetic neutron scattering from an ordered ferromagnet will has a momentum dependence on the magnetic form factor $F(\boldsymbol{\tau})$, polarisation factor $\left(1-\frac{\tau_z^2}{\tau^2}\right)$, and a delta function which will only allow magnetic scattering when the scattering vector $\mathbf{Q}$ is equal to a reciprocal lattice vector $\boldsymbol{\tau}$. For magnetic structures which are commensurate with the structural unit cell, a magnetic unit cell with the periodicity of the magnetic structure can be defined. The magnetic unit cell will have reciprocal lattice vectors $\boldsymbol{\tau}_m$, and the elastic magnetic scattering signal will have sharp features when the scattering vector $\mathbf{Q}$ is equal to the reciprocal lattice vectors of the magnetic unit cell, $\boldsymbol{\tau}_m$. As a magnetic material cools below a magnetic transition temperature T_N and the magnetic phase transitions from the disordered paramagnetic phase to an ordered commensurate magnetic phase, the elastic magnetic neutron scattering intensity transforms from being diffuse and featureless above T_N, to a sharply peaked diffuse intensity at T_N, and then transforms to sharp Bragg peaks at $\mathbf{Q}=\boldsymbol{\tau}_m$ as the temperature cools below T_N [4].

In magnetic neutron scattering, a neutron may transfer energy of $\hbar\omega$ via the magnetic scattering potential to a magnetically ordered crystal. Such an excitation can be considered as a spin-flip that promotes the magnetic ground state of the scattering system to an excited state. This spin-flip excitation may then propagate throughout the lattice in the form of a spinwave, and these quantised excitations are known as magnons. The inelastic magnetic neutron scattering cross section will include a one-magnon contribution which will provide

sharp modes. The calculation of the inelastic magnetic neutron scattering intensity and comparison with the experimentally neutron scattering data for the quantum magnetic materials $CoTiO_3$ and $FeTiO_3$ forms a key part of the work presented in chapters 4 and 5, respectively.

3.2 Time of Flight Spectrometry

The neutron scattering experiments performed for the work presented in this thesis were all undertaken at the ISIS Neutron and Muon Source using the MERLIN and LET time-of-flight (ToF) spectrometers - both depicted with the schematic diagrams in figure 3.2. At this facility, bunches of H^- ions are accelerated in a linear accelerator to 70 MeV. These H^- ions are then stripped of their electrons and the resulting protons are accelerated in a synchrotron to 800 MeV. Bunches of protons are extracted at a rate of 50 Hz with an average current of 200 μA, and sent to spallation targets. Spallation is a nuclear process where high energy particles bombard heavy nuclei - in this case, tungsten nuclei - which then undergo an energetic cascade and emit on average 20 to 40 neutrons per incident particle. The neutron pulses are then sent from the spallation target to a moderator to slow the neutrons down to thermal energies. For ToF spectrometry, it is necessary that the time width of each pulses is much smaller than the period between the pulses [5]. There are two spallation target stations at ISIS - TS1 and TS2. TS1 receives four of every five proton pulses from the synchrotron, and so the period of the neutron pulses from the spallation target is 50 Hz; TS2 receives only one of every five proton pulses and so the period of neutron pulses is 10 Hz. TS1 operates a water moderator at room temperature for the MERLIN spectrometer, in contrast to TS2 which uses a solid-methane moderator at 40 K for the LET spectrometer. Depending on the thermal coupling of the moderator to the spallation target, a significant fraction of the neutrons will thermalise with the moderator. The thermal neutrons will have energies that satisfy a Maxwellian distribution and will be accompanied by a high energy pulse of neutrons that did not thermalise with the moderator [5]. The neutron pulses will travel from the moderator to the sample via a supermirror guide.

The neutron pulse from the spallation target will be a white beam consisting of many

neutron energies. Both MERLIN and LET make use of choppers to extract monochromatic pulses from the white neutron beam. The choppers are rotating disks made of a neutron absorbing material with cutaway sections to allow neutrons to pass when aligned with the neutron beam. For MERLIN, the choppers are made of gadolinium [6], whereas the LET choppers are constructed from boron-10 coated carbon fibre disks [7]. By independently varying the rotation frequencies of several choppers, multiple energy ranges can be extracted from a single neutron pulse. This is known as repetition rate multiplication (RRM), and allows for simultaneous collection of inelastic neutron scattering data sets enabling more time efficient use of the spectrometers [8].

Neutron scattering processes are treated quite effectively within first order perturbation theory, as in equation 3.3, which is physically justified by the fact that the interaction between neutrons and matter is quite weak. The weakness of this interaction makes the detection of neutrons difficult, but is nonetheless possible via a nuclear capture mechanism. Both LET and MERLIN make use of a gas mixture that contains helium-3 to detect neutrons in which case the nuclear capture reaction is [5]

$$^{3}\mathrm{He} + \mathrm{n} \rightarrow \ ^{3}\mathrm{H} + \mathrm{p} + 0.8 \text{ MeV}. \tag{3.24}$$

The reaction products ionise the gas mixture, and the ionisation can be collected by a high-voltage anode. The gas detector is constructed within a cylindrical tube (3 m in length for MERLIN, and 4 m in length for LET) which is a position sensitive detector (PSD). A single PSD effectively consists of multiple pixels in a single detector. Forming a bank of PSD tubes creates a two-dimensional array of detector pixels where the distance and direction of each pixel from the sample position is known.

Furthermore, both MERLIN and LET ToF spectrometers operate in a direct geometry, where the incident neutron energy E_i is selected by the chopper configuration and the scattered neutron energy is measured via time-of-flight. The incident neutron wavevector is calculated from

$$E_i = \frac{\hbar^2 k_i^2}{2m}.$$

There is a known distance L_1 from the first chopper disk to the sample from which neutrons will be scattered. The time of flight in this region $\tau_{\text{samp.}}$ is given by

$$\tau_{\text{samp.}} = \frac{mL_1}{\hbar k_i}.$$

The neutron then scatters from the sample and into a detector element. The distance between the sample and the detector element is L_2, and the time of flight from the first chopper disk to the detector element detecting a neutron is $\tau_{\text{det.}}$. The magnitude of the scattered wavevector can then be calculated by

$$k_f = \frac{mL_2}{\hbar(\tau_{\text{det.}} - \tau_{\text{samp.}})}.$$

The direction of $\mathbf{k}_i$ will be along the direction of the incident beam, and the direction of $\mathbf{k}_f$ can be determined from the spherical angles θ and ϕ subtended by the detector element to the sample. Consequently the momentum and energy transfer $\mathbf{Q}$ and $\hbar\omega$ can be calculated by

$$\begin{aligned} \mathbf{Q} &= \mathbf{k}_i - \mathbf{k}_f, \\ \hbar\omega &= \frac{\hbar^2}{2m}\left(k_i^2 - k_f^2\right). \end{aligned}$$

For an neutron of incident energy E_i, there are 3 degrees of freedom that define each detected neutron - θ, ϕ, and $\tau_{\text{det.}}$. The range of these three values are determined by the size of the detector array and the incident neutron energy E_i, and give a three dimensional manifold throughout the four dimensions spanned by $\mathbf{Q}$ and ω. By performing a number of ToF scans and rotating the sample between each run, this three dimensional manifold will sweep across $\mathbf{Q}$ and ω to enable a four dimensional measurement of the INS intensity. The detector arrays of both MERLIN and LET cover a 180° angular range in the horizontal plane and a ±30° angular range in the vertical direction, providing a solid angle coverage of π steradians. This large solid angle coverage enabled the measurement of magnetic excitations throughout the entire Brillouin zone for both $CoTiO_3$ and $FeTiO_3$ [6, 7].

Although the MERLIN and LET instruments have many similarities, there are some design differences between the two instruments that suit them for different experimental requirements. For example, LET has a dynamical range of $0.6-80$ meV [7], whereas MERLIN is optimised to operate over a larger dynamical range of $10-1000$ meV [6]. Although TS2 receives a significantly smaller proton current than TS1, the cold solid methane moderator is a very effective moderator, compensating for the reduction in proton current by providing a large increase in neutron flux. The chopper system in LET is specifically designed to provide a very sharp energy resolution (around $0.8\%E_i$), and utilises the larger 100 ms time frame between pulses to make good use of RRM [7]. On the other hand, MERLIN was designed to operate with high intensity and medium energy resolution. Furthermore, there is a large aperture exposing the instrument to the moderator, increasing the neutron flux at the cost of reducing the $|\mathbf{Q}|$ resolution [6].

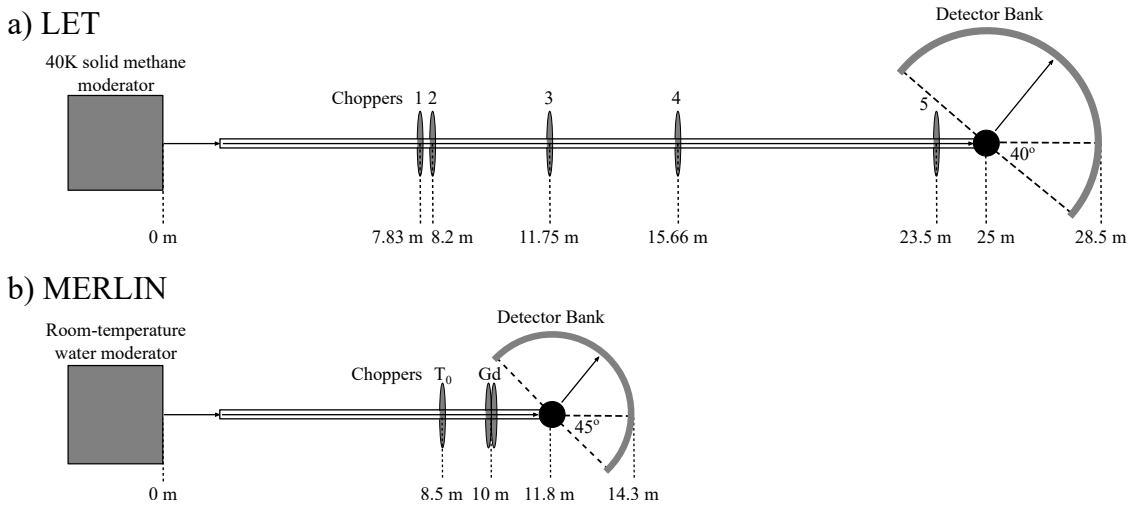

Figure 3.2: Schematic diagrams of the (a) LET [7] and (b) MERLIN [6] time-of-flight-spectrometers, depicted in plan view. The relative positions of the moderator (shaded square), flight path of a neutron (arrows), supermirror guide (rectangle), choppers (ellipses), sample (filled circle), and detector (shaded arc) are shown. LET uses a more complex system of choppers to obtain a higher energy resolution. MERLIN uses a system of gadolinium choppers to operate in RRM mode. LET has a larger detector array positioned further from the sample to obtain a greater wavevector resolution than MERLIN.

For the single crystal INS experiments, the $CoTiO_3$ and $FeTiO_3$ single crystal samples were mounted on custom designed sample holders. These sample holders were made of aluminium which has a small neutron absorption cross section and can be observed in the

scattering signal as powder rings on the elastic line. The sample holders were covered in cadmium foil, which has a high neutron absorption cross-section, in order to shield the bulk of the sample holder from the incident neutron beam. In order to ensure the scattering systems are in their respective ground states during the INS measurements, the experiments are performed at low temperatures. For both the single crystal experiments on $CoTiO_3$ and the zero-field measurements on $FeTiO_3$, a closed-cycle refrigerator (CCR) was used to cool the sample. A CCR operates via the compression and expansion of helium gas and can ideally cool the system down to 4 K, which is far below the magnetic ordering temperatures of $CoTiO_3$ ($T_N = 38$ K [9]) and $FeTiO_3$ ($T_N = 58$ K [10]). In the 'Orange Cryostat' design, helium exchange gas is used to cool the sample at the end of a 1 m long probe placed in a closed environment. The sample at the bottom of the probe is cooled to base temperature with the top of the probe at room temperature. The sample volume contains low pressure (2 mbar) helium gas, and the helium coolant flows around the outside of this volume. Baffles are placed along the probe to minimise convection between the warmer and colder regions in the sample volume [5]. INS measurements were also performed in an applied magnetic field in order to measure the evolution of the magnetic structure and magnetic excitations supported by $FeTiO_3$. In this case a cryomagnet, which is capable of applying a magnetic field up to 9 T, was used. The cryomagnet uses a pair of solenoids with a small gap in between to allow for neutrons to enter and be scattered out of the sample space. The presence of the solenoids near the sample space, however, restricts the angular range of the neutrons to 90° in the horizontal plane, and ±15° in the vertical direction [7].

The collection of INS data from a ToF spectrometer in direct geometry requires the processing and visualisation of large data sets, which is made possible by the recent availability of computational power and high capacity data storage. The processing of all time-of-flight neutron scattering data presented in this thesis was performed using the MANTID[11] and HORACE[12] data analysis packages.

3.3 Elastic and Resonant Elastic X-Ray Scattering

X-ray scattering is an experimental technique that can be used to complement inelastic neutron scattering, as lab based x-ray scattering instruments allow for the characterisation and alignment of crystal structures prior to a neutron scattering experiment at an external facility. Additionally, resonant elastic x-ray scattering (REXS) allows for measurements of magnetic structures, and in some instances may be preferred over elastic neutron scattering if only small sized samples are available or the sample is composed of isotopes that are strong neutron absorbers. Aspects of non-resonant and resonant elastic x-ray scattering will be presented to outline their respective use in determining structural and magnetic properties of crystalline materials.

3.3.1 Elastic X-Ray Scattering Amplitude

For coherent elastic x-ray scattering, the bound electrons in an atom will be exposed to incoming x-rays - of incident wavevector $\mathbf{k}$ - which have a time-dependent electric field. The bound electrons will oscillate with the same frequency of this applied electric field, and in turn radiate an electromagnetic wave of the same frequency and will have a scattered wavevector $\mathbf{k}'$. In a crystalline sample, many atoms are simultaneously irradiated. Consider atomic sites labelled by s, located at positions $\mathbf{R}_s$ that have an electron density $n_s(\mathbf{x})$, where $\mathbf{x}$ is defined as the displacement from the position $\mathbf{R}_s$. The x-rays scattered at a position $\mathbf{r}$ will have a phase difference of $e^{-i(\mathbf{k}'-\mathbf{k})\cdot\mathbf{r}}$. The coherent scattering amplitude from the electron density of all atoms in the sample is given by [13, 14]

$$f_{\text{coh.}}(\mathbf{Q}) = r_0 \sum_s \int n_s(\mathbf{r}-\mathbf{R}_s) e^{-i\mathbf{Q}\cdot\mathbf{r}} d\mathbf{r}, \tag{3.25}$$

where r_0 is the classical radius of the electron, the sum is over all atomic sites s in the sample, and the integral is over all space. The x-ray scattering intensity is then proportional to the absolute square of this scattering amplitude. $\mathbf{Q}$ is the scattered wavevector given by $\mathbf{k}'-\mathbf{k}$. The convention used in the x-ray scattering community is to define the scattering wavevector $\mathbf{Q}=\mathbf{k}'-\mathbf{k}$; the neutron scattering community defines the scattering wavevector in terms of momentum transfer: $\mathbf{Q}=\mathbf{k}-\mathbf{k}'$. Despite these two different definitions, the

fundamental physics is unchanged between the two conventions. Both conventions will be used in this thesis, but it should be noted that the definition of $\mathbf{Q}$ will change depending on the context in which it is used. Since the crystal has a periodic atomic structure, the sum over all atomic sites can be split into a sum over all unit cells m and all atomic sites j in a single unit cell. Consequently, the position $\mathbf{R}_s$ can be written as the sum of the position of the unit cell and the position of the atom j in the unit cell: $\mathbf{R}_m + \mathbf{R}_j$. Equation 3.25 then can be written in the form

$$f_{\text{coh.}}(\mathbf{Q}) = r_0 \sum_m e^{-i\mathbf{Q}\cdot\mathbf{R}_m} \sum_j e^{-i\mathbf{Q}\cdot\mathbf{R}_j} \int n_j(\mathbf{x}) e^{-i\mathbf{Q}\cdot\mathbf{x}} d\mathbf{x}. \tag{3.26}$$

Since $\mathbf{R}_m$ can be written as a linear combination of real-space lattice vectors, the term summed over all unit cells m will vanish unless $\mathbf{Q}$ is a reciprocal lattice vector $\boldsymbol{\tau}$. Furthermore, the integral is a Fourier transform of the electronic distribution of the atoms j, and is the atomic form factor - denoted by $f_j(\mathbf{Q})$. The expression for the coherent x-ray scattering amplitude in equation 3.26 can therefore be written in an even more concise form

$$f_{\text{coh.}}(\mathbf{Q}) = N r_0 \sum_j f_j(\mathbf{Q}) e^{-i\mathbf{Q}\cdot\mathbf{R}_j} \times \delta\left(\boldsymbol{\tau} - \mathbf{Q}\right), \tag{3.27}$$

where N is the number of unit cells in the sample. The form factor $f_j(\mathbf{Q})$ increases as the number of electrons Z in the scattering atom increases, and will decrease with increasing $\mathbf{Q}$ and so Bragg peaks will become weaker for larger values of $|\boldsymbol{\tau}|$. In x-ray diffraction, a set of Bragg peaks will be observed for $\mathbf{Q} = \boldsymbol{\tau}$, and so the x-ray scattering pattern will be defined by the reciprocal lattice of the crystal structure. By measuring the scattering pattern, details of the real-space lattice can be calculated from the reciprocal lattice. Since the scattering amplitude at the Bragg peak position $\boldsymbol{\tau}$ is proportional to the sum of atomic structure factors each multiplied by a phase factor $e^{-i\mathbf{Q}\cdot\mathbf{R}_j}$, the comparison of the intensities of a large collection of Bragg peaks allows for the refinement of atomic coordinates within the unit cell.

3.3.2 Resonant Elastic X-Ray Scattering Amplitude

There are additional elastic scattering processes resulting from the excitation of a core electron to a higher excited state in the atomic electronic configuration when the x-ray energy is tuned to the corresponding resonant energy. The atom will de-excite to its initial state and release a photon of the same energy. Consequently the partially filled electron shells may be probed in diffraction, and if such atoms possess a local magnetic moment, the resonant scattering amplitude will be dependent on the magnitude and direction of the local moment. The resonant contribution to the coherent elastic scattering amplitude from an electric 2^L-pole is given by [15]

$$f^{(e)}_{res.}(\omega) = \frac{4\pi}{k} f_D \sum_{M=-L}^{L} \left[\hat{\boldsymbol{\epsilon}}' \cdot \mathbf{Y}^{(e)}_{LM}(\hat{\mathbf{k}}') \mathbf{Y}^{(e)*}_{LM}(\hat{\mathbf{k}}) \cdot \hat{\boldsymbol{\epsilon}} \right] F^{(e)}_{LM}(\omega), \tag{3.28}$$

where f_D is the Debye-Waller factor as introduced in the expressions for neutron scattering and arises due to thermal fluctuations in the positions of the atomic positions about their equilibrium positions. $\boldsymbol{\epsilon}$ and $\boldsymbol{\epsilon}'$ are the polarisation vectors of the incident and scattered x-rays, which have wavevectors $\mathbf{k}$ and $\mathbf{k}'$, respectively. $\mathbf{Y}^{(e)}_{LM}$ are vector spherical harmonics and the factor $F^{(e)}_{LM}(\omega)$ is dependent on properties of the scattering atom and is given by [16]

$$F^{(e)}_{LM}(\omega) = \frac{1}{2} \sum_{n,m} \frac{P_n P_{n\to m} P^{(e)}_{rad.n,m}}{E_m - E_n - \hbar\omega - i\Gamma_{n,m}/2}, \tag{3.29}$$

where the sum is over initial state n and excited states m. P_n is the probability that the system is in the initial state n, and $P_{n\to m}$ is the probability that the system transitions from state n (of energy E_n) to a state m (of energy E_m) under the application of radiation with energy $\hbar\omega$. $P^{(e)}_{rad.n,m}$ is the probability that the process that de-excites the atom from the excited state m to the initial state n is due to the radiative decay of an electric 2^L-pole. $\Gamma_{n,m}$ is the linewidth of the radiative transition from n to m.

The resonant cross-section is typically dominated by electric dipole transitions. For example, in the resonant x-ray scattering experiments performed on the Li-doped samples of Na_2IrO_3, the x-ray energy was tuned to the Ir L_3 absorption edge which corresponds

to the $2p_{3/2} \rightarrow 5d_{1/2}$ transition. In the case of an electric dipole transition, the square bracketed term in equation 3.28 can be evaluated for $L = 1$ and $M = 0, \pm 1$ [16]

$$\begin{aligned}\left[\hat{\boldsymbol{\epsilon}}' \cdot \mathbf{Y}^{(e)}_{1,\pm1}(\hat{\mathbf{k}}')\mathbf{Y}^{(e)*}_{1,\pm1}(\hat{\mathbf{k}}) \cdot \hat{\boldsymbol{\epsilon}}\right] &= \frac{3}{16\pi}\left[\hat{\boldsymbol{\epsilon}}' \cdot \hat{\boldsymbol{\epsilon}} \mp i\left(\hat{\boldsymbol{\epsilon}}' \times \hat{\boldsymbol{\epsilon}}\right) \cdot \hat{\mathbf{z}}_n - \left(\hat{\boldsymbol{\epsilon}}' \cdot \hat{\mathbf{z}}_n\right)\left(\hat{\boldsymbol{\epsilon}} \cdot \hat{\mathbf{z}}_n\right)\right], \\ \left[\hat{\boldsymbol{\epsilon}}' \cdot \mathbf{Y}^{(e)}_{1,0}(\hat{\mathbf{k}}')\mathbf{Y}^{(e)*}_{1,0}(\hat{\mathbf{k}}) \cdot \hat{\boldsymbol{\epsilon}}\right] &= \frac{3}{8\pi}\left(\hat{\boldsymbol{\epsilon}}' \cdot \hat{\mathbf{z}}_n\right)\left(\hat{\boldsymbol{\epsilon}} \cdot \hat{\mathbf{z}}_n\right),\end{aligned} \tag{3.30}$$

where $\hat{\mathbf{z}}_n$ is a unit vector in the direction of the magnetic moment on the ion labelled by n. Consequently, by substituting the expressions in equation 3.30 into equation 3.28, the following expression is obtained for the resonant electric dipole contribution to the x-ray scattering amplitude of the nth ion

$$f^{(E1)}_{n,res.}(\omega) = \left[\left(\hat{\boldsymbol{\epsilon}}' \cdot \hat{\boldsymbol{\epsilon}}\right) F^{(0)} - i\left(\hat{\boldsymbol{\epsilon}}' \times \hat{\boldsymbol{\epsilon}}\right) \cdot \hat{\mathbf{z}}_n F^{(1)} + \left(\hat{\boldsymbol{\epsilon}}' \cdot \hat{\mathbf{z}}_n\right)\left(\hat{\boldsymbol{\epsilon}} \cdot \hat{\mathbf{z}}_n\right) F^{(2)}\right], \tag{3.31}$$

where the terms F^0, F^1, and F^2 are linear combinations of $F^{(e)}_{LM}(\omega)$ introduced in equation 3.29

$$\begin{aligned} F^{(0)} &= F^{(e)}_{1,1} + F^{(e)}_{1,-1}, \\ F^{(1)} &= F^{(e)}_{1,1} - F^{(e)}_{1,-1}, \\ F^{(2)} &= 2F^{(e)}_{1,0} - F^{(e)}_{1,1} - F^{(e)}_{1,-1}. \end{aligned} \tag{3.32}$$

The first term in equation 3.31 has no dependence on the magnetic moment direction and so will be proportional to the resonant charge scattering. The second and third terms are dependent on the direction of the magnetic moment and so are the magnetic contributions to the resonant scattering amplitude. This demonstrates that, in principle, the direction of the magnetic moment can be measured in resonant elastic x-ray scattering (REXS) provided that there is a degree of control over the incident polarisation $\boldsymbol{\epsilon}$ and by selectively measuring the scattering intensity for differing polarisations $\boldsymbol{\epsilon}'$ of the scattered beam. The polarisation

dependent terms in equation 3.31 can be written in the form of 2×2 matrices in the basis of polarisation states that are perpendicular and parallel to the scattering plane. The term proportional to the resonant charge scattering response takes the form [17]

$$\boldsymbol{\epsilon}' \cdot \hat{\boldsymbol{\epsilon}} = \begin{pmatrix} \hat{\boldsymbol{\epsilon}}'_{\perp} \cdot \hat{\boldsymbol{\epsilon}}_{\perp} & \hat{\boldsymbol{\epsilon}}'_{\perp} \cdot \hat{\boldsymbol{\epsilon}}_{\parallel} \\ \hat{\boldsymbol{\epsilon}}'_{\parallel} \cdot \hat{\boldsymbol{\epsilon}}_{\perp} & \hat{\boldsymbol{\epsilon}}'_{\parallel} \cdot \hat{\boldsymbol{\epsilon}}_{\parallel} \end{pmatrix} = \begin{pmatrix} 1 & 0 \\ 0 & \cos 2\theta \end{pmatrix}, \tag{3.33}$$

whereas the second term - which is the first order contribution of the magnetic scattering amplitude - takes the form [17]

$$\left(\hat{\boldsymbol{\epsilon}}' \times \hat{\boldsymbol{\epsilon}}\right) = \begin{pmatrix} 0 & \hat{\mathbf{k}} \\ -\hat{\mathbf{k}}' & \hat{\mathbf{k}}' \times \hat{\mathbf{k}} \end{pmatrix}. \tag{3.34}$$

The third term is second order in the magnetic moment direction. The form of this term in this matrix formalism is slightly more complicated and is not used in the REXS studies presented in chapter 6. The resonant charge scattering term will provide structural peaks when the scattering wavevector $\mathbf{Q}$ is equal to a reciprocal lattice vector $\boldsymbol{\tau}$. As the sample is cooled below the magnetic transition temperature, the moments may order with a single ordering wavevector $\mathbf{q}$ - note that this is not true in the general case, but it does hold for the samples measured in Chapter 6. The first resonant magnetic scattering term will result in weaker magnetic peaks when the scattering wavevector $\mathbf{Q}$ is equal to $\boldsymbol{\tau} \pm \mathbf{q}$, and so magnetic Bragg peaks will appear as $\pm\mathbf{q}$ satellite peaks near each structural Bragg peak $\boldsymbol{\tau}$. The second resonant magnetic scattering term will provide even weaker magnetic peaks at $\mathbf{Q} = \boldsymbol{\tau} \pm 2\mathbf{q}$ [16]. By measuring the location of the magnetic Bragg peaks in relation to the structural Bragg peaks, the magnetic ordering wavevector $\mathbf{q}$ can be experimentally determined. Furthermore, since the magnetic resonant x-ray scattering intensity is dependent on the direction of the magnetic moments in the scattering system, REXS can also be used to experimentally solve the magnetic structure.

Consider a scattering experiment with a setup as depicted in figure 3.3. An x-ray with incident wavevector $\mathbf{k}$ and polarisation $\boldsymbol{\epsilon}$ is incident onto a sample. The x-ray scatters elastically with scattered wavevector $\mathbf{k}'$ and polarisation $\boldsymbol{\epsilon}'$. Polarisations perpendicular to the scattering plane will be denoted by σ, whereas polarisations parallel to the scattering

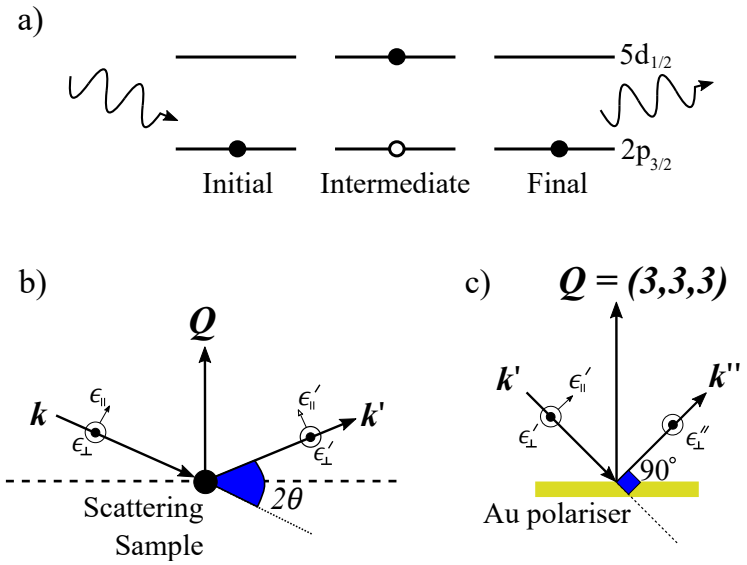

Figure 3.3: Scattering geometry for a resonant elastic x-ray scattering experiment. a) An incident x-ray can be tuned to the iridium L_3 edge - this is equal to the energy difference between the $2p_{3/2}$ and $5d_{1/2}$ states. This will excite a core electron to the valence shell. This excited state will transition back to the initial lower energy state, emitting a photon with the same energy as the incident x-ray. Consequently, this process is an elastic scattering process. b) The geometry of scattering an x-ray of incident momentum $\mathbf{k}$ and polarisation $\boldsymbol{\epsilon}$ onto a sample, after elastically scattering, the scattered x-ray will have momentum $\mathbf{k}'$ and polarisation $\boldsymbol{\epsilon}'$. The incident and scattered polarisation vectors have components parallel and perpendicular to the corresponding wavevector. Note that the scattered wavevector is defined by $\mathbf{Q} = \mathbf{k}' - \mathbf{k}$. c) The x-ray scattered from the sample can subsequently be scattered from the (333) Bragg reflection in gold. Close to the iridium L_3 edge, the scattering angle is 90°, whereby only the component of polarisation perpendicular to the scattering plane will undergo charge scattering.

plane are denoted by π. If the incident beam is σ polarised, then the scattered beam will have components polarised along σ' due to charge scattering, and π' due to magnetic scattering. By discriminating between the two scattered polarisations, the resonant magnetic scattering intensity can be measured solely in the $\sigma \rightarrow \pi'$ scattering process. In order to distinguish between the σ' and π' polarisation of the scattered beam, an analyser crystal can be used. The x-ray beam will have a wavevector $\mathbf{k}'$ and polarisation components σ' and π'. These can be made to scatter from an analyser crystal with scattered wavevector $\mathbf{k}''$ and polarisations σ'' and π''. As seen in equations 3.31, 3.33, and 3.34, if the scattering plane of the analyser crystal is parallel to the scattering plane of the REXS experiment, only the σ' polarised beam will undergo resonant charge scattering from the analyser crystal if $\cos 2\theta = 0$. If the

analyser crystal is instead rotated 90° about $\mathbf{k}'$, only the π' polarised beam will undergo resonant charge scattering. The analyser crystal will be positioned as to scatter the x-ray beam onto a detector. Now, the $(3,3,3)$ reflection in Au has a scattering angle of $2\theta = 90°$ for $E = 11.16$ keV. This energy is very close to the resonant L_3 edge in Ir at 11.215 keV, making Au$(3,3,3)$ an ideal reflection to use as a polarisation analyser [18].

3.4 X-Ray Scattering Instrumentation

This section will present technical details on the operation of a number of x-ray diffractometers, two of which are lab-based instruments and two instruments located on synchrotron beamlines.

3.4.1 Lab-based Diffractometers

Some diffraction experiments undertaken for work presented in this thesis were performed on an Oxford Diffraction SuperNova diffractometer. X-rays are generated by a molybdenum x-ray tube - with a wavelength $\lambda = 0.707$ Å- and collimated onto the sample. The scattered beams are detected by a CCD area detector, placed in a vacuum chamber with a beryllium window - beryllium has four electrons per atom and so the x-ray scattering amplitude from beryllium is small, allowing x-rays to pass through the window with very little attenuation. The incoming and scattered x-rays have wavevectors $\mathbf{k}$ and $\mathbf{k}'$, respectively. In elastic scattering, these wavevectors will have the same magnitude, and so the locus of points defined by $\mathbf{k}' - \mathbf{k}$ will be a sphere - called the Ewald sphere [19]. The direction of $\mathbf{k}$ is fixed and the orientation of the crystal is varied - with three angles ω, κ, and ψ - along with the orientation of the detector, with angle θ. These angles form a four-circle geometry. The reciprocal lattice will rotate with the crystal, and points on the reciprocal lattice will sweep out orbits of constant $|\boldsymbol{\tau}|$, as depicted in figure 3.4b. Scattering will occur when these reciprocal lattice points $\boldsymbol{\tau}$ lie on the Ewald sphere.

Other diffraction experiments were performed on a Rigaku SmartLab diffractometer, shown in figure 3.5a. This instrument was used to determine to orientation of crystal axes and to characterise twinning of thin crystalline samples. The x-rays used in this instrument

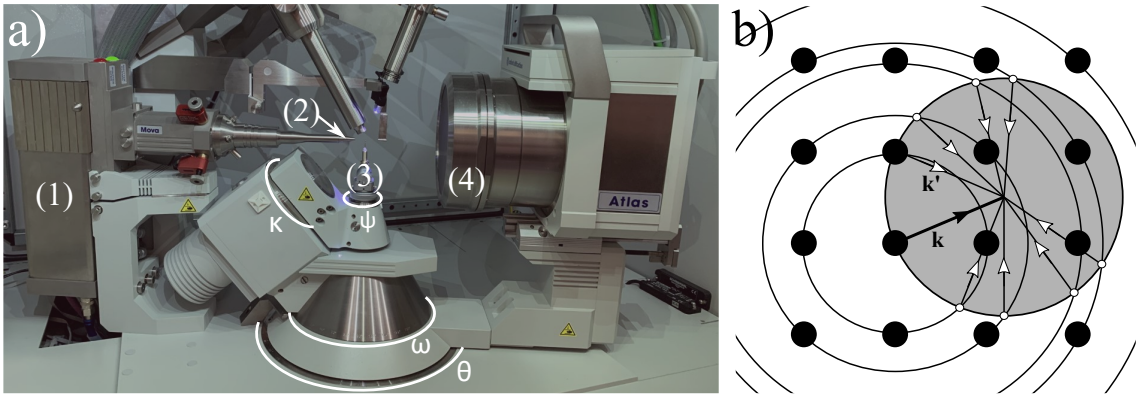

Figure 3.4: Depiction of the Oxford Diffraction Supernova x-ray scattering instrument. a) The instrument has the components: 1) molybdenum x-ray tube, 2) collimator, 3) goniometer mount for scattering sample, 4) detector with beryllium window. The rotational angles θ, ω, κ, and ψ of the four-circle geometry are shown. b) Ewald sphere in the rotating crystal geometry. The incident wavevector $\mathbf{k}$ is fixed and the reciprocal lattice points (filled circles) sweep out orbits (circular arcs) as the crystal is rotated. The detector can be rotated in order to select a scattered wavevector $\mathbf{k}'$ that lies on the edge of the Ewald sphere (shaded circle). The scattering condition can be satisfied at positions where the reciprocal lattice orbits and Ewald sphere coincide (open circles).

were the $K\alpha$ radiation generated by a copper x-ray tube. Such radiation corresponds to the $2p \rightarrow 1s$ transition in copper, and due to spin-orbit coupling the $2p$ level is split into a lower $j = 1/2$ state and an upper $j = 3/2$ state. Consequently, the $K\alpha$ radiation consists of two wavelengths $\lambda_{K\alpha 1} = 1.541$ Å and $\lambda_{K\alpha 2} = 1.544$ Å. This instrument has configurable incident optics, receiving optics, and sample stages. The experimental configuration used for these measurements had a set of Soller slits to collimate the incident beam; an $\chi\varphi Z$ stage upon which the sample was mounted, allowing for the rotation of the sample to move reciprocal lattice vectors $\boldsymbol{\tau}$ onto the scattering wavevector $\mathbf{Q}$; the receiving optics also had a set of Soller slits with the same angular divergence as the set of slits in the incident optics. A HyPix-3000 two-dimensional detector was placed at the end of the receiving optics. By measuring the count rate across the whole detector, the area detector can effectively be used as a point detector of x-rays. The incident and receiving optics can be rotated within the scattering plane, and respectively subtend angles ω and θ from the horizontal. A $2\theta/\omega$ scan is performed by measuring the X-ray scattering count rate while ω and θ are uniformly increased. If the sample normal lies along a reciprocal lattice vector, then $|\mathbf{Q}|$ can be scanned along the sample normal. The angles 2θ at which Bragg reflections are observed in the $2\theta/\omega$

scan allow the direction of the sample normal to be found. As an illustrative example, figure 3.5b shows a silicon sample mounted on the sample stage. The (004) axis was found to lie along the surface normal. Since silicon has an FCC lattice, the (100) and (010) axes lie in the plane of the sample, but with their exact orientation in the plane unknown. Now, the (111) direction will be offset from (004) by an angle of $\chi_0 = 54.8°$, and so - as shown in figure 3.5c - the (111) will lie somewhere along a cone with an opening angle of χ_0. Similarly, the $(\bar{1}11)$, $(1\bar{1}1)$, and $(\bar{1}\bar{1}1)$ directions will also lie on this cone, and will be equally spaced out by 90° intervals. This sample can be rotated about the rocking curve χ by the angle χ_0, moving the sample so one point of the cone will be vertical. Furthermore, the magnitude of the scattering vector $|\mathbf{Q}|$ can be adjusted by changing 2θ to select the magnitude of the reciprocal lattice vector $\boldsymbol{\tau}$, and adjusting ω to measure a vertical scattering vector. A scan can then be performed by rotating the sample about the surface normal by the angle φ. A full 360° scan of φ on a single crystal sample of silicon will contain four peaks corresponding to the (111), $(\bar{1}11)$, $(1\bar{1}1)$, and $(\bar{1}\bar{1}1)$ reciprocal lattice vectors. The in-plane orientations of the (100) and (010) axes can then be determined by taking the values φ when the sample is in the scattering condition and finding the interleaving values.

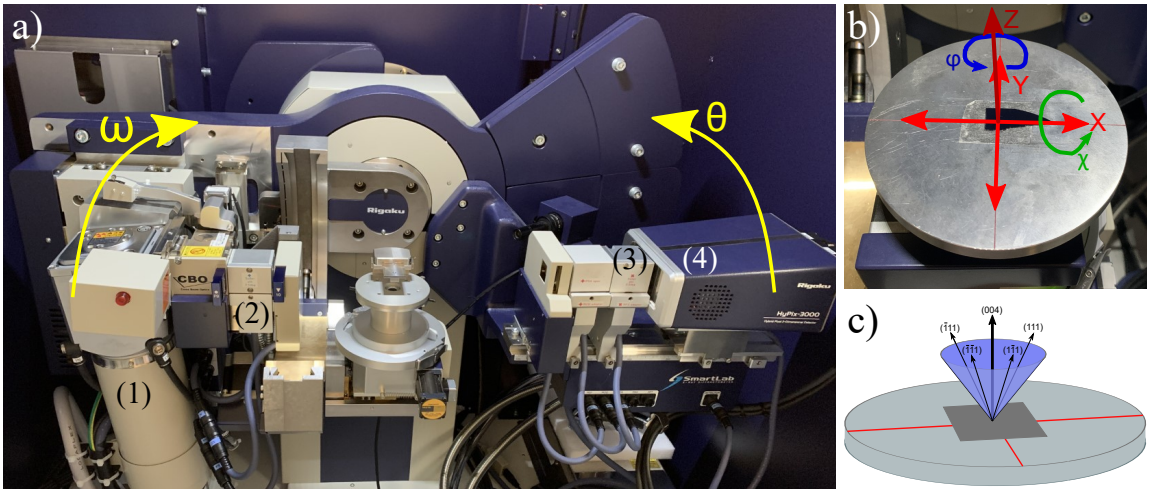

Figure 3.5: Depiction of the Rigaku Smartlab x-ray scattering instrument. a) The instrument has the components: 1) copper x-ray tube, 2) Soller slits in incident optics, 3) Soller slits in receiving optics, 4) HyPix-3000 two-dimensional detector. The arms of the incident and receiving optics subtend angles ω and θ from the horizontal. b) The sample is mounted on a $\chi\varphi Z$ stage. The stage can be translated along the X, Y, and Z axes to move the sample into the incident beam. The angles χ and φ angles correspond to rotations about the X and Z angles, respectively. c) Schematic diagram of some reciprocal lattice vectors. The (004) axis of this sample is along the surface normal and the (111), ($\bar{1}$11), (1$\bar{1}$1), and ($\bar{1}\bar{1}$1) directions lie along the surface of a cone. By rotating about χ by the opening angle of the cone, and rotating about φ, the (111), ($\bar{1}$11), (1$\bar{1}$1), and ($\bar{1}\bar{1}$1) directions can be brought into the scattering condition.

3.4.2 Synchrotron Diffractometers

Resonant elastic x-ray diffraction measurements were undertaken at the P09 beamline at the PETRA III synchrotron [20, 21], and the I16 beamline at the Diamond Light Source [22]. The operation of P09 and I16 are similar to the lab-based diffractometers in that x-rays are focused with an incident wavevector **k** and scattered elastically from a sample into a detector. The sample and the detector can be rotated, this time in a six-circle geometry, in order to map out reciprocal space. The rotation of the crystal and detector relative to the fixed incident beam allows the mapping of the x-ray scattering intensity profile throughout reciprocal space. There are however a number of differences between the diffractometers based at synchrotron sources and lab-based diffractometers. At a synchrotron, a high intensity and high energy beam of x-rays are produced via the acceleration of electrons. The energy of the x-rays is tuned via an undulator on P09 and by silicon focusing lenses on I16 [23] to the iridium L_3 resonant edge at 11.215 keV. A set of aluminium foils which can

be placed in or out of the incident beam path act as attenuators on both beamlines.

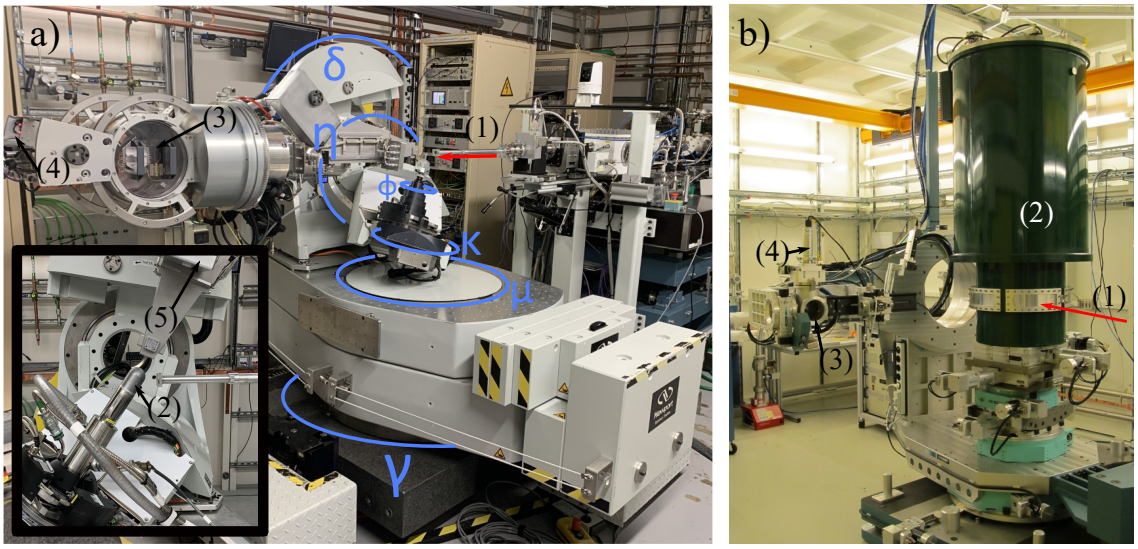

Figure 3.6: Photographs of the a) I16 and b) P09 x-ray diffractometers. Both diffractometers operate in a six-circle geometry, with angles γ, μ, δ, η, κ, and ϕ labelled by blue circular arcs in (a). The diffractometers have components 1) polarised incident beam, 2) cryostat with beryllium windows - on I16, a CCR is used with concentric beryllium domes in order to reach temperatures of 5 K; on P09, an evaporation cryostat is used to achieve colder temperatures down to 1.3 K. 3) Polarisation analyser crystal, in both cases the gold (333) reflection is used. 4) APD used as a detector of the scattered x-rays, 5) a Pilatus area detector (the edge of which can be seen inset to (a)).

On I16, the sample can be cooled down to temperatures around 5 K using a CCR refrigerator - as discussed in section 3.2. The sample is enclosed within two concentric beryllium domes to seal the cold exchange gas around the sample while also allowing the x-ray beam to scatter with minimal attenuation. On P09, even colder temperatures - down to 1.3 K can be achieved by an evaporation cryostat. Liquid ^{4}He at 4.2 K and at atmospheric pressure flows via a needle valve into a small chamber pumped down to millibar pressures. As the chamber is pumped, ^{4}He vapour is removed, cooling down the remaining liquid ^{4}He in the chamber to 1.3 K [24]. The x-rays were detected by a Pilatus area detector [25] - which consists of a two-dimensional array of semiconducting silicon pixels, allowing the position sensitive detection of scattered x-rays - or by an avalanche photodiode (APD)

which acts as a point detector of scattered x-rays.

References

1. Squires, G. L. *Introduction to the Theory of Thermal Neutron Scattering* 3rd ed. (Cambridge University Press, 2012).
2. Boothroyd, A. T. *Principles of Neutron Scattering from Condensed Matter* (Oxford University Press, 2020).
3. Lovesey, S. W. *Theory of Neutron Scattering from Condensed Matter, Volume 2* (Oxford University Press, 1984).
4. White, R. M. *Quantum Theory of Magnetism* 2nd ed. (Springer, 1983).
5. Willis, B. T. M. & Carlile, C. J. *Experimental Neutron Scattering* (Oxford University Press, 2009).
6. Bewley, R. *et al.* MERLIN, a new high count rate spectrometer at ISIS. *Phys. B Condens. Matter* **385-386,** 1029–1031 (2006).
7. Bewley, R., Taylor, J. & Bennington., S. LET, a cold neutron multi-disk chopper spectrometer at ISIS. *Nuclear Instruments and Methods in Physics Research Section A: Accelerators, Spectrometers, Detectors and Associated Equipment* **637,** 128–134 (2011).
8. Russina, M. & Mezei, F. First implementation of Repetition Rate Multiplication in neutron spectroscopy. *Nuclear Instruments and Methods in Physics Research Section A: Accelerators, Spectrometers, Detectors and Associated Equipment* **604,** 624–631. ISSN: 0168-9002 (2009).
9. Newnham, R. E., Fang, J. H. & Santoro, R. P. Crystal structure and magnetic properties of $CoTiO_3$. *Acta. Cryst.* **17,** 240 (1964).

10. Shirane, G., E. Cox, D., J. Takei, W. & L. Ruby, S. A Study of the Magnetic Properties of the FeTiO3-αFe2O3 System by Neutron Diffraction and the Mössbauer Effect. *Journal of the Physical Society of Japan* **17,** 1598–1611 (1962).

11. Arnold, O. *et al.* Mantid—Data analysis and visualization package for neutron scattering and μSR experiments. *Nucl. Instruments Methods Phys. Res. Sect. A Accel. Spectrometers, Detect. Assoc. Equip.* **764,** 156–166 (2014).

12. Ewings, R. *et al.* Horace: Software for the analysis of data from single crystal spectroscopy experiments at time-of-flight neutron instruments. *Nucl. Instruments Methods Phys. Res. Sect. A* **834,** 132–142 (2016).

13. Kittel, C. *Introduction to Solid State Physics* 8th ed. (Wiley, 2004).

14. Lovesey, S. W. & Collins, S. P. *X-Ray Scattering and Absorption by Magnetic Materials* (Oxford University Press, 1996).

15. Hannon, J. P., Trammell, G. T., Blume, M. & Gibbs, D. X-Ray Resonance Exchange Scattering. *Phys. Rev. Lett.* **61,** 1245–1248 (10 1988).

16. Hill, J. P. & McMorrow, D. F. Resonant Exchange Scattering: Polarization Dependence and Correlation Function. *Acta Crystallographica Section A* **52,** 236–244 (1996).

17. De Bergevin, F. & Brunel, M. Diffraction of X-rays by magnetic materials. I. General formulae and measurements on ferro- and ferrimagnetic compounds. *Acta Crystallographica Section A* **37,** 314–324 (1981).

18. Detlefs, C., Sanchez del Rio, M. & Mazzoli, C. X-ray polarization: General formalism and polarization analysis. *The European Physical Journal Special Topics* **208,** 353–371 (2012).

19. Ashcroft, N. W. & Mermin, N. D. *Solid State Physics* (Harcourt College Publishers, 1976).

20. Strempfer, J. *et al.* Resonant scattering and diffraction beamline P09 at PETRA III. *Journal of Synchrotron Radiation* **20,** 541–549 (2013).

21. Francoual, S. *et al.* Single-crystal X-ray diffraction and resonant X-ray magnetic scattering at helium-3 temperatures in high magnetic fields at beamline P09 at PETRA III. *Journal of Synchrotron Radiation* **22,** 1207–1214 (2015).

22. Collins, S. P. *et al.* Diamond Beamline I16 (Materials & Magnetism). *AIP Conference Proceedings* **1234,** 303–306 (2010).

23. Alianelli, L. *et al.* Germanium and silicon kinoform focusing lenses for hard x-rays. *Journal of Physics: Conference Series* **186,** 012062 (2009).

24. Pobell, F. *Matter and Methods at Low Temperatures* 3rd ed. (Springer, 2006).

25. Brönnimann, C. & Trüb, P. in *Synchrotron Light Sources and Free-Electron Lasers: Accelerator Physics, Instrumentation and Science Applications* (eds Jaeschke, E. J., Khan, S., Schneider, J. R. & Hastings, J. B.) 995–1027 (Springer International Publishing, Cham, 2016).

Chapter 4

Order by Disorder, Bond Dependent Exchange, and Nodal Quasiparticles in $CoTiO_3$

Recent theoretical proposals have argued that cobaltates with edge-sharing octahedral coordination can have significant bond-dependent exchange couplings, thus offering a platform in materials with $3d$ ions for such physics beyond the much-explored realisations in $4d$ and $5d$ materials. In this chapter, results from high-resolution inelastic neutron scattering experiments with the magnetically ordered phase of the stacked honeycomb magnet $CoTiO_3$ are presented. A finite energy gap is found to be present which implies the presence of bond-dependent anisotropic couplings. High resolution inelastic scattering measurements revealed a small spectral gap, and theoretical analysis shows that the spectral gap further implies the existence of a quantum order-by-disorder mechanism that, in this material, crucially involves virtual crystal field fluctuations. The inelastic neutron scattering data also provide an experimental observation of a universal winding of the scattering intensity in angular scans around linear band-touching points for both magnons and dispersive spin-orbit excitons, which is directly related to the non-trivial topology of the quasiparticle wavefunction in momentum space near nodal points.

4.1 Crystal and Magnetic Structure

4.1.1 Structural and Magnetic Unit Cells

$CoTiO_3$ has a stacked honeycomb lattice crystal structure with the space group $R\bar{3}$. The crystal structure can be considered in a hexagonal setting where the lattice parameters satisfy $a_h = b_h \neq c_h$, $\alpha_h = \beta_h = 90°$, and $\gamma_h = 120°$. The cobalt and titanium ions are surrounded by oxygen ions in an edge sharing octahedral configuration. When projected into the ab plane in the hexagonal unit cell, the transition metal ions form honeycomb layers with a stacking vector $\left(-\vec{a}_h + \vec{b}_h + \vec{c}_h\right)/3$. This describes 'ABC stacking' of the honeycomb layers, where layers are translated by an integer combination of lattice vectors once every three layers, and so the hexagonal unit cell has three layers of each transition metal ion. Alternatively, a rhombohedral unit cell with $a_{rh} = b_{rh} = c_{rh}$ and $\alpha_{rh} = \beta_{rh} = \gamma_{rh}$ can be considered. The rhombohedral unit cell is the primitive structural unit cell containing two Co^{2+} ions, two Ti^{4+} ions, and six O^{2-} ions; the hexagonal unit cell, however, contains three times the number of ions reflecting the ABC stacking of the honeycomb layers of transition metal ions. The hexagonal basis vectors $\vec{a}_h$, $\vec{b}_h$, $\vec{c}_h$ can be mapped to the structural rhombohedral basis vectors $\vec{a}_{rh}$, $\vec{b}_{rh}$, $\vec{c}_{rh}$ by:

$$\begin{pmatrix} \mathbf{a}_{rh} \\ \mathbf{b}_{rh} \\ \mathbf{c}_{rh} \end{pmatrix} = \frac{1}{3} \begin{pmatrix} -1 & -2 & 1 \\ 2 & 1 & 1 \\ -1 & 1 & 1 \end{pmatrix} \begin{pmatrix} \mathbf{a}_h \\ \mathbf{b}_h \\ \mathbf{c}_h \end{pmatrix} \tag{4.1}$$

Previous studies of the magnetic structure of $CoTiO_3$ have identified a magnetic structure with spins on the Co^{2+} sites aligned in the hexagonal ab plane with moments ferromagnetically aligned in each honeycomb layer and antiferromagnetically aligned between neighbouring layers, with a magnetic ordering temperature $T_N = 38$ K [1]. In the hexagonal setting, the unit cell of the magnetic structure is simply doubled along c_h. This magnetic structure can also be described in terms of a rhombohedral antiferromagnetic primitive cell with unit vectors rotated and scaled with respect to the structural vectors as:

$$\begin{pmatrix} \mathbf{a}_{rhA} \\ \mathbf{b}_{rhA} \\ \mathbf{c}_{rhA} \end{pmatrix} = \begin{pmatrix} 0 & 1 & 1 \\ 1 & 0 & 1 \\ 1 & 1 & 0 \end{pmatrix} \begin{pmatrix} \mathbf{a}_{rh} \\ \mathbf{b}_{rh} \\ \mathbf{c}_{rh} \end{pmatrix} = \frac{1}{3} \begin{pmatrix} 1 & 2 & 2 \\ -2 & -1 & 2 \\ 1 & -1 & 2 \end{pmatrix} \begin{pmatrix} \mathbf{a}_h \\ \mathbf{b}_h \\ \mathbf{c}_h \end{pmatrix} . \tag{4.2}$$

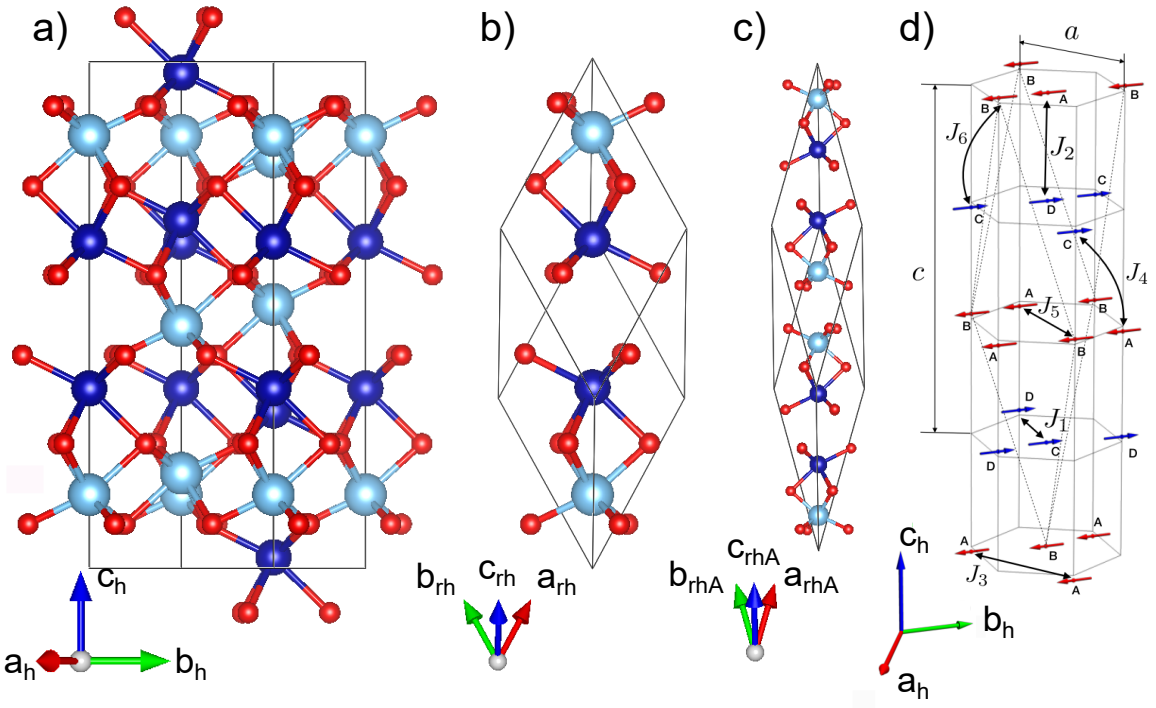

Figure 4.1: Models of the crystallographic unit cell, magnetic unit cell, and magnetic structure of $CoTiO_3$. Crystallographic unit cell for the a) hexagonal and b) rhombohedral settings. Upon the onset of magnetic order, the primitive unit cell doubles from the structural unit cell to the magnetic unit cell - c) depicted in the rhombohedral setting. In a-c) the solid lines define the edges of the unit cell, with dark/light blue spheres depicting Co^{2+}/Ti^{4+} ions. d) Overview of the magnetic structure of $CoTiO_3$. Moments (denoted by red and blue arrows) are confined to the *ab* plane in the hexagonal setting, with ferromagnetic alignment within each honeycomb layer and antiferromagnetic stacking. Labels A, B, C, and D indicate the four magnetic sublattices and the black arrows labelled J_1 to J_6 denote exchange paths up to 6th nearest neighbour - these details are used in the spinwave calculations in section 4.4. Dashed lines indicate the boundary of the magnetic unit cell in the rhombohedral setting denoted in c). In all parts of the figure, the appropriate lattice vectors are depicted below and to the left by the red, green, and blue arrows.

The hexagonal and rhombohedral unit cells, and the magnetic structure defined above are depicted in figure 4.1. This magnetic structure can be stabilised by exchange interactions between the nearest and next nearest neighbouring magnetic moments - denoted by J_1 and J_2 respectively in figure 4.1. The most general exchange between two spins can be modelled

by $\hat{H}_{ij} = \hat{\mathbf{S}}_i^T \mathcal{J}_{ij} \hat{\mathbf{S}}_j$. First consider the nearest neighbour exchange - J_1 - spins in each honeycomb layer are ferromagnetically aligned and ordered in the honeycomb plane if the exchange matrix has distinct in-plane and out-of-plane components, with the magnitude of the in-plane component ($J_1^{\perp}$) larger than that of the out-of-plane component (J_1^z), and $J_1^{\perp} < 0$ favours ferromagnetic rather than antiferromagnetic coupling in the plane. Now consider the next nearest neighbour exchange - J_2, antiferromagnetic alignment is favoured if the in-plane component $J_2^{\perp}$ satisfies $J_2^{\perp} > 0$. Although nearest and next nearest neighbour interactions are sufficient to stabilise this magnetic structure, couplings up to sixth nearest neighbour are treated in the spinwave model in section 4.4.

It is also useful to define a Cartesian coordinate system in which basis exchange matrices and bond vectors that define the crystallographic and magnetic structure can be written. The $\hat{x}$ unit vector may be taken to be along the $\mathbf{a}_h$ direction, and the $\hat{z}$ unit vector taken to be along the $\mathbf{c}_h$ direction. To make the coordinate system right-handed, the $\hat{y}$ unit vector can be defined by $\hat{y} = -\hat{x} \times \hat{z}$. In this basis, the exchange matrix for the nth nearest neighbour coupling can be written as $\mathcal{J}_n = \text{diag}(J_n^{\perp}, J_n^{\perp}, J_n^z)$. Furthermore, the hexagonal and antiferromagnetic rhombohedral lattice vectors can be written in terms of the basis vectors of the xyz frame via

$$\begin{pmatrix} \mathbf{a}_h \\ \mathbf{b}_h \\ \mathbf{c}_h \end{pmatrix} = a_h \begin{pmatrix} 1 & 0 & 0 \\ \cos\gamma_h & \sin\gamma_h & 0 \\ 0 & 0 & c_h/a_h \end{pmatrix} \begin{pmatrix} \hat{x} \\ \hat{y} \\ \hat{z} \end{pmatrix},$$

and

$$\begin{pmatrix} \mathbf{a}_{rhA} \\ \mathbf{b}_{rhA} \\ \mathbf{c}_{rhA} \end{pmatrix} = \frac{a_h}{3} \begin{pmatrix} 0 & \sqrt{3} & 2c_h/a_h \\ -3/2 & -\sqrt{3}/2 & 2c_h/a_h \\ 3/2 & -\sqrt{3}/2 & 2c_h/a_h \end{pmatrix} \begin{pmatrix} \hat{x} \\ \hat{y} \\ \hat{z} \end{pmatrix}.$$

Now, another Cartesian frame can be defined in terms of the antiferromagnetic rhombohedral lattice vectors, denoted by xyz - where $\hat{\mathsf{x}}$ is a unit vector parallel to $\mathbf{a}_{rhA}$, $\hat{\mathsf{z}}$ is a unit vector parallel to $\mathbf{a}_{rhA} \times \mathbf{b}_{rhA}$, and $\hat{\mathsf{y}} = -\hat{\mathsf{x}} \times \hat{\mathsf{z}}$. By defining the angle θ by $\tan\theta = 2c_h/\left(\sqrt{3}a_h\right)$, the two Cartesian frames can be related by a change of basis

$$\begin{pmatrix} \hat{\mathsf{x}} \\ \hat{\mathsf{y}} \\ \hat{\mathsf{z}} \end{pmatrix} = \frac{1}{\sqrt{1+3\sin^2\theta}} \begin{pmatrix} 0 & \cos\theta\sqrt{1+3\sin^2\theta} & \sin\theta\sqrt{1+3\sin^2\theta} \\ -1 & -\sqrt{3}\sin^2\theta & \sqrt{3}\sin\theta\cos\theta \\ \sqrt{3}\sin\theta & -\sin\theta & \cos\theta \end{pmatrix} \begin{pmatrix} \hat{x} \\ \hat{y} \\ \hat{z} \end{pmatrix}.$$

The matrix - including the prefactor of $\frac{1}{\sqrt{1+3\sin^2\theta}}$ - is henceforth denoted by R. Column vectors $\mathbf{v}$, with components $(v_x, v_y, v_z)^T$, and matrices $\mathcal{J}$ written in the basis of the xyz frame transform as $R\mathbf{v}$ and $R\mathcal{J}R^T$, respectively into the basis of the xyz frame.

4.1.2 Structural Domains

Room temperature single crystal x-ray diffraction using a Mo-source Oxford Diffraction Supernova diffractometer was performed on flakes of $CoTiO_3$ in order to determine the lattice parameters, crystal orientation, and fractional positions of the constituent ions. Previous measurements on $CoTiO_3$ fit an $R\bar{3}$ space group, place cobalt and titanium ions at $6c$ Wyckoff positions - $(0, 0, z_{Co})$ and $(0, 0, z_{Ti})$, and place oxygen ions at $18f$ Wyckoff positions - (x_O, y_O, z_O)[2]. The x-ray diffraction experiments also fit an $R\bar{3}$ space group with the lattice parameters $a = b = 5.0662(3)$Å and $c = 13.918(2)$Å in the hexagonal setting where unit cell angles are constrained to $\alpha = \beta = 90°$, and $\gamma = 120°$. The fractional coordinates found by previous work and by these single crystal x-ray diffraction experiments are summarised in the table 4.1.

		Kidoh, et. al. [2]			Present Work		
Atom	Site	x	y	z	x	y	z
Co	$6c$	0	0	0.355110(9)	0	0	0.35515(3)
Ti	$6c$	0	0	0.14558(1)	0	0	0.14564(4)
O	$18f$	0.31623(8)	0.02091(8)	0.24588(3)	0.3162(2)	0.0213(2)	0.2458(1)

Table 4.1: Fractional coordinates and Wyckoff positions of constituent ions of $CoTiO_3$ extracted from room temperature single crystal x-ray diffraction data.

The crystal structure of each $CoTiO_3$ sample used in single crystal x-ray diffraction was solved using the SHELXS 97 software package [3]. The best fits to the single crystal x-ray diffraction data come in two classes, related by a π rotation around the [110] axis, which is

not a symmetry operation of the crystal space group, and are summarised in table 4.2.

	Sample I	Sample II	Sample III	Sample IV
z_{Co}	0.35515(3)	0.35516(3)	0.14487(2)	0.14487(2)
z_{Ti}	0.14564(4)	0.14560(3)	0.35439(3)	0.35435(3)
x_O	0.31624(25)	0.31633(21)	0.29531(17)	0.29529(20)
y_O	0.02132(27)	0.02075(21)	−0.02103(17)	−0.02132(19)
z_O	0.24579(8)	0.24591(6)	0.25409(5)	0.25426(6)

Table 4.2: Solutions for the fractional positions of the constituent atoms from single crystal x-ray diffraction of four samples of $CoTiO_3$ at room temperature

The fits for the fractional coordinates for sample I and II are consistent with each other and with those found by Kidoh, et. al. This solution will be hereafter called 'domain A'. Conversely, the solutions for sample III and IV are consistent with each other but not with those for samples I and II - these solutions will hereafter be called 'domain B'. Domain B can be obtained from domain A by rotating about the [110] direction in the hexagonal setting through the origin by an angle π. Since the arrangement of the cobalt and titanium ions are invariant under this operation, but the arrangement of the oxygen ions different, any measurement used to differentiate between the two domains must be sensitive to positions of the oxygen ions.

Calculations of the x-ray diffraction pattern of the $hk1$ plane for domain A show prominent Bragg peaks at $(-3, 2, 1)$, $(1, -3, 1)$, and $(2, 1, 1)$; whereas prominent Bragg peaks at $(-2, 3, 1)$, $(-1, -2, 1)$, and $(3, -1, 1)$ occur in calculations of the x-ray diffraction pattern of domain B. If the oxygen ions are not taken into account for these calculations, then the two domains have identical diffraction patterns. If the transition metal ions are not taken into account, then the structure factors of the $(-3, 2, 1)$, $(1, -3, 1)$, and $(2, 1, 1)$ Bragg peaks are of a similar magnitude, but of opposite sign to the structure factors to the $(-2, 3, 1)$, $(-1, -2, 1)$, and $(3, -1, 1)$ Bragg peaks. Therefore at these Bragg peak positions, constructive or destructive interference occurs between the transition metal ions and the oxygen ions. In order to distinguish between domain A and domain B in X-ray diffraction, it is necessary to measure beyond the inner two triangles of figure 4.3a and d. Since the crystal has three fold symmetry about the [001] axis, if the (h, k, l) peak is present in diffraction, then there will be peaks of equal intensity at the symmetry equivalent positions $(-h-k, h, l)$

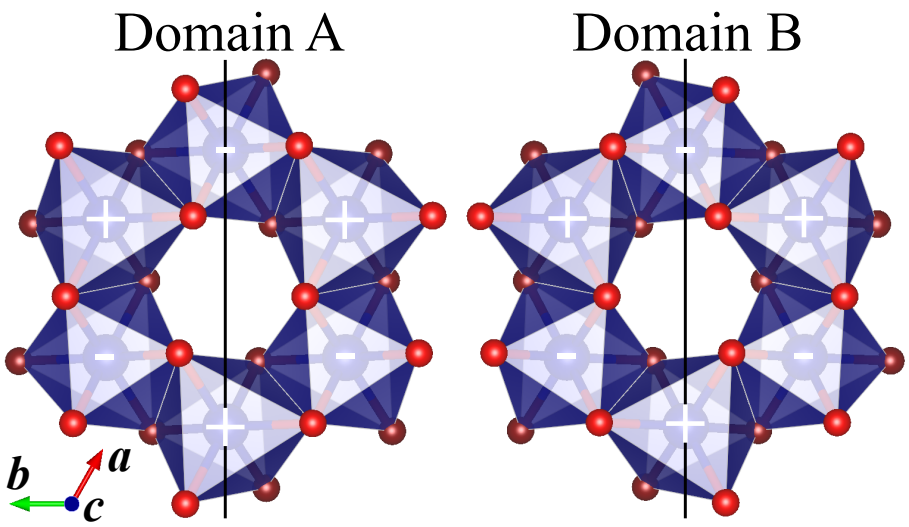

Figure 4.2: Projection of a single honeycomb layer onto the ab plane for domain A and domain B. The two domains are related by a (101) mirror plane - denoted by the solid vertical line. The $\pm$ signs on the cobalt ions (large blue balls) denote the buckling of the ions in a direction normal to the plane. The red/brown colour for the oxygens (small balls) indicate positions above/below the plane. The lattice vectors (lower left) are in the hexagonal setting.

and $(k, -h-k, l)$. Additionally, there will be Friedel twins at $(-h, -k, -l)$, $(h+k, -h, -l)$, and $(-k, h+k, -l)$. Rotating by π about the [110] axis will map these Friedel twins to $(-k, -h, l)$, $(-h, h+k, l)$, and $(h+k, -k, l)$, respectively; equating this set of Bragg peak positions to those symmetry equivalent to (h, k, l) gives a set of conditions for a Bragg peak to be present in diffraction for both domains: either $h = -k$, or $h = 0$, or $k = 0$. These conditions are satisfied for peaks on the two innermost triangles in figure 4.3a and d. In the same figure, this technique of comparing the intensity of structural Bragg peaks in the $hk1$ and $hk\bar{1}$ planes of reciprocal space was applied to determine whether domain A or domain B is the best fit for the x-ray diffraction data.

Similar calculations for x-ray diffraction measurements of the $hk1$ and $hk\bar{1}$ planes were performed for neutron diffraction. From these calculations, similarly to the x-ray data, the intensities of the $(1, -3, 1)$ and $(3, -2, -1)$ Bragg peaks would be considerably stronger than the intensities of the $(3, -1, 1)$ and $(2, -3, -1)$ Bragg peaks for domain A. Conversely the $(3, -1, 1)$ and $(2, -3, -1)$ Bragg peaks are stronger in domain B. However, by comparing these calculations with data from the elastic line in INS measurements, in figure 4.4, these Bragg peaks were all of similar intensities. It can therefore be concluded that the sample

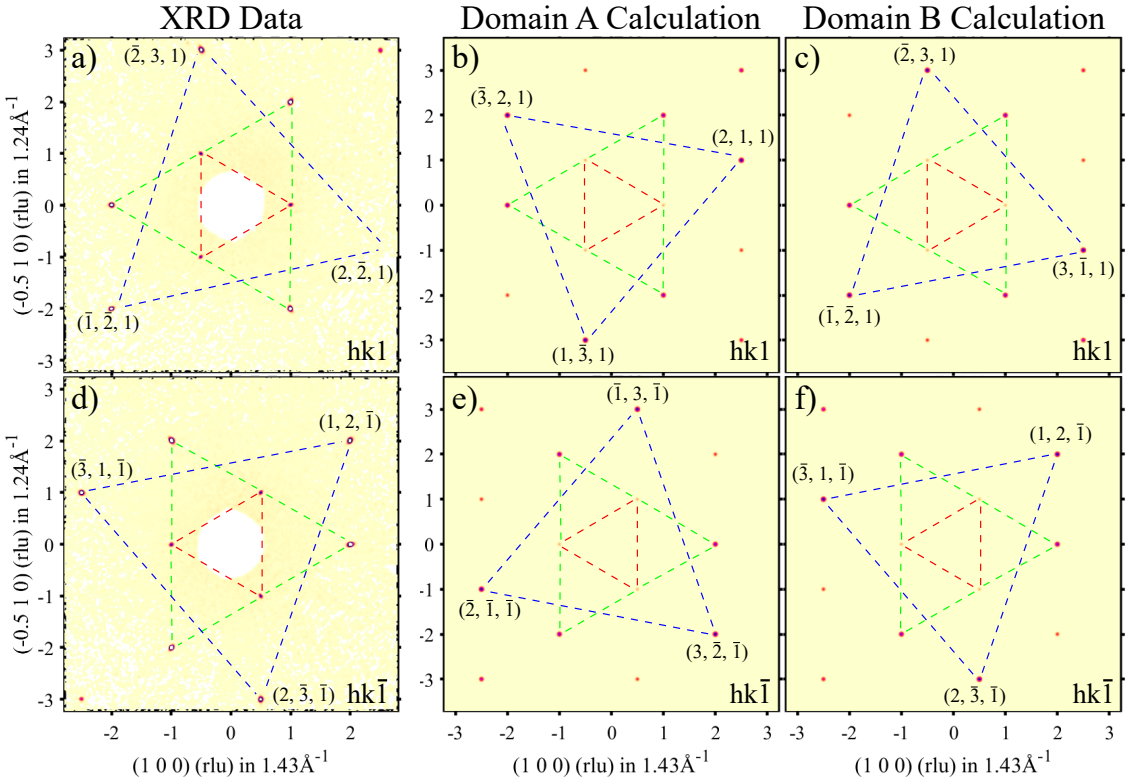

Figure 4.3: Determination of the structural domain of a $CoTiO_3$ sample measured using x-ray diffraction. Measurements of the a) $hk1$ and d) $hk\bar{1}$ planes were made in single crystal x-ray diffraction. Compared to calculations of the $hk1$ plane for b) domain A and c) domain B, and to calculations of the $hk\bar{1}$ plane for e) domain A and f) domain B. Triangles of dotted red, green, and blue lines are overplotted in each plane with the brightest Bragg peaks at the vertices of the triangles. The red and green triangles have the same orientations, whereas the blue triangles have differing orientations between the two domains. The relative intensity of the $(\bar{2}, 3, 1)$ and $(\bar{3}, 2, 1)$ Bragg peaks may be used to determine whether domain A or B is the best fit. For the x-ray diffraction data in a) and d), domain B is the best fit.

used in the single crystal neutron experiments - outlined in section 4.2 - consists of both structural domains A and B of similar weight. The X-ray experiments were performed on small crystalline flakes of $CoTiO_3$ that were mounted in a 150μm microloop; whereas the neutron diffraction experiments were performed on a much larger sample of mass 5.8g. An equal proportion of the structural domains is found in the larger sample, whereas single structural domains can be observed in sufficiently small thin-flake samples.

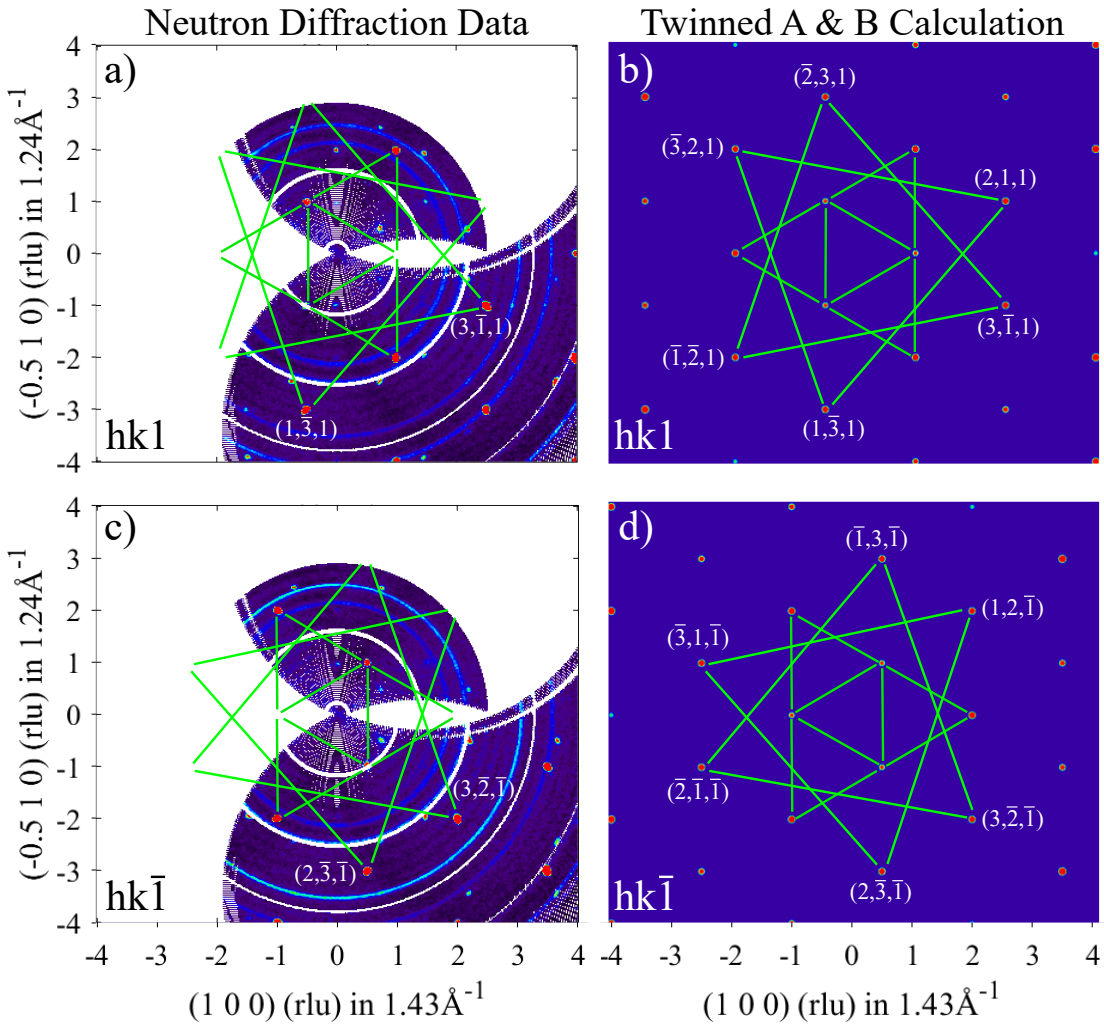

Figure 4.4: Measurement and of the a) $hk1$ and c) $hk\bar{1}$ planes on the elastic line in INS measurements of $CoTiO_3$ using monochromated neutrons with an incident energy of $E_i = 45$ meV, with E integrated over $[-1, 1]$ meV. b/d) Calculations of the diffraction patterns of the same planes as a/c) with an equal weight of domains A and B. The overplotted green triangles show the position of Bragg peaks in each plane for increasing $|Q|$; both domains are required to account for the appearance of equally intense Bragg peaks on the two outermost triangles.

4.2 Neutron Scattering Results

Inelastic neutron scattering experiments were performed using the MERLIN time-of-flight spectrometer at ISIS [4]. The sample consisted of a pair of co-aligned crystals shown in figure 4.5 with a total mass of 5.8 g aligned with the $\mathbf{c}^*$ axis vertical. The crystals were synthesised by Dr. D. Prabhakaran in the Clarendon Laboratory using an image furnace.

Upon cooling the sample to a base temperature of 8 K via a closed-cycle refrigerator,

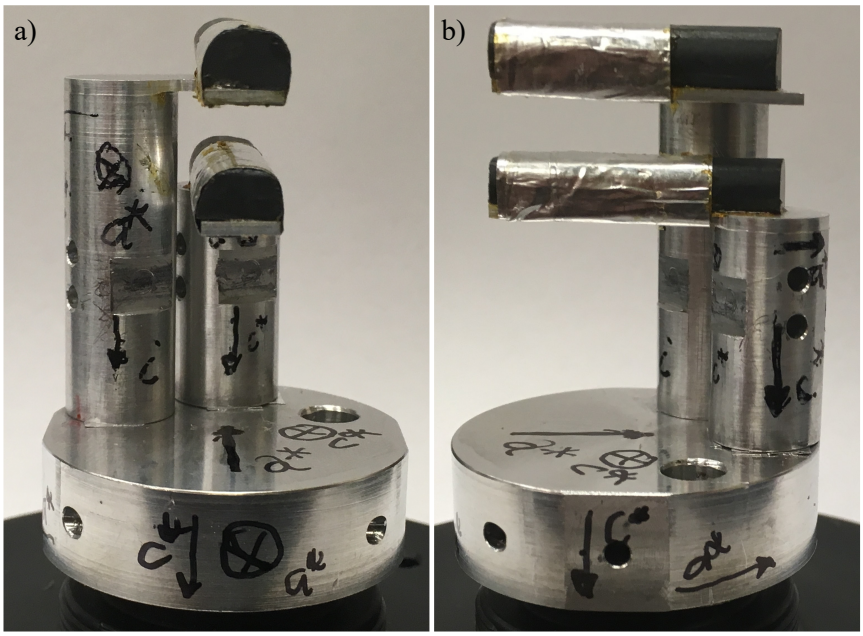

Figure 4.5: Coaligned single crystal samples of $CoTiO_3$ mounted on an aluminium sample holder with crystallographic axes labelled. The $\mathbf{c}^*$ axis is vertically downwards and the sample holder is viewed a) along and b) perpendicularly to the direction of the $\mathbf{a}^*$ axis.

an initial measurement with monochromated neutrons with an incident energy of 81.5 meV - as seen in figure 4.6 - indicated a large scattering weight below 15 meV with bumps in scattering intensity centred at 28 and 58 meV. A Horace scan was then performed by rotating the sample 120° in steps of 0.5°. The spectrometer was operated during this scan in repetition rate multiplication mode in order to simultaneously collect inelastic scattering data for monochromated neutrons with incident energies of 9.6 meV, 18 meV, and 45 meV. The time-of-flight neutron data were processed using the MANTID[5] and HORACE[6] data analysis packages.

Although the crystal structure has $\bar{3}$ point group symmetry, the magnetic Co^{2+} and non-magnetic Ti^{4+} ions from arrangements that have a higher point group symmetry, $\bar{3}m$. In addition, due to equal mixing of structural twins related by a 2-fold rotation about the [110] axis, the diffraction signal should have a $\bar{3}m$ point group symmetry even accounting for contributions of the oxygen sites. For this reason, the pixels in the Horace scans were mapped using symmetry operations belonging to the $\bar{3}m$ point group into a reduced 60° sector for $l > 0$. By symmetrising these data, the counting statistics are improved with the imposition that cuts and slices taken through the data set should be restricted to this

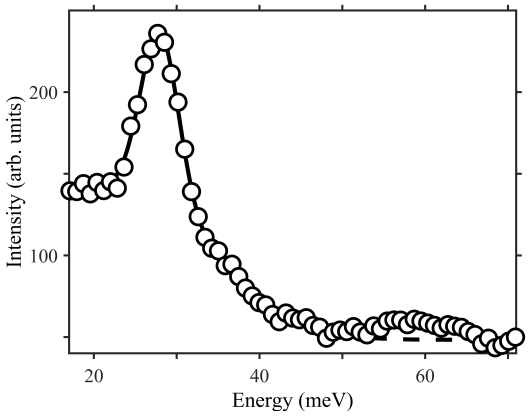

Figure 4.6: Inelastic neutron scattering energy scan in $CoTiO_3$ taken using monochromated neutrons with an incident energy of $E_i = 81.5$ meV. Scattering intensity due to two transitions to excited levels around 28 and 58 meV can be seen - with the solid line as a guide to the eye.

region of reciprocal space.

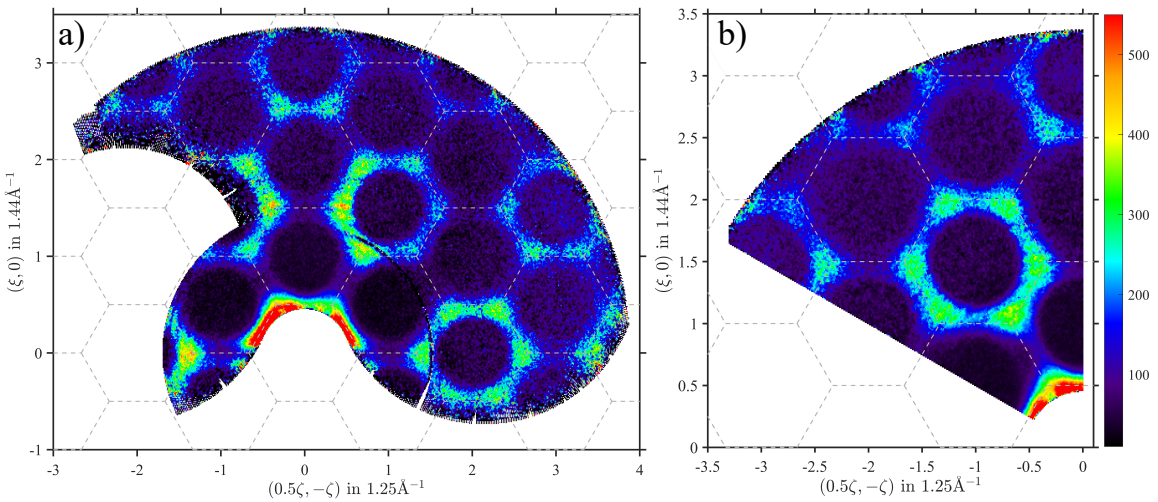

Figure 4.7: Constant energy slices through a) unsymmetrised and b) symmetrised data sets in $CoTiO_3$. Scans are integrated over an energy range from 7 to 9 meV and over all available values of l. The pixels in the unsymmetrised data set are mapped via symmetry operations in the $\bar{3}m$ point group to a wedge-shaped volume of reciprocal space defined by $h > 0$, $k > 0$, and $l > 0$.

Slices along high symmetry directions can then be taken through the inelastic data sets in order to identify key features of the excitation spectra. In slices through the $E_i = 45$ meV data set, there are two sets of dispersive modes: one set from the elastic line up to around 12 meV, and the other set from 25 to 30 meV. The upper set of modes can be considered to be the dispersion of a spin-orbit exciton - the incoming neutron excites a single-ion site from

the $J_{\text{eff}} = 1/2$ ground state to one of the first excited $J_{\text{eff}} = 3/2$ states, and this excitation can then hop between sites on the honeycomb lattice of the Co^{2+} ions. Modelling of this spin-orbit exciton will be treated in section 4.9, this exciton was reported concurrently by another research group [7]. The modes below 14 meV are magnons and can be resolved in greater detail in the $E_i = 18$ meV data set.

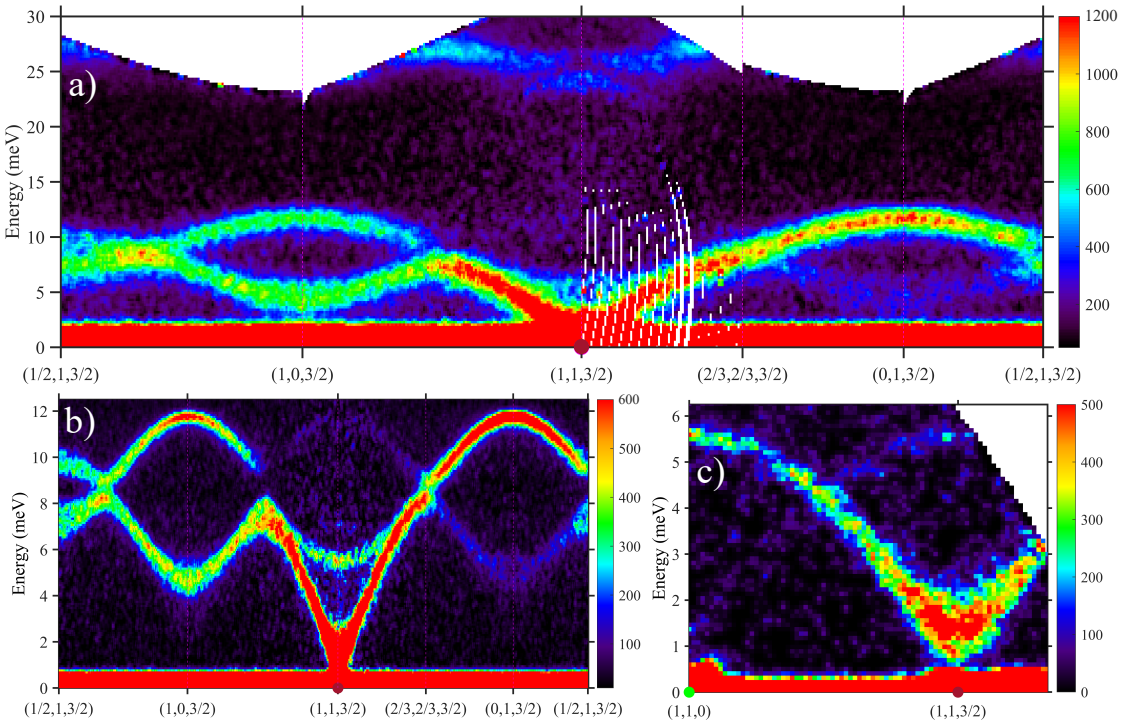

Figure 4.8: INS data in $CoTiO_3$ at 8 K for $E_i = 45$ (a), 18 (b), and 9.6 meV (c). a) An in-plane slice through high symmetry points through the $E_i = 45$ meV data shows a dispersive set of low energy magnon modes and higher energy spin-orbit exciton modes. b) The same in-plane path through high symmetry points through the $E_i = 18$ meV data shows dispersions of magnon bands in higher resolution. c) A slice along the out-of-plane L-direction through the $E_i = 9.6$ meV data shows a small spectral gap of around 1 meV between the elastic line and the lowest energy magnon mode at the $(1, 1, 3/2)$ magnetic Bragg peak position.

Near the $(1, 1, 3/2)$ magnetic Bragg peak position in the $E_i = 18$meV data set, the lowest energy mode has a near linear dispersion - indicative of an easy-plane exchange anisotropy - which appears to be near gapless. However, the higher resolution of the $E_i = 9.6$ meV data set allows a small spectral gap on the order of 1 meV to be resolved. Such a spectral gap has been previously proposed, but was not observed in earlier lower resolution INS data [8]. The primitive magnetic unit cell for the magnetically ordered structure contains four magnetic

Co^{2+} ions and so an XXZ model in linear spin wave theory - presented in section 4.4 - gives four modes in the magnon spectrum. The two lower bands are resolved in the $E_i = 18$ meV and $E_i = 9.6$ meV data sets, whereas the two higher bands appear to be degenerate. An XXZ model would have a gapless mode corresponding to moments rotating freely in the ab-plane - a phenomenological model that accounts for this gap is presented in section 4.5, and a physical mechanism that may be responsible for opening such a gap is presented in section 4.7. Another key feature in the INS data is that there are linear touching points of the upper and lower magnon bands around 8.5meV. Figure 4.8b shows a crossing at $(2/3, 2/3, 3/2)$, appearing in two places along the slice. One instance of the crossing point appears to have the scattering weight split evenly between the modes, conversely the other instance appears to have the scattering intensity concentrated in one mode with the other mode having very little scattering intensity. The nature of these crossing points, including their intensity profile will be treated in section 4.8.

In addition to single crystal measurements performed using the MERLIN time-of-flight spectrometer, a neutron powder diffraction measurement was performed using the WISH time-of-flight diffractometer [9], also at ISIS. A 3.125 g sample of powder $CoTiO_3$ was mounted into a cryostat and high counting statistics data were collected at 1.5 and 150 K, corresponding to temperatures well within the magnetically ordered and paramagnetic phases, respectively. Additional data was collected upon warming in 2.5 K steps between 1.5 and 50 K in order to obtain the order parameter. Rietveld analysis of the nuclear and magnetic structure was performed with FullProf [10], showing a good agreement with the previously published crystal structure of $CoTiO_3$ [1]. The fitted unit cell parameters are presented in table 4.3. Below T_N, additional diffraction peaks were observed (labelled "M" in figure 4.9), which could be indexed using the T-point propagation vector $\mathbf{Q} = (0, 0, 3/2)$. Representational analysis of the magnetic structure using ISODISTORT [11, 12] showed that the high intensity of the magnetic Bragg peak indexed by $\mathbf{Q}$ indicates ferromagnetic honeycomb layers stacked antiferromagnetically with moments perpendicular to the c axis. Rietveld refinement of this magnetic structure gave good agreement between this model of the magnetic structure and the low temperature diffraction data. At 1.5 K, the cobalt magnetic moment refined to 3.08(1) μ_B. The temperature dependence of the magnetic moment

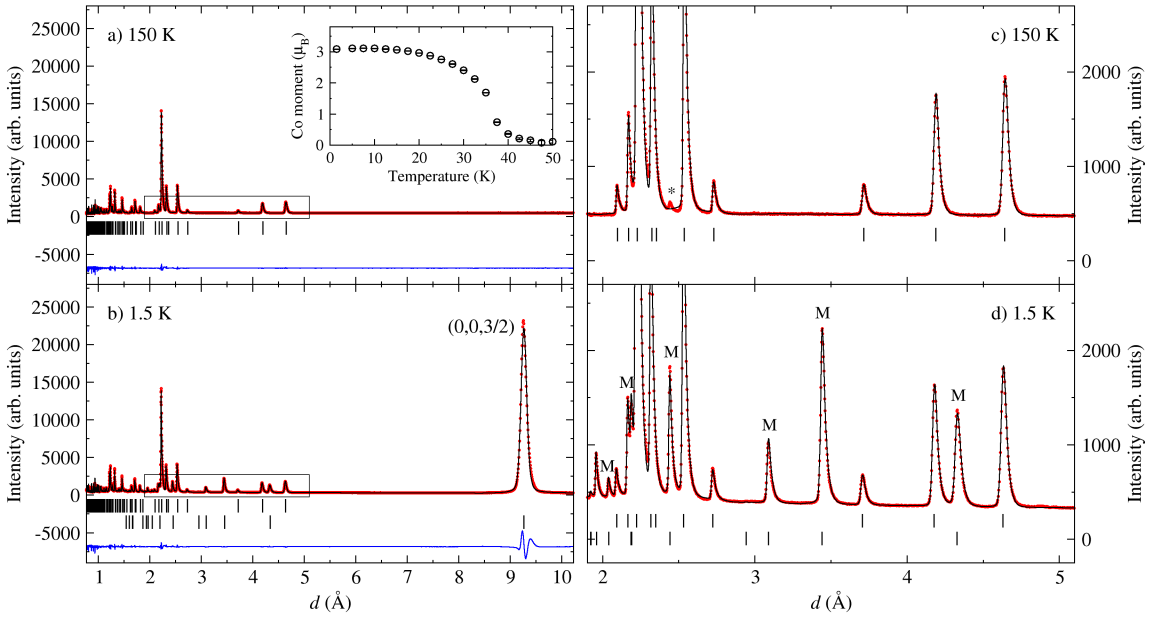

Figure 4.9: Neutron powder diffraction data in $CoTiO_3$ collected at 150 K for (a) and (c), and 1.5 K for (b) and (d). Panels (c) and (d) show an enlarged region of the diffraction pattern, as indicated by the black rectangle in (a) and (b), highlighting magnetic diffraction intensities labelled "M". The weak diffraction peak labelled by an asterisk (*) in (c) likely originates from a small $CoTi_2O_5$ impurity. Its presence did not affect the quantitative analysis of the diffraction pattern. Fits to the data are shown as solid black lines, and the difference $I_{obs} - I_{calc}$ is given as a blue line at the bottom of the panes. In (a) and (c) nuclear peak positions are denoted by black tick marks, and in (b) and (d) nuclear and magnetic peak positions are denoted by top and bottom black tick marks, respectively. The temperature dependence of the cobalt magnetic moment evaluated by fitting variable temperature neutron powder diffraction data is shown in the inset to panel a).

was extracted from fits to data collected on warming and is shown in the inset to figure 4.9a).

4.3 Single Ion Physics

The crystal structure described in section 4.1 contains Co^{2+} ($3d^7$) ions surrounded by an octahedron of O^{2-} ions. In order to find the spectrum of single-ion states, the effects of the crystal field and spin-orbit interaction must be considered. The Hund's rule ground state of a free Co^{2+} ion has a total orbital angular momentum quantum number of $L = 3$ and a total spin quantum number of $\mathsf{S} = 3/2$. Assuming the energy scale of the crystal field interaction is much smaller than the electrostatic repulsion of the electrons in the Co^{2+}

Cell parameters
Space group: $R\bar{3}$ (#148, hexagonal axes, obverse setting)
a, b, c (Å) 5.06383(3) 5.06383(3) 13.9076(1)
Volume (Å^3) 308.845(4)

Atomic fractional coordinates

Atom	Site	x	y	z	U_{iso}(Å^{-2})
Co	$6c$	0	0	0.3562(3)	0.0132(9)
Ti	$6c$	0	0	0.1454(2)	0.0066(6)
O	$18f$	0.3161(2)	0.0203(2)	0.24605(5)	0.0074(2)

($R_{\mathrm{p}} = 4.1\%$, $R_{\mathrm{wp}} = 3.7\%$, $R_{\mathrm{Bragg}} = 4.1\%$).

Table 4.3: Refined 150 K crystal structure parameters of $CoTiO_3$

ion, the crystal field interaction between the Co^{2+} ion and the surrounding inhomogeneous electric field of a perfect octahedron of O^{2-} ions can be treated as a perturbation on the $L = 3$ orbital ground state. In this case, the crystal field Hamiltonian is given by

$$\hat{H}_{cf} = -B\left(\hat{O}_4^0 + 5\hat{O}_4^4\right) \tag{4.3}$$

where $B > 0$ and the Stevens operators $\hat{O}_4^0$ and $\hat{O}_4^4$ are given by [13]

$$\begin{aligned} \hat{O}_4^0 &= 35\hat{L}_z^4 - (30X - 25)\hat{L}_z^2 + (3X^2 - 6X), \\ \hat{O}_4^4 &= \frac{1}{2}\left[\hat{L}_+^4 + \hat{L}_-^4\right], \end{aligned} \tag{4.4}$$

where $X = L(L+1)$. In the basis of the $|L = 3, L_z\rangle$ states, the crystal field Hamiltonian can be written as a 7×7 matrix

$$\hat{H}_{cf} = -60B \begin{pmatrix} 3 & 0 & 0 & 0 & \sqrt{15} & 0 & 0 \\ 0 & -7 & 0 & 0 & 0 & 5 & 0 \\ 0 & 0 & 1 & 0 & 0 & 0 & \sqrt{15} \\ 0 & 0 & 0 & 6 & 0 & 0 & 0 \\ \sqrt{15} & 0 & 0 & 0 & 1 & 0 & 0 \\ 0 & 5 & 0 & 0 & 0 & -7 & 0 \\ 0 & 0 & \sqrt{15} & 0 & 0 & 0 & 3 \end{pmatrix}, \tag{4.5}$$

which can be diagonalised to give a ground state orbital triplet of states that belong to the T_{1u} irreducible representation

$$\sqrt{\frac{5}{8}}\,|\pm 3\rangle + \sqrt{\frac{3}{8}}\,|\mp 1\rangle\,, \quad |0\rangle\,,$$

an excited triplet (at energy $+480B$) of states that belong to the T_{2u} irreducible representation

$$\sqrt{\frac{3}{8}}\,|\pm 3\rangle - \sqrt{\frac{5}{8}}\,|\mp 1\rangle\,, \quad \frac{1}{\sqrt{2}}\left(|+2\rangle + |-2\rangle\right),$$

and an excited singlet (at energy $+1080B$) that belongs to the A_{2u} irreducible representation

$$\frac{1}{\sqrt{2}}\left(|+2\rangle - |-2\rangle\right),$$

where the above states are written in the $|L_z\rangle$ basis. The splitting of the seven-fold degenerate $L = 3$ state into two triplets and a singlet is as expected from representation theory. In a spherically symmetric potential, the Co^{2+} ion has symmetry operations belonging to the group O(3), and the basis functions for this group are the spherical harmonics with characters given by [14]

$$\begin{aligned}\chi^{(L)}(E) &= 2L+1 \\ \chi^{(L)}(\alpha) &= \frac{\sin((L+1/2)\alpha)}{\sin(\alpha/2)} \\ \chi^{(L)}(i) &= (-1)^L(2L+1)\end{aligned} \tag{4.6}$$

where E, α, and i denote the symmetry operations of the identity, proper rotation of angle α, and inversion respectively. The octahedral crystal field will not possess full rotational symmetry, but instead will be a discrete subgroup - O_h - of $O(3)$. The irreducible representation corresponding to $L = 3$, $\Gamma^{(L=3)}$, in the continuous group $O(3)$ can be decomposed into irreducible representations of the discrete subgroup O_h.

Rep^{r}	E	$3C_4^2$	$6C_4$	$6C_2'$	$8C_3$	i	$3iC_4^2$	$6iC_4$	$6iC_2'$	$8iC_3$
A_{1g}	1	1	1	1	1	1	1	1	1	1
A_{2g}	1	1	-1	-1	1	1	1	-1	-1	1
E_g	2	2	0	0	-1	2	2	0	0	-1
T_{1g}	3	-1	1	-1	0	3	-1	1	-1	0
T_{2g}	3	-1	-1	1	0	3	-1	-1	1	0
A_{1u}	1	1	1	1	1	-1	-1	-1	-1	-1
A_{2u}	1	1	-1	-1	1	-1	-1	1	1	-1
E_u	2	2	0	0	-1	-2	-2	0	0	1
T_{1u}	3	-1	1	-1	0	-3	1	-1	1	0
T_{2u}	3	-1	-1	1	0	-3	1	1	-1	0
$\Gamma^{(L=2)}$	5	1	-1	1	-1	5	1	-1	1	-1
$\Gamma^{(L=3)}$	7	-1	-1	-1	1	-7	1	1	1	-1

Table 4.4: Character table of the O_h point group, with the $L = 3$ representation of the $O(3)$ group included in the bottom row.

By summing the rows of the character table corresponding to the A_{2u}, T_{1u}, and T_{2u} irreducible representations, the characters of the $\Gamma^{(L=3)}$ representation are recovered. As a result, the $\Gamma^{(L=3)}$ representation is reducible when restricted to the O_h point group and can be written as a sum of irreducible representations $A_{2u} \oplus T_{1u} \oplus T_{2u}$. Therefore, the $L = 3$ level is seven-fold degenerate when the Co^{2+} ion is in a rotationally symmetric potential, but in an octahedral crystal field will split into two triplets and a singlet. Although the exact energies of the levels will depend on the Hamiltonian in equation 4.3, their degeneracies will only depend on the symmetry.

The ground state orbital triplet can be written in terms of an effective $l = 1$ orbital angular momentum state, with the correspondence between $|l_z\rangle$ and $|L_z\rangle$ given by [15]

$$|l_z = \pm 1\rangle = \sqrt{\frac{5}{8}}\,|\mp 3\rangle + \sqrt{\frac{3}{8}}\,|\pm 1\rangle\,,$$
$$|l_z = 0\rangle = -\,|0\rangle\,,$$

where the Hilbert space spanned by the states $|L_z\rangle$ is projected onto the subspace spanned by the states $|l_z\rangle$, and the orbital angular momentum operator $\hat{\mathbf{L}}$ maps onto the effective orbital angular momentum operator $\hat{\mathbf{l}}$ with the equivalency relation $\hat{\mathbf{L}} = -3\hat{\mathbf{l}}/2$.

The exchange interaction, spin-orbit coupling, and distortions to the octahedral crystal field can then be treated as perturbations to the crystal field ground state consisting of an effective $l = 1$ orbital triplet coupled to a total spin $\mathsf{S} = 3/2$ degree of freedom. In the full $L = 3$ manifold, the spin-orbit Hamiltonian is given by $\hat{H}_{so} = -|\lambda|\hat{\mathbf{L}} \cdot \hat{\mathsf{S}}$, and the minus sign is included since the valence shell of the $3d^7$ ion is more than half-occupied. By using the equivalency $\hat{\mathbf{L}} = -3\hat{\mathbf{l}}/2$, the spin-orbit Hamiltonian acting on the orbital $l = 1$ ground state triplet of the crystal field, $\hat{H}_{so} = \frac{3}{2}\lambda\hat{\mathbf{l}} \cdot \hat{\mathsf{S}}$ for $\lambda > 0$. This Hamiltonian acts on the 12 dimensional Hilbert space spanned by the $|l_z, \mathsf{S}_z\rangle$ states. By defining a total angular momentum operator $\hat{\mathbf{J}}_{\text{eff}} = \hat{\mathbf{l}} + \hat{\mathsf{S}}$ such that $\hat{J}^2_{\text{eff}}$ and $\hat{J}_{\text{eff},z}$ commute with the spin-orbit Hamiltonian allows states to be written in the basis $|J_{\text{eff}}, J_{\text{eff},z}\rangle$. By taking the Kronecker product of the matrix forms of $\hat{\mathbf{l}}$ and $\hat{\mathsf{S}}$, the spin-orbit Hamiltonian can be written as $\hat{H}_{so} = \frac{3\lambda}{2}\left[\frac{1}{2}(\hat{l}_+ \otimes \hat{\mathsf{S}}_- + \hat{l}_- \otimes \hat{\mathsf{S}}_+) + \hat{l}_z \otimes \hat{\mathsf{S}}_z\right]$.
Diagonalising gives a ground state $J_{\text{eff}} = 1/2$ doublet at $-15\lambda/4$, an excited $J_{\text{eff}} = 3/2$ quadruplet at $-3\lambda/2$, and an excited $J_{\text{eff}} = 5/2$ sextuplet at $9\lambda/4$. The states in the $|J_{\text{eff}}, J_{\text{eff},z}\rangle$ basis can be written in terms of the $|l_z, \mathsf{S}_z\rangle$ states either by diagonalising the spin-orbit Hamiltonian, or by looking up tabulated values of the Clebsch-Gordan coefficients.

$$|J_{\text{eff}} = 1/2, J_{\text{eff},z} = \pm 1/2\rangle = \frac{1}{\sqrt{6}}|\pm 1, \mp 1/2\rangle - \frac{1}{\sqrt{3}}|0, \pm 1/2\rangle + \frac{1}{\sqrt{2}}|\mp 1, \pm 3/2\rangle$$
$$|J_{\text{eff}} = 3/2, J_{\text{eff},z} = \pm 3/2\rangle = \sqrt{\frac{2}{5}}|\pm 1, \pm 1/2\rangle - \sqrt{\frac{3}{5}}|0, \pm 3/2\rangle$$
$$|J_{\text{eff}} = 3/2, J_{\text{eff},z} = \pm 1/2\rangle = \sqrt{\frac{8}{15}}|\pm 1, \mp 1/2\rangle - \sqrt{\frac{1}{15}}|0, \pm 1/2\rangle - \sqrt{\frac{2}{5}}|\mp 1, \pm 3/2\rangle$$
$$|J_{\text{eff}} = 5/2, J_{\text{eff},z} = \pm 5/2\rangle = |\pm 1, \pm 3/2\rangle$$
$$|J_{\text{eff}} = 5/2, J_{\text{eff},z} = \pm 3/2\rangle = \sqrt{\frac{3}{5}}|\pm 1, \pm 1/2\rangle + \sqrt{\frac{2}{5}}|0, \pm 3/2\rangle$$
$$|J_{\text{eff}} = 5/2, J_{\text{eff},z} = \pm 1/2\rangle = \sqrt{\frac{3}{10}}|\pm 1, \mp 1/2\rangle + \sqrt{\frac{3}{5}}|0, \pm 1/2\rangle + \sqrt{\frac{1}{10}}|\mp 1, \pm 3/2\rangle$$

In the crystal structure of $CoTiO_3$, the octahedra of O^{2-} ions are trigonally distorted, reducing the local point group symmetry of the Co^{2+} ions from $\bar{4}3m$ to 3. This distortion can be modelled by the Hamiltonian $\hat{H}_{trig} = \delta[\hat{l}_z^2 - 2/3]$, where z denotes the **c**-axis, and the Hamiltonian acts on the effective orbital angular momentum ground state of the crystal field. Since $\hat{H}_{trig}$ commutes with $\hat{J}_{\text{eff}}^2$, but not with $\hat{J}_{\text{eff},z}$, the effect of the trigonal distortion will be to mix $|J_{\text{eff}}, J_{\text{eff},z}\rangle$ states of the same $J_{\text{eff},z}$ quantum number, but of differing J_{eff}, and the $(2J_{\text{eff}} + 1)$-fold degeneracy of the spin-orbital states will be lifted. $\hat{H}_{trig}$, however, will respect time reversal symmetry and the J_{eff} levels will be split into doubly degenerate Kramers doublets. By treating $\hat{H}_{trig}$ as a perturbation on the eigenstates of the spin-orbital Hamiltonian, the first-order shift in energy, $\delta E_{\text{trig}}^{(1)}$, for each state can be calculated and the results are tabulated in Table 4.5. The trigonal distortion and spin-orbit coupling can be treated on the same order, and the spectrum of states in the $|l_z, \mathsf{S}_z\rangle$ basis can be found by diagonalising the combined Hamiltonian $\hat{H}_{so} + \hat{H}_{trig}$. In order to have a first and second excited state of 28 meV and 58 meV, as seen in the energy scan in figure 4.6, the crystal field parameters $\delta = 45$ meV and $\lambda = 18$ meV were fitted.

The crystal field model presented thus far provides a ground state doublet, and the magnetic moment of this doublet has the operator $\hat{\boldsymbol{\mu}}$ which can be written in terms of the $\hat{\mathsf{l}}$ and $\hat{\mathsf{S}}$ operators:

$$\hat{\boldsymbol{\mu}} = -g_l \mu_B \hat{\mathbf{l}} - g_{\mathsf{S}} \mu_B \hat{\mathsf{S}} \tag{4.7}$$

J_{eff}	$J_{\text{eff},z}$	$\delta E^{(1)}_{\text{trig}}$
1/2	$\pm 1/2$	0
3/2	$\pm 3/2$	$-2\delta/75$
	$\pm 1/2$	$+2\delta/75$
5/2	$\pm 5/2$	$+\delta/30$
	$\pm 3/2$	$-\delta/150$
	$\pm 1/2$	$-2\delta/75$

Table 4.5: First order perturbation in energy of eigenstates of the spin-orbital Hamiltonian for Co^{2+} ions in a trigonally distorted octahedral crystal field of O^{2-} ions.

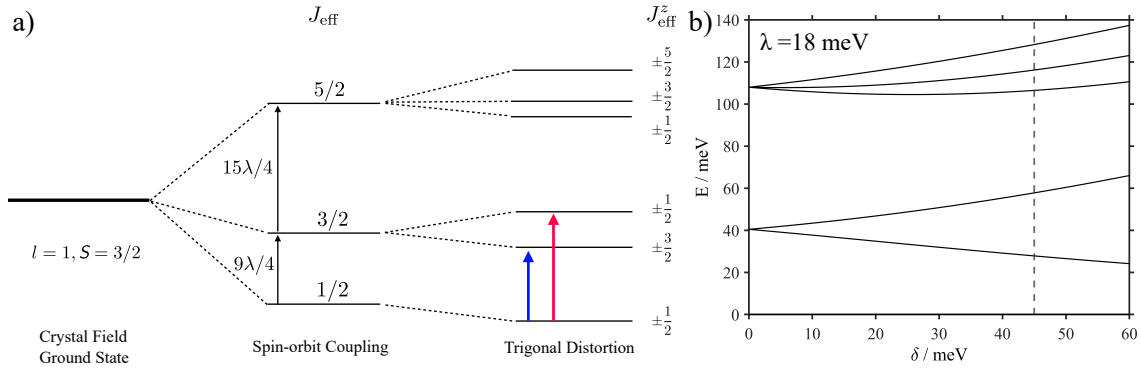

Figure 4.10: Single-ion spectrum a) within the lowest $l = 1$, $\mathsf{S} = 3/2$ sector for a Co^{2+} ion in an octahedral crystal field where trigonal distortion lifts the $(2J_{\text{eff}} + 1)$ degeneracy of the J_{eff} levels. b) Splitting of the crystal field levels as a function of the trigonal distortion δ at fixed $\lambda = 18$ meV. The dashed vertical line corresponds to parameter values that agree with the experimentally observed transitions to excited single-ion levels.

where $g_l = -3/2$, $g_{\mathsf{S}} = 2$, and μ_B is the Bohr magneton. The application of an external magnetic field $\mathbf{B}$ can be modelled with the Hamiltonian $\hat{H}_{ext} = -\hat{\boldsymbol{\mu}} \cdot \mathbf{B}$. Applying this external field will break time reversal symmetry and so the degeneracy of each of the Kramers doublets will be lifted. The splitting of the ground state doublet is given by $\Delta E = g_i \mu_B B_i$, where $i = x, y, z$ denotes the direction of the applied field, and the splitting can be found by diagonalising the combined Hamiltonian $\hat{H}_{so} + \hat{H}_{trig} + \hat{H}_{ext}$. In the absence of trigonal distortion, the g-factor for the ground state $J_{\text{eff}} = 1/2$ doublet is isotropic in which case $g_\perp = g_\parallel = 13/3$. Trigonal distortion will make z a special direction, and so the g-factor will become anisotropic with an in-plane x and y component - denoted by $g_\perp$ - different from the out of plane component - $g_\parallel$ - for an applied field along z. A plot of $g_\perp$ and $g_\parallel$

as a function of δ/λ is given in figure 4.11, and for the fitted crystal field parameters the g-factors can be read off as $g_{\parallel} = 2.90$ and $g_{\perp} = 4.95$. As a result, the in-plane moment has a value $g_{\perp}\mu_B S = 2.5\mu_B$, which is smaller than the experimentally determined value of $3\mu_B$, this shortcoming is due to interaction effects beyond the single-ion physics, to be described below.

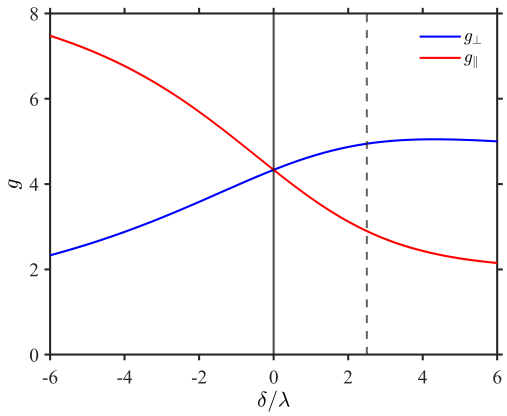

Figure 4.11: Anisotropic g-factors along and perpendicular to the trigonal axis for $CoTiO_3$ as a function δ/λ. The solid vertical line corresponds to the isotropic limit where the g-factor is equal to 13/3; the dashed vertical line corresponds to the best fit parameter values corresponding to the experimentally observed transitions to excited single-ion levels.

For the consideration of the effects of an octahedral crystal field, spin-orbit coupling, and trigonal distortion of the crystal field on the state of a single Co^{2+} ion, the total spin quantum number was denoted by S. The fitted single-ion parameters split the twelve degenerate levels of the $l = 1$, $\mathsf{S} = 3/2$ crystal field ground state to give a ground state doublet which may be treated as an effective spin-1/2 degree of freedom. This effective spin is denoted by S. The crystal structure of $CoTiO_3$ consists of a large number of the single-ion sites arranged in buckled honeycomb layers with ABC stacking. These single-ion sites will then interact with each other via exchange, which can be considered to be mediated via a mean field - h - that interacts with each spin S to give an easy-plane ground state. The Hamiltonian describing the interaction of the in-plane component of the spin of a single ion $\mathsf{S}_{\perp}$ with the in-plane component of the mean field $\mathsf{h}_{\perp}$ can be written as $\hat{H}_{mf} = -\mathsf{h}_{\perp} \cdot \mathsf{S}_{\perp}$. In general, the Hamiltonian describing spin-orbit coupling, trigonal distortion, exchange, and external magnetic field acting on the crystal field ground state can be written as $\hat{H} = \hat{H}_{so} + \hat{H}_{trig} + \hat{H}_{ext} + \hat{H}_{mf}$ which will take one parameter for each additive

term: λ, δ, $\mathbf{B}$, and $\mathsf{h}_\perp$, respectively. For any given set of parameters, diagonalising this Hamiltonian allows the spectrum of single-ion states to be determined. By calculating the energy shift of the ground state upon varying the in-plane component of $\mathbf{B}$, the magnitude of the in-plane magnetic moment can be plotted as a function of the mean field $\mathsf{h}_\perp$ - this plot is shown in figure 4.12a. Furthermore, for fixed λ and δ in zero external field, the energies of the states can be plotted as a function of mean field $\mathsf{h}_\perp$ - this plot is shown in figure 4.12b. The mean field due to exchange lifts the degeneracy of the ground state $S = 1/2$ level, and an incident neutron may create an excitation within the effective spin-1/2 state. The propagation of this excitation throughout the lattice is a magnon and will be treated from section 4.4 onwards. Additionally, higher energy excitations due to transitions to higher crystal field levels are possible, and such excitations are spin-orbit excitons - treated in section 4.9. The next section will introduce an effective XXZ exchange Hamiltonian, in equation 4.10. For that Hamiltonian, the magnitude of the mean-field acting on the effective spin-1/2 degree of freedom, S is given by

$$h_\perp = \left| S \sum_{n=1}^{6} (-1)^{n+1} z_n J_n^\perp \right| \tag{4.8}$$

where $h_\perp$ is the perpendicular component of the mean field $\mathbf{h}$ that acts on the effective spin-1/2 denoted by S (as opposed to h which acts on the total spin $\mathsf{S} = 3/2$ degrees of freedom). The sum is over the first to sixth nearest neighbouring Co^{2+} sites in the lattice, z_n is the coordination number of the nth nearest neighbour bond, and $J_n^\perp$ is the in-plane component of the exchange parameter for the nth nearest neighbour bond. Using fitted values of the exchange parameters in equation 4.34, the magnitude of the mean field is $h_\perp = 9.1$ meV. By relating the mean field parameters by $\hat{H}_{mf} = -\mathbf{h}_\perp \cdot \mathbf{S}_\perp = -\mathsf{h}_\perp \cdot \mathsf{S}_\perp$ and matching the Zeeman splitting of the lowest doublet under the exchange mean field, a mean field of $\mathsf{h}_\perp = 4.2$ meV is obtained. The magnitude of the in-plane component of the moment can then be read off from figure 4.12b as $2.95\mu_B$. Therefore, the mean field due to exchange re-scales the in-plane component of the magnetic moment closer to the value of $3.08\mu_B$ found experimentally.

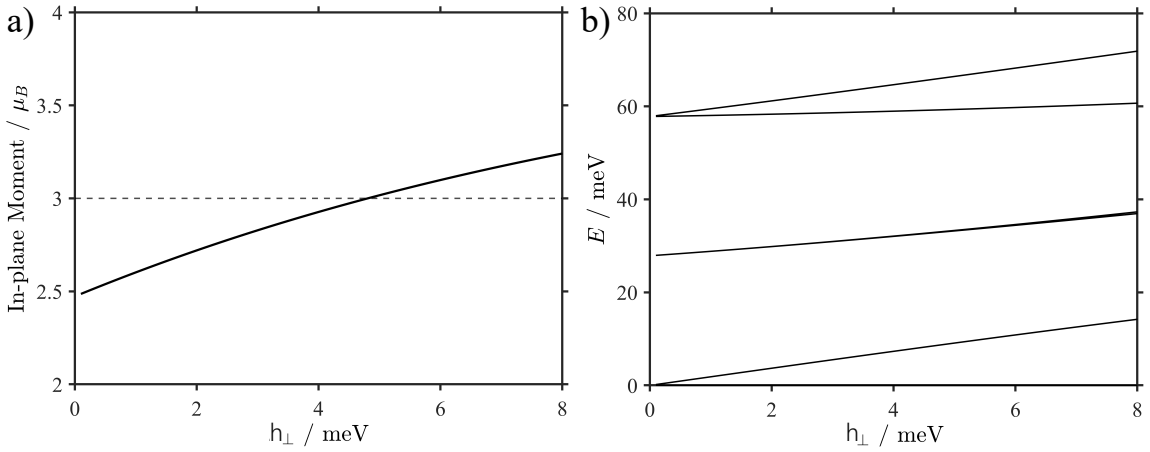

Figure 4.12: Ground state moment and energy levels for Co^{2+} ions as a function of the in-plane mean field. a) In-plane magnetic moment in the ground state as a function of in-plane mean field $\mathsf{h}_\perp$. b) Splitting of the single-ion levels as a function of $\mathsf{h}_\perp$. Note that the splitting of the first excited $J^z_{\text{eff}} = \pm 3/2$ levels is very small.

4.4 XXZ Easy-Plane Spin Wave Model for Magnons

In order to model the magnon spectrum, the XXZ Hamiltonian is introduced in equation 4.10 and can be written into a quadratic form in terms of boson operators via a Holstein-Primakoff expansion. In order to reduce the number of operators required in the expansion, a transformation from the global frame to a local frame in which all spins are parallel can be defined.

First, the global frame is defined with a Cartesian basis denoted by xyz such that $\mathbf{x}$ is parallel to the hexagonal $\mathbf{a}$ axis, $\mathbf{z}$ is parallel to the hexagonal $\mathbf{c}$ axis, and the frame is defined to be right handed so $\mathbf{y} = \mathbf{z} \times \mathbf{x}$. A second, local frame with differing orientation for each sublattice, denoted by $\tilde{x}\tilde{y}\tilde{z}$, can be defined. The $\tilde{\mathbf{y}}$ axis is defined to be along the hexagonal $\mathbf{c}$ axis, and the frame will be rotated about $\tilde{\mathbf{y}}$ for each sublattice such that the $\tilde{\mathbf{z}}$ axis is along the local magnetic moment. This gives the following relationship between the two frames:

$$\begin{aligned} \mathbf{x} &= \cos(\phi + m\pi)\tilde{\mathbf{z}} - \sin(\phi + m\pi)\tilde{\mathbf{x}}, \\ \mathbf{y} &= \sin(\phi + m\pi)\tilde{\mathbf{z}} + \cos(\phi + m\pi)\tilde{\mathbf{x}}, \\ \mathbf{z} &= \tilde{\mathbf{y}}, \end{aligned} \tag{4.9}$$

where ϕ is the in plane angle of the moment with respect to the global $\mathbf{x}$ axis, where $m = 0$ for the A and B sublattices, and $m = 1$ for the C and D sublattices, see 4.1d. In the global frame, the XXZ exchange Hamiltonian for the nth nearest neighbour coupling is written as

$$\hat{H}_n = \sum_{\langle i,j \rangle_n} J_n^{\perp} \left(\hat{S}_i^x \hat{S}_j^x + \hat{S}_i^y \hat{S}_j^y \right) + J_n^z \hat{S}_i^z \hat{S}_j^z, \tag{4.10}$$

where the sum is over all n^{th} nearest neighbour bonds between Co^{2+} sites i and j such that each bond is counted only once. Here, the convention for ferromagnetic coupling is $J < 0$ and antiferromagnetic exchange is $J > 0$ and will continue to be used in the following sections in this chapter. Transforming to the local frame puts the Hamiltonian into the following form

$$\begin{aligned} \hat{H}_{\text{odd}} &= \sum_{\langle i,j \rangle_n} J_n^{\perp} \left(\hat{S}_i^{\tilde{z}} \hat{S}_j^{\tilde{z}} + \hat{S}_i^{\tilde{x}} \hat{S}_j^{\tilde{x}} \right) + J_n^z \hat{S}_i^{\tilde{y}} \hat{S}_j^{\tilde{y}}, \\ \hat{H}_{\text{even}} &= \sum_{\langle i,j \rangle_n} -J_n^{\perp} \left(\hat{S}_i^{\tilde{z}} \hat{S}_j^{\tilde{z}} + \hat{S}_i^{\tilde{x}} \hat{S}_j^{\tilde{x}} \right) + J_n^z \hat{S}_i^{\tilde{y}} \hat{S}_j^{\tilde{y}}. \end{aligned} \tag{4.11}$$

The local transformation will make all spins parallel and so the local frame will only have two sublattices, these are denoted by $\tilde{A}$ and $\tilde{B}$. The A and C sublattices in the global frame will map to the $\tilde{A}$ sublattice, and the B and D sublattices in the global frame will map to the $\tilde{B}$ sublattice. In order to obtain terms up to quadratic order in operators, the spin-operators can be written in terms of raising and lowering operators for spin-flips on the $\tilde{A}$ and $\tilde{B}$ sublattices using the Holstein-Primakoff transformation [16] in the following manner

$$
\begin{aligned}
\hat{S}_i^{\tilde{A}\tilde{z}} &= S - \hat{a}_i^\dagger \hat{a}_i, \\
\hat{S}_i^{\tilde{A}\tilde{x}} &= \sqrt{S/2}(\hat{a}_i^\dagger + \hat{a}_i), \\
\hat{S}_i^{\tilde{A}\tilde{y}} &= i\sqrt{S/2}(\hat{a}_i^\dagger - \hat{a}_i), \\
\hat{S}_i^{\tilde{B}\tilde{z}} &= S - \hat{b}_i^\dagger \hat{b}_i, \\
\hat{S}_i^{\tilde{B}\tilde{x}} &= \sqrt{S/2}(\hat{b}_i^\dagger + \hat{b}_i), \\
\hat{S}_i^{\tilde{B}\tilde{y}} &= i\sqrt{S/2}(\hat{b}_i^\dagger - \hat{b}_i).
\end{aligned}
\tag{4.12}
$$

The raising and lowering operators can also be written in the basis of momentum states via the change of basis

$$
\begin{aligned}
\hat{a}_{\mathbf{k}} &= \sqrt{\frac{2}{N}} \sum_{i \in \tilde{A}} e^{-i\mathbf{k}\cdot\mathbf{x}_i} \hat{a}_i, \\
\hat{a}_{\mathbf{k}}^\dagger &= \sqrt{\frac{2}{N}} \sum_{i \in \tilde{A}} e^{i\mathbf{k}\cdot\mathbf{x}_i} \hat{a}_i^\dagger, \\
\hat{b}_{\mathbf{k}} &= \sqrt{\frac{2}{N}} \sum_{i \in \tilde{B}} e^{-i\mathbf{k}\cdot\mathbf{x}_i} \hat{b}_i, \\
\hat{b}_{\mathbf{k}}^\dagger &= \sqrt{\frac{2}{N}} \sum_{i \in \tilde{B}} e^{i\mathbf{k}\cdot\mathbf{x}_i} \hat{b}_i^\dagger.
\end{aligned}
\tag{4.13}
$$

The raising and lowering operators obey the usual commutation relations for bosonic operators,

$$
\begin{aligned}
[\hat{a}_i^\dagger, \hat{a}_j] &= \delta_{ij}, \quad [\hat{b}_i^\dagger, \hat{b}_j] &= \delta_{ij}, \\
[\hat{a}_{\mathbf{k}}^\dagger, \hat{a}_{\mathbf{k}'}] &= \delta_{\mathbf{k}\mathbf{k}'}, \quad [\hat{b}_{\mathbf{k}}^\dagger, \hat{b}_{\mathbf{k}'}] &= \delta_{\mathbf{k}\mathbf{k}'},
\end{aligned}
\tag{4.14}
$$

and all other commutation relations equal to zero. Expanding all terms in the Hamiltonian in equation 4.10 to quadratic order in raising and lowering operators up to sixth nearest neighbour gives a Hamiltonian of the form

$$\hat{H} = \frac{1}{2}\sum_{\mathbf{k}} \hat{\mathbf{\Psi}}^{\dagger}_{\mathbf{k}} \mathcal{D}(\mathbf{k}) \hat{\mathbf{\Psi}}_{\mathbf{k}}, \tag{4.15}$$

where $\hat{\mathbf{\Psi}}^{\dagger}_{\mathbf{k}} = \left(\hat{a}^{\dagger}_{\mathbf{k}}, \hat{b}^{\dagger}_{\mathbf{k}}, \hat{a}_{-\mathbf{k}}, \hat{b}_{-\mathbf{k}}\right)$, the sum is over all wavevectors $\mathbf{k}$ within the Brillouin zone, and $\mathcal{D}(\mathbf{k})$ is the dynamical matrix with the form

$$\mathcal{D}(\mathbf{k}) = \begin{pmatrix} A & B & C & D^* \\ B^* & A & D & C \\ C^* & D^* & A & B \\ D & C^* & B^* & A \end{pmatrix}, \tag{4.16}$$

where the matrix elements are given by

$$\begin{aligned}
A &= \left[-3J_1^{\perp} + J_2^{\perp} - 6J_3^{\perp} + \frac{1}{2}\left(J_3^{\perp} + J_3^{z}\right)\gamma_{3\mathbf{k}} + 6J_4^{\perp} - \frac{1}{2}\left(J_4^{\perp} - J_4^{z}\right)\gamma_{4\mathbf{k}} - 3J_5^{\perp} + 3J_6^{\perp}\right] S, \\
B &= \left[\frac{1}{2}\left(J_1^{\perp} + J_1^{z}\right)\gamma_{1\mathbf{k}} - \frac{1}{2}\left(J_2^{\perp} - J_2^{z}\right)\gamma_{2\mathbf{k}} + \frac{1}{2}\left(J_5^{\perp} + J_5^{z}\right)\gamma_{5\mathbf{k}} - \frac{1}{2}\left(J_6^{\perp} - J_6^{z}\right)\gamma_{6\mathbf{k}}\right] S, \\
C &= \left[\frac{1}{2}\left(J_3^{\perp} - J_3^{z}\right)\gamma_{3\mathbf{k}} - \frac{1}{2}\left(J_4^{\perp} + J_4^{z}\right)\gamma_{4\mathbf{k}}\right] S, \\
D &= \left[\frac{1}{2}\left(J_1^{\perp} - J_1^{z}\right)\gamma^*_{1\mathbf{k}} - \frac{1}{2}\left(J_2^{\perp} + J_2^{z}\right)\gamma^*_{2\mathbf{k}} + \frac{1}{2}\left(J_5^{\perp} - J_5^{z}\right)\gamma^*_{5\mathbf{k}} - \frac{1}{2}\left(J_6^{\perp} + J_6^{z}\right)\gamma^*_{6\mathbf{k}}\right] S,
\end{aligned} \tag{4.17}$$

and $\gamma_{n\mathbf{k}}$ is defined by

$$\gamma_{n\mathbf{k}} = \sum_{ni \in \mathrm{NN}(n)} e^{i\mathbf{k}\cdot\boldsymbol{\delta}_{ni}}. \tag{4.18}$$

Here ni denotes the ith member of the set of nth nearest neighbour bonds, and $\boldsymbol{\delta}_{ni}$ is the vector along each of these bonds. A list of these up to sixth nearest neighbour is given below:

$$\begin{array}{llll}
\boldsymbol{\delta}_{11} = \frac{-\mathbf{a}+\mathbf{b}}{3} + \epsilon\mathbf{c} & \boldsymbol{\delta}_{31} = \mathbf{a} & \boldsymbol{\delta}_{41} = \frac{-\mathbf{a}+\mathbf{b}+\mathbf{c}}{3} & \boldsymbol{\delta}_{51} = \frac{2\mathbf{a}+4\mathbf{b}}{3} + \epsilon\mathbf{c} \\
\boldsymbol{\delta}_{12} = \frac{2\mathbf{a}+\mathbf{b}}{3} + \epsilon\mathbf{c} & \boldsymbol{\delta}_{32} = \mathbf{b} & \boldsymbol{\delta}_{42} = \frac{2\mathbf{a}+\mathbf{b}+\mathbf{c}}{3} & \boldsymbol{\delta}_{52} = \frac{-4\mathbf{a}-2\mathbf{b}}{3} + \epsilon\mathbf{c} \\
\boldsymbol{\delta}_{13} = \frac{-\mathbf{a}-2\mathbf{b}}{3} + \epsilon\mathbf{c} & \boldsymbol{\delta}_{33} = \mathbf{a}+\mathbf{b} & \boldsymbol{\delta}_{43} = \frac{-\mathbf{a}-2\mathbf{b}+\mathbf{c}}{3} & \boldsymbol{\delta}_{53} = \frac{2\mathbf{a}-2\mathbf{b}}{3} + \epsilon\mathbf{c} \\
 & \boldsymbol{\delta}_{34} = -\mathbf{a} & \boldsymbol{\delta}_{44} = \frac{\mathbf{a}-\mathbf{b}-\mathbf{c}}{3} & \boldsymbol{\delta}_{61} = \frac{\mathbf{a}-\mathbf{b}+\mathbf{c}}{3} + \epsilon\mathbf{c} \\
\boldsymbol{\delta}_{2} = \frac{-\mathbf{c}}{3} + \epsilon\mathbf{c} & \boldsymbol{\delta}_{35} = -\mathbf{b} & \boldsymbol{\delta}_{45} = \frac{-2\mathbf{a}-\mathbf{b}-\mathbf{c}}{3} & \boldsymbol{\delta}_{62} = \frac{\mathbf{a}+2\mathbf{b}+\mathbf{c}}{3} + \epsilon\mathbf{c} \\
 & \boldsymbol{\delta}_{36} = -\mathbf{a}-\mathbf{b} & \boldsymbol{\delta}_{46} = \frac{\mathbf{a}+2\mathbf{b}-\mathbf{c}}{3} & \boldsymbol{\delta}_{63} = \frac{-2\mathbf{a}+2\mathbf{b}+\mathbf{c}}{3} + \epsilon\mathbf{c}
\end{array} \tag{4.19}$$

where $\mathbf{a}$, $\mathbf{b}$, and $\mathbf{c}$ are the lattice vectors of the unit cell in the hexagonal setting, and $\epsilon = 2\,(z_{Co} - 1/3)$ is a parameter that describes the buckling of the honeycomb layers.

The dispersions and intensities of the magnon modes are calculated by defining a change of basis of the operators in $\hat{\boldsymbol{\Psi}}_{\mathbf{k}}$. By following the method of White, et. al. [17], this change of basis can be written as $\hat{\boldsymbol{\Psi}}_{\mathbf{k}} = S\hat{\boldsymbol{\Phi}}_{\mathbf{k}}$ such that the dynamical matrix is diagonalised - $S^{-1}g\mathcal{D}S = g\mathcal{D}'$ - in addition to a normalisation condition $SgS^{\dagger} = g$ which when satisfied ensures the commutation relations in equation 4.14 are preserved in the new basis. The matrix g has matrix elements given by $g_{\mu\nu} = [\hat{\Psi}^{\dagger}_{\mathbf{k}\mu}, \hat{\Psi}_{\mathbf{k}\nu}]$. In this case, $g = \mathrm{diag}(1, 1, -1, -1)$ and $\mathcal{D}'$ is a diagonal matrix which will be of the form $\mathrm{diag}(\omega_+, \omega_-, \omega_+, \omega_-)$. Explicitly, the operators and Hamiltonian in equation 4.15 will transform as follows

$$\hat{\boldsymbol{\Psi}}_{\mathbf{k}} = \begin{pmatrix} \hat{a}_{\mathbf{k}} \\ \hat{b}_{\mathbf{k}} \\ \hat{a}^{\dagger}_{-\mathbf{k}} \\ \hat{b}^{\dagger}_{-\mathbf{k}} \end{pmatrix} = S \begin{pmatrix} \hat{\alpha}_{\mathbf{k}} \\ \hat{\beta}_{\mathbf{k}} \\ \hat{\alpha}^{\dagger}_{-\mathbf{k}} \\ \hat{\beta}^{\dagger}_{-\mathbf{k}} \end{pmatrix} = S\hat{\boldsymbol{\Phi}}_{\mathbf{k}} \tag{4.20}$$

$$\hat{H} = \frac{1}{2}\sum_{\mathbf{k}} \hat{\boldsymbol{\Phi}}^{\dagger}_{\mathbf{k}}\mathcal{D}'(\mathbf{k})\hat{\boldsymbol{\Phi}}_{\mathbf{k}} = \sum_{\mathbf{k}} \omega_+(\mathbf{k})\hat{\alpha}^{\dagger}_{\mathbf{k}}\hat{\alpha}_{\mathbf{k}} + \omega_-(\mathbf{k})\hat{\beta}^{\dagger}_{\mathbf{k}}\hat{\beta}_{\mathbf{k}}. \tag{4.21}$$

The ground state of the system $|0\rangle$ can be defined by $\hat{\alpha}_{\mathbf{k}}|0\rangle = \hat{\beta}_{\mathbf{k}}|0\rangle = 0$. Since the commutation relations typical of raising and lowering operators for bosonic excitations have been preserved, the singly excited states can be defined by $|\alpha_{\mathbf{k}}\rangle = \hat{\alpha}^{\dagger}_{\mathbf{k}}|0\rangle$ and $|\beta_{\mathbf{k}}\rangle = \hat{\beta}^{\dagger}_{\mathbf{k}}|0\rangle$ with energies $\omega_+(\mathbf{k})$ and $\omega_-(\mathbf{k})$, respectively. Therefore, the dispersions in the local frame are obtained by finding the eigenvalues of the matrix $g\mathcal{D}$

$$\begin{aligned}\omega^2_{\pm}(\mathbf{k}) = A^2 + |B|^2 - |C|^2 - |D|^2 \pm \\ \sqrt{(2AB - CD^* - C^*D^*)(2AB^* - CD - C^*D) + (BD - B^*D^*)^2}\end{aligned} \tag{4.22}$$

Provided the bucking does not change the number of nth nearest neighbour bonds and taking the exchange coefficients to be adjustable parameters of the model, then the only place the buckling parameter ϵ enters the model will be via bonds that connect the $\tilde{A}$ and $\tilde{B}$ sublattices, that is in the $\boldsymbol{\delta}_n$ terms for $n = 1, 2, 5, 6$. This buckling will give a phase factor of $2\pi\epsilon L$ in $\gamma_{n\mathbf{k}}$. Following this through to the dynamical matrix elements means that A and C as defined in equation 4.25 are independent of the buckling parameter, whereas $B = B(\epsilon = 0)e^{2\pi i\epsilon L}$ and $D = D(\epsilon = 0)e^{-2\pi i\epsilon L}$. The dispersion relation in equation 4.22 contains terms such as $|B|^2$, $|D|^2$, BD, and B^*D^* and as such will be independent of buckling. Now, if buckling is absent, then the local frame defined in equation 4.9 will be equivalent to a rotating frame $x'y'z'$ defined by

$$\begin{aligned}\mathbf{x} &= \cos(\phi + \mathbf{Q}\cdot\mathbf{r})\mathbf{z}' - \sin(\phi + \mathbf{Q}\cdot\mathbf{r})\mathbf{x}', \\ \mathbf{y} &= \sin(\phi + \mathbf{Q}\cdot\mathbf{r})\mathbf{z}' + \cos(\phi + \mathbf{Q}\cdot\mathbf{r})\mathbf{x}', \\ \mathbf{z} &= \mathbf{y}',\end{aligned} \tag{4.23}$$

where $\mathbf{Q} = 3\pi/c\hat{\mathbf{z}}$ is the magnetic ordering wavevector, and $\mathbf{r}$ is the position of a Co^{2+} site. As a consequence, there are four modes for the unbuckled lattice and their dispersions at any given point in the Brillouin zone are given by $\omega_+(\mathbf{k})$, $\omega_-(\mathbf{k})$, $\omega_+(\mathbf{k}+\mathbf{Q})$, $\omega_-(\mathbf{k}+\mathbf{Q})$. Since the dispersions are independent of buckling, these expressions for the dispersions also hold for the buckled lattice. Note that $\mathbf{Q}$ is half of a reciprocal lattice vector $\boldsymbol{\tau}$, and so

$\mathbf{k}+\mathbf{Q}$ is equivalent to $\mathbf{k}-\mathbf{Q}$ up to a translation by a reciprocal lattice vector, giving four - rather than six - modes.

The transformation matrix S is found by constructing a matrix with columns that are eigenvectors of $g\mathcal{D}$

$$S = \begin{pmatrix} \bar{W}(\omega_+) & \bar{W}(\omega_-) & \bar{W}(-\omega_+) & \bar{W}(-\omega_-) \\ \bar{Y}(\omega_+) & \bar{Y}(\omega_-) & \bar{Y}(-\omega_+) & \bar{Y}(-\omega_-) \\ \bar{X}(\omega_+) & \bar{X}(\omega_-) & \bar{X}(-\omega_+) & \bar{X}(-\omega_-) \\ \bar{Z}(\omega_+) & \bar{Z}(\omega_-) & \bar{Z}(-\omega_+) & \bar{Z}(-\omega_-) \end{pmatrix} \tag{4.24}$$

where W, X, Y, and Z are defined by

$$\begin{aligned} W(\omega) &= -(A+\omega)(A^2+|B|^2-|C|^2-|D|^2-\omega^2)+2A|B|^2-BDC^*-B^*D^*C \\ X(\omega) &= (A^2C^*+|B|^2C^*-|C|^2C^*+|D|^2C-C^*\omega^2)-A(BD+B^*D^*)+\omega(BD-B^*D^*) \\ Y(\omega) &= B^*\left[(A+\omega)^2-|B|^2+|C|^2\right]-(A+\omega)(C+C^*)D+BD^2 \\ Z(\omega) &= D(A^2+C^{*2}-|D|^2-\omega^2)+B^{*2}D^*-2AB^*C^* \end{aligned} \tag{4.25}$$

and the barred values $\bar{W}(\omega)=W(\omega)/\sqrt{N(\omega)}$ are normalised so the condition $SgS^\dagger=g$ is satisfied, where N is given by

$$N(\omega)=\left||W|^2-|X|^2+|Y|^2-|Z|^2\right|.$$

The dynamical correlation functions in the rotating frame - $S^{x'x'}(\mathbf{k},\omega)$ and $S^{y'y'}(\mathbf{k},\omega)$ - are given by $\sum_\lambda |\langle\lambda|\hat{S}^{x'}_{\mathbf{k}}|0\rangle|^2\delta(\omega-\omega_\lambda(\mathbf{k}))$ and $\sum_\lambda |\langle\lambda|\hat{S}^{y'}_{\mathbf{k}}|0\rangle|^2\delta(\omega-\omega_\lambda(\mathbf{k}))$, respectively; where the sum is over singly excited states λ. $\hat{S}^{x'}_{\mathbf{k}}|0\rangle$ and $\hat{S}^{y'}_{\mathbf{k}}|0\rangle$ satisfy

$$\begin{aligned}\hat{S}^{x'}_{\mathbf{k}}\left|0\right\rangle &= \frac{\sqrt{S}}{2}\left[(\bar{W}+\bar{X}+\bar{Y}+\bar{Z})_{(-\omega_-)}\hat{\alpha}^{\dagger}_{-\mathbf{k}} + (\bar{W}+\bar{X}+\bar{Y}+\bar{Z})_{(-\omega_+)}\hat{\beta}^{\dagger}_{-\mathbf{k}}\right]\left|0\right\rangle, \\ \hat{S}^{y'}_{\mathbf{k}}\left|0\right\rangle &= i\frac{\sqrt{S}}{2}\left[(-\bar{W}+\bar{X}-\bar{Y}+\bar{Z})_{(-\omega_-)}\hat{\alpha}^{\dagger}_{-\mathbf{k}} + (-\bar{W}+\bar{X}-\bar{Y}+\bar{Z})_{(-\omega_+)}\hat{\beta}^{\dagger}_{-\mathbf{k}}\right]\left|0\right\rangle,\end{aligned} \tag{4.26}$$

where terms proportional to $\hat{\alpha}_{\mathbf{k}}\left|0\right\rangle$ and $\hat{\beta}_{\mathbf{k}}\left|0\right\rangle$ have been omitted since they are identically zero. Therefore, the local frame correlation functions are given by:

$$\begin{aligned}S^{x'x'}(\mathbf{k},\omega) &= \frac{S}{4N}\left|W+X+Y+Z\right|^2 \times \left[\delta(\omega-\omega_-(\mathbf{k})) + \delta(\omega-\omega_+(\mathbf{k}))\right], \\ S^{y'y'}(\mathbf{k},\omega) &= \frac{S}{4N}\left|W-X+Y-Z\right|^2 \times \left[\delta(\omega-\omega_-(\mathbf{k})) + \delta(\omega-\omega_+(\mathbf{k}))\right].\end{aligned} \tag{4.27}$$

For the case of $\epsilon = 0$, i.e. where there is no buckling of the honeycomb layers and the rotating frame defined by 4.23 can be used, the elements of S will be given by W_0, X_0, Y_0 and Z_0, which are defined analogously to the elements of the dynamical matrix in the rotating frame, e.g. $A(\epsilon = 0)$. Transforming from the rotating to the global frame, and assuming that $\phi = 0$, gives the following expressions for $\hat{S}^{y}_{0\mathbf{k}}\left|0\right\rangle$ and $\hat{S}^{z}_{0\mathbf{k}}\left|0\right\rangle$

$$\begin{aligned}\hat{S}^{y}_{0\mathbf{k}}\left|0\right\rangle &= \frac{\sqrt{S}}{2}[(\bar{W}_0+\bar{X}_0+\bar{Y}_0+\bar{Z}_0)_{(\mathbf{k}+\mathbf{Q},-\omega_-)}\hat{\alpha}^{\dagger}_{-\mathbf{k}+\mathbf{Q}} \\ &\quad + (\bar{W}_0+\bar{X}_0+\bar{Y}_0+\bar{Z}_0)_{(\mathbf{k}+\mathbf{Q},-\omega_+)}\hat{\beta}^{\dagger}_{-\mathbf{k}+\mathbf{Q}}]\left|0\right\rangle, \\ \hat{S}^{z}_{0\mathbf{k}}\left|0\right\rangle &= i\frac{\sqrt{S}}{2}\left[(-\bar{W}_0+\bar{X}_0-\bar{Y}_0+\bar{Z}_0)_{(-\omega_-)}\hat{\alpha}^{\dagger}_{-\mathbf{k}} + (-\bar{W}_0+\bar{X}_0-\bar{Y}_0+\bar{Z}_0)_{(-\omega_+)}\hat{\beta}^{\dagger}_{-\mathbf{k}}\right]\left|0\right\rangle,\end{aligned} \tag{4.28}$$

and therefore the global frame spin-spin correlation functions in the absence of buckling ($\epsilon = 0$) of the honeycomb layers are given by:

$$\begin{aligned}S^{yy}_0(\mathbf{k},\omega) &= \frac{S}{4N}\left|W_0+X_0+Y_0+Z_0\right|^2_{\mathbf{k}+\mathbf{Q}} \times \left[\delta(\omega-\omega_-(\mathbf{k}+\mathbf{Q})) + \delta(\omega-\omega_+(\mathbf{k}+\mathbf{Q}))\right] \\ S^{zz}_0(\mathbf{k},\omega) &= \frac{S}{4N}\left|W_0-X_0+Y_0-Z_0\right|^2_{\mathbf{k}} \times \left[\delta(\omega-\omega_-(\mathbf{k})) + \delta(\omega-\omega_+(\mathbf{k}))\right]\end{aligned} \tag{4.29}$$

So the modes shifted by the magnetic ordering wavevector are due to fluctuations in the plane of the honeycomb layers, whereas the modes that remain unshifted in momentum space are due to fluctuations out of the plane of the honeycomb layers. For the case of finite buckling ($\epsilon \neq 0$), W and X remain unchanged, but $Y = Y_0 e^{-2\pi i \epsilon L}$ and $Z = Z_0 e^{-2\pi i \epsilon L}$. By comparison with SpinW [18] and code modelling generic multi-sublattice collinear antiferromagnets [19] models - as shown in figure 4.13 - the global frame spin-spin correlation function is found to be:

$$\begin{aligned} S^{yy}(\mathbf{k},\omega) &= \frac{S}{4N} \left| W_0 + X_0 + (Y_0 + Z_0) e^{2\pi i \epsilon L} \right|^2_{\mathbf{k}+\mathbf{Q}} \times [\delta(\omega - \omega_-(\mathbf{k}+\mathbf{Q})) + \delta(\omega - \omega_+(\mathbf{k}+\mathbf{Q}))] \\ S^{zz}(\mathbf{k},\omega) &= \frac{S}{4N} \left| W_0 - X_0 + (Y_0 - Z_0) e^{-2\pi i \epsilon L} \right|^2_{\mathbf{k}} \times [\delta(\omega - \omega_-(\mathbf{k})) + \delta(\omega - \omega_+(\mathbf{k}))] \end{aligned} \tag{4.30}$$

For the in-plane correlation function, $S^{yy}(\mathbf{k},\omega)$, the matrix elements of S are evaluated at $\mathbf{k}+\mathbf{Q}$ and correspond to modes shifted by $\mathbf{Q}$, but the phase factor of the Y_0 and Z_0 terms corresponds to the z-component of the unshifted momentum $\mathbf{k}$. For the out-of-plane correlation function, $S^{zz}(\mathbf{k},\omega)$, all terms are simply evaluated at $\mathbf{k}$. From these correlation functions, it may be concluded that although the buckling of the honeycomb layers does not change the form of the dispersion of the modes, the buckling does introduce a correction to the spin-spin correlations and the INS intensity of the modes. The eigenvalues and eigenvectors of the 4×4 dynamical matrix for the system with no buckling can be calculated, and then the phase factors of $e^{\pm 2\pi i \epsilon L}$ only need to be added as an intensity modulation when computing the dynamical correlations. This intensity modulation can be considered as arising from interference scattering from the offset A and B Co^{2+} sublattices, and is non-zero when the momentum transfer has a component perpendicular to the plane of the honeycomb layers. Although this intensity modulation has a long period of $1/\epsilon$, it will have a very noticeable effect on the INS intensity profile of the crossing points - as shown in section 4.8.

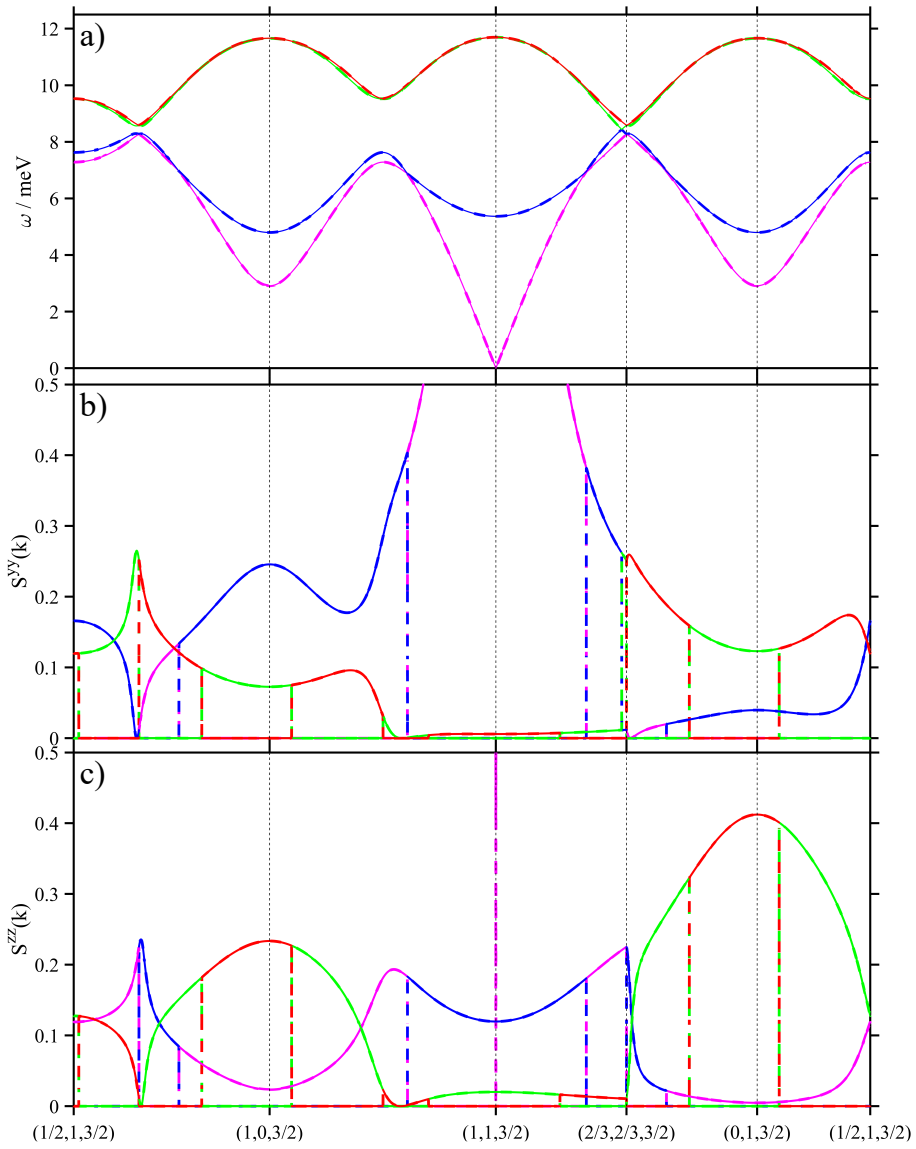

Figure 4.13: Comparison of a) dispersions and b/c) dynamical correlations for the in-/out-of-plane fluctuations calculated analytically using equation 4.30 (dotted lines) with the same quantities calculated from a SpinW model (dashed lines). The plots show perfect agreement between the two methods of calculation.

4.5 Spectral Gap and Fitting of XXZΔ Model

Although the XXZ model defined in section 4.4 above is able to reproduce many features of the magnon dispersions - including a linear in-plane dispersive mode at the magnetic Bragg peak position, the mode at this position is constrained by symmetry to be gapless, as shown in 4.13a. This model cannot reproduce the slices taken along L, as shown in figure 4.14a-b, where a mode with a spectral gap of 1 meV is observed above the magnetic Bragg

peak. The reason for this disparity between the model and the experimental data is due to the symmetry of the XXZ Hamiltonian. The XXZ Hamiltonian (equation 4.10) is invariant under a rotation of the spin degrees of freedom with an arbitrary angle in the xy-plane and is thus said to possess $U(1)$ symmetry. The crystal structure of the Co^{2+} ions, however, remains invariant under threefold rotations about the **c** axis, inversion, and reflection in a mirror plane containing **c** and $\mathbf{a}-\mathbf{b}$; these symmetry operations constitute the point group $\bar{3}m$. Upon cooling below 38K, the system magnetically orders, and the moments order along some direction in the crystallographic ab-plane. Although the XXZ Hamiltonian has $U(1)$ symmetry, the magnetic structure only possesses inversion symmetry - with point group $\bar{1}$. In this case, there is a spontaneous symmetry breaking from a continuous symmetry group - i.e. $U(1)$ - to a discrete symmetry group - i.e. $\bar{1}$. As a result, the XXZ model must possess a gapless Goldstone mode.

To further confirm the spectral gap observed at $(1, 1, 3/2)$, a set of mutually perpendicular slices through the $(1, 1, 3/2)$ position along the $(0, 0, 1)$, $(1, 1, 0)$, and $(1, -1, 0)$ directions were taken. Figure 4.14a,c,d shows that the slices are all centred at the nominal positions and the observed gap at $(1, 1, 3/2)$ is indeed a genuine spectral gap and not an artifact of some misalignment. It is also important to note that the spectral gap is only clearly resolved in the $E_i = 9.6$ meV dataset since the higher incident energy datasets have coarser energy resolutions which cannot resolve the 1 meV spectral gap.

Any model that includes a reduction of the continuous $U(1)$ symmetry of the XXZ Hamiltonian to the discrete $\bar{3}m$ point group symmetry of the crystal structure of the Co^{2+} ions would no longer be constrained by symmetry to have a gapless mode at the magnetic Bragg peak positions. In this case, the spontaneous symmetry breaking upon the onset of magnetic order would be from one discrete symmetry group to another. Furthermore, the onset of magnetic order in a macroscopic sample would give rise to six distinct and equally populated magnetic domains which can be parametrised by the angle ϕ - in plane angle of the moment with respect to the crystallographic **a** axis. Consider the primary magnetic domain with an in-plane angle given by $\phi = \phi_0$. The five other magnetic domains then have an in-plane angle given by $\phi = \phi_0 + n\pi/3$ for $n = 1$ to 5. Assuming equal weight between all six magnetic domains, the INS scattering intensity for a system with these domains will

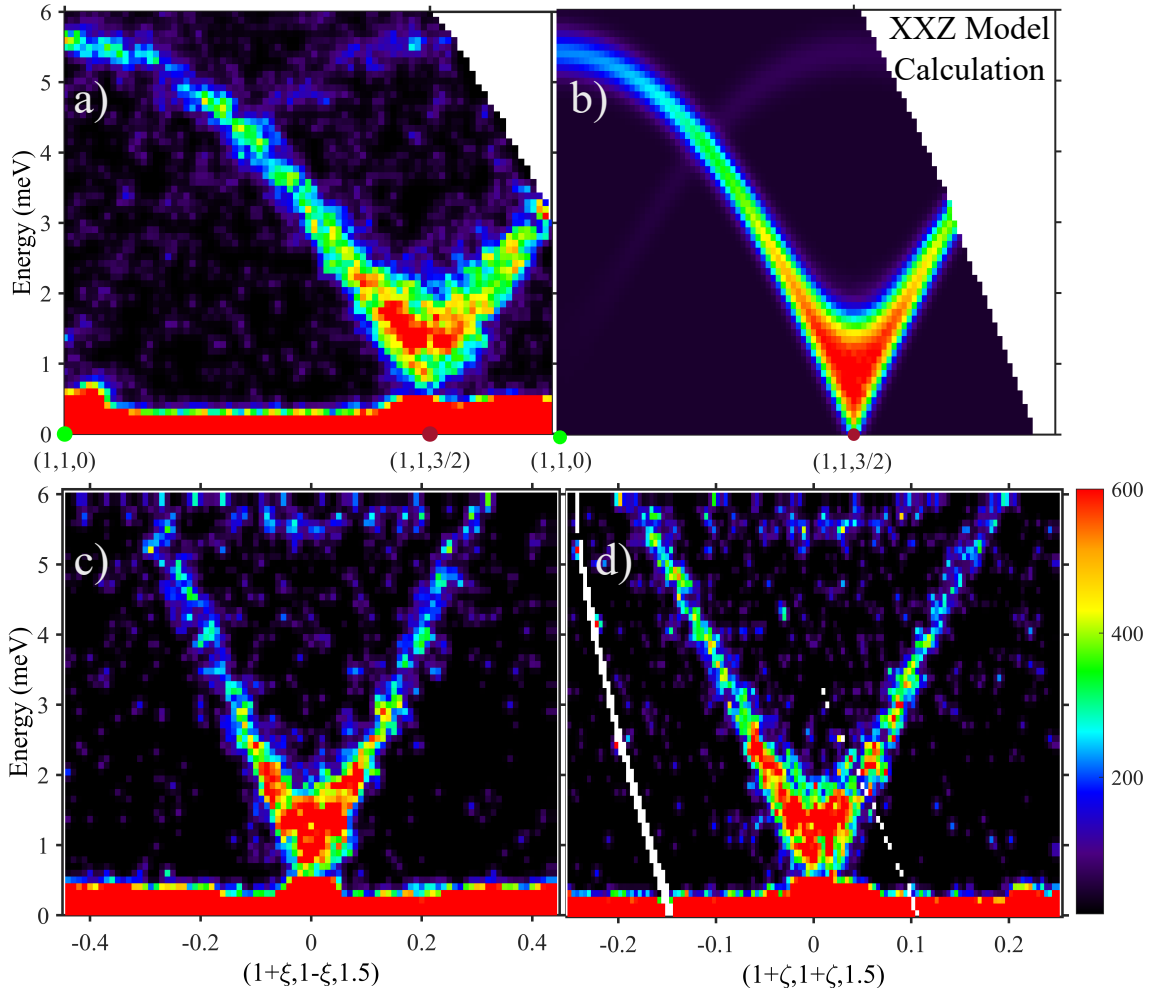

Figure 4.14: INS intensity in slices along $(0, 0, L)$ a) observed in the 9.6 meV data set and b) calculated using the XXZ model - note the absence of a gap in the latter. INS intensity in slices along c) $(\xi, -\xi, 0)$ and d) $(\zeta, \zeta, 0)$ directions through the $(1, 1, 3/2)$ magnetic Bragg peak. In all slices through the data, a strong V-shaped magnetic signal is observed with a small gap around 1 meV between the elastic line and the magnon mode, above the (1,1,3/2) magnetic Bragg peak position (denoted by the brown circle). This is inconsistent with the XXZ model calculation, which has a V shaped mode along the L direction, gapless at the magnetic Bragg peak position. The slices are integrated over a transverse wavevector range of $\pm 0.1 \text{Å}^{-1}$ for (a) and (b), $\pm 0.062 \text{Å}^{-1}$ for (c), and $\pm 0.072 \text{Å}^{-1}$ for (d). The in-plane slices (c) and (d) are averaged over $L = [1.375, 1.625]$. The colour bar indicates scattering intensity in arbitrary units on a linear scale.

be proportional to the domain average of

$$p_{x'} g_{\perp}^2 S^{x'x'}(\mathbf{k} + \mathbf{Q}, \omega) + p_{y'} g_{\parallel}^2 S^{y'y'}(\mathbf{k}, \omega), \tag{4.31}$$

where $p_{x'}$ and $p_{y'}$ are the polarisation factors $1 - (k_\zeta/k)^2$, where $\zeta = x', y'$, for fluctuations

perpendicular to the moment direction - $\mathbf{z}'$ - in- and out-of-plane respectively. k_ζ is the component of the wavevector transfer along the $\zeta = x', y'$ direction. $g_\perp$ and $g_\parallel$ are the in-plane and out-of-plane components of the anisotropic g-factor, respectively - as introduced in section 4.3.

Both $S^{x'x'}$ and $S^{y'y'}$ functions possess $\bar{3}m$ symmetry in the XXZ model and so are invariant under rotations of the in-plane spin angle ϕ by multiples of $\pi/3$. The g-factor components are invariant under arbitrary rotations of the spin angle provided the axis of rotation is normal to the ab-plane. Due to these symmetry considerations, the domain average only affects the polarisation factor terms - assuming there is an equal proportion of all six domains.

$$\begin{aligned} \langle p_{x'} \rangle &= \frac{1}{6} \sum_{n=0}^{5} \left(1 - \frac{k_\perp^2 \cos^2(n\pi/3 + \phi_0)}{k_\perp^2 + k_z^2} \right) = \frac{1}{2} \left(1 + \frac{k_z^2}{k^2} \right), \\ \langle p_{y'} \rangle &= 1 - \frac{k_z^2}{k^2}, \end{aligned} \tag{4.32}$$

where k_z ($k_\perp$) is the component of wavevector transfer along (perpendicular to) the c-axis. Performing the domain average removes all dependence of these terms on ϕ_0. The domain averaged INS scattering intensity in the global frame is obtained as

$$\frac{1}{2} \left(1 + \frac{k_z^2}{k^2} \right) g_\perp^2 S^{yy}(\mathbf{k}, \omega) + \left(1 - \frac{k_z^2}{k^2} \right) g_\perp^2 S^{zz}(\mathbf{k}, \omega), \tag{4.33}$$

where the dynamical correlations are those as given by equation 4.30.

When fitting to the experimental dispersions, it is assumed that the correction to the analytical XXZ dispersion is to add a gap in quadrature. Let the dispersion of the four modes in the XXZ model be denoted by $\omega_m(\mathbf{k})$, where $m = 1$ to 4 labels the modes at any given point $\mathbf{k}$ in the Brillouin zone in order of increasing energy. The dispersion can then be modified to $\tilde{\omega}_m(\mathbf{k}) = \sqrt{\omega_m(\mathbf{k})^2 + \Delta^2}$, where Δ is taken to be an additional parameter that phenomenologically accounts for the spectral gap at the magnetic Bragg peak position.

By taking a series of constant energy cuts at fixed momentum points along paths of high symmetry through the four dimensional INS dataset, and fitting Gaussian peaks to

these scans, a set of empirical dispersion points labelled by (h, k, l, E, m) can be extracted from the dataset. For a given set of parameters in the XXZΔ model, the energy of each mode m at (hkl) can be computed and compared to the fitted value. A χ^2 value can be assigned to a given set of parameters, calculated by $\sum_i (\omega_{\text{obs},i} - \tilde{\omega}_{\text{calc},i})^2$, where the sum is over all fitted modes and values of h, k, and l; $\omega_{\text{obs},i}$ denotes the energy of the ith fitted dispersion point; $\tilde{\omega}_{\text{calc},i}$ denotes the energy of the ith dispersion point in the XXZΔ model. Parameter sets with a smaller χ^2 value have a better goodness of fit. By starting with an initial set of parameters, the χ^2 value can be minimised by a method of steepest descent to perform a fitting of a parameter set to the empirical dispersion points. The best fit exchange parameters (with values given in units of meV) are,

$$\begin{aligned}
J_1^{\perp} &= -6.36 & J_1^{z} &= 1.97 \\
J_2^{\perp} &= -0.33 & J_2^{z} &= 0.30 \\
J_3^{\perp} &= 0.78 & J_3^{z} &= 0.15 \\
J_4^{\perp} &= 0.11 & J_4^{z} &= 0.32 \\
J_5^{\perp} &= -0.39 & J_5^{z} &= 0.20 \\
J_6^{\perp} &= 0.79 & J_6^{z} &= 0.68
\end{aligned} \tag{4.34}$$

and the gap parameter was fitted to be $\tilde{\Delta} = 1.23(7)$ meV. For the exchange parameters, a negative value denotes ferromagnetic coupling, and a positive value denotes antiferromagnetic coupling following the same convention used in equation 4.10. A plot of ω_{obs} against $\tilde{\omega}_{\text{calc}}$ calculated in the XXZΔ model for the fitted set of parameters above is shown in figure 4.15.

The gap parameter is denoted by $\tilde{\Delta}$ in order to indicate that it is an overestimation of the optimal gap parameter. The gap parameter, Δ, will be the energy of the minimum of the lowest mode in the XXZΔ model. Furthermore, any slice or cut taken from the dataset through the magnetic Bragg peak position will have a finite transverse integration range and will include pixels which will carry intensity concentrated systematically upwards in

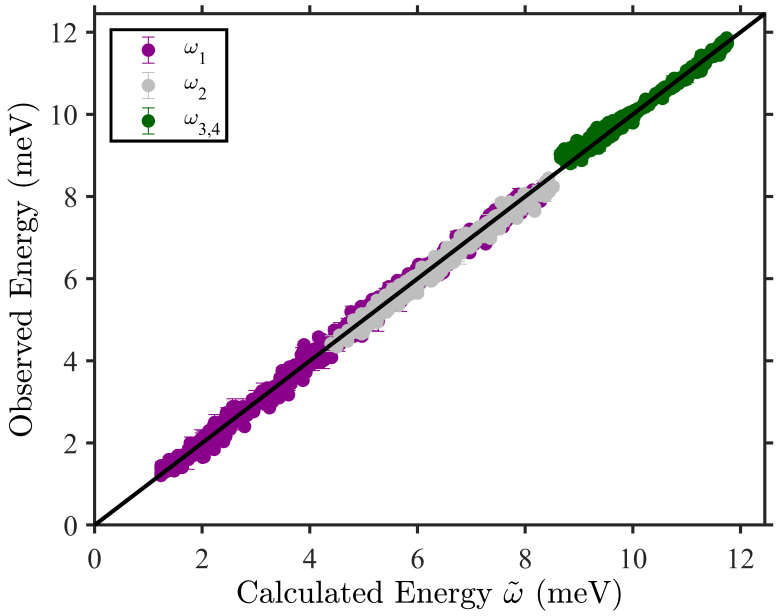

Figure 4.15: Plot of observed and calculated magnon energies in $CoTiO_3$, with magenta, grey, and green points corresponding to magnon bands indexed in order of increasing energy. The upper magnon modes $\tilde{\omega}_3$ and $\tilde{\omega}_4$ are unresolved up to the resolution of INS datasets and so a single symbol is used to represent their average weighted by the neutron scattering intensity. The error bars on each point represent one standard deviation, and the solid line shows the 1:1 agreement.

energy from Δ. If the modes are strongly dispersive throughout this integration range, this will have a noticeable effect on the position of the minimum of the mode which will appear to be above the nominal position and by fitting the gap parameter to such slices, an overestimation - $\tilde{\Delta}$ - is obtained. In the energy scan taken through $(1, 1, 3/2)$, as shown in figure 4.16, $\Delta = 1.0(1)$ meV provides the best agreement between the experimental intensity profile and the profile calculated with full pixel averaging and the XXZΔ model.

Now that the XXZΔ model has been constructed and a parameter set fitted, a comparison between simulated slices and slice through the INS dataset can be made. As shown in figure 4.17, many features in the INS data are accounted for - including, by construction, the spectral gap. However, there remain some features in modes in a path along the Brillouin zone boundary that are not accounted for - this will be accounted for in section 4.6.

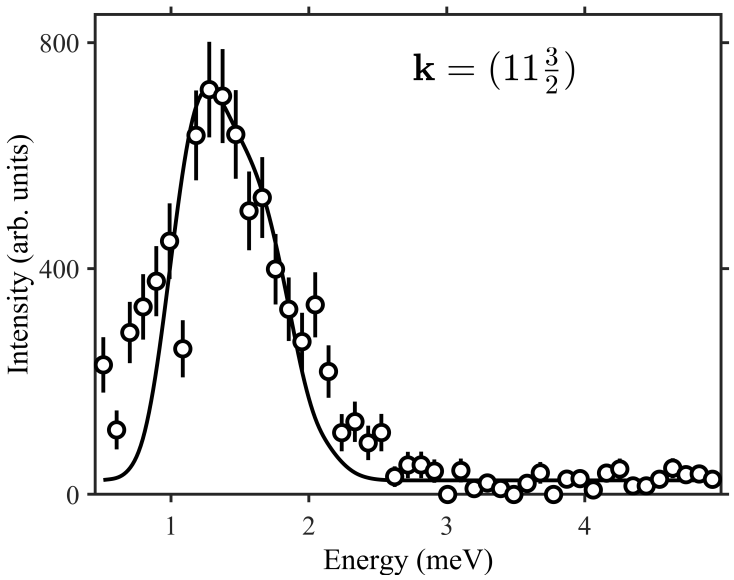

Figure 4.16: Energy scan above the $(1, 1, 3/2)$ magnetic Bragg peak. The solid line a fit to the XXZΔ model with the XXZ exchange parameters listed in table 4.34 and gap parameter $\Delta = 1.0$ meV.

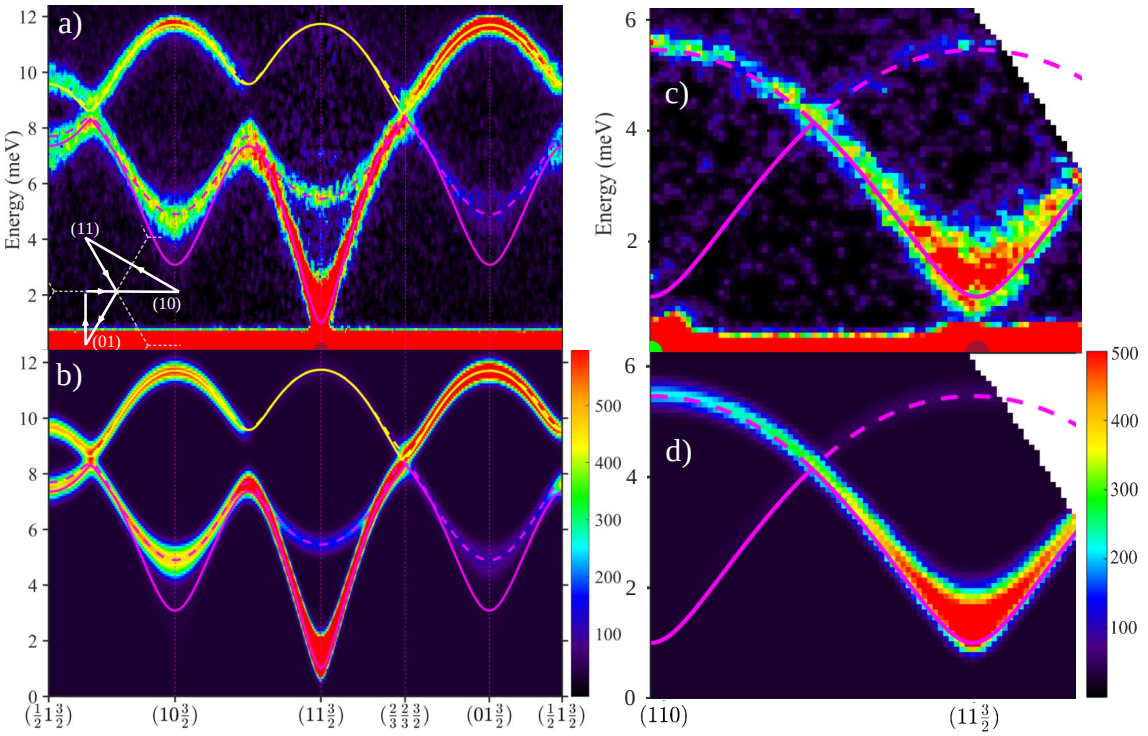

Figure 4.17: INS data at 8 K observing the magnon dispersions along high-symmetry directions a) in-plane and c) out-of-plane, compared in b) and d) with the XXZΔ model. Lines are the model dispersions $\tilde{\omega}(\mathbf{k})$ with green and brown dots on the elastic line indicating the location of structural and magnetic Bragg peaks, respectively. Lower left inset in (a) shows the wavevector path in (a) and (b) (arrowed solid white lines) projected onto the (hk) plane, with grey dashed lines as the 2D Brillouin zone boundaries. Intensities are averaged for a transverse wavevector range of ± 0.1 Å^{-1}. The incident neutron energy was $E_i = 18$ meV in (a) and $E_i = 9.6$ meV in (c). The colour bars indicate scattering intensity in arbitrary units on a linear scale.

4.6 Bond Dependent Exchange

So far, the magnon dispersions have been modelled with an XXZ model - with anisotropy between the in-plane and out-of-plane exchange couplings - adequate in describing the overall shape of the magnon modes observed in the INS data. In order to capture a spectral gap above the magnetic Bragg peak, an additional phenomenological gap parameter Δ was added. This model captures most of the features of the neutron scattering data, however there are still differences between this XXZΔ model and the observed spectrum of the magnon modes - particularly along the boundary of the magnetic Brillouin zone.

The exchange interactions considered in the XXZ model range from nearest neighbour bonds out to sixth nearest neighbour bonds, and in the global xyz frame can be written in the form

$$\begin{pmatrix} J_n^{\perp} & 0 & 0 \\ 0 & J_n^{\perp} & 0 \\ 0 & 0 & J_n^{z} \end{pmatrix}.$$

There are, however, additional symmetry allowed exchange couplings not captured in this XXZ form. For the nearest neighbour bonds, the midpoint of the bond has inversion symmetry and so the exchange matrix must be symmetric. If the exchange is anisotropic, then a coordinate system is defined for each bond, related to each other by lattice transformations and the point group rotational symmetry of the lattice. The exchange on each bond is then defined with the exchange matrix in the basis coordinate system of each bond. For XXZ or Heisenberg exchange, the exchange matrices remain unchanged under the basis transformation from the global xyz frame to the local coordinate system of the bond, as a result this additional step is only required for exchange anisotropies beyond XXZ anisotropy. For second nearest neighbour couplings, the exchange is restricted to be of the XXZ form. The third and fourth nearest neighbour couplings, however, are totally unconstrained by symmetry and can be written as six totally symmetric couplings, and three totally antisymmetric (or Dzyaloshinskii-Moriya) couplings. The fifth and sixth neighbour couplings both possess

inversion symmetry at the centre of the bond and the exchange matrix is constrained to be symmetric. For such symmetric exchange, the exchange Hamiltonian for the nth nearest neighbor bond can be written in the form

$$\hat{H}_n = \sum_{\langle i,j \rangle_n} \hat{\mathbf{S}}_i^{\intercal} \mathcal{J}_n \hat{\mathbf{S}}_j,$$

where the exchange matrix $\mathcal{J}_n$ in the local coordinate system of each bond $\langle i,j \rangle_n$ is given by

$$\mathcal{J}_n = \begin{pmatrix} J_n^{xx} & J_n^{xy} & J_n^{xz} \\ J_n^{xy} & J_n^{yy} & J_n^{yz} \\ J_n^{xz} & J_n^{yz} & J_n^{zz} \end{pmatrix}. \tag{4.35}$$

Since the dominant coupling in the XXZΔ model is the in-plane component of the first nearest neighbour exchange, it is reasonable to assume that if bond dependent exchange were to be present in $CoTiO_3$ then the largest such anisotropy would be associated with this bond. As a result, consider the term $\eta = J_1^{yy} - J_1^{xx}$, which parametrises the bond-dependence of the in-plane component of the exchange interaction on the nearest neighbour bonds. Note that for $\eta = 0$, then $J_1^{xx} = J_1^{yy} = J_1^{\perp}$ and the XXZ model is recovered. The exchange matrix components J_1^{xx} and J_1^{yy} are given by

$$\begin{aligned} J_1^{xx} &= J_1^{\perp} - \eta/2, \\ J_1^{yy} &= J_1^{\perp} + \eta/2, \end{aligned} \tag{4.36}$$

and so for $\eta = \pm 2J_1^{\perp}$, either J_1^{xx} or J_1^{yy} would be identically zero and the in plane exchange would be entirely along or perpendicular to the bond direction. Hence, this XXZη model will contain the XXZ exchange couplings as in 4.34 in addition to a bond-dependent exchange term - η - on the nearest neighbour bonds.

The contribution of the η component to the exchange Hamiltonian in equation 4.10 is

$$\hat{H}_{\text{aniso}} = \frac{\eta}{2}\sum_{m=1}^{3}\sum_{i\in A}\left(\hat{S}_i^{y_m}\hat{S}_{i+\delta_{1m}}^{y_m} - \hat{S}_i^{x_m}\hat{S}_{i+\delta_{1m}}^{x_m}\right) + (A \to C), \tag{4.37}$$

where spin operators are in the coordinate system of each bond, and the sums are over the three different $\boldsymbol{\delta}_{1m}$ bonds as defined in equation 4.19 which connect the A to the B sublattice and the C to the D sublattice. The coordinate system for each bond is defined such that the y_m direction is parallel to the bond, the z_m direction is parallel to the **c** axis, and the x_m direction is defined such that $x_m y_m z_m$ is a right-handed coordinate system. These coordinate systems in terms of the global xyz frame are given by

$$\begin{aligned}
\mathbf{x}_1 &= -\frac{\mathbf{x}}{2} - \frac{\sqrt{3}\mathbf{y}}{2}, & \mathbf{x}_2 &= -\frac{\mathbf{x}}{2} + \frac{\sqrt{3}\mathbf{y}}{2}, & \mathbf{x}_3 &= \mathbf{x},\\
\mathbf{y}_1 &= \frac{\sqrt{3}\mathbf{x}}{2} - \frac{\mathbf{y}}{2}, & \mathbf{y}_2 &= -\frac{\sqrt{3}\mathbf{x}}{2} - \frac{\mathbf{y}}{2}, & \mathbf{y}_3 &= \mathbf{y},\\
\mathbf{z}_1 &= \mathbf{z}, & \mathbf{z}_2 &= \mathbf{z}, & \mathbf{z}_3 &= \mathbf{z}.
\end{aligned} \tag{4.38}$$

The $m = 3$ term in equation 4.37 can then be written in the global xyz frame, and subsequently transformed to the rotating $x'y'z'$ frame as defined in equation 4.23

$$\hat{H}_{\text{aniso},3} = \frac{\eta}{2}\sum_{i\in\tilde{A}}\left[\cos 2\phi\left(\hat{S}_i^{x'}\hat{S}_{i+\delta_{13}}^{x'} - \hat{S}_i^{z'}\hat{S}_{i+\delta_{13}}^{z'}\right) + \sin 2\phi\left(\hat{S}_i^{x'}\hat{S}_{i+\delta_{13}}^{z'} + \hat{S}_i^{z'}\hat{S}_{i+\delta_{13}}^{x'}\right)\right], \tag{4.39}$$

here, the $\hat{S}^{z'}\hat{S}^{x'}$ and $\hat{S}^{x'}\hat{S}^{z'}$ terms will not contain any bilinear terms in the Holstein-Primakoff transformation as defined in equation 4.12. By collecting the terms quadratic in the raising and lowering operators and Fourier transforming, the $m = 3$ term of equation 4.37 becomes

$$\hat{H}_{\text{aniso},3} = \frac{\eta S}{4}\cos 2\phi\sum_{\mathbf{k}}\left[e^{i\mathbf{k}\cdot\boldsymbol{\delta}_{13}}\left(\hat{a}_{\mathbf{k}}^{\dagger}\hat{b}_{\mathbf{k}} + \hat{a}_{\mathbf{k}}^{\dagger}\hat{b}_{-\mathbf{k}}^{\dagger}\right) + \hat{a}_{\mathbf{k}}^{\dagger}\hat{a}_{\mathbf{k}} + \hat{b}_{\mathbf{k}}^{\dagger}\hat{b}_{\mathbf{k}} + \text{h.c.}\right]. \tag{4.40}$$

The $m = 1$ and $m = 2$ terms take a similar form, with a differing ϕ dependence and $e^{i\mathbf{k}\cdot\boldsymbol{\delta}_{13}}$

replaced by $e^{i\mathbf{k}\cdot\boldsymbol{\delta}_{11}}$ and $e^{i\mathbf{k}\cdot\boldsymbol{\delta}_{12}}$ respectively.

$$\hat{H}_{\text{aniso},1} = \frac{\eta S}{4}\left(-\frac{1}{2}\cos 2\phi + \frac{\sqrt{3}}{2}\sin 2\phi\right)\sum_{\mathbf{k}}\left[e^{i\mathbf{k}\cdot\boldsymbol{\delta}_{11}}\left(\hat{a}^{\dagger}_{\mathbf{k}}\hat{b}_{\mathbf{k}} + \hat{a}^{\dagger}_{\mathbf{k}}\hat{b}^{\dagger}_{-\mathbf{k}}\right) + \hat{a}^{\dagger}_{\mathbf{k}}\hat{a}_{\mathbf{k}} + \hat{b}^{\dagger}_{\mathbf{k}}\hat{b}_{\mathbf{k}} + \text{h.c.}\right],$$
$$\hat{H}_{\text{aniso},2} = \frac{\eta S}{4}\left(-\frac{1}{2}\cos 2\phi - \frac{\sqrt{3}}{2}\sin 2\phi\right)\sum_{\mathbf{k}}\left[e^{i\mathbf{k}\cdot\boldsymbol{\delta}_{12}}\left(\hat{a}^{\dagger}_{\mathbf{k}}\hat{b}_{\mathbf{k}} + \hat{a}^{\dagger}_{\mathbf{k}}\hat{b}^{\dagger}_{-\mathbf{k}}\right) + \hat{a}^{\dagger}_{\mathbf{k}}\hat{a}_{\mathbf{k}} + \hat{b}^{\dagger}_{\mathbf{k}}\hat{b}_{\mathbf{k}} + \text{h.c.}\right]. \tag{4.41}$$

In order to recover the full bond-anisotropic part of the Hamiltonian in equation 4.37, the $\hat{H}_{\text{aniso},m}$ terms for $m = 1, 2,$ and 3 must be summed. Since the ϕ dependent terms sum to zero, the $\hat{a}^{\dagger}_{\mathbf{k}}\hat{a}_{\mathbf{k}}$ and $\hat{b}^{\dagger}_{\mathbf{k}}\hat{b}_{\mathbf{k}}$ terms all cancel, and so $\hat{H}_{\text{aniso}}$ can be written in the form

$$\hat{H}_{\text{aniso}} = \sum_{\mathbf{k}} X_{\mathbf{k}}\left(\hat{a}^{\dagger}_{\mathbf{k}}\hat{b}_{\mathbf{k}} + \hat{a}^{\dagger}_{\mathbf{k}}\hat{b}^{\dagger}_{-\mathbf{k}}\right) + \text{h.c.} \tag{4.42}$$

where $X_{\mathbf{k}}$ is contains all of the angular and momentum dependent multiplicative factors of the a and b operators. Writing $\hat{H}_{\text{aniso}}$ in the form of equation 4.15 will give additional contributions to the dynamical matrix $\mathcal{D}(\mathbf{k})$. Specifically, the B and D matrix elements will pick up the additive terms B' and D' respectively, where

$$B' = -\frac{\eta S}{8}\left[\left(\cos 2\phi - \sqrt{3}\sin 2\phi\right)e^{i\mathbf{k}\cdot\boldsymbol{\delta}_{11}} + \left(\cos 2\phi + \sqrt{3}\sin 2\phi\right)e^{i\mathbf{k}\cdot\boldsymbol{\delta}_{12}} - 2\cos 2\phi e^{i\mathbf{k}\cdot\boldsymbol{\delta}_{13}}\right],$$
$$D' = B'^{*}. \tag{4.43}$$

This shows that for non-zero bond-dependent exchange interactions, i.e. for $\eta \neq 0$, the dynamical matrix, and hence the magnon dispersions and INS intensities will be dependent on the spin orientation angle ϕ. In section 4.7, it will be demonstrated that this ϕ dependence will be responsible for an order-by-disorder mechanism that selects $\phi = n\pi/3$ for $\eta > 0$ and $\phi = n\pi/3 + \pi/2$ for $\eta < 0$. As can be seen in figure 4.22a-b, the largest changes to the magnon spectrum will occur close to the edges of the magnetic Brillouin zone, where the surfaces of constant energy for each magnon band will become stretched

along a direction dependent on the orientation of the moment. One consequence of this dispersion surface distortion is that the separation between the second and third magnon mode in a slice along the edge of the Brillouin zone boundary will be dependent on the spin orientation angle. B' and D' are both dependent on trigonometric functions of 2ϕ and thus are invariant under the transformation $\phi \to \phi + \pi$. Since this invariance does not hold under $\phi \to \phi \pm 2\pi/3$, the magnetic domains related by three-fold rotation will now have distinct magnon dispersions. As a result, the dispersions $\omega_{\pm}(\mathbf{k})$ will no longer have the $\bar{3}m$ symmetry of the magnetic Brillouin zone, but will have the $\bar{1}$ symmetry of the magnetic structure. Consider the path $(0, 1, 5/4) \to (2, 0, 5/4)$ through momentum space, which due to the translational periodicity of the magnetic Brillouin zone will be equivalent to a path along the top diagonal of the first Brillouin zone, depicted in figure 4.18c, and plotted in figure 4.19a. The top diagonal can be mapped onto the same diagonal on the bottom face via a twofold rotation about the **b** axis followed by a threefold rotation about the **c** axis. In the XXZ model, since the dispersions possess the same $\bar{3}m$ symmetry as the Brillouin zone, this will imply that $\omega_{\pm}(\mathbf{k}) = \omega_{\pm}(\mathbf{k} - \mathbf{Q})$, and the magnetic domains have the same dispersions, and so this model will predict two sets of doubly degenerate modes along this path - contrary to what is observed experimentally, as shown in figure 4.19a.

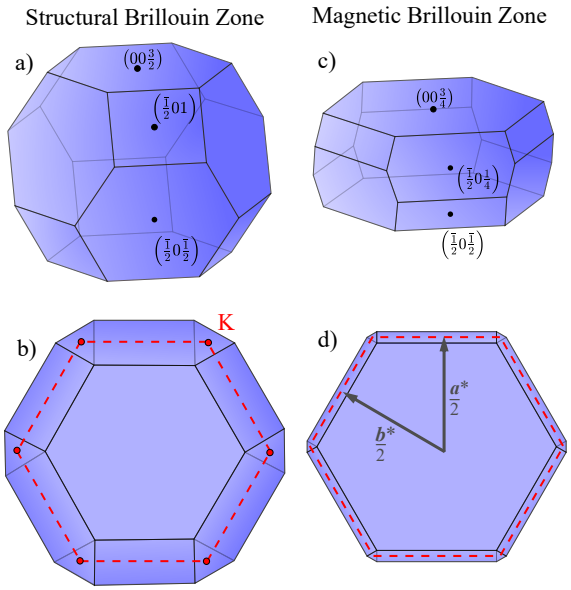

Figure 4.18: a) Structural and c) magnetic Brillouin zones with selected mid-face points labelled and projected onto the hk plane in b) and d), respectively. The dashed red outline is the 2D hexagonal Brillouin zone for a single honeycomb layer.

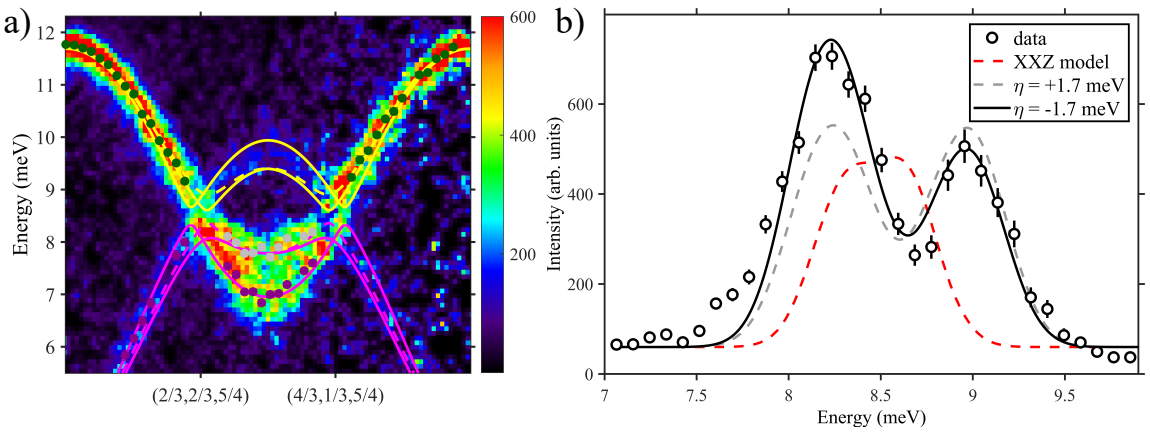

Figure 4.19: a) Slice along the Brillouin zone boundary that also passes through two K points. The overplotted lines are dispersions of the XXZη model with parameters in equation 4.34 and $\eta = -1.7$ meV with solid/dashed lines for magnetic domains with $\phi = \pi/2$ and $\pi/2 \pm 2\pi/3$, respectively. The clear splitting between the two lower modes cannot be reproduced in the XXZ model, and allows the magnitude of the bond dependent exchange η to be determined. b) Energy scan in a cylindrical region of radius 0.03Å^{-1} centred at the K points and summed over $L = [0, 2.3]$, compared to the domain average for the XXZ model (red dashed line), for $\eta > 0$ (dashed grey line), and for $\eta < 0$ (solid black line). The calculations with the XXZη model use the same parameters as per equation 4.34 in addition to the listed value of η, but with an additional shift of $\Delta E = +0.11$ meV to provide better agreement with the data. Error bars represent one standard deviation

For $\eta \neq 0$, the symmetry of the dispersions is lowered and the magnetic domains have distinct dispersions, meaning that the splitting of the magnon modes along this path may be captured within this XXZη model. In order to reproduce the splitting of the magnon modes on the path $(2/3, 2/3, 5/4) \rightarrow (4/3, 1/3, 5/4)$ along the edge of the Brillouin zone, the XXZη model must be used where $|\eta| = 1.7$ meV. The magnon dispersions calculated using this model are plotted in figure 4.19a). The upper and lower magnon bands no longer cross at the K points - this will be explained in further detail in section 4.8. Since the expression of 4.43 is invariant under the transformation $\eta \rightarrow -\eta$ and $\phi \rightarrow \phi + \pi/2$, the dispersions and the dynamical correlations for $\eta > 0$ and $\eta < 0$ are identical and it is not possible to determine the sign of η from the shape of the magnon dispersions alone.

Despite the dispersions and the dynamical correlations not depending on the sign of η, the INS intensity for a system of domains is still given by equation 4.31, which is no longer independent on the spin orientation angle by virtue of the polarisation factors, and therefore will be dependent on the sign of η. By taking an energy scan only including pixels in a

cylinder with a relatively small radius 0.03Å^{-1} centred at the K points and along L, a two peak structure is found. As seen in figure 4.19b, this two peak structure is almost absent in the XXZ model, and is more pronounced for $|\eta| = 1.7$ meV. Due to the polarisation factor in equation 4.31, the asymmetry between the two peaks in intensity can only be captured for $\eta < 0$, providing evidence for bond dependent exchange in $CoTiO_3$, that can capture experimental features in the INS data that otherwise cannot be captured in the XXZ model. In the next section - section 4.7 - it will be shown that bond dependent exchange also leads to a spectral gap via the order by disorder mechanism.

4.7 Quantum Order by Disorder

As mentioned previously, the spectral gap - Δ - observed in the magnon spectra in the INS data implies that upon magnetic ordering the spins align along a direction chosen from a discrete set of symmetry related directions. At the mean field level in the XXZ model, the spectrum remains gapless and no two-spin interaction can lift the continuous ϕ degeneracy of the ground state manifold. In the local frame defined in equation 4.9, the moments can be rotated by an angle ϕ in the easy plane to give a spin configuration $\mathbf{m}_i = m_0 \text{Re}\left[e^{i\phi}(\tilde{x}_i + i\tilde{z}_i)\right]$. The order parameter for this system can be written as $\Psi = m_0 e^{i\phi}$ and the mean field free energy for quadratic spin interactions can be written as $\text{F}_{\text{MFT}}[\Psi] = \alpha|\Psi|^2 + \beta\Psi^2 + \beta^*(\Psi^*)^2$. Threefold rotations about $\tilde{y}$ transform the order parameter as $\Psi \rightarrow e^{\pm 2\pi i/3}\Psi$. Invariance of the free energy under these transformations force $\beta = 0$. Consequently, the mean field free energy cannot depend on the in-plane spin angle orientation angle ϕ and so effects beyond the mean field are required to describe the physics of this system.

Order by disorder has been developed to explain the breaking of a classical degeneracy of ground states into a smaller set of allowed states via thermal or quantum disorder. In the case where the classical mean-field contribution to the ground state energy is independent of a degree of freedom, but the quantum contribution is dependent on the same degree of freedom, then the classically degenerate ground state manifold is explicitly broken by zero-point fluctuations. This order by disorder mechanism allows a subset of these states

to become energetically favourable even at zero temperature. Order by disorder due to quantum fluctuations has been proposed to explain the features of magnetisation data in $CoTiO_3$ [8], although no spectral gap has been previously resolved and no model has been provided until now. Order by disorder in the presence of bond dependent exchange has also been reported in the rare-earth pyrochlore $Er_2Ti_2O_7$ [20, 21]. A spectral gap of 0.09 meV has been reportedly observed in $Er_2Ti_2O_7$, and so the spectral gap of 1.0(1) meV observed in $CoTiO_3$ is a very clear experimental signature of an order by disorder mechanism. It is also interesting to note that $CoTiO_3$ - a transition metal honeycomb - and $Er_2Ti_2O_7$ - a rare earth pyrochlore - are two very different systems, and yet exhibit very similar manifestations of order by disorder.

The XXZη model outlined in section 4.6 demonstrates that the inclusion of bond dependence to the in-plane component of the nearest neighbour exchange will reduce the symmetry of the magnon dispersions $\omega_m(\mathbf{k})$ from the $\bar{3}m$ point group symmetry of the Co^{2+} positions in the lattice to the $\bar{1}$ symmetry of the magnetic structure. The configuration of a single spin can be parametrised by a polar angle θ - the angle subtended by the spin from the **c** axis - and an azimuthal angle ϕ - the angle subtended by the projection of the spin onto the ab-plane from the **a** axis. The ground state is then given by θ_0 and ϕ_0 such that the energy density $\epsilon(\theta, \phi)$ is minimised. The classical mean field energy density is a function of θ only, $\epsilon_{cl} = \epsilon_{cl}(\theta)$, and the easy plane ground state manifold is defined by $\theta_0 = \pi/2$ and ϕ_0 ranging from 0 to 2π. Furthermore, for the ground state manifold to be stable to fluctuations in θ around the equilibrium value of θ_0, the classical energy density must satisfy

$$\left(\frac{\partial \epsilon_{cl}}{\partial \theta}\right)_0 = 0, \qquad \left(\frac{\partial^2 \epsilon_{cl}}{\partial \theta^2}\right)_0 > 0 \tag{4.44}$$

As a result, fluctuations in θ - i.e. the out of plane fluctuations - will have the effective Hamiltonian $\frac{1}{2}\left(\frac{\partial^2 \epsilon_{cl}}{\partial \theta^2}\right)_0 (\delta\theta)^2$ and the corresponding mode will be gapped. For fluctuations in ϕ, however, there is no such contribution from the classical energy density, and the mode corresponding to the in plane fluctuations will be gapless. However, due to the symmetry of the magnon dispersions $\omega_m(\mathbf{k})$ in the XXZη model, the quantum zero-point energy would be

dependent on ϕ and this may break the ϕ degeneracy of the energy density. The quantum energy density has a leading order contribution from zero-point fluctuations

$$E_0 = N_{mag} S \epsilon_{qu} = \sum_m \frac{\langle \omega_m(\mathbf{k}) \rangle_{\mathbf{k}}}{2}, \tag{4.45}$$

where the average is over all points $\mathbf{k}$ in the magnetic Brillouin zone and all magnon modes m, and $N_{mag} = 4$ denotes the number of magnetic sublattices.

The average over the magnetic Brillouin zone can be performed numerically using Monte Carlo methods - a random distribution of points within the Brillouin zone can be generated, and the mean of $\omega_m(\mathbf{k})/2$ summed over every mode will approach the actual value of the sum in equation 4.45. This average was found by using the experimentally fitted values of the exchange parameters in 4.34, a range of η values ranging from -6.36 meV to 6.36 meV in steps of 0.265 meV were chosen, and a range of ϕ values ranging from 0° to 60° in steps of 5°. For each η and ϕ value, the sum was evaluated using 10^6 Monte Carlo points in the magnetic Brillouin zone. One advantage of having found analytic expressions for the magnon dispersions in equation 4.22 is that this function can be simply evaluated - rather than numerically diagonalising the dynamical matrix - at all sampled points in the Brillouin zone; this method reduces the computation time per k-point, speeding up the computation time. This process can be sped up further by splitting the η steps between a number of workers in order to perform the computation using parallel processing in MATLAB. At the end of each run the η value, ϕ value, average and error of $\omega_m(\mathbf{k})/2$, and the number of Monte Carlo points used are output to a file. In order to obtain sensible counting statistics to fit the ϕ dependence of E_0, each run was repeated a number of times, the runs for smaller values of η were iterated over more than the runs for higher values of η. For example, the runs for $|\eta|$ ranging from 6 meV to 3.1875 meV were repeated 10 times, whereas the runs for $|\eta|$ ranging from 0.375 meV to 0.1875 meV were repeated 240 times. The zero-point contribution to the ground state energy was found to have a six-fold modulation in ϕ, with a ground state spin orientation ϕ_0 of $\phi_0 = n\pi/3$ for $\eta > 0$ and $\phi_0 = \pi/2 + n\pi/3$ for $\eta < 0$, the functional form of the zero-point energy can be parametrised by

$$E_0 = \bar{E}_0 - \frac{\Lambda}{2}\cos 6(\phi - \phi_0), \tag{4.46}$$

where Λ is the peak-to-peak amplitude of the zero-point fluctuations, and in order to reproduce the selection of the ground state spin orientation must be a function of odd powers of η. The coefficient of the term linear in η vanishes, and so the leading order contribution to Λ is found to be of order η^3.

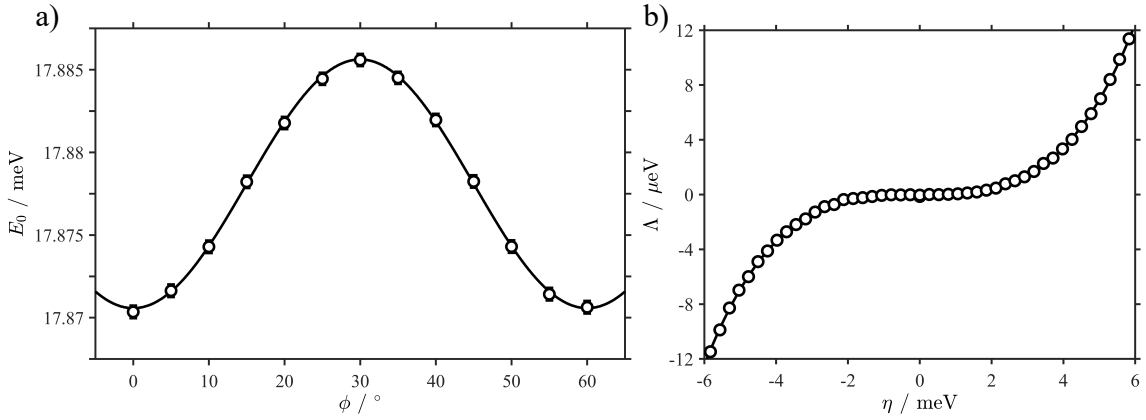

Figure 4.20: Parametrisation of quantum zero-point energy in $CoTiO_3$. a) Leading zero-point contribution to the ground state energy - E_0 in equation 4.45 - as a function of the in-plane angle ϕ, for exchange anisotropy $\eta = 6.36$ meV. The solid line is a fit to the cosinusoidal form in equation 4.46 with parameters $\bar{E}_0 = 17.878$ meV and $\Lambda = 0.0151$ meV at fixed $\phi_0 = 0$. b) Zero-point energy oscillation amplitude Λ as a function of exchange anisotropy η for fixed $\phi_0 = 0$, fitted to an odd polynomial form $a\eta^3 + b\eta^5$ (solid line) with $a = 5.01(8) \times 10^{-5}$ meV^{-2} and $b = 2.18(17) \times 10^{-7}$ meV^{-4}.

Therefore, due to quantum fluctuations, the energy density has now picked up a modulation in ϕ

$$\epsilon(\theta, \phi) = \epsilon_{cl}(\theta) + \epsilon_{qu}(\theta, \phi), \tag{4.47}$$

and the spectral gap becomes [22]

$$\Delta = \frac{1}{S}\sqrt{\left(\frac{\partial^2\epsilon}{\partial\theta^2}\right)_0\left(\frac{\partial^2\epsilon}{\partial\phi^2}\right)_0} = \frac{1}{S}\sqrt{\left(\frac{\partial^2\epsilon_{cl}}{\partial\theta^2}\right)_0\left(\frac{\partial^2\epsilon_{qu}}{\partial\phi^2}\right)_0}. \tag{4.48}$$

An expression for the classical energy density - ϵ_{cl} - can be derived by considering each spin as a classical vector in the global xyz frame, and parametrised by the spherical polar angles

θ and ϕ

$$\mathbf{S} = \pm S \begin{pmatrix} \sin\theta\cos\phi \\ \sin\theta\sin\phi \\ \cos\theta \end{pmatrix}, \tag{4.49}$$

where the + sign applies the A and B sublattices; the − sign applies for the C and D sublattices. By substitution into the XXZ Hamiltonian in equation 4.10, the classical ground state energy is obtained

$$\epsilon_{cl} = -\frac{S^2}{2}\sum_{n=1}^{6}(-1)^n z_n \left[J_n^{\perp}\sin^2\theta + J_n^z\cos^2\theta\right], \tag{4.50}$$

where the sum is over the nth nearest neighbour couplings, and z_n is the coordination number - i.e. the number of distinct bonds $\boldsymbol{\delta}_{nm}$ - for each coupling. This term can equivalently be found by taking the $\mathcal{O}(S^2)$ term when performing the Holstein-Primakoff transformation on the ABC stacked honeycomb for a ground state with ferromagnetic ordering in each honeycomb layer, and antiferromagnetic coupling between each layer. The orientation of the spins are given by equation 4.49, and this term can be minimised to obtain the ground state configuration. By taking the derivatives with respect to θ and evaluating at the easy-plane orientation $\theta = \pi/2$, $\left(\frac{\partial^2\epsilon_{cl}}{\partial\theta^2}\right)_0$ is given by

$$\left(\frac{\partial^2\epsilon_{cl}}{\partial\theta^2}\right)_0 = S^2\sum_{n=1}^{6}(-1)^n z_n\left[J_n^{\perp} - J_n^z\right]. \tag{4.51}$$

The $\mathcal{O}(\eta)$ contribution to the classical energy density can be found by finding the $\mathcal{O}(S^2)$ term in equation 4.37. Each term from the three $\boldsymbol{\delta}_{1m}$ bonds will provide a ϕ dependent term, which upon summation will exactly cancel. Similarly, an expression for the quantum energy density local to the selected ground state can be derived using equations 4.45 and 4.46

$$\left(\frac{\partial^2\epsilon_{qu}}{\partial\theta^2}\right)_0 = \frac{36}{N_{mag}S}\frac{|\Lambda(\eta)|}{2} = 9|\Lambda(\eta)|. \tag{4.52}$$

Where the peak to peak amplitude has been written as $\Lambda(\eta)$ to emphasise that this is the only place in Δ that is dependent on the magnitude of η. Since the leading order term in Λ is $\mathcal{O}(\eta^3)$, the spectral gap will scale as $\mathcal{O}(|\eta|^{3/2})$.

By using the fitted values of the exchange parameters in 4.34, the value of $\left(\frac{\partial^2 \epsilon_{cl}}{\partial \theta^2}\right)_0$ is 5.36 meV. For a bond dependent term $|\eta| = 1.7$ meV, the value of $\left(\frac{\partial^2 \epsilon_{qu}}{\partial \theta^2}\right)_0$ using the parametrisation in figure 4.20b is 2.23 μeV. Therefore, these fitted exchange parameters provide a spectral gap of 0.22 meV through order by disorder through quantum fluctuations. This predicted gap is much smaller than the experimentally observed gap, suggesting that either the formula for the gap in equation 4.48 in the $S = 1/2$ case undervalues the spectral gap, or that other mechanisms, such as virtual crystal field fluctuations [23, 24] provide additional contributions to the spectral gap.

4.8 Nodal Lines and Isospin Winding

In the case of a two-dimensional honeycomb lattice with ferromagnetic Heisenberg nearest neighbour exchange interactions, the resulting magnon bandstructure consists of two bands that cross at the corners of the Brillouin zone. Furthermore, in the vicinity of these touching points at $\mathbf{K}$, the dispersion will be linear and take the form $\omega(\mathbf{K} + \delta\mathbf{k}) = \pm v|\delta\mathbf{k}|$ [25], with reference to the nodal point energy with $\pm$ representing the top/bottom band. The effective Hamiltonian for points $\mathbf{K} + \delta\mathbf{k}$ in the vicinity of these high symmetry points will take the form $\hat{H}_{\text{eff}} = v\delta\mathbf{k} \cdot \boldsymbol{\sigma}$, which is the massless Dirac equation in two dimensions [26] and where the index of the Pauli matrices $\boldsymbol{\sigma}$ refers to the sublattice index of the honeycomb sites, and is also called the isospin index. As a result of the excitations local to the K points obeying the Dirac equation, these touching points are called Dirac points. In three dimensions, such as in the ABC stacked honeycombs of $CoTiO_3$, the crossing points of the magnons still exist and form Dirac nodal lines along L. Such features are of interest in neutron scattering studies since the inelastic neutron scattering intensity in the vicinity of these points is proportional to the projection of a unit vector $\hat{\mathbf{n}}$ characteristic of the Dirac point onto the isospin polarisation $\boldsymbol{\sigma}$ [27]. As a result, this intensity can be written as $1 \pm \cos(\alpha - \alpha_0)$, where α is an azimuthal angle around the nodal point, α_0 is an angular

offset and is dependent on the direction of the unit vector $\hat{\mathbf{n}}$, and the sign is dependent on the isospin polarisation of the magnon band. Now an analytical model of the magnon bandstructure and inelastic neutron scattering intensities has been established, the features of the nodal lines such as their path through momentum space, and the INS intensity profile around the nodal points will be investigated in this section. It is insightful to consider first a minimal model to capture the behaviour of the nodal lines.

4.8.1 Nodal Line Fine Structure

For a $J_1 - J_2$ Heisenberg ferromagnet on the ABC stacked honeycomb, the contribution to the Hamiltonian that is quadratic in boson operators on the A and B sublattices is given by [28]

$$\hat{H}_{FM} = S \sum_{\mathbf{k}} \begin{pmatrix} \hat{a}^\dagger_{\mathbf{k}}, & \hat{b}^\dagger_{\mathbf{k}} \end{pmatrix} \begin{pmatrix} -3J_1 - J_2 & J_1\gamma_{1\mathbf{k}} + J_2\gamma_{2\mathbf{k}} \\ J_1\gamma^*_{1\mathbf{k}} + J_2\gamma^*_{2\mathbf{k}} & -3J_1 - J_2 \end{pmatrix} \begin{pmatrix} \hat{a}_{\mathbf{k}} \\ \hat{b}_{\mathbf{k}} \end{pmatrix}. \tag{4.53}$$

This Hamiltonian describes two magnon modes and their dispersions at any point $\mathbf{k}$ in the Brillouin zone are given by the eigenvalues of the dynamical matrix. These modes are degenerate when the off-diagonal terms equal zero and so the nodal lines are the loci of points $\mathbf{k}$ that satisfy

$$J_1\gamma_{1\mathbf{k}} + J_2\gamma_{2\mathbf{k}} = 0. \tag{4.54}$$

First consider the case where there is no interlayer coupling, and so $J_2 = 0$. The condition for a nodal line will reduce to $\gamma_{1\mathbf{k}} = 0$, which is the case precisely at the K points for all values of L. Therefore, the nodal lines would be straight lines along L situated at the K points.

Now consider the case where the neighbouring honeycomb layers interact and $J_2 < 0$ stabilises the ferromagnetic ground state across the entire ABC stacked honeycomb. Since $\gamma_{2\mathbf{k}}$ does not vanish at the K points, the solutions to equation 4.54 - if they exist at all - are no longer situated at the K points. This is hardly surprising since in three dimensions,

the edges of the Brillouin zone wind around the K and K' points. Consequently, the ABC stacking of the honeycombs eliminates any symmetry-imposed constraints - unlike the two-dimensional case - on the crossing points of the magnon bands. Consider points in reciprocal space that are nearby a K point, these can be denoted by $\mathbf{k} = \mathbf{K} + \delta\mathbf{k} + L\mathbf{c}^*$ where $\mathbf{K}$ and $\delta\mathbf{k}$ are in the hk-plane, and $\delta\mathbf{k}$ has components $\delta k_x = |\delta\mathbf{k}| \cos\alpha$ and $\delta k_y = |\delta\mathbf{k}| \sin\alpha$. The leading order contributions to $\gamma_{1\mathbf{k}}$ and $\gamma_{2\mathbf{k}}$ in powers of $|\delta\mathbf{k}|$ are given by

$$\begin{aligned} \gamma_{1\mathbf{k}} &= \pm\frac{\sqrt{3}a}{2}|\delta k| e^{\pm i\alpha} e^{2\pi i\epsilon L}, \\ \gamma_{2\mathbf{k}} &= e^{-2\pi i L/3} e^{2\pi i\epsilon L}, \end{aligned} \tag{4.55}$$

where $\gamma_{1\mathbf{k}}$ is evaluated in the vicinity of the K points at $(2/3, 5/3)$ and $(4/3, 1/3)$, the choice of sign changing between the two choices of K point. The equation for the nodal lines to leading order in $|\delta\mathbf{k}|$ then becomes

$$\frac{\sqrt{3}a}{2} J_1 |\delta\mathbf{k}| e^{\pm i\alpha} = J_2 e^{-2\pi i L/3}, \tag{4.56}$$

where the buckling term $e^{2\pi i\epsilon L}$ has exactly cancelled, indicating that the positions of the nodal lines in reciprocal space are not affected by buckling of the honeycomb layers along the $\mathbf{c}$ axis. The solution of this equation gives the coordinates the nodal lines, parametrised by L, in the vicinity of $(4/3, 1/3)$ and $(2/3, 5/3)$, respectively

$$(\delta k_x, \delta k_y) = \pm\frac{2}{\sqrt{3}a}\frac{J_2}{J_1}\left(\cos\frac{2\pi L}{3}, \pm\sin\frac{2\pi L}{3}\right). \tag{4.57}$$

Hence solutions of equation 4.54 for $J_1, J_2 < 0$ are helices with a radius proportional to J_2/J_1 centred at the K points, that wind clockwise in the vicinity of the K point at $(2/3, 5/3)$ - and counter-clockwise around the K point at $(4/3, 1/3)$ - for increasing L. The helical nodal lines have a period of 3 along L.

For an antiferromagnetic interlayer coupling of ferromagnetically aligned honeycomb layers with an XXZ-type anisotropy such that spins are ordered in the ab-plane, the nodal lines occur at all points $\mathbf{k}$ in the Brillouin zone that satisfy $\omega_+(\mathbf{k}) = \omega_-(\mathbf{k})$, where $\omega_\pm(\mathbf{k})$ is

defined in equation 4.22. Furthermore, due to the antiferromagnetic ordering with wavevector $\mathbf{Q}$, if $\mathbf{k}$ is a nodal point, then so is $\mathbf{k}+\mathbf{Q}$, leading to a doubling of the nodal lines. The condition $\omega_+(\mathbf{k}) = \omega_-(\mathbf{k})$ is equivalent to

$$(2AB - CD^* - C^*D^*)(2AB^* - CD - C^*D) + (BD - B^*D^*)^2 = 0, \tag{4.58}$$

where A, B, C, and D are dynamical matrix elements of the XXZ Hamiltonian and are defined in equation 5.75.

Now consider the XXZ model with only first and second nearest neighbour couplings. The dynamical matrix element $C = 0$ and so the condition for a nodal line reduced to all values of $\mathbf{k}$ that satisfy $B = 0$:

$$(J_1^\perp + J_1^z)\gamma_{1\mathbf{k}} = (J_2^\perp - J_2^z)\gamma_{2\mathbf{k}}. \tag{4.59}$$

As is the case for the Heisenberg ferromagnet, $\gamma_{1\mathbf{k}}$ vanishes at the K points, whereas $\gamma_{2\mathbf{k}}$ does not. To leading order in $|\delta k|$, the condition for a nodal line becomes

$$\pm\frac{\sqrt{3}a}{2}|\delta\mathbf{k}|e^{\pm i\alpha}|J_1^\perp + J_1^z| = (J_2^\perp - J_2^z)e^{-2\pi iL/3} \tag{4.60}$$

where once again the buckling term has exactly cancelled and the expression has been evaluated in the vicinity of $(2/3, 5/3)$ and $(4/3, 1/3)$ - with the phase factor $e^{+i\alpha}$ and $e^{-i\alpha}$, respectively. The solution to this equation gives helical nodal lines centred at the K point with a radius of

$$|\delta\mathbf{k}| = \frac{2}{\sqrt{3}a}\left|\frac{J_2^\perp - J_2^z}{J_1^\perp + J_1^z}\right|, \tag{4.61}$$

and the change in sign in the phase factor $e^{\pm i\alpha}$ once again indicates a clockwise (for $(2/3, 5/3)$) and counter-clockwise (for $(4/3, 1/3)$) sense of rotation about K in the direction of increasing L. The helices have a period of 3 along L, and are accompanied by an additional helix translated along L by the propagation vector $\mathbf{Q}$. Since $\mathbf{Q}$ is exactly half the period of the nodal line helices, each K point has a pair of nodal line helices that rotate along L with the same sense and radius. Furthermore, for any given value of L the midpoint

of the two nodal points is the K point around which they orbit. The $J_1 - J_2$ XXZ model has nodal lines straight along L and located precisely at the K points for isotropic J_2 couplings.

Since the function $\gamma_{3\mathbf{k}}$ does not vanish at the K points, it is possible to have a helical nodal line for isotropic J_2 couplings provided that there are non-zero XXZ J_1 and J_3 couplings. For such a model, the dynamical matrix elements are given by

$$\begin{aligned} A &= \left[-3J_1^{\perp} + J_2 - 6J_3^{\perp} + \frac{1}{2}(J_3^{\perp} + J_3^z)\gamma_{3\mathbf{k}}\right] S, \\ B &= \frac{1}{2}(J_1^{\perp} + J_1^z)\gamma_{1\mathbf{k}} S, \\ C &= \frac{1}{2}(J_3^{\perp} - J_3^z)\gamma_{3\mathbf{k}} S, \\ D &= \left[\frac{1}{2}(J_1^{\perp} - J_1^z)\gamma_{1\mathbf{k}}^* - J_2\gamma_{2\mathbf{k}}^*\right] S. \end{aligned} \tag{4.62}$$

The functions $\gamma_{2\mathbf{k}}$ and $\gamma_{3\mathbf{k}}$ do not vanish at the K points and take the values $e^{-2\pi i L/3}e^{2\pi i \epsilon L}$ and -3, respectively. The function $\gamma_{1\mathbf{k}}$ does vanish, but has a leading order contribution linear in $|\delta\mathbf{k}|$. As a result the dynamical matrix elements may be written as a power series in $|\delta\mathbf{k}|$

$$\begin{aligned} A &= A^{(0)} + \mathcal{O}(|\delta\mathbf{k}|), \\ B &= B^{(1)}|\delta k| + \mathcal{O}(|\delta\mathbf{k}|^2), \\ C &= C^{(0)} + \mathcal{O}(|\delta\mathbf{k}|), \\ D &= D^{(0)} + \mathcal{O}(|\delta\mathbf{k}|). \end{aligned} \tag{4.63}$$

The condition of the nodal line - equation 4.58 - then has an $\mathcal{O}(1)$ term $|2C^{(0)}D^{(0)}|^2$ and an $\mathcal{O}(|\delta\mathbf{k}|)$ term $-4A^{(0)}C^{(0)}(D^{(0)*}B^{(1)*} + D^{(0)}B^{(1)})$. By truncating the power series at $\mathcal{O}(|\delta\mathbf{k}|^2)$, the nodal line radius $|\delta\mathbf{k}|$ is given by

$$|\delta\mathbf{k}| \simeq \frac{C^{(0)}|D^{(0)}|^2}{A^{(0)}(D^{(0)*}B^{(1)*} + D^{(0)}B^{(1)})}, \tag{4.64}$$

the buckling only enters via the $D^{(0)}B^{(1)}$ terms, where - as in all previous cases - it exactly

cancels. Assuming that the exchange is dominated by the $J_1^\perp$ term, the nodal line radius is given by

$$|\delta\mathbf{k}| \simeq \frac{2}{\sqrt{3}a}\left|\frac{J_2(J_3^\perp - J_3^z)}{J_1^\perp(J_1^\perp + J_1^z)}\right|. \tag{4.65}$$

Therefore, the nodal line radius in the XXZ model for isotropic J_2 exchange will be proportional to $|J_3^\perp - J_3^z|$, although for anisotropic J_2 exchange the leading order contribution to the nodal line radius will be from the term proportional to $|J_2^\perp - J_2^z|$. For completeness, it is important to note that since the functions $\gamma_{4\mathbf{k}}$, $\gamma_{5\mathbf{k}}$, and $\gamma_{6\mathbf{k}}$ all vanish at the K point, adding anisotropic $J_4 - J_6$ couplings to the model with isotropic J_2 coupling will not cause the nodal lines to be helical, and instead will lie along the K points.

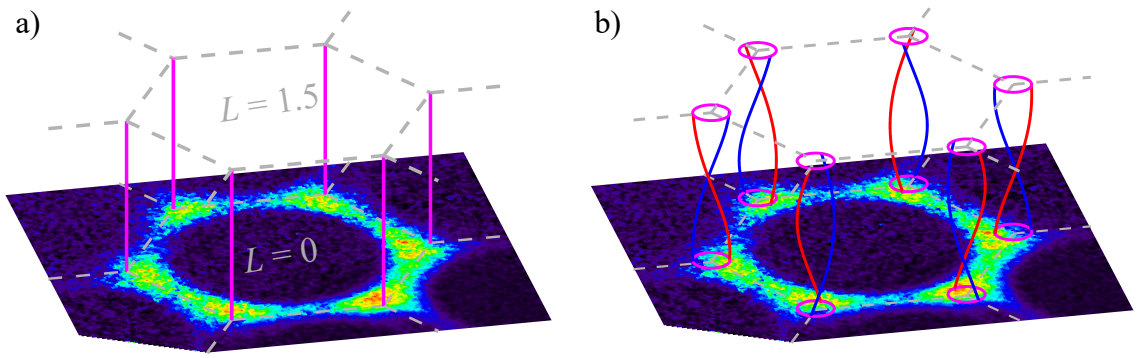

Figure 4.21: Nodal lines along L for a) Heisenberg and b) XXZ interlayer couplings in $CoTiO_3$. In a) the nodal lines lie along the K points, at the corners of the Brillouin zone for the 2D honeycomb layer - as denoted by the dashed grey outline. In b) the diameter of the helix - denoted by the magenta circles - is amplified by $\times 3$ for visibility. The blue/red lines correspond to the nodal lines for the in-/out-of-plane polarised modes.

In addition to XXZ-type couplings, bond dependent exchange as in the XXZη model of section 4.6 is necessary to capture key features of the magnon dispersion and to account for the presence of the spectral gap via order by disorder. In order to model the effect of bond dependent exchange on the nodal line position, consider the XXZη model with non-zero couplings $J_1^\perp$, J_1^z, $J_2^\perp$, J_2^z, and η. By neglecting third and fourth nearest neighbour couplings, the dynamical matrix element C is taken to be zero and the nodal lines are the locus of all points $\mathbf{k}$ such that $B = 0$. However, in the presence of bond dependent exchange, B has an additional contribution B' as in equation 4.43. Assuming $\eta < 0$ and the system is

in a magnetic domain where the $\phi = \pi/2$ ground state spin orientation has been selected, the nodal line condition becomes

$$(J_1^{\perp} + J_1^z)\gamma_{1\mathbf{k}} - (J_2^{\perp} - J_2^z)\gamma_{2\mathbf{k}} - \frac{|\eta|}{4}\left[e^{i\mathbf{k}\cdot\boldsymbol{\delta}_{11}} + e^{i\mathbf{k}\cdot\boldsymbol{\delta}_{12}} - 2e^{i\mathbf{k}\cdot\boldsymbol{\delta}_{13}}\right] = 0. \tag{4.66}$$

All $\gamma_{\mathbf{k}}$ and $\boldsymbol{\delta}_{1m}$ terms on the left hand side have a buckling term $e^{2\pi i\epsilon L}$, and so the effect of buckling can be neglected. By taking the leading order term in an expansion in powers of $|\delta\mathbf{k}|$ in the vicinity of the $(4/3, 1/3)$ K point, the nodal lines will be parametrised by $(\delta k_x, \delta k_y) = |\delta\mathbf{k}|(\cos\alpha, \sin\alpha)$ where $|\delta\mathbf{k}|$ and α satisfy

$$|\delta\mathbf{k}|e^{-i\alpha} = \frac{2}{\sqrt{3}a}\left|\frac{J_2^{\perp} - J_2^z}{J_1^{\perp} + J_1^z}\right| e^{-2\pi iL/3} + \frac{\sqrt{3}}{2a}\left|\frac{\eta}{J_1^{\perp} + J_1^z}\right| e^{-i\pi/3}. \tag{4.67}$$

Now consider four cases: i) isotropic J_2 and $\eta = 0$, ii) anisotropic J_2 and $\eta = 0$, iii) isotropic J_2 and $\eta \neq 0$, and iv) anisotropic J_2 and $\eta \neq 0$. The first two cases are treated above and in the first case nodal lines will be straight along L, and in the second case the nodal lines will be helical and wind around the K point as L increases. The third case will give straight nodal lines along L, but shifted away from the K point by an offset - $\delta\kappa = \frac{\sqrt{3}}{2a}\left|\frac{\eta}{J_1^{\perp}+J_1^z}\right|$. The final case will give nodal lines precessing with period of 3 around a point that is shifted away from the K point by $\delta\kappa$. The projection of the helix in the hk-plane will evolve from a circle for $\eta = 0$ to a more distorted shape for $\eta \neq 0$. In case ii) and case iv), each helix will be accompanied by another helix offset by the magnetic ordering wavevector $\mathbf{Q}$. For case iv) domain averaging over the selected ground states $\phi = \pi/2 + n\pi/3$ will give three distinct pairs of nodal lines around each K point - each pair arising from $\phi = \pi/2,\ \pi/2 + 2\pi/3,$ and $\pi/2 - 2\pi/3$.

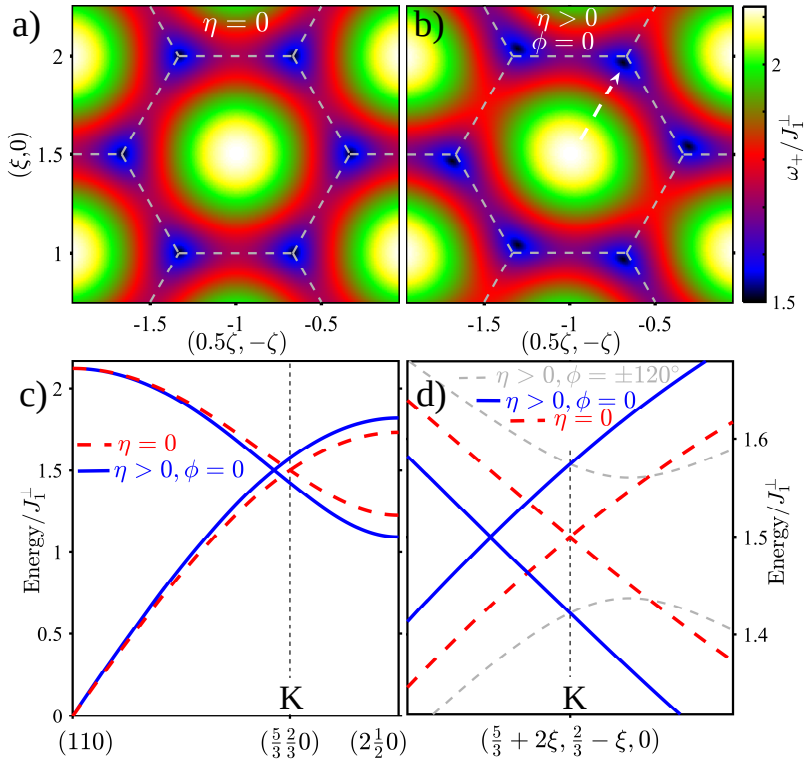

Figure 4.22: Shift of the Dirac nodal points in momentum space for bond dependent exchange in a honeycomb layer. a,b) Contour plot of the top magnon dispersion ω_+ for a single honeycomb layer with in-plane XY exchange $J_1^\perp < 0$ and bond dependent exchange in a) $\eta = 0$, and in b) $\eta > 0$ for a ground state moment orientation $\phi = 0°$ - direction denoted by the dashed arrow in (b). c) Dispersion relation along the $(1, -\frac{1}{2}, 0)$ direction, and d) the same dispersion zoomed in near the K-point. The dashed red, solid blue, and dashed grey lines in (c) and (d) denote the dispersions for $\eta = 0$; $\eta > 0$ and $\phi = 0°$; and $\eta > 0$ and $\phi = \pm 120°$. The presence of bond dependent exchange will displace the nodal lines from the K point by $\delta\kappa$. An energy scan at the K points would then display a two peak structure - just as in figure 4.19b - with a separation of $2\hbar v\delta\kappa$, where v is the Dirac velocity.

4.8.2 Isospin Winding

As demonstrated in the section 4.2, the distribution of scattering intensity between the magnon modes near the nominal linear crossing points around 8.5meV appears to be dependent on the direction of the slice through reciprocal space. Consider the K point at $(2/3, 2/3, L)$, a momentum-energy slice along the $(1, -1, 0)$ direction, as in figure 4.23a, shows a near-linear band crossing with the scattering intensity split almost equally between the upper and lower bands. Conversely, a momentum energy slice along the orthogonal $(1, 1, 0)$ direction, as in figure 4.23b, shows that only one of the magnon modes carries most

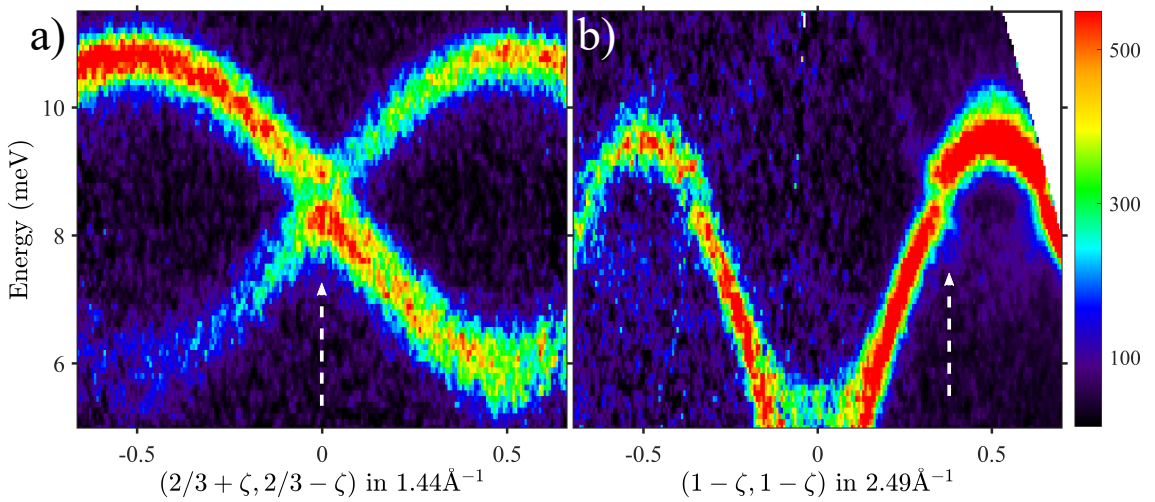

Figure 4.23: INS data through the $(2/3, 2/3)$ K point - marked by white dashed arrows - along orthogonal in-plane directions that maximise the asymmetry in the scattering intensity. In a) the scan is along the $(1, -1)$ direction and both crossing modes are visible; in b) the scan is along the $(1, 1)$ direction and only one mode carries scattering intensity. The intensities are averaged over $L = [0, 2.4]$; for an in-plane transverse momentum range of ± 0.026 and ± 0.028 Å^{-1}, respectively; and are indicated by the colour bar in arbitrary units on a linear scale.

of the scattering intensity at any given momentum point on the slice, and that the intensity shifts from the top band to the bottom band at the linear crossing points near K.

Another way to visualise this asymmetry of the scattering intensity is to take slices at constant energy for energy ranges above and below the nominal crossing point. For an energy range exclusively above the crossing point, the scattering intensity is mostly concentrated outside of the Brillouin zone in a direction radially outwards from the Brillouin zone centre, see figure 4.24a. On the other hand, for an energy range exclusively below the crossing point, the scattering intensity is concentrated inside the Brillouin zone, see figure 4.24b. These constant energy slices are reproduced to good agreement with experiment by using the fitted parameters in the XXZη model, see figures 4.24c,d compared to figures 4.24a,b, respectively. The shift of the scattering intensity from mostly inside the Brillouin zone below the crossing point to mostly outside the Brillouin zone above the crossing point is captured, in addition to a slight rotation of the scattering intensity around the corners of the Brillouin zone.

In order to investigate the intensity dependence as a function of angle α around the

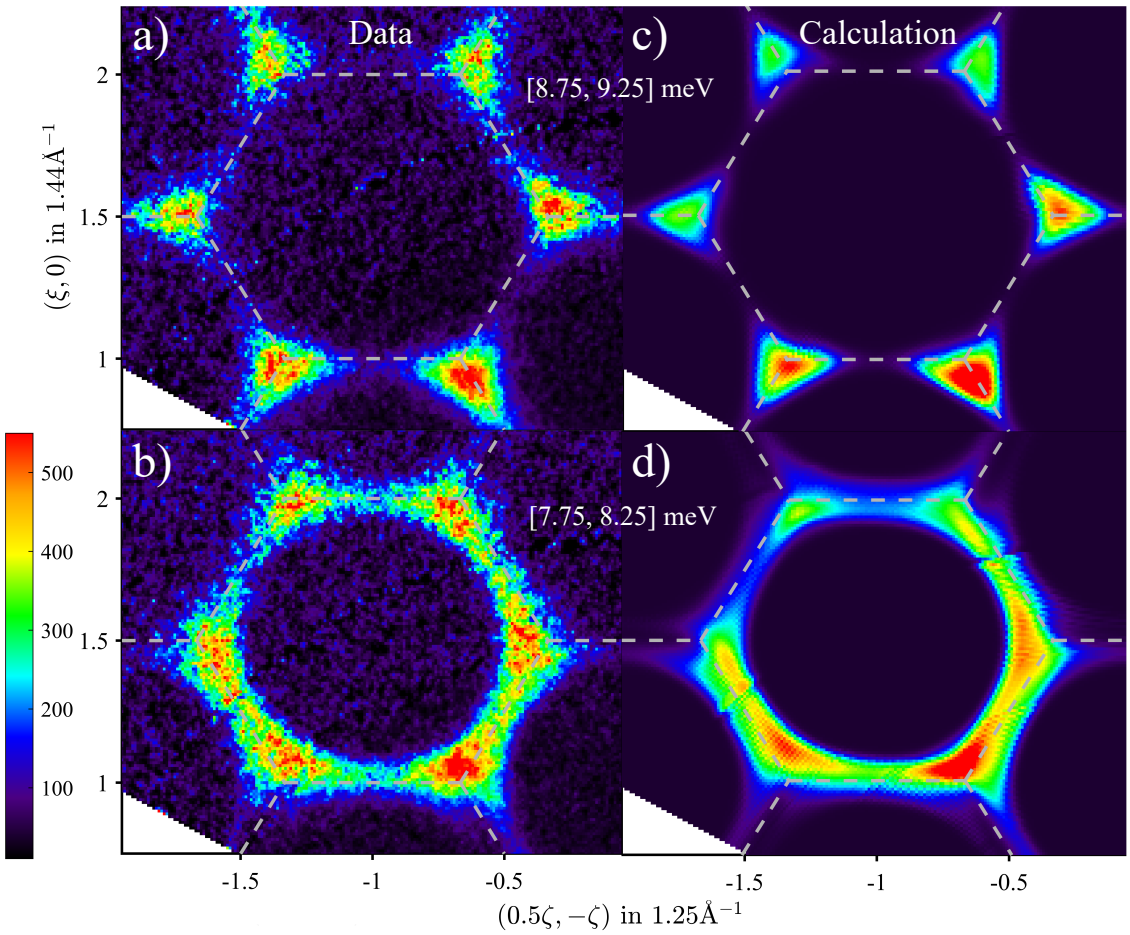

Figure 4.24: Momentum intensity maps above (top) and below (bottom) the Dirac node energy in $CoTiO_3$ compared between experimental data (left) and the XXZη model (right). The calculation parameters are as in figure 4.19a. The colour bar indicates scattering intensity in arbitrary units on a linear scale.

K point for both the upper and lower bands, an intensity scan over an annular region of $[0.05, 0.2]$Å^{-1} around the $(2/3, 2/3)$ K point, integrated over $L = [0, 2.4]$, for both the upper and lower band was taken. The scan shows the intensity takes the cosinusoidal form $\mathcal{A}_\pm \pm \mathcal{B}_\pm \cos(\alpha - \alpha_0)$ with period of 360° for both bands, with the intensity profile exactly 180° out of phase between the two bands. The unit vector $\hat{\mathbf{n}}$ in the direction from the centre of the Brillouin zone to the $(2/3, 2/3)$ K point corresponds to an angle of $\alpha = -60°$. However, the extremal point in intensity from the fitted cosinusoidal form was found to have an azimuthal angle $\alpha_0 = -80(3)°$, meaning the intensity has a rotational offset clockwise around the K point. The offset from $-60°$ is due to the buckling of the honeycomb layers

which introduces an intensity modulation of $e^{2\pi i\epsilon L}$ due to interference scattering in the buckled honeycomb layers. Indeed, the simulated value of $-81(1)^\circ$ can only be obtained if the buckling parameter ϵ is non-zero. The L dependence of α_0 can be investigated further by repeating the azimuthal intensity scans for three different integration ranges of L: i) positive values of L $[0, 2.4]$, ii) L range $[-1, 1]$ centred at zero, and iii) negative values of L $[-2.4, 0]$. For all scans, the intensity takes a cosinusoidal form with the two bands in anti-phase. In the case of an L range centred at zero, the points of extremal intensity occur at $\alpha_0 = -60^\circ$, whereas for negative values of L only, the points of extremal intensity are offset counterclockwise about the $(2/3, 2/3)$ K-point. This rotational offset explains the rotation of the scattering intensity around the corners of the Brillouin zone in the experimental and simulated constant energy slices.

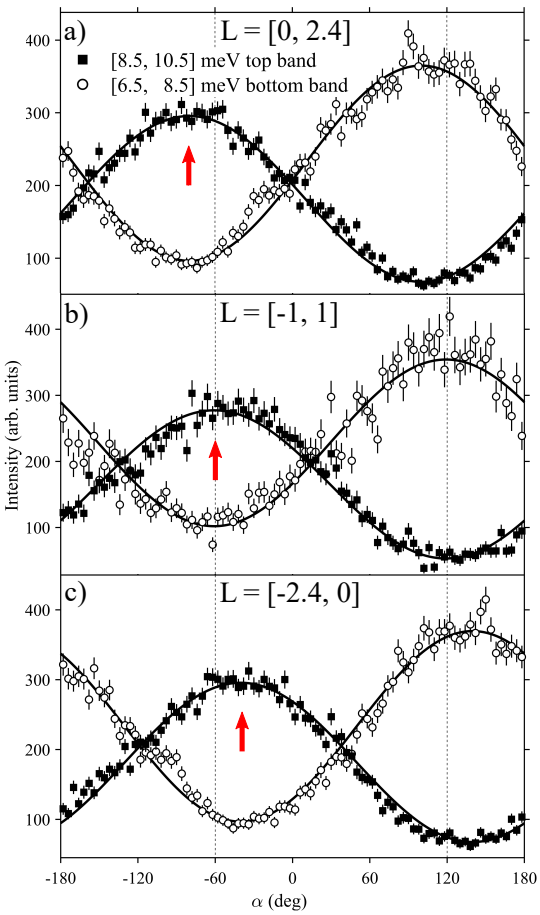

Figure 4.25: Azimuthal intensity dependence around $(2/3, 2/3)$ K point for differing L values in $CoTiO_3$, decreasing from a) to c). The black squares/white circles denote the inelastic neutron scattering intensity for the top/bottom bands, with error bars representing one standard deviation. Solid lines are fits to cosine dependencies 180° out of phase with each other. The dashed vertical lines at $\alpha = -60$ and 120° show the expected extremal points of intensity for flat honeycombs (i.e. for $\epsilon = 0$). Red arrows show the expected position of the extremal points of intensity for buckled honeycomb layers averaged over the stated L-range of each scan.

4.9 Tight Binding Model for Spin-Orbit Excitons

Returning to the higher crystal field levels detailed in section 4.3, the dispersion of the 28 meV mode observed in the inelastic neutron scattering data will be modelled. At low temperatures, the crystal can be considered as a number of effective spin-1/2 sites that interact via an exchange mean field. An incident neutron can create a spin-flip excitation within the effective $S = 1/2$ doublet, and such excitations - magnons - are treated in previous sections. Now consider an excitation of a single ion from lowest Kramers doublet

to the next higher energy Kramers doublet. Consider a single honeycomb layer consisting of an A and a B sublattice, where sites on either sublattice may be transition from the ground state to some excited state of energy E_0. The energy of the system can be found by summing the number of excited sites, characterised by the Hamiltonian

$$\hat{H}_0 = E_0 \sum_{i \in A} \hat{a}_i^\dagger \hat{a}_i + E_0 \sum_{j \in B} \hat{b}_j^\dagger \hat{b}_j, \tag{4.68}$$

where $\hat{a}_i^\dagger$ and $\hat{b}_j^\dagger$ create excitations on the A and B sublattices, and satisfy the same commutation relations as equation 4.14. Excitations on the lattice can then hop from one site to another nearby site via the interaction Hamiltonians

$$\begin{aligned}
\hat{H}_{I_1} &= -t_1 \sum_{i \in A} \sum_{m=1}^{3} \left(\hat{b}_{i+\delta_{1m}}^\dagger \hat{a}_i + \hat{a}_i^\dagger \hat{b}_{i+\delta_{1m}} \right), \\
\hat{H}_{I_3} &= -t_3 \sum_{m=1}^{6} \left(\sum_{i \in A} \hat{a}_{i+\delta_{3m}}^\dagger \hat{a}_i + \sum_{i \in B} \hat{b}_{i+\delta_{3m}}^\dagger \hat{b}_i \right), \\
\hat{H}_{I_5} &= -t_5 \sum_{i \in A} \sum_{m=1}^{3} \left(\hat{b}_{i+\delta_{5m}}^\dagger \hat{a}_i + \hat{a}_i^\dagger \hat{b}_{i+\delta_{5m}} \right),
\end{aligned} \tag{4.69}$$

where the parameters t_1, t_3, t_5 are 'hopping parameters', the sums are over lattice sites i on a given sublattice, and over the mth distinct bond in the list of the nth nearest neighbours listed in equation 4.19. The first, third, and fifth in-plane nearest neighbour bonds in $CoTiO_3$ are intra-layer connections between sites in the honeycomb layer. By transforming the creation and annihilation operators to act on states in momentum space using the transformation in 4.13, the combined tight-binding Hamiltonian can be written as:

$$\hat{H}_{TB} = \sum_{\mathbf{k}} \begin{pmatrix} \hat{a}_{\mathbf{k}}^\dagger, & \hat{b}_{\mathbf{k}}^\dagger \end{pmatrix} \begin{pmatrix} E_0 - t_3\gamma_{3\mathbf{k}} & -(t_1\gamma_{1\mathbf{k}} + t_5\gamma_{5\mathbf{k}}) \\ -(t_1\gamma_{1\mathbf{k}} + t_5\gamma_{5\mathbf{k}})^* & E_0 - t_3\gamma_{3\mathbf{k}} \end{pmatrix} \begin{pmatrix} \hat{a}_{\mathbf{k}} \\ \hat{b}_{\mathbf{k}} \end{pmatrix}. \tag{4.70}$$

The dispersions in this tight-binding model are given by the eigenvalues of the dynamical matrix. As a result, there will be two modes that cross when the off-diagonal term vanishes,

and this condition is satisfied at the K point. This must hold since the Kramers degeneracy of the crystal field modes is preserved and there are two sublattices in the paramagnetic regime. Therefore the two dispersive bands are expected to be analogous to the two bands of mobile electrons in graphene, which touch at the corners (K points) of the two-dimensional Brillouin zone [29]. The dynamical matrix above can be diagonalised by performing a Bogoliubov transformation [30]. This transformation is performed by defining a new set of operators:

$$\begin{pmatrix} \hat{a}_{\mathbf{k}} \\ \\ \hat{b}_{\mathbf{k}} \end{pmatrix} = \begin{pmatrix} \cos\theta & e^{i\phi_{\mathbf{k}}}\sin\theta \\ \\ -e^{-i\phi_{\mathbf{k}}}\sin\theta & \cos\theta \end{pmatrix} \begin{pmatrix} \hat{\alpha}_{\mathbf{k}} \\ \\ \hat{\beta}_{\mathbf{k}} \end{pmatrix} \tag{4.71}$$

where the form of the transformation matrix is chosen in order to preserve the form of the commutation relations from the $\hat{a}_{\mathbf{k}}$ and $\hat{b}_{\mathbf{k}}$ operators to the $\hat{\alpha}_{\mathbf{k}}$ and $\hat{\beta}_{\mathbf{k}}$ operators. By writing $-(t_1\gamma_{1\mathbf{k}} + t_5\gamma_{5\mathbf{k}}) = |\Gamma_{\mathbf{k}}|e^{i\varphi_{\mathbf{k}}}$, the unitary matrix diagonalises the dynamical matrix when $\theta = \pi/4$ and $\phi_{\mathbf{k}} = \varphi_{\mathbf{k}}$. The tight-binding Hamiltonian can then be written in the form

$$\hat{H}_{TB} = \sum_{\mathbf{k}} \omega_-(\mathbf{k})\hat{\alpha}^\dagger_{\mathbf{k}}\hat{\alpha}_{\mathbf{k}} + \omega_+(\mathbf{k})\hat{\beta}^\dagger_{\mathbf{k}}\hat{\beta}_{\mathbf{k}}, \tag{4.72}$$

where the dispersions are given by $\omega_\pm(\mathbf{k}) = E_0 \pm |\Gamma_{\mathbf{k}}| - t_3\gamma_{3\mathbf{k}}$. The ground state of the Hamiltonian $|0\rangle$ is defined by $\hat{\alpha}_{\mathbf{k}}|0\rangle = \hat{\beta}_{\mathbf{k}}|0\rangle = 0$. In inelastic neutron scattering, the incoming neutron creates an excitation from the ground state $|0\rangle$ on either the A or B sublattice, which then propagates via the tight-binding model as states $\hat{\alpha}_{\mathbf{k}}|0\rangle$ or $\hat{\beta}_{\mathbf{k}}|0\rangle$ with dispersion $\omega_-(\mathbf{k})$ or $\omega_+(\mathbf{k})$, respectively. Therefore, the intensity due to inelastic neutron scattering via the tight binding levels will be proportional to

$$I_{TB}(\mathbf{k},\omega) = \sum_{\lambda} \left|\langle\lambda|\hat{a}^\dagger_{\mathbf{k}} + \hat{b}^\dagger_{\mathbf{k}}|0\rangle\right|^2 \delta(\omega - \omega_\lambda(\mathbf{k})), \tag{4.73}$$

where the sum λ is over the singly excited eigenstates of the tight-binding Hamiltonian. The matrix element $\langle\lambda|\hat{a}^\dagger_{\mathbf{k}} + \hat{b}^\dagger_{\mathbf{k}}|0\rangle$ can be evaluated by using the Bogoliubov transformation in equation 4.71 to write the $\hat{a}^\dagger_{\mathbf{k}}$ and $\hat{b}^\dagger_{\mathbf{k}}$ operators in terms of $\hat{\alpha}^\dagger_{\mathbf{k}}$ and $\hat{\beta}^\dagger_{\mathbf{k}}$ operators. The intensity of the modes $\omega_\pm(\mathbf{k})$ is then given by

$$I_{TB}(\mathbf{k},\omega) = I_+(\mathbf{k})\delta(\omega - \omega_+(\mathbf{k})) + I_-(\mathbf{k})\delta(\omega - \omega_-(\mathbf{k})), \tag{4.74}$$

where the intensity dependence $I_\pm(\mathbf{k})$, determined by interference scattering from the A and B sublattices, takes the form $1 \pm \cos\varphi_{\mathbf{k}}$, as does the ARPES intensity in graphene [31].

By fitting dispersion points to the INS data, the parameters E_0, t_1, t_3, and t_5 can be fitted by minimising the sums of the square of the difference in the experimental and modelled dispersion points. The fitted parameters in the tight-binding model for the dispersive modes at 28 meV are

$$\begin{aligned} E_0 &= 28.01 \text{ meV}, \\ t_1 &= 0.846 \text{ meV}, \\ t_3 &= 0.027 \text{ meV}, \\ t_5 &= 0.084 \text{ meV}. \end{aligned} \tag{4.75}$$

Slices through the high energy modes can be simulated using this parametrisation, and as seen in figure 4.26, the dispersions and intensities of the modes around 28 meV are captured well.

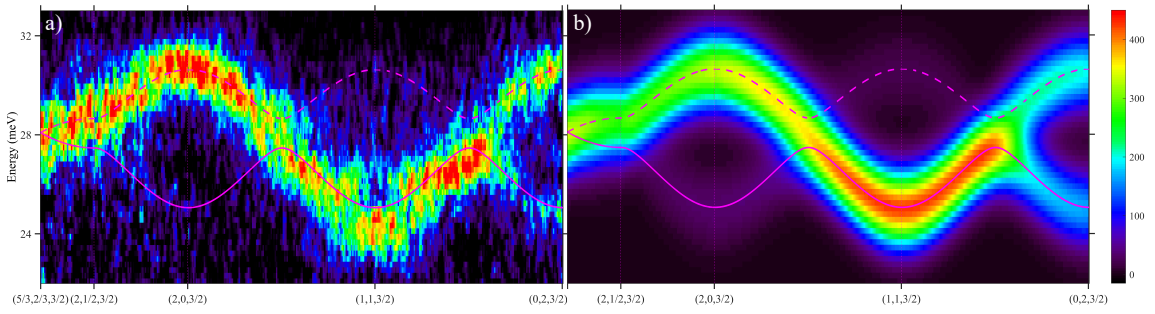

Figure 4.26: a) INS data observing the dispersions of the first excited crystal field level along high-symmetry directions compared in b) with the tight-binding model. Solid and dashed lines overplot in both plots show the dispersions from the best fit tight-binding parameters in equation 4.75. The colour bar indicates scattering intensity in arbitrary units on a linear scale.

Since the off-diagonal term in the dynamical matrix - $|\Gamma_{\mathbf{k}}|e^{i\varphi_{\mathbf{k}}}$ - vanishes at the K point, the two dispersive exciton bands will cross at the K point - as seen in figure 4.27a.

Furthermore, the phase $\varphi_{\mathbf{k}}$ is undefined at the crossing point of the exciton bands. For an in-plane displacement of $\delta\mathbf{k} = |\delta k|(\cos\alpha, \sin\alpha)$ in the vicinity of the K points at $(2/3, 5/3, L)$ and $(4/3, 1/3, L)$, $\gamma_{1\mathbf{k}}$ has the leading order term

$$\gamma_{1\mathbf{k}} = \pm\frac{\sqrt{3}a}{2}|\delta k|e^{\pm i\alpha}e^{2\pi i\epsilon L}. \tag{4.76}$$

In the limit of $t_5/t_1 \to 0$, the phase angle of $\Gamma_{\mathbf{k}}$ will be given by $\varphi_{\mathbf{k}} = \alpha_{\delta\mathbf{k}} + \pi + 2\pi\epsilon L$ in the vicinity of $(2/3, 5/3, L)$, and $\varphi_{\mathbf{k}} = -\alpha_{\delta\mathbf{k}} + 2\pi\epsilon L$ in the vicinity of $(4/3, 1/3, L)$. In this case, the azimuthal intensity profile in the vicinity of the K points should exhibit similar features for crossing points in the exciton band as for the magnon bands. As seen in figure 4.27b), the intensity profile around $(2/3, 5/3, L)$ has a twofold cosinusoidal pattern with the intensity of the top and bottom bands in anti-phase. In the absence of bucking - i.e. for $\epsilon = 0$ - the intensity of the lower band will be minimal for $\alpha = 0$. Since the integration range includes points for $L > 0$ only, the extremal points in intensity for both the upper and lower bands are shifted clockwise at the $(2/3, 5/3)$ K point.

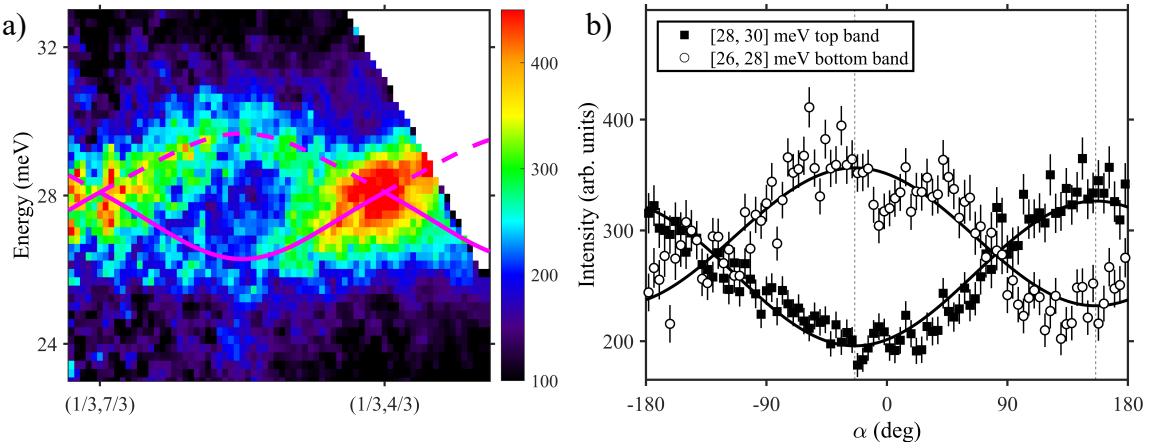

Figure 4.27: INS data observing a) the dispersions in a slice along the $\mathbf{b}^*$ direction through the $(1/3, 7/3)$ and $(1/3, 4/3)$ K points, and b) the azimuthal intensity profile around the $(2/3, 5/3)$ K point for the top and bottom exciton bands - denoted by black squares and white circles, respectively. The magenta lines in (a) show the dispersions calculated from the tight-binding model. Modelled crossing points at the K points coincide with a narrowing of the separation between the experimentally observed modes. The black lines in (b) are a fit of the azimuthal intensity scan with the form $\mathcal{A}_\pm \pm \mathcal{B}_\pm \cos(\alpha - \alpha_0)$. The fitted value of $\alpha_0 = 155(3)^\circ$ give the fitted extremal points of intensity, denoted by the grey vertical dotted lines, in agreement with the calculated value $\alpha_{\text{calc.}} = 153(1)^\circ$, which takes into account interference scattering due to the buckling of the honeycomb layer.

4.10 Conclusions

In summary, INS measurements of the magnon and spin-orbit exciton dispersions of the stacked honeycomb $CoTiO_3$ were performed. These measurements revealed the presence of a spectral gap and Dirac nodal lines. The existence of a spectral gap implies the presence of bond-dependent anisotropic exchange couplings. A minimal model compatible with the experimental data has been proposed, which includes the breaking of the continuous $U(1)$ symmetry of the XXZ Hamiltonian via a quantum order-by-disorder mechanism. Key signatures of proximity to Dirac magnon physics have also been observed, namely a near-linear band touching and a two-fold intensity periodicity in azimuthal scans attributed to isospin winding around the Dirac node. Similar features are also observed in the vicinity of the band crossing points in the dispersive spin-orbital exciton bands.

References

1. Newnham, R. E., Fang, J. H. & Santoro, R. P. Crystal structure and magnetic properties of $CoTiO_3$. *Acta. Cryst.* **17,** 240 (1964).
2. Kidoh, K., Tanaka, K., Marumo, F. & Takei, H. Electron density distribution in an ilmenite-type crystal of cobalt(II) titanium(IV) trioxide. *Acta Crystallographica Section B* **40,** 92–96 (1984).
3. Sheldrick, G. M. A short history of SHELX. *Acta Crystallographica Section A: Foundations of Crystallography* **64,** 112–122 (2008).
4. Bewley, R. *et al.* MERLIN, a new high count rate spectrometer at ISIS. *Phys. B Condens. Matter* **385-386,** 1029–1031 (2006).

5. Arnold, O. *et al.* Mantid—Data analysis and visualization package for neutron scattering and μSR experiments. *Nucl. Instruments Methods Phys. Res. Sect. A Accel. Spectrometers, Detect. Assoc. Equip.* **764,** 156–166 (2014).

6. Ewings, R. *et al.* Horace: Software for the analysis of data from single crystal spectroscopy experiments at time-of-flight neutron instruments. *Nucl. Instruments Methods Phys. Res. Sect. A* **834,** 132–142 (2016).

7. Yuan, B. *et al.* Spin-orbit exciton in a honeycomb lattice magnet $CoTiO_3$: Revealing a link between magnetism in d- and f-electron systems. *Phys. Rev. B* **102,** 134404 (2020).

8. Yuan, B. *et al.* Dirac Magnons in a Honeycomb Lattice Quantum XY Magnet $CoTiO_3$. *Phys. Rev. X* **10,** 011062 (2020).

9. Chapon, L. C. *et al.* Wish: The new Powder and Single Crystal Magnetic Diffractometer on the Second Target Station. *Neutron News* **22,** 22 (2011).

10. Rodriguez-Carvajal, J. Recent advances in magnetic structure determination by neutron powder diffraction. *Physica B* **192,** 55 (1993).

11. Campbell, B. J., Stokes, H. T., Tanner, D. E. & Hatch, D. M. ISODISPLACE: a web-based tool for exploring structural distortions. *J. Appl. Crystallogr.* **39,** 607 (2006).

12. Stokes, H. T., Hatch, D. M. & Campbell, B. J. *ISOTROPY* 2007. `http://stokes.byu.edu/isotropy.html`.

13. Abragam, A. & Bleaney, B. *Electron Paramagnetic Resonance of Transition Ions* (Oxford University Press, 1970).

14. Dresselhaus, M. S., Dresselhaus, G. & Jorio, A. *Group Theory: Application to the Physics of Condensed Matter* (Springer, 2008).

15. Stamokostas, G. L. & Fiete, G. A. Mixing of $t_{2g} - e_g$ orbitals in $4d$ and $5d$ transition metal oxides. *Phys. Rev. B* **97,** 085150 (2018).

16. Holstein, T. & Primakoff, H. Field Dependence of the Intrinsic Domain Magnetization of a Ferromagnet. *Phys. Rev.* **58,** 1098–1113 (1940).

17. White, R. M., Sparks, M. & Ortenburger, I. Diagonalization of the Antiferromagnetic Magnon-Phonon Interaction. *Phys. Rev.* **139,** A450–A454.

18. Toth, S. & Lake, B. Linear spin wave theory for single-Q incommensurate magnetic structures. *Journal of Physics: Condensed Matter* **27** (2015).

19. Coldea, R. *spinwave_dispersions MATLAB code* 2011.

20. Savary, L., Ross, K. A., Gaulin, B. D., Ruff, J. P. C. & Balents, L. Order by Quantum Disorder in $Er_2Ti_2O_7$. *Phys. Rev. Lett.* **109,** 167201 (2012).

21. Zhitomirsky, M. E., Gvozdikova, M. V., Holdsworth, P. C. W. & Moessner, R. Quantum Order by Disorder and Accidental Soft Mode in $Er_2Ti_2O_7$. *Phys. Rev. Lett.* **109,** 077204 (2012).

22. Rau, J. G., McClarty, P. A. & Moessner, R. Pseudo-Goldstone Gaps and Order-by-Quantum Disorder in Frustrated Magnets. *Phys. Rev. Lett.* **121,** 237201 (2018).

23. Elliot, M. *et al.* Order-by-disorder from bond-dependent exchange and intensity signature of nodal quasiparticles in a honeycomb cobaltate. *Nat. Commun.* **12,** 3936 (2021).

24. Rau, J. G., Petit, S. & Gingras, M. J. P. Order by virtual crystal field fluctuations in pyrochlore XY antiferromagnets. *Phys. Rev. B* **93,** 184408 (2016).

25. Owerre, S. A first theoretical realization of honeycomb topological magnon insulator. *Journal of Physics: Condensed Matter* **28,** 386001 (2016).

26. McClarty, P. A. Topological Magnons: A Review. *arXiv:2106.01430* (2021).

27. Shivam, S., Coldea, R., Moessner, R. & McClarty, P. Neutron Scattering Signatures of Magnon Weyl Points. *arXiv:1712.08535* (2017).

28. Pershoguba, S. S. *et al.* Dirac Magnons in Honeycomb Ferromagnets. *Phys. Rev. X* **8** (2018).

29. Castro Neto, A. H., Guinea, F., Peres, N. M. R., Novoselov, K. S. & Geim, A. K. The electronic properties of graphene. *Rev. Mod. Phys.* **81,** 109–162 (2009).

30. Abrikosov, A. A., Gorkov, L. P. & Dzyaloshinskii, I. E. *Methods of Quantum Field Theory in Statistical Mechanics* (Dover Publications, 1975).

31. Mucha-Kruczyński, M. *et al.* Characterization of graphene through anisotropy of constant-energy maps in angle-resolved photoemission. *Phys. Rev. B* **77,** 195403 (2008).

Chapter 5

Isospin Winding, Crystal Field Excitations, and Spin-Flip Transition in the Easy-Axis Honeycomb Quantum Magnet $FeTiO_3$

Recent experiments have explored bosonic Dirac quasiparticles on the honeycomb lattice in transition metal halides CrX_3 ($X = Cl, Br, I$) [1–3] and the titanate $CoTiO_3$ [4, 5] - with planar anisotropy. In this chapter, high-resolution inelastic neutron scattering data within the magnetically ordered phase of the easy-axis stacked honeycomb $FeTiO_3$ is presented. The magnetic ground state consists of magnetic moments aligned along the **c** axis, with ferromagnetic alignment within the honeycomb layers and antiferromagnetic stacking along the **c** axis. The magnon dispersion relations exhibit easy-axis anisotropy with a pair of doubly degenerate modes. Upon applying a magnetic field along the **c** axis, the degeneracy of each of these modes is lifted until the magnetic field strength exceeds a critical value upon which the magnetic structure becomes spin polarised in a first order spin-flip transition. For both the zero field and spin-polarised phases, the magnon dispersions have an avoided

crossing at the corners of the two-dimensional Brillouin zone. The winding of the scattering intensity in both antiferromagnetic and spin-polarised phases is explored via angular scans near the avoided crossing points of the magnon dispersions, which is directly related to the non-trivial topology of the quasiparticle wavefunction in momentum space in proximity of nodal points. The INS data show additional modes which hybridise with the dispersive magnons at certain wavevectors.

5.1 Crystal and Magnetic Structure

$FeTiO_3$ is isostructural to $CoTiO_3$ and as such has a crystal structure with the space group $R\bar{3}$. In the hexagonal setting - shown in figure 5.1a - the room temperature lattice parameters are given by $a_h = b_h = 5.08854(7)$Å, $c_h = 14.0924(3)$Å, $\alpha = \beta = 90°$, $\gamma = 120°$ [6]. The iron and titanium ions are surrounded by oxygen ions in an edge sharing octahedral configuration with the transition metal ions forming honeycomb layers in the hexagonal ab plane and stacked in the 'ABC' configuration. As detailed previously in section 4.1, the crystal structure has a rhombohedral primitive unit cell - shown in figure 5.1b - containing two Fe^{2+} ions. The relation between the hexagonal basis vectors $\vec{a}_h$, $\vec{b}_h$, $\vec{c}_h$ and the structural rhombohedral basis vectors $\vec{a}_{rh}$, $\vec{b}_{rh}$, $\vec{c}_{rh}$ is given by equation 4.1.

Initial studies of the magnetic properties [7] proposed an antiferromagnetic state with a Nèel temperature of 58 K, with the magnetic moments of the Fe^{2+} ions aligned along the hexagonal **c** axis, with ferromagnetic alignment between moments within the honeycomb layer and antiferromagnetic alignment between moments in adjacent honeycomb layers [8]. Later studies via neutron scattering techniques [9–11] observed a reflection corresponding to the magnetic ordering wavevector $\mathbf{Q} = (0, 0, 3/2)$. Due to the polarisation factor, such a reflection would have zero scattering intensity in neutron diffraction for a system of magnetic ions aligned along the $\mathbf{c}^*$ axis. Consequently, such studies proposed a slight canting - estimated at 7° [9] - of the magnetic moment away from the **c** axis. The potential presence of this small tilt is neglected in the analysis of the INS results in this chapter. The antiferromagnetically ordered structure has a unit cell that can be described in the hexagonal setting by a doubling along the hexagonal $\mathbf{c}_h$ axis, or in a rhombohedral setting - shown

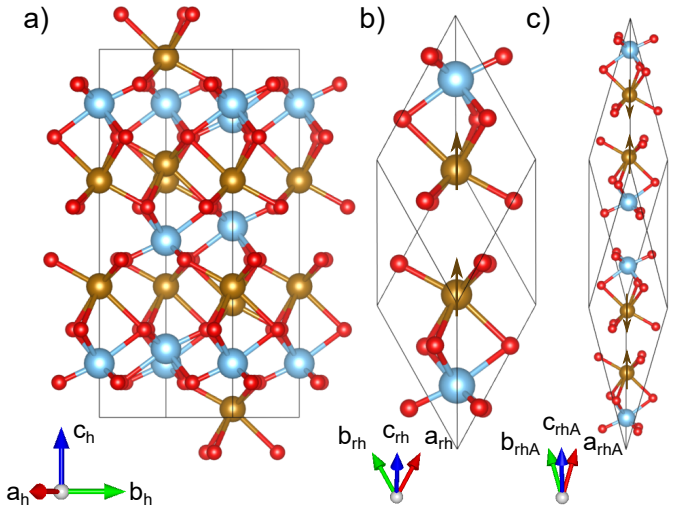

Figure 5.1: Models of the crystallographic and magnetic unit cells of $FeTiO_3$. The crystallographic unit cells are shown for the a) hexagonal and b) rhombohedral settings. Upon the onset of antiferromagnetic magnetic order, the unit cell doubles from the structural unit cell to the magnetic unit cell - c) depicted in the rhombohedral setting. Upon applying an external field along the hexagonal $\mathbf{c}_h$ axis with a field strength higher than 8 T, the magnetic structure becomes spin polarised and the primitive magnetic unit cell is equivalent to the primitive structural unit cell in b). The solid lines define the edges of the unit cell, with orange/light-blue spheres depicting the Fe^{2+}/Ti^{4+} ions.

in figure 5.1c - by mapping each basis vector to the sum of the other two basis vectors - i.e. $\mathbf{a}_{rhA} = \mathbf{b}_{rh} + \mathbf{c}_{rh}$ - as described in equation 4.2. For an externally applied magnetic field along the hexagonal $\mathbf{c}_h$ axis, the low temperature magnetic structure undergoes a first order spin-flip transition at 8.03(1) T [7], see magnetisation curve in figure 5.2. In the spin polarised phase, all spins are aligned along the $\mathbf{c}_h$ axis with an ordered magnetic moment of 4.6(1) μ_B per Fe^{2+} ion - as shown in figure 5.1b. In this phase, the primitive magnetic unit cell is the same as the rhombohedral structural unit cell.

Rietveld refinement of the structural parameters of a powder sample of $FeTiO_3$, synthesised by Dr. D. Prabhakaran in the Clarendon Laboratory, was performed using x-ray diffraction data taken at 300 K with the FullProf software suite [12]. The structural parameters obtained through refinement are tabulated in table 5.1, showing lattice parameters and fractional atomic coordinates that are consistent with published values to within 0.06%. The data quality, however, is insufficient to determine the isotropic displacement parameters $U_{\text{iso.}}$.

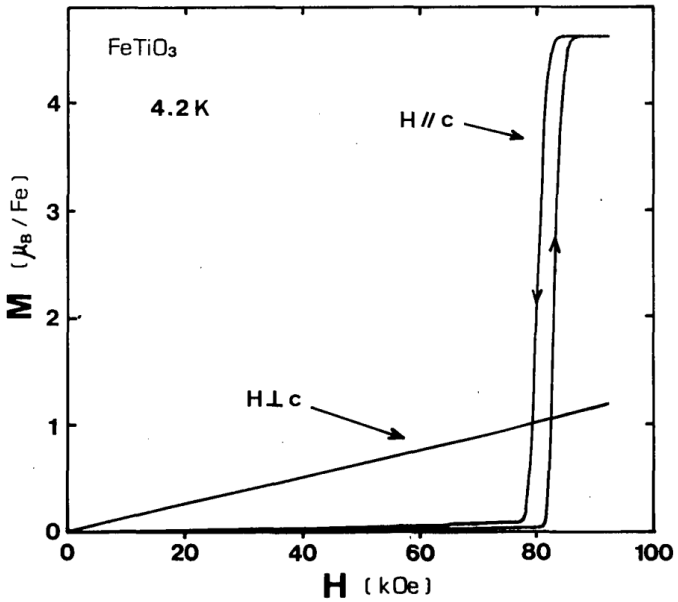

Figure 5.2: Isothermal magnetization curves in $FeTiO_3$ at 4.2 K with an external magnetic field applied parallel and perpendicular to the hexagonal **c** axis. Figure taken from [7].

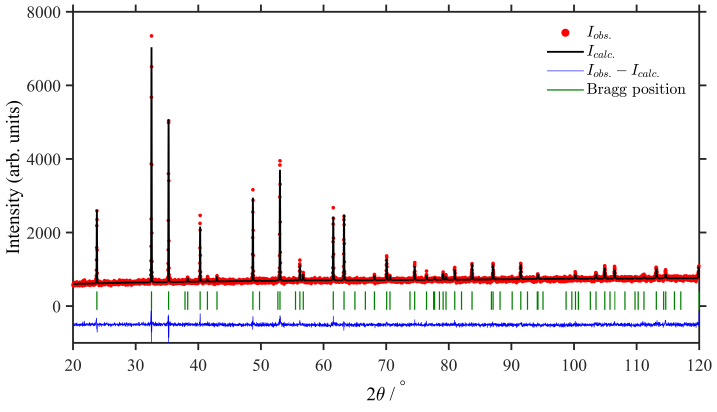

Figure 5.3: X-ray powder diffraction data in $FeTiO_3$ collected at 300 K compared to the fit from structural refinement (shown as a solid black line). The difference $I_{\text{obs}} - I_{\text{calc}}$ is given as a blue line at the bottom of the panes. The structural Bragg peak positions are denoted by green tick marks.

Cell parameters

Space group: $R\bar{3}$ (#148)			
a, b, c (Å)	5.08812(11)	5.08812(11)	14.08510(38)
α, β, γ (°)	90	90	120
Volume (Å^3)	315.795(22)		

Atomic fractional coordinates

Atom	Site	x	y	z
Fe	$6c$	0	0	0.3562(6)
Ti	$6c$	0	0	0.1469(6)
O	$18f$	0.3561(13)	0.0397(18)	0.2384(7)

Table 5.1: Refined 300 K crystal structure parameters of $FeTiO_3$ from analysis of the powder x-ray diffraction data in figure 5.3.

5.2 Inelastic Neutron Scattering Results

Inelastic neutron scattering experiments were performed using the LET time-of-flight spectrometer at ISIS [13]. The sample consisted of a pair of co-aligned single crystals with a total mass 9.56 g aligned with the $\mathbf{c}^*$ axis vertical, shown in figure 5.4, was cooled to a base temperature of 7 K via a closed-cycle refrigerator. A Horace scan was performed by rotating the sample 120° about the $\mathbf{c}^*$ axis in steps of 0.5°. The spectrometer was operated in repetition rate multiplication mode in order to simultaneously collect inelastic scattering data using monochromatic neutrons with incident energies 22.45 meV and 7.48 meV. In a subsequent experiment using the same sample and setup, the Horace scans were repeated by applying an external magnetic field along the $\mathbf{c}^*$ axis of strengths 4, 7, and 8.75 T. For the in-field measurements, the neutrons had incident energies of 25.10 meV and 5.30 meV. The raw time-of-flight neutron data were processed using the MANTID[14] and HORACE[15] data analysis packages.

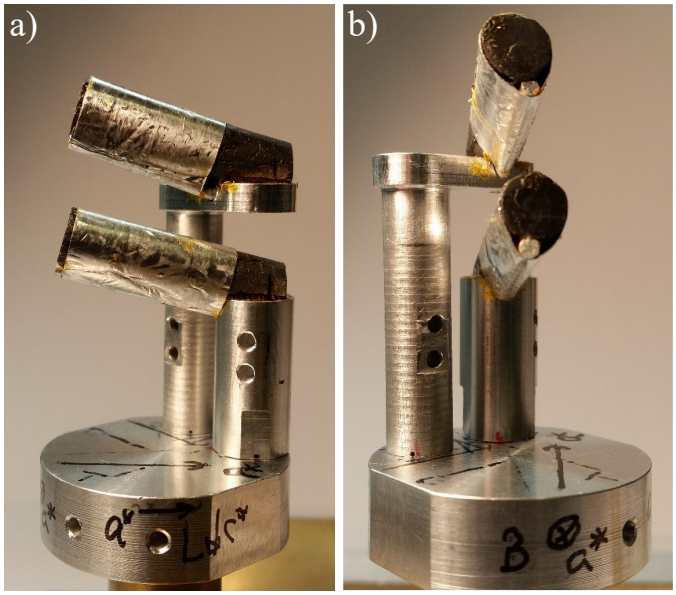

Figure 5.4: Coaligned single crystal samples of $FeTiO_3$ mounted on an aluminium sample holder with crystallographic axes labelled. The $\mathbf{c}^*$ axis is vertically downwards and the sample holder is viewed a) perpendicularly to the $\mathbf{a}^*$ axis and b) along the $\mathbf{a}^*$ axis.

As for the INS data taken on $CoTiO_3$, the data were symmetrised by mapping the pixels in the Horace scans to a 60° sector bordered by the $\mathbf{a}_h^*$ and $\mathbf{b}_h^*$ axes and $l > 0$. Slices through the symmetrised data sets could be taken through high symmetry directions

in order to observe key features of the excitation spectra. Slices through the zero field 22.45 meV data along the plane of the honeycomb layer - shown in figure 5.5d,h - reveal highly intense dispersive modes in the ranges of $6-10$ meV and $10-15$ meV. The two modes almost touch at the high symmetry K points in the two-dimensional Brillouin zone, but there also appears to be a small gap of approximately 1 meV between the modes. Additionally, there is an additional scattering signal between $8-10$ meV in addition to a faint gapless 'V' shaped signal from $0-4$ meV above the $(1,1,3/2)$ magnetic Bragg peak position.

Upon applying a magnetic field of 4 T and 7 T - hereafter referred to as 'intermediate fields' - along the $\mathbf{c}_h$ axis, as can be seen in figure 5.5f,g, the intense modes between $6-10$ meV and $10-15$ meV each split into two distinct modes. The faint scattering signal near 8 meV and gapless 'V' shaped mode above the $(1,1,1.5)$ magnetic Bragg peak position remain unsplit. Upon applying a magnetic field of 8.75 T - hereafter referred to as 'high field' - the material undergoes a spin-flip transition and - as can be seen in figure 5.5b - there are once again only two highly intense dispersive modes - one in an energy range of $1-9$ meV, and another in an energy range $9-14$ meV. As in the zero field dispersion, the two modes almost meet - but there appears to be a non-zero gap - at the high symmetry K points. The lowest energy mode has a small energy gap of around 1 meV. This gap occurs at a wavevector where magnetic Bragg peaks occur in the low field antiferromagnetic phase - such as $(1,1,3/2)$ - and these antiferromagnetic Bragg peaks disappear in the polarised phase. Figure 5.5a shows that the acoustic mode above the structural Bragg peak position $(1,1,0)$ is 'V' shaped, and the $6-8$ meV mode carries a lot of scattering weight at this position.

The strategy adopted to model the dispersions observed in inelastic neutron scattering will be to first apply linear spinwave theory in the magnetically ordered state. The number of magnon modes obtained via linear spin wave theory is equal to the number of magnetic sites in the primitive magnetic unit cell. In zero and intermediate fields, the primitive magnetic unit cell contains four magnetic sites. As presented later in subsection 5.4.1, the two intense modes in the zero field case are each doubly degenerate and acquire a shift in energy of $\pm g\mu_B B$ in the intermediate field cases. Furthermore, the primitive magnetic

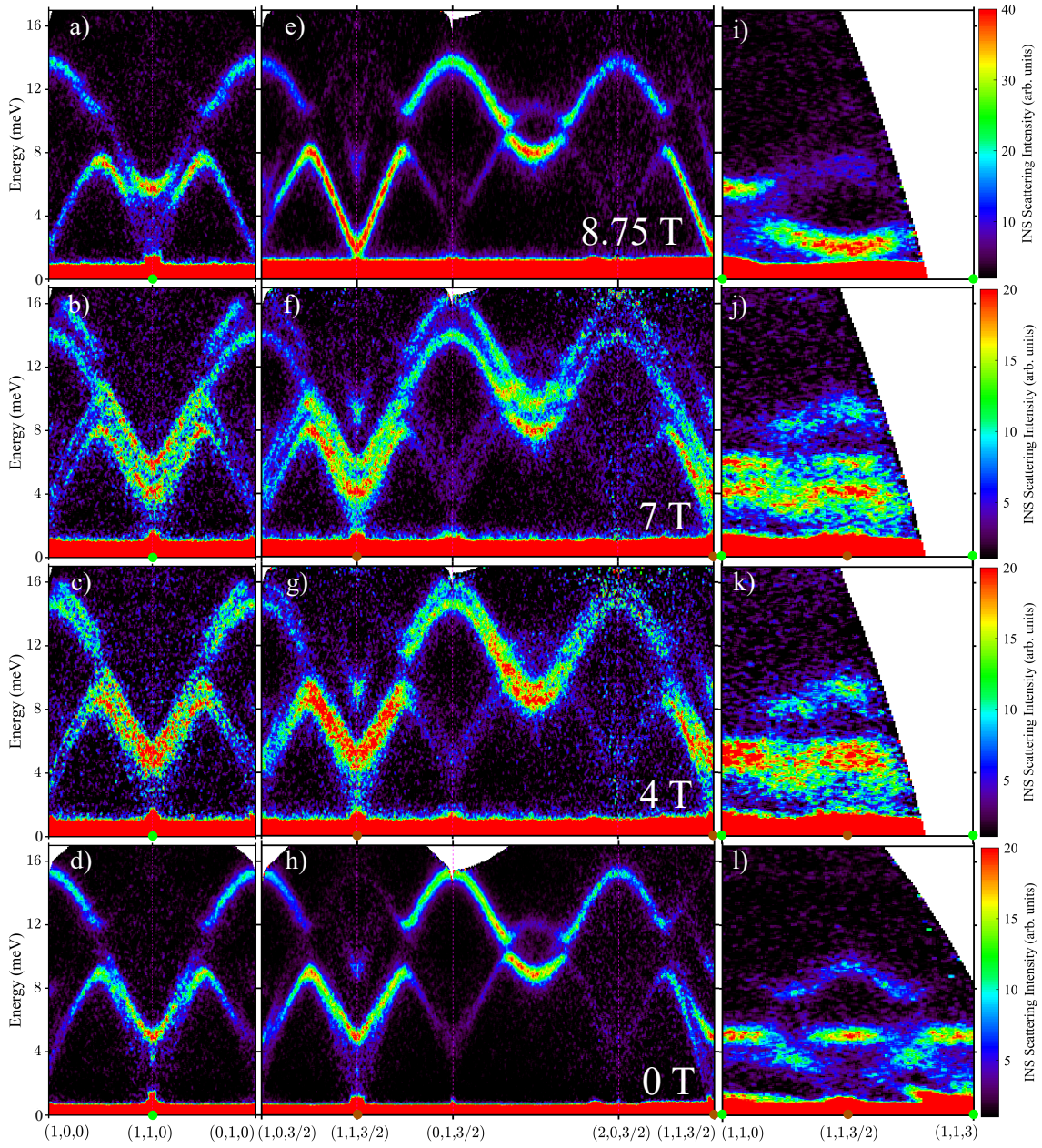

Figure 5.5: INS data in $FeTiO_3$ taken in applied magnetic fields of a, e, i) 8.75 T, b, f, j) 7 T, c, g, k) 4 T, and d, h, l) without an externally applied magnetic field. The incident neutron energies were $E_i = 25.10$ meV for the data sets taken with an applied field and $E_i = 22.45$ meV for the zero-field data. Slices have been taken along paths a-d) and e-h) in the hexagonal hk plane, and i-l) along the $(00L)$ direction normal to the honeycomb layers. Structural/antiferromagnetic Bragg peak positions are indicated by green/brown circles on the elastic line.

unit cell in the high field case is equivalent to the primitive structural unit cell and hence will contain two magnetic sites. Consequently, linear spin wave theory will describe two non-degenerate modes - as presented later in subsection 5.4.3. In all four data sets - zero

field, two intermediate fields, and high field - there are additional modes that cannot be explained within the scope of linear spin wave theory. Modelling these additional modes as acoustic XY magnons would provide a mode with the correct periodicity, but with a far higher INS intensity compared to that observed experimentally. The interaction between these additional modes and magnon modes will be presented in section 5.6 and will provide a quantitative description of the observed dispersions.

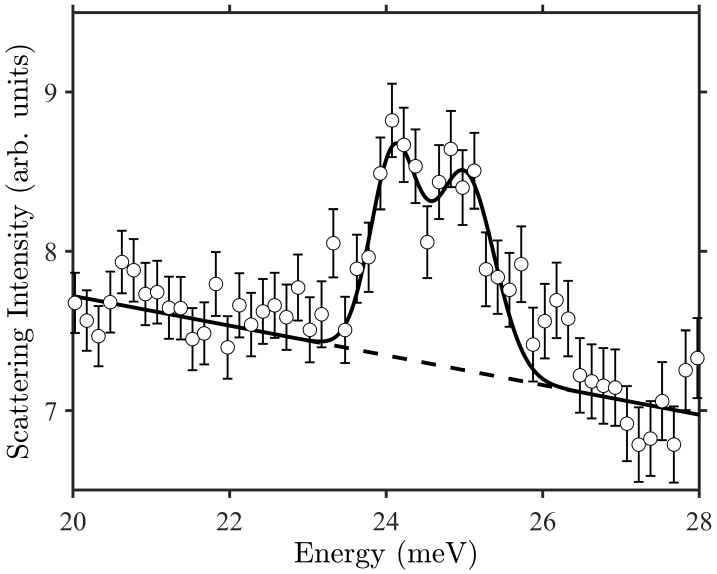

Figure 5.6: Cut in energy taken from INS data in $FeTiO_3$ with incident neutron energies of 36 meV, revealing the presence of excited crystal field levels. There is an increase in the INS intensity, fitted with two Gaussian peaks centred at 24.2 meV and 25.4 meV, above the sloping background - plotted as a dashed line.

Additional INS measurements were performed using the MERLIN time-of-flight spectrometer [16] in order to investigate transitions to higher energy crystal field levels. Two chopper settings in repetition rate multiplication mode were used to provide multiple pulses of monochromated neutrons. The first configuration provided incident neutron energies of 160 meV and 56 meV; the second configuration provided incident neutron energies of 90 meV and 36 meV. The incident energies for each setting were adjusted to have the elastic line at zero energy transfer and the detector counts were normalised to data collected with a vanadium standard under the same conditions, allowing the data sets to have scattering intensities plotted on the same scale. After correcting for the magnetic form factor of the Fe^{2+} ions, small bumps in the scattering intensity at low Q - as shown in figure 5.6 - were

observed around 25 meV. These peaks in intensity were found to be around 1% of the scattering intensity of the lower energy magnon modes, and were hence difficult to characterise in detail. Nonetheless, this excited crystal field level is described by a single-ion model - presented in section 5.3 - combining spin-orbit, crystal field, and magnetic exchange.

5.3 Single Ion Physics and Crystal Field Excitations

In this section, the single-ion physics of the octahedrally coordinated Fe^{2+} ions will be presented. By following similar treatment of the Co^{2+} ions in section 4.3, the spectrum of excited single-ion states in the presence of spin-orbit coupling and trigonal distortion of the octahedral crystal field can be determined. A model incorporating exchange between the multilevel single-ion sites can then be constructed in order to describe both the low energy spinwaves and the higher energy crystal field excitations on the same footing.

5.3.1 Single Ion Physics

The crystal structure of $FeTiO_3$ contains Fe^{2+} ($3d^6$) ions surrounded by a trigonally distorted octahedron of O^{2-} ions. By assuming that electrostatic repulsion of the orbital electrons in the Fe^{2+} ion is the dominant energy scale, the ground state of a single free Fe^{2+} ion can be obtained via Hund's rules, and has a total orbital angular momentum quantum number of $L = 2$ and a total spin quantum number $\mathsf{S} = 2$. By assuming that the the crystal field interaction between the Fe^{2+} ion and the surrounding inhomogeneous electric field of a perfect octahedron of O^{2-} ions is the next leading order perturbation, the crystal field Hamiltonian can be written in terms of the $L = 2$ orbital ground state and is given by

$$\hat{H}_{cf} = B\left(\hat{O}_4^0 + 5\hat{O}_4^4\right) \tag{5.1}$$

where $B > 0$ and the Stevens operators $\hat{O}_4^0$ and $\hat{O}_4^4$ are given by equation 4.4. In the basis of the $|L = 2, L_z\rangle$ states - where $|L = 2, L_z = 2\rangle = (1, 0, 0, 0, 0)^T$ and states of decreasing L_z can be written by shifting the unit vector one place to the right - the crystal field Hamiltonian can be written as a 5×5 matrix

$$\hat{H}_{cf} = 12B \begin{pmatrix} 1 & 0 & 0 & 0 & 5 \\ 0 & -4 & 0 & 0 & 0 \\ 0 & 0 & 6 & 0 & 0 \\ 0 & 0 & 0 & -4 & 0 \\ 5 & 0 & 0 & 0 & 1 \end{pmatrix}, \tag{5.2}$$

which can be diagonalised to give a ground state triplet (at energy $-48B$) with wavefunctions

$$\sqrt{\frac{1}{2}}\left(|2\rangle - |-2\rangle\right), \quad \mp|\pm 1\rangle,$$

an excited doublet (at energy $+72B$) with wavefunctions

$$\sqrt{\frac{1}{2}}\left(|2\rangle + |-2\rangle\right), \quad |0\rangle,$$

where the above states are written in the $|L_z\rangle$ basis. The splitting of the five-fold degenerate $L = 2$ state into a lower T_{2g} triplet and an upper E_g doublet is as expected from representation theory. In a spherically symmetric potential, the Fe^{2+} ion has symmetry operations belonging to the group O(3), and the basis functions for this group are the spherical harmonics. The $L = 2$ irreducible representation of O(3) - $\Gamma^{(L=2)}$ - has characters given in the character table 4.4. When restricted to the discrete subgroup O_h, the $\Gamma^{(L=2)}$ representation can be decomposed into the E_g and T_{2g} irreducible representations of O_h.

The ground state orbital triplet can be described as an effective $l = 1$ orbital angular momentum state, with the correspondence between $|l_z\rangle$ and $|L_z\rangle$ given by

$$|l_z = \pm 1\rangle = \pm|\mp 1\rangle,$$
$$|l_z = 0\rangle = \sqrt{\frac{1}{2}}\left(|2\rangle - |-2\rangle\right),$$

under this correspondence, the total orbital angular momentum operator $\hat{\mathbf{L}}$ maps onto the effective orbital angular momentum operator $\hat{\mathbf{l}}$ with the equivalency relation $\hat{\mathbf{L}} = -\hat{\mathbf{l}}$.

Now considering only a single Fe^{2+} ion with the surrounding octahedron of O^{2-} ions, the next leading order perturbation - which will act on the $l = 1$, $\mathsf{S} = 2$ crystal field ground state - will be a combination of spin-orbit coupling and trigonal distortion. The spin-orbit Hamiltonian in terms of the total orbital and total spin angular momentum operators can be written as $\hat{H}_{so} = -\lambda\hat{\mathbf{L}} \cdot \hat{\mathsf{S}}$, where $\lambda > 0$ and the minus sign is added since the free-ion electronic configuration - $3d^6$ - has a more than half filled valence shell. Using the equivalency relation between the total and effective orbital angular momentum operators, the spin-orbit Hamiltonian can be written as $\hat{H}_{so} = \lambda\hat{\mathbf{l}} \cdot \hat{\mathsf{S}}$ and will act on the 15 dimensional Hilbert space spanned by the $|l_z, \mathsf{S}_z\rangle$ states. Defining a total angular momentum operator $\hat{\mathbf{J}}_{\text{eff}} = \hat{\mathbf{l}} + \hat{\mathsf{S}}$ such that $\hat{J}^2_{\text{eff}}$ and $\hat{J}_{\text{eff},z}$ commute with the spin-orbit Hamiltonian allows states to be written in the basis of $|J_{\text{eff}}, J_{\text{eff},z}\rangle$ states. Diagonalising the spin-orbit Hamiltonian gives a ground state $J_{\text{eff}} = 1$ triplet at energy -3λ, an excited $J_{\text{eff}} = 2$ quintet at energy $-\lambda$, and an excited $J_{\text{eff}} = 3$ septuplet at energy 2λ. The states in the $|J_{\text{eff}}, J_{\text{eff},z}\rangle$ basis can be written in terms of the $|l_z, \mathsf{S}_z\rangle$ states as follows

$$
\begin{aligned}
|J_{\text{eff}} = 3, J_{\text{eff},z} = \pm 3\rangle &= |\pm 1, \pm 2\rangle \\
|J_{\text{eff}} = 3, J_{\text{eff},z} = \pm 2\rangle &= \sqrt{\frac{2}{3}}\,|\pm 1, \pm 1\rangle + \sqrt{\frac{1}{3}}\,|0, \pm 2\rangle \\
|J_{\text{eff}} = 3, J_{\text{eff},z} = \pm 1\rangle &= \sqrt{\frac{2}{5}}\,|\pm 1, 0\rangle + \sqrt{\frac{8}{15}}\,|0, \pm 1\rangle + \sqrt{\frac{1}{15}}\,|\mp 1, \pm 2\rangle \\
|J_{\text{eff}} = 3, J_{\text{eff},z} = 0\rangle &= \sqrt{\frac{1}{5}}\,|+1, -1\rangle + \sqrt{\frac{3}{5}}\,|0, 0\rangle + \sqrt{\frac{1}{5}}\,|-1, +1\rangle \\
|J_{\text{eff}} = 2, J_{\text{eff},z} = \pm 2\rangle &= \sqrt{\frac{1}{3}}\,|\pm 1, \pm 1\rangle - \sqrt{\frac{2}{3}}\,|0, \pm 2\rangle \\
|J_{\text{eff}} = 2, J_{\text{eff},z} = \pm 1\rangle &= \sqrt{\frac{1}{2}}\,|\pm 1, 0\rangle - \sqrt{\frac{1}{6}}\,|0, \pm 1\rangle - \sqrt{\frac{1}{3}}\,|\mp 1, \pm 2\rangle \\
|J_{\text{eff}} = 2, J_{\text{eff},z} = 0\rangle &= \sqrt{\frac{1}{2}}\,|+1, -1\rangle - \sqrt{\frac{1}{2}}\,|-1, +1\rangle \\
|J_{\text{eff}} = 1, J_{\text{eff},z} = \pm 1\rangle &= \sqrt{\frac{1}{10}}\,|\pm 1, 0\rangle - \sqrt{\frac{3}{10}}\,|0, \pm 1\rangle + \sqrt{\frac{3}{5}}\,|\mp 1, \pm 2\rangle \\
|J_{\text{eff}} = 1, J_{\text{eff},z} = 0\rangle &= \sqrt{\frac{3}{10}}\,|+1, -1\rangle - \sqrt{\frac{2}{5}}\,|0, 0\rangle + \sqrt{\frac{3}{10}}\,|-1, +1\rangle
\end{aligned}
$$

As for the crystal structure of $CoTiO_3$, the octahedra of O^{2-} ions around each transition

metal ion site in $FeTiO_3$ are trigonally distorted, and this distortion can be modelled by the Hamiltonian $\hat{H}_{trig} = \delta\left[\hat{l}_z^2 - 2/3\right]$, which acts on the effective $l = 1$ orbital angular momentum ground state of the crystal field Hamiltonian. The trigonal distortion will mix the $|J_{\text{eff}}, J_{\text{eff},z}\rangle$ states of the same $J_{\text{eff},z}$ quantum number but of differing J_{eff}. Consequently, the $(2J_{\text{eff}}+1)$-fold degeneracy of the eigenstates of the spin-orbit Hamiltonian will be lifted. By treating $\hat{H}_{trig}$ as a perturbation on the eigenstates of the spin-orbital Hamiltonian, the first-order shift in energy, $\delta E^{(1)}_{\text{trig}}$, for each state can be calculated and the results are tabulated in Table 5.2.

J_{eff}	$J_{\text{eff},z}$	$\delta E^{(1)}_{\text{trig}}$
1	± 1	$+\delta/30$
	0	$-\delta/15$
2	± 2	$-\delta/3$
	± 1	$+\delta/6$
	0	$+\delta/3$
3	± 3	$+\delta/3$
	± 2	0
	± 1	$-\delta/5$
	0	$-4\delta/15$

Table 5.2: Energy of eigenstates of the spin-orbital Hamiltonian for Fe^{2+} ions in an octahedral crystal field of O^{2-} ions to first order in the trigonal distortion parameter δ.

From the tabulated first order shifts in energy due to trigonal distortion, it can be seen that for $\delta < 0$, the doublet with quantum numbers $J_{\text{eff},z} = \pm 1$ will be selected as the ground state. This ground state doublet selects easy axis ordering since $\langle \hat{\mathsf{S}}^z \rangle = \pm 2$. Conversely, $\delta > 0$ will select an easy plane $J_{\text{eff},z} = 0$ ground state. By treating the spin-orbit coupling and trigonal distortion at the same order, the spectrum of excited single-ion states can be found by diagonalising the combined Hamiltonian $\hat{H}_{so} + \hat{H}_{trig}$. As shown in figure 5.7, the single-ion parameters of $\lambda = 7.8$ meV and $\delta = -27.2$ meV give a ground state doublet in addition to excited levels at 2.7, 11.1, 14.6, 21.7, 34.4, 51.0, 53.7, and 54.5 meV. The wavefunctions of the ground state doublet can be written in terms of the $|l_z, \mathsf{S}_z\rangle$ states

$$|\psi_{\pm}\rangle = 0.2022\,|\pm1,0\rangle - 0.2834\,|0,\pm1\rangle + 0.9375\,|\mp1,\pm2\rangle\,, \tag{5.3}$$

where the ground state expectation value of $\langle \hat{J}_{\mathrm{eff},z} \rangle = \pm 1$ and $\langle \hat{\mathsf{S}}^z \rangle = \pm 1.838$. Consequently the single-ion ground state is an easy-axis state, albeit with an expectation value of $\hat{\mathsf{S}}^z$ that is somewhat reduced in magnitude from ± 2. The low-lying 2.7 meV level is an easy plane state which will become further separated from the single-ion ground state upon the addition of a mean field due to exchange. Transitions from the single-ion ground state doublet to this excited level correspond to the low energy $4 - 16$ meV dispersive magnons observed in the inelastic neutron scattering data in figure 5.5d.

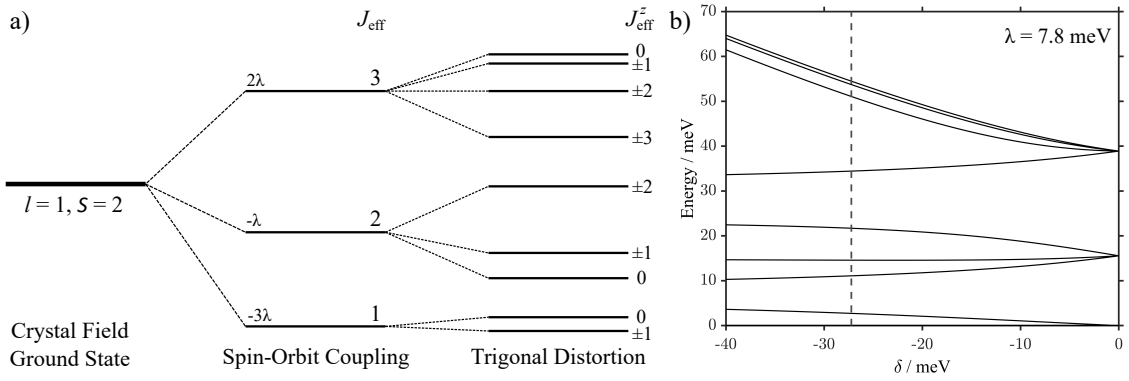

Figure 5.7: Single-ion spectrum a) within the lowest $l = 1$, $\mathsf{S} = 2$ sector for a Fe^{2+} ion in an octahedral crystal field. The trigonal distortion lifts the degeneracy of the J_{eff} levels. b) Splitting of the crystal field levels for fixed spin-orbit coupling ($\lambda = 7.8$ meV) as a function of the trigonal distortion δ. The dashed vertical line corresponds to $\delta = -27.2$ meV, which places the low energy dispersions and excited single-ion levels close to the experimentally observed transitions.

5.3.2 Dispersive Single Ion Excitations

This section will present a model of the dispersions of magnetic excitations of the single-ion levels. In order to include the higher energy crystal field levels in an exchange model, a mean field due to exchange must be added to each single-ion site. The mean-field Hamiltonian at a site i is given by

$$\hat{H}_{MF,i} = \sum_j J_{ij} \langle \hat{\mathsf{S}}_j \rangle \cdot \hat{\mathsf{S}}_i, \tag{5.4}$$

where the sum is over all sites j in the lattice where there is a non-zero Heisenberg exchange coupling J_{ij} between sites i and j. At low temperatures, it may be assumed that $\langle \hat{\mathsf{S}}_j \rangle$ is the expectation value of the operator S evaluated with the ground state of the single-ion Hamiltonian defined on the site j. The mean field term can be added to the spin-orbit and trigonal distortion terms which act on the $l = 1$ and $\mathsf{S} = 2$ crystal field ground state on each site i to give a single-ion Hamiltonian:

$$\hat{H}_{1,i} = \lambda \hat{\mathbf{l}}_i \cdot \hat{\mathsf{S}}_i + \delta \left[\hat{l}^2_{z,i} - 2/3 \right] + \sum_j J_{ij} \langle \hat{\mathsf{S}}_j \rangle \cdot \hat{\mathsf{S}}_i. \tag{5.5}$$

Since the expectation value $\langle \hat{\mathsf{S}}_j \rangle$ depends on the ground state of $\hat{H}_{1,j}$, the values of $\langle \hat{\mathsf{S}}_i \rangle$ over each sublattice must be solved self-consistently which will provide the magnetic ground state stabilised by single-ion terms and the mean field due to exchange. In the case of $FeTiO_3$, the single-ion parameters $\lambda > 0$ and $\delta < 0$ will produce a ground state of $\langle \hat{\mathsf{S}}_i \rangle = \pm 2$ in the limit $|\lambda| << |\delta|$. The inclusion of exchanges $J_1 < 0$ and $J_2 > 0$ will stabilise a magnetic ground state that will satisfy

$$\langle \hat{\mathsf{S}}_\mathrm{A} \rangle = \langle \hat{\mathsf{S}}_\mathrm{B} \rangle = - \langle \hat{\mathsf{S}}_\mathrm{C} \rangle = - \langle \hat{\mathsf{S}}_\mathrm{D} \rangle ,$$

where A, B, C, and D denote the sublattice on which the operators are defined. The remaining exchange terms will act on pairs of sites and will allow for the dispersion of magnetic excitations throughout the lattice. The pairwise term is given by [17]

$$\hat{H}_2 = \sum_{\langle i,j \rangle} J_{ij} \left[\hat{\mathsf{S}}^z_i \left(\hat{\mathsf{S}}^z_j - 2 \langle \hat{\mathsf{S}}^z_j \rangle \right) + \frac{1}{2} \left(\hat{\mathsf{S}}^+_i \hat{\mathsf{S}}^-_j + \hat{\mathsf{S}}^-_i \hat{\mathsf{S}}^+_j \right) \right], \tag{5.6}$$

where the sum $\langle i, j \rangle$ is defined such that each bond between sites i and j that has an exchange coupling J_{ij} is counted once only. The $-2 \langle \hat{\mathsf{S}}^z_j \rangle$ term is included to be exactly opposite to the single-ion mean field contribution in equation 5.4. For N lattice sites, the Hilbert space is $15N$ dimensional and is spanned by the states $|i, l_z, \mathsf{S}_z\rangle$, where i denotes the sublattice site. The single-ion Hamiltonian for any given site acts on 15 of these states and can be diagonalised into a spectrum of states with energy of the pth excited level denoted by $\Delta_{p,i}$. In this case, the single-ion Hamiltonian is given by

$$\hat{H}_{1,i} = \sum_{p=1}^{d-1} \Delta_{p,i} \hat{a}^{\dagger}_{p,i} \hat{a}_{p,i}, \tag{5.7}$$

where $d = 15$ denotes the number of single ion levels in the $|l_z, \mathsf{S}_z\rangle$ basis. In order to write this in a form more familiar to the previous bosonisation procedures in sections 4.4 and 5.4, the $\hat{a}^{\dagger}_{p,i}$ operators are defined as a raising operator from the ground state to the pth excited state on the ith site of the A sublattice. Similarly, $\hat{b}^{\dagger}_{p,i}$, $\hat{c}^{\dagger}_{p,i}$, and $\hat{d}^{\dagger}_{p,i}$ operators can be defined on the B, C, and D sublattices respectively. Furthermore, the spectrum of excited single-ion levels in the model for $FeTiO_3$ is independent of the sublattice - and so the Hamiltonian of all of the single-ion terms is given by

$$\hat{H}_1 = \sum_i \hat{H}_{1,i} = \sum_{p=1}^{d-1} \Delta_{p,i} \left[\sum_{i \in A} \hat{a}^{\dagger}_{p,i} \hat{a}_{p,i} + \sum_{i \in B} \hat{b}^{\dagger}_{p,i} \hat{b}_{p,i} + \sum_{i \in C} \hat{c}^{\dagger}_{p,i} \hat{c}_{p,i} + \sum_{i \in D} \hat{d}^{\dagger}_{p,i} \hat{d}_{p,i} \right], \tag{5.8}$$

where the commutation relations are given by $\left[\hat{x}_{p,i}, \hat{y}^{\dagger}_{q,j}\right] = \delta_{xy}\delta_{ij}\delta_{pq}$. Now, the α component of the spin operators $\hat{\mathbf{S}}_i$, for the site i on sublattice X can be written in the basis of the diagonalised single-ion Hamiltonian. In this basis, $\hat{S}^{X\alpha}_i$ is a $d \times d$ matrix and has components denoted by $c^{X\alpha}_{pq}$. The operator $\hat{S}^{X\alpha}_i$ can be written in terms of the boson operators and components $c^{X\alpha}_{pq}$ in a generalisation of the Holstein-Primakoff expansion [5]

$$\hat{S}^{X\alpha}_i = c^{X\alpha}_{00} + \sum_{p=1}^{d-1} \left[c^{X\alpha}_{0p} \hat{x}_{p,i} + c^{X\alpha}_{p0} \hat{x}^{\dagger}_{p,i} \right] + \sum_{p=1}^{d-1} \sum_{q=1}^{d-1} \left[c^{X\alpha}_{pq} - \delta_{pq} c^{X\alpha}_{00} \right] \hat{x}^{\dagger}_{p,i} \hat{x}_{q,i}. \tag{5.9}$$

For the J_1-J_2 Heisenberg model on the lattice of $FeTiO_3$ single-ion sites, the coefficients satisfy the following properties

$$\begin{aligned} c^{A\alpha}_{pq} &= c^{B\alpha}_{pq}, \quad c^{C\alpha}_{pq} = c^{D\alpha}_{pq}, \\ c^{A\pm}_{00} &= c^{C\pm}_{00}, \quad c^{Az}_{00} = -c^{Cz}_{00}. \end{aligned} \tag{5.10}$$

In the expansion of $\hat{H}_2$ in terms of boson operators up to quadratic order, the following $(d-1) \times (d-1)$ matrix terms appear

$$\begin{aligned}
\mathcal{M}_{pq}^{\alpha\beta} &= c_{0p}^{\alpha z} c_{0q}^{\beta z} + \frac{1}{2}\left(c_{0p}^{\alpha +} c_{0q}^{\beta -} + c_{0p}^{\alpha -} c_{0q}^{\beta +}\right), \\
\mathcal{N}_{pq}^{\alpha\beta} &= c_{p0}^{\alpha z} c_{q0}^{\beta z} + \frac{1}{2}\left(c_{p0}^{\alpha +} c_{q0}^{\beta -} + c_{p0}^{\alpha -} c_{q0}^{\beta +}\right), \\
\mathcal{P}_{pq}^{\alpha\beta} &= c_{0p}^{\alpha z} c_{q0}^{\beta z} + \frac{1}{2}\left(c_{0p}^{\alpha +} c_{q0}^{\beta -} + c_{0p}^{\alpha -} c_{q0}^{\beta +}\right), \\
\mathcal{Q}_{pq}^{\alpha\beta} &= c_{p0}^{\alpha z} c_{0q}^{\beta z} + \frac{1}{2}\left(c_{p0}^{\alpha +} c_{0q}^{\beta -} + c_{p0}^{\alpha -} c_{0q}^{\beta +}\right),
\end{aligned} \tag{5.11}$$

which have the following symmetry properties

$$\begin{aligned}
\mathcal{M}_{pq}^{\alpha\beta} &= \mathcal{N}_{pq}^{\alpha\beta}, \quad \mathcal{P}_{pq}^{\alpha\beta} = \mathcal{Q}_{pq}^{\alpha\beta}, \\
\mathcal{M}_{pq}^{\alpha\beta} &= \mathcal{M}_{pq}^{\beta\alpha}, \quad \mathcal{P}_{pq}^{\alpha\beta} = \mathcal{P}_{pq}^{\beta\alpha}.
\end{aligned} \tag{5.12}$$

Furthermore, by writing the raising and lowering operators via the Fourier transform

$$\begin{aligned}
\hat{a}_{p,\mathbf{k}} &= \frac{1}{\sqrt{N/4}} \sum_{i \in A} e^{-i\mathbf{k}\cdot\mathbf{x}_i} \hat{a}_{p,i}, \\
\hat{a}_{p,\mathbf{k}}^{\dagger} &= \frac{1}{\sqrt{N/4}} \sum_{i \in A} e^{i\mathbf{k}\cdot\mathbf{x}_i} \hat{a}_{p,i}^{\dagger},
\end{aligned} \tag{5.13}$$

where N denotes the total number of Fe^{2+} ions, with $N/4$ ions in each sublattice, and similarly for each of the $\hat{b}_{p,i}$, $\hat{c}_{p,i}$, and $\hat{d}_{p,i}$ operators on the respective B, C, and D sublattices. The Hamiltonian $\hat{H}_1 + \hat{H}_2$ can be written in the form

$$\hat{H}_1 + \hat{H}_2 = \frac{1}{2} \sum_{\mathbf{k}} \sum_{p,q} \hat{\mathbf{\Psi}}_{p,\mathbf{k}}^{\dagger} \mathcal{D}_{pq}(\mathbf{k}) \hat{\mathbf{\Psi}}_{q,\mathbf{k}}, \tag{5.14}$$

where $\hat{\mathbf{\Psi}}^{\dagger}$ is a vector of the boson operators and takes the form

$$\hat{\mathbf{\Psi}}_{p,\mathbf{k}}^{\dagger} = \left(\hat{a}_{p,\mathbf{k}}, \hat{b}_{p,\mathbf{k}}, \hat{c}_{p,\mathbf{k}}, \hat{d}_{p,\mathbf{k}}, \hat{a}_{p,-\mathbf{k}}^{\dagger}, \hat{b}_{p,-\mathbf{k}}^{\dagger}, \hat{c}_{p,-\mathbf{k}}^{\dagger}, \hat{d}_{p,-\mathbf{k}}^{\dagger}\right), \tag{5.15}$$

and the dynamical matrix $\mathcal{D}_{pq}(\mathbf{k})$ takes the form

$$\mathcal{D}_{pq}(\mathbf{k}) = \begin{pmatrix} \Delta_p\delta_{pq} & \mathcal{P}^{AA}_{pq,\mathbf{k}} & 0 & \mathcal{P}^{AC}_{pq,\mathbf{k}} & 0 & \mathcal{M}^{AA}_{pq,\mathbf{k}} & 0 & \mathcal{M}^{AC}_{pq,\mathbf{k}} \\ \mathcal{P}^{AA*}_{qp,\mathbf{k}} & \Delta_p\delta_{pq} & \mathcal{P}^{CA*}_{qp,\mathbf{k}} & 0 & \mathcal{M}^{AA*}_{qp,\mathbf{k}} & 0 & \mathcal{M}^{CA*}_{qp,\mathbf{k}} & 0 \\ 0 & \mathcal{P}^{CA}_{pq,\mathbf{k}} & \Delta_p\delta_{pq} & \mathcal{P}^{CC}_{pq,\mathbf{k}} & 0 & \mathcal{M}^{CA}_{pq,\mathbf{k}} & 0 & \mathcal{M}^{CC}_{pq,\mathbf{k}} \\ \mathcal{P}^{AC*}_{qp,\mathbf{k}} & 0 & \mathcal{P}^{CC*}_{qp,\mathbf{k}} & \Delta_p\delta_{pq} & \mathcal{M}^{AC*}_{qp,\mathbf{k}} & 0 & \mathcal{M}^{CC*}_{qp,\mathbf{k}} & 0 \\ 0 & \mathcal{M}^{AA}_{pq,\mathbf{k}} & 0 & \mathcal{M}^{AC}_{pq,\mathbf{k}} & \Delta_p\delta_{pq} & \mathcal{P}^{AA}_{pq,\mathbf{k}} & 0 & \mathcal{P}^{AC}_{pq,\mathbf{k}} \\ \mathcal{M}^{AA*}_{qp,\mathbf{k}} & 0 & \mathcal{M}^{CA*}_{qp,\mathbf{k}} & 0 & \mathcal{P}^{AA*}_{qp,\mathbf{k}} & \Delta_p\delta_{pq} & \mathcal{P}^{CA*}_{qp,\mathbf{k}} & 0 \\ 0 & \mathcal{M}^{CA}_{pq,\mathbf{k}} & 0 & \mathcal{M}^{CC}_{pq,\mathbf{k}} & 0 & \mathcal{P}^{CA}_{pq,\mathbf{k}} & \Delta_p\delta_{pq} & \mathcal{P}^{CC}_{pq,\mathbf{k}} \\ \mathcal{M}^{AC*}_{qp,\mathbf{k}} & 0 & \mathcal{M}^{CC*}_{qp,\mathbf{k}} & 0 & \mathcal{P}^{AC*}_{qp,\mathbf{k}} & 0 & \mathcal{P}^{CC*}_{qp,\mathbf{k}} & \Delta_p\delta_{pq} \end{pmatrix} \tag{5.16}$$

where each matrix element is itself a $(d-1)\times(d-1)$ matrix, defined by

$$\begin{aligned} \mathcal{M}^{AA}_{pq,\mathbf{k}} &= J_1\mathcal{M}^{AA}_{pq}\gamma_{1\mathbf{k}}, \quad \mathcal{M}^{CC}_{pq,\mathbf{k}} = J_1\mathcal{M}^{CC}_{pq}\gamma_{1\mathbf{k}}, \\ \mathcal{M}^{AC}_{pq,\mathbf{k}} &= J_2\mathcal{M}^{AC}_{pq}\gamma_{2\mathbf{k}}, \quad \mathcal{M}^{CA}_{pq,\mathbf{k}} = J_2\mathcal{M}^{CA}_{pq}\gamma_{2\mathbf{k}}, \\ \mathcal{P}^{AA}_{pq,\mathbf{k}} &= J_1\mathcal{P}^{AA}_{pq}\gamma_{1\mathbf{k}}, \qquad \mathcal{P}^{CC}_{pq,\mathbf{k}} = J_1\mathcal{P}^{AA}_{pq}\gamma_{1\mathbf{k}}, \\ \mathcal{P}^{AC}_{pq,\mathbf{k}} &= J_2\mathcal{P}^{AC}_{pq}\gamma_{2\mathbf{k}}, \qquad \mathcal{P}^{CA}_{pq,\mathbf{k}} = J_2\mathcal{P}^{CA}_{pq}\gamma_{2\mathbf{k}}. \end{aligned} \tag{5.17}$$

The spectrum of dispersive magnetic excitations is then determined by diagonalising $g\mathcal{D}_{pq}(\mathbf{k})$ where $g = \mathrm{diag}(\mathbb{1}_{56}, -\mathbb{1}_{56})$ via the method of White et. al. [18]. The INS intensity is then proportional to

$$S(\mathbf{k},\omega) = \sum_{\alpha,\beta}(\delta_{\alpha\beta} - \hat{k}_\alpha\hat{k}_\beta)S^{\alpha\beta}(\mathbf{k},\omega), \tag{5.18}$$

where the correlation function $S^{\alpha\beta}(\mathbf{k},\omega)$ is can be defined over a sum of excited levels $|\lambda\rangle$ with dispersions $\omega_\lambda(\mathbf{k})$ as follows

$$S^{\alpha\beta}(\mathbf{k},\omega) = \sum_{\lambda} \langle 0|\hat{\mu}^{\alpha}_{-\mathbf{k}}|\lambda\rangle \langle \lambda|\hat{\mu}^{\beta}_{\mathbf{k}}|0\rangle \, \delta\left(\omega - \omega_{\lambda}(\mathbf{k})\right),$$

where $\hat{\boldsymbol{\mu}}_{\mathbf{k}}$ is the Fourier transform of $\hat{\boldsymbol{\mu}} = -\hat{\mathbf{l}} + 2\hat{\mathbf{S}}$. By integrating the INS intensity $S(\mathbf{k},\omega)$ over rings where $\mathbf{k}$ is of constant wavevector transfer $|\mathbf{Q}|$, for a fixed crystal orientation where the $\mathbf{a}^*$ axis is parallel to the incident beam direction, $\mathbf{k}_i$. By multiplying the calculated values of $S(\mathbf{k},\omega)$ by the absolute square of the magnetic form factor of the Fe^{2+} ion, the ring averaged inelastic scattering pattern can be calculated.

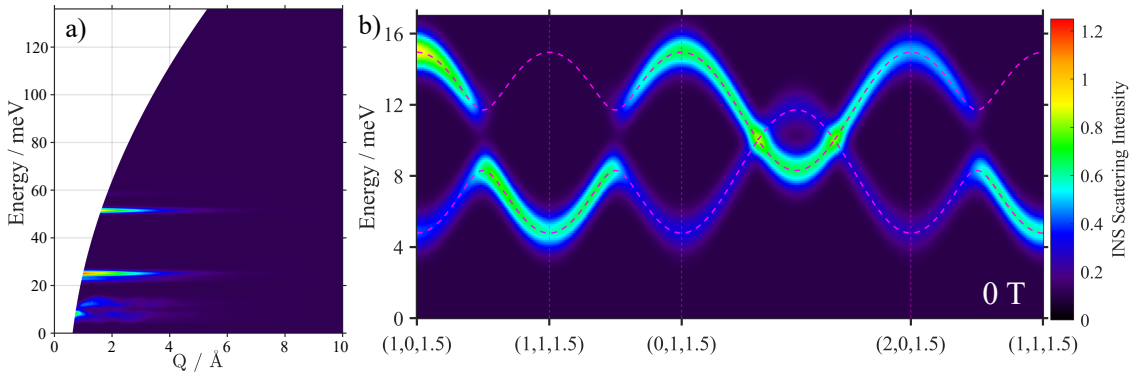

Figure 5.8: Calculated INS intensities for a nearest neighbour exchange model over the spectrum of excited Fe^{2+} single-ion states a) plotted as a function of $|\mathbf{Q}|$ for energies up to 136 meV. Pixel averaging over equal $|\mathbf{Q}|$ with $\mathbf{k}_i$ parallel to the hexagonal $\mathbf{a}^*$ axis was performed assuming $E_i = 160$ meV. b) Dispersions plotted over a reciprocal space path in the plane of the honeycomb layers for energies up to 17 meV in zero field. The parameters used in each plot were $\delta = -27.2$ meV, $\lambda = 7.8$ meV, and $J_1 = -0.86$ meV.

The parameters $\lambda = 7.8$ meV, $\delta = -27.2$ meV, and $J_1 = -0.86$ meV were used in the calculations in figure 5.8. This choice of parameters captures the main dispersions at zero field quite well, compare figure 5.8b with the INS data in figure 5.5d. The calculated ring averaged pattern is presented in figure 5.8a, and shows a faint mode centred at 22.3 meV and a much more intense mode centred at 25.7 meV. The calculated 25.7 meV mode is attributed to the inelastic signal seen in figure 5.6. The mean field arising from the exchange interaction will provide a ground state of single-ion site wavefunctions that can be written in terms of the $|l_z, \mathsf{S}_z\rangle$ states

$$|\psi_{\pm}\rangle = 0.1154\,|\pm1,0\rangle - 0.2413\,|0,\pm1\rangle + 0.9636\,|\mp1,\pm2\rangle\,, \tag{5.19}$$

where the ground state expectation value of $\hat{S}^z$ is ± 1.915. The pair of doubly degenerate dispersive modes seen in figure 5.8b have the same features as modes produced in model describing easy-axis single-ion anisotropy with first nearest neighbour Heisenberg exchange - as presented later in figure 5.10 in section 5.4.

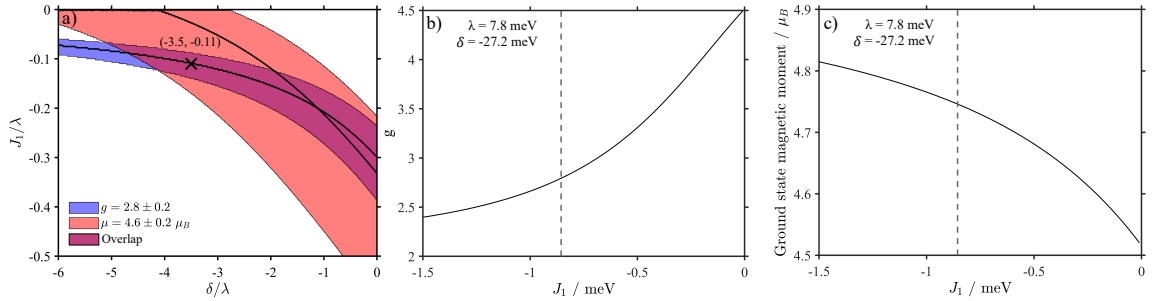

Figure 5.9: Ground state magnetic moment and g-factor for an exchange model over the spectrum of excited Fe^{2+} single-ion states. a) The regions of $(J_1/\lambda, \delta/\lambda)$ parameter space where $g = 2.8 \pm 0.2$ and $\mu = 4.6 \pm 0.2\ \mu_B$ are shaded in blue and red, respectively. The selected point $(\delta/\lambda = -3.5, J_1/\lambda = -0.11)$ is marked with a cross. b/c) The g-factor/ground state magnetic moment plotted as a function of J_1 for $\lambda = 7.8$ meV and $\delta = -27.2$ meV. The grey dashed line at $J_1 = -0.86$ meV shows that the chosen parameters result in a g-factor of 2.8 and a ground state magnetic moment of magnitude 4.75 μ_B, consistent with the magnetisation data.

In order to fit the δ, λ, and J_1 parameters to accurately describe $FeTiO_3$, a g-factor of 2.8 (as shown in section 5.4.2) and a ground state ordered moment of $4.6 \pm 0.2\ \mu_B$ is required. Additionally, the lowest energy excitations are required to be dispersive and have energies ranging from 4 meV to 16 meV. There is also a crystal field excitation around 25 meV that is to be reproduced. The parameter space of $(\delta/\lambda, J_1/\lambda)$ is shown in figure 5.9a, with regions corresponding to $g = 2.8 \pm 0.2$ and $\mu = 4.6 \pm 0.2\ \mu_B$ are shaded in blue and red, respectively. This places some constraints on the set of parameters to choose from. By selecting a value of $(\delta/\lambda, J_1/\lambda) = (-3.5, -0.11)$, the low energy dispersions with a well separated higher crystal field excitation are captured. By keeping $(\delta/\lambda, J_1/\lambda)$ fixed, adjusting the value of λ will adjust the energy scale of the modelled dispersions. The parameters $\lambda = 7.8$ meV, $\delta = -27.2$ meV, and $J_1 = -0.86$ meV provide an accurate modelling of the low energy dispersions in addition to a g-factor of 2.8 and a ground state magnetic moment of magnitude 4.75 μ_B.

5.4 Easy-Axis Spin Wave Models for Magnons

This section will present a model of the low energy spinwave excitations of the ordered magnetic structure including additional further neighbour exchange couplings and Dzyaloshinskii-Moriya interactions. A single-ion anisotropy term may be used in order to capture the effects of the single-ion Hamiltonian that stabilise an easy-axis ground state. The LSWT model treated in chapter 4 for the case of easy-plane ordering can be generalised to model spinwave dispersions and inelastic neutron scattering intensities for easy-axis ordered moments - in the zero, intermediate, and high field limits. This will be performed on $S = 2$ spins, and linear spinwave theory will allow single spin-flip excitations to be modelled.

5.4.1 Spin Wave Model in Zero Field

The presence of a gap between the elastic line and the lowest energy magnon mode in the zero field inelastic neutron scattering data, see figure 5.5a and e, indicates an easy-axis anisotropy which can be parametrised in the form of a Heisenberg exchange model with single ion anisotropy of the form $-D\left(\hat{S}^z\right)^2$, for $D > 0$. This model has a direct spin-flip transition to a polarised phase if D is sufficiently strong. This phase diagram will be discussed in detail in section 5.4.3.

Following the treatment of an easy-plane ordered magnet with XXZ exchange couplings in section 4.4, the exchange Hamiltonian for nearest neighbour Heisenberg exchange couplings (up to sixth nearest neighbour) with single-ion anisotropy can be written as

$$\hat{H}_n = \sum_n \sum_{\langle i,j \rangle_n} J_n \hat{\mathbf{S}}_i \cdot \hat{\mathbf{S}}_j - \sum_i D\left(\hat{S}_i^z\right)^2, \tag{5.20}$$

where the same conventions as in equation 4.10 have been used: the sum is over all n^{th} nearest neighbour bonds between Fe^{2+} sites i and j where each bond is counted once and only once. Heisenberg exchanges are recovered in the limit where $J_n^{\perp} = J_n^z = J_n$. Ferromagnetic exchange couplings along the nth nearest neighbour bonds have $J_n < 0$, conversely antiferromagnetic exchange couplings have $J_n > 0$. In this case, it is assumed that the J_1 exchange interaction is dominant and negative so that the honeycomb layers have ferromagnetically

coupled spins, and the J_2 interaction is positive so that the honeycomb layers stack antiferromagnetically. The single-ion anisotropy term D is taken to be positive such that the ground state $S_i^z = \pm 2$ is stabilised. A Heisenberg exchange model with single ion anisotropy is presented here rather than an XXZ exchange model since the two models turn out to provide similar expressions for the dispersions and INS intensities of the magnon modes, and both stabilise a first-order spin flip transition between the antiferromagnetic phase and a spin-polarised phase. The Heisenberg exchange model with single-ion anisotropy has five fewer parameters than the XXZ exchange model, and the additional XXZ exchange parameters cannot be uniquely fitted to the INS data. Between the parameters sets of the two models, a mapping can be constructed that preserves the dispersions and dynamical correlations of the magnon modes, and so the INS results are insensitive to the two models.

The Hamiltonian in equation 5.20 is defined in the global frame denoted by **xyz** such that **x** is parallel to the hexagonal **a** axis, **z** is parallel to the hexagonal **c** axis, and $\mathbf{y} = \mathbf{z} \times \mathbf{x}$ is chosen such that the **xyz** frame is right-handed. A second frame, defined locally to each magnetic sublattice - denoted by $\tilde{\mathbf{x}}\tilde{\mathbf{y}}\tilde{\mathbf{z}}$ - can be defined such that the $\tilde{\mathbf{x}}$ axis is parallel to the hexagonal **a** axis, and the frame will rotate about $\tilde{\mathbf{x}}$ such that the $\tilde{\mathbf{z}}$ axis is along the moment direction on each magnetic sublattice. The global and local frames satisfy the following relationship:

$$\begin{aligned} \mathbf{x} &= \tilde{\mathbf{x}}, \\ \mathbf{y} &= \cos(m\pi)\tilde{\mathbf{y}} + \sin(m\pi)\tilde{\mathbf{z}}, \\ \mathbf{z} &= -\sin(m\pi)\tilde{\mathbf{y}} + \cos(m\pi)\tilde{\mathbf{z}}, \end{aligned} \tag{5.21}$$

where $m = 0$ is taken for the A and B sublattices, $m = 1$ is taken for the C and D sublattices. The A, B, C, D sublattices are as defined for $CoTiO_3$ in figure 4.1d. Since the $\sin(m\pi)$ terms cancel for any integer m, the $\tilde{\mathbf{y}}$ and $\tilde{\mathbf{z}}$ axes simply reverse direction between alternate honeycomb layers. $FeTiO_3$ is isostructural to and shares the same bond geometry to $CoTiO_3$, shown in figure 4.1d. The odd numbered exchange couplings J_1, J_3, and J_5 couple magnetic moments on the same honeycomb layer, whereas the even numbered

exchange couplings J_2, J_4, and J_6 couple magnetic moments on adjacent honeycomb layers. Therefore, the odd and even n terms of the exchange Hamiltonian for the nth nearest neighbour couplings can be written in the local frame as

$$\begin{aligned}\hat{H}_{\text{odd}} &= J_n \sum_{\langle i,j\rangle_n} \hat{S}_i^{\tilde{x}}\hat{S}_j^{\tilde{x}} + \hat{S}_i^{\tilde{y}}\hat{S}_j^{\tilde{y}} + \hat{S}_i^{\tilde{z}}\hat{S}_j^{\tilde{z}}, \\ \hat{H}_{\text{even}} &= J_n \sum_{\langle i,j\rangle_n} \hat{S}_i^{\tilde{x}}\hat{S}_j^{\tilde{x}} - \hat{S}_i^{\tilde{y}}\hat{S}_j^{\tilde{y}} - \hat{S}_i^{\tilde{z}}\hat{S}_j^{\tilde{z}}.\end{aligned} \tag{5.22}$$

Once again, writing the Hamiltonian in terms of a local frame has made all moments parallel and reduced the problem to two sublattices - denoted by $\tilde{A}$ and $\tilde{B}$. The A and C sublattices in the global frame will map to the $\tilde{A}$ sublattice, and the B and D sublattices in the global frame will map to the $\tilde{B}$ sublattice. Using the Holstein-Primakoff transformation in equation 4.12 and the Fourier transformation in equation 4.13 allows the terms of the exchange Hamiltonian up to sixth nearest neighbour in equation 5.20 to be expanded to quadratic order in raising and lowering operators. This Hamiltonian will take the form of equation 4.15 where the dynamical matrix $\mathcal{D}(\mathbf{k})$ takes the form

$$\mathcal{D}(\mathbf{k}) = \begin{pmatrix} A & B & C & D^* \\ B^* & A & D & C \\ C^* & D^* & A & B \\ D & C^* & B^* & A \end{pmatrix}, \tag{5.23}$$

and the matrix elements are given by

$$\begin{aligned} A &= \left[-3J_1 + J_2 - 6J_3 + J_3\gamma_{3\mathbf{k}} + 6J_4 - 3J_5 + 3J_6 + 2D\right] S, \\ B &= \left[J_1\gamma_{1\mathbf{k}} + J_5\gamma_{5\mathbf{k}}\right] S, \\ C &= J_4\gamma_{4\mathbf{k}} S, \\ D &= \left[J_2\gamma^*_{2\mathbf{k}} + J_6\gamma^*_{6\mathbf{k}}\right] S. \end{aligned} \tag{5.24}$$

The $\gamma_{n\mathbf{k}}$ terms are given by equation 4.18, and the same bond geometry listed in equation 4.19 can be used with the buckling parameter given by $\epsilon = 2\left(z_{Fe} - 1/3\right)$. Now the dynamical matrix elements have been determined, the dispersions and intensities can be found by the same procedure as for the easy-plane magnons in section 4.4. First, the dispersions are calculated in the absence of buckling - i.e. for $\epsilon = 0$. In this case, the local frame defined in equation 5.21 is equivalent to the rotating frame - denoted by $x'y'z'$ - defined by

$$\begin{aligned} \mathbf{x} &= \mathbf{x}', \\ \mathbf{y} &= \cos(\mathbf{Q}\cdot\mathbf{r})\mathbf{y}' + \sin(\mathbf{Q}\cdot\mathbf{r})\mathbf{z}', \\ \mathbf{z} &= -\sin(\mathbf{Q}\cdot\mathbf{r})\mathbf{y}' + \cos(\mathbf{Q}\cdot\mathbf{r})\mathbf{z}', \end{aligned} \tag{5.25}$$

where $\mathbf{Q} = 3\pi/c\hat{\mathbf{z}}$ is the magnetic ordering wavevector, and $\mathbf{r}$ is the position of a Fe^{2+} ion. The four modes for the unbuckled lattice are $\omega_+(\mathbf{k})$, $\omega_-(\mathbf{k})$, $\omega_+(\mathbf{k}+\mathbf{Q})$, $\omega_-(\mathbf{k}+\mathbf{Q})$ where $\omega_\pm(\mathbf{k})$ are obtained by diagonalising the matrix $g\mathcal{D}$ as

$$\begin{aligned} \omega^2_\pm(\mathbf{k}) = A^2 + |B|^2 - |C|^2 - |D|^2 \pm \\ \sqrt{(2AB - CD^* - C^*D^*)(2AB^* - CD - C^*D) + (BD - B^*D^*)^2}. \end{aligned} \tag{5.26}$$

Since $\mathbf{Q}$ is half of a reciprocal lattice vector, $\mathbf{k}+\mathbf{Q}$ is equivalent to $\mathbf{k}-\mathbf{Q}$ up to a translation of the Brillouin zone, giving four - rather than six - modes. Although the unbuckled lattice has four magnon modes, these come in doubly degenerate pairs. The dynamical matrix elements satisfy the following properties

$$\begin{aligned} A_0(\mathbf{k}) &= A_0(\mathbf{k}+\mathbf{Q}), \\ B_0(\mathbf{k}) &= B_0(\mathbf{k}+\mathbf{Q}), \\ C_0(\mathbf{k}) &= -C_0(\mathbf{k}+\mathbf{Q}), \\ D_0(\mathbf{k}) &= -D_0(\mathbf{k}+\mathbf{Q}), \end{aligned} \tag{5.27}$$

where the subscript 0 denotes the dynamical matrix element evaluated for $\epsilon = 0$. Consequently, the dispersions satisfy $\omega_{\pm}(\mathbf{k}) = \omega_{\pm}(\mathbf{k}+\mathbf{Q})$ and the modes are doubly degenerate. Furthermore, the A and C dynamical matrix elements are invariant under buckling, whereas the effect of buckling upon the B and D dynamical matrix elements are $B = B_0 e^{2\pi i \epsilon L}$ and $D = D_0 e^{-2\pi i \epsilon L}$. The buckling parameter will enter the $|B|^2$, $|D|^2$, BD, and B^*D^* terms of the dispersion relation in equation 5.26 and hence the dispersion relations are independent of buckling, however as shown below, the intensities are sensitive to buckling.

In the local frame, the dynamical correlators are obtained as:

$$\begin{aligned} S^{\tilde{x}\tilde{x}}(\mathbf{k},\omega) &= \frac{S}{4N} \left|W + X + Y + Z\right|^2 \times \left[\delta(\omega - \omega_-(\mathbf{k})) + \delta(\omega - \omega_+(\mathbf{k}))\right], \\ S^{\tilde{y}\tilde{y}}(\mathbf{k},\omega) &= \frac{S}{4N} \left|W - X + Y - Z\right|^2 \times \left[\delta(\omega - \omega_-(\mathbf{k})) + \delta(\omega - \omega_+(\mathbf{k}))\right]. \end{aligned} \tag{5.28}$$

where W, X, Y, and Z are given by the eigenvectors of $g\mathcal{D}$, and take the form as defined in equation 4.25. In the rotating frame, for $\epsilon = 0$, the dynamical correlators are given by

$$\begin{aligned} S_0^{x'x'}(\mathbf{k},\omega) &= \frac{S}{4N} \left|W_0 + X_0 + Y_0 + Z_0\right|^2_{\mathbf{k}} \times \left[\delta(\omega - \omega_-(\mathbf{k})) + \delta(\omega - \omega_+(\mathbf{k}))\right], \\ S_0^{y'y'}(\mathbf{k},\omega) &= \frac{S}{4N} \left|W_0 - X_0 + Y_0 - Z_0\right|^2_{\mathbf{k}+\mathbf{Q}} \times \left[\delta(\omega - \omega_-(\mathbf{k}+\mathbf{Q})) + \delta(\omega - \omega_+(\mathbf{k}+\mathbf{Q}))\right], \end{aligned} \tag{5.29}$$

where once again the subscript 0 denotes the correlator or eigenvector component evaluated for $\epsilon = 0$. $\mathcal{N}$ is a normalisation factor given by

$$\mathcal{N}(\omega) = \left| |W|^2 - |X|^2 + |Y|^2 - |Z|^2 \right|.$$

The components of the eigenvectors satisfy the following properties

$$\begin{aligned} W_0(\mathbf{k}) &= W_0(\mathbf{k}+\mathbf{Q}), \\ X_0(\mathbf{k}) &= -X_0(\mathbf{k}+\mathbf{Q}), \\ Y_0(\mathbf{k}) &= Y_0(\mathbf{k}+\mathbf{Q}), \\ Z_0(\mathbf{k}) &= -Z_0(\mathbf{k}+\mathbf{Q}), \end{aligned} \tag{5.30}$$

and consequently the two correlation functions are equal $S_0^{xx} = S_0^{yy}$ as expected by symmetry. Upon reintroducing buckling, the correlation functions are given by

$$\begin{aligned} S^{xx}(\mathbf{k},\omega) = S^{yy}(\mathbf{k},\omega) = \frac{S}{4N} \left| W_0 + X_0 + (Y_0 + Z_0)e^{-2\pi i \epsilon L} \right|_{\mathbf{k}}^2 \times \\ \left[\delta(\omega - \omega_-(\mathbf{k})) + \delta(\omega - \omega_+(\mathbf{k}))\right]. \end{aligned} \tag{5.31}$$

As noted for the magnon dispersions in $CoTiO_3$, the phase factors of $e^{-2\pi i \epsilon L}$ due to buckling of the honeycomb layers introduces an intensity modulation due to interference scattering with a long $1/\epsilon$ period in L. This will have an effect on the intensity profile in the vicinity of the K points - as detailed subsequently in section 5.5. The magnon dispersions and intensities for the zero field data can be calculated using these expressions, these analytical expressions have been tested against numerical models using SpinW [19] and code modelling generic multi-sublattice collinear antiferromagnets [20]. As shown in figure 5.10, the in-plane magnon dispersions are captured well using a Heisenberg first nearest neighbour coupling $J_1 = -0.833$ meV and an easy-axis single ion anisotropy $D = 1.360$ meV. This minimal model can be compared to the experimental data, and has a number of shortcomings in explaining all features. Due to the easy-axis ordering, there are two pairs of doubly degenerate modes which reproduce two branches of the observed magnon dispersions. The modelled magnon dispersions also have a crossing point at the K points, whereas these

modes show clear avoided crossings at such points in the experimental data. Furthermore, there is also a small amount of scattering intensity between $0-4$ meV and $8-10$ meV observed above the magnetic Bragg peak positions in the experimental data that are not reproduced.

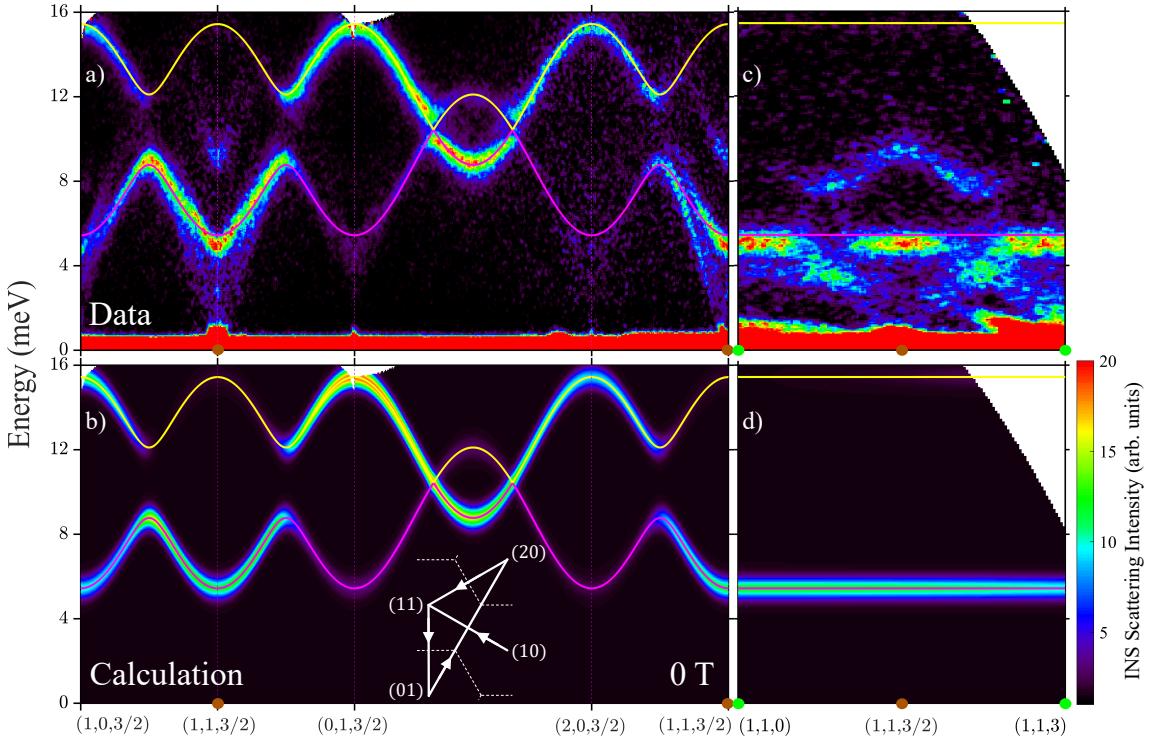

Figure 5.10: a, c) Slice taken through the zero field INS data in $FeTiO_3$ with modelled dispersions from a Heisenberg exchange model with an easy-axis single ion anisotropy overplotted with magenta and yellow curves. The exchange parameters to fit the dispersions are $J_1 = -0.833$ meV and $D = 1.360$ meV. b, d) The same slices as in a) and c) obtained by calculating the INS intensity in the exchange model for each pixel in the data slice. The slices through the INS data are in the hk plane for a) and b), and along the out-of-plane direction, L, for c) and d). The in-plane path through reciprocal space is shown in the inset to b). Structural/antiferromagnetic Bragg peak positions are indicated by green/brown circles on the elastic line.

One of the limitations of the model including single-ion anisotropy with Heisenberg exchange interactions between moments can be overcome, namely a gap can be opened between the optical and acoustic magnons at the K point, via the introduction of a Dzyaloshinskii-Moriya (DM) interaction on the third nearest neighbour bonds. Of the third nearest neighbour bonds in equation 4.19, three bonds connect sites within the $\tilde{A}$ sublattice: $\mathbf{a}$, $\mathbf{b}$, and $\mathbf{a}+\mathbf{b}$ - these are denoted by $\boldsymbol{\delta}_{3A}$; three bonds connect sites within the $\tilde{B}$ sublattice: $-\mathbf{a}$,

$-\mathbf{b}$, and $-\mathbf{a}-\mathbf{b}$ - these are denoted by $\boldsymbol{\delta}_{3B}$. The Hamiltonian corresponding to the DM interaction between sites labelled i and j is given by

$$\hat{H}_{D(i,j)} = \mathbf{D}_3 \cdot \left(\hat{\mathbf{S}}_i \times \hat{\mathbf{S}}_j\right). \tag{5.32}$$

Where $\mathbf{D}_3$ denotes the DM vector on the third nearest neighbour bond. Since the midpoint of this bond has a mirror plane perpendicular to the bond direction, this interaction is symmetry allowed for a DM vector along the $\hat{\mathbf{z}}$ axis, given by $\mathbf{D}_3 = D\hat{\mathbf{z}}$, in which case the Hamiltonian corresponding to DM interactions is given by

$$\hat{H}_D = D_3^z \sum_{\langle i,j\rangle_3} \left(\hat{S}_i^x \hat{S}_j^y - \hat{S}_i^y \hat{S}_j^x\right), \tag{5.33}$$

the sum $\langle i,j\rangle_3$ is over the third nearest neighbour bonds such that each bond is only counted once. This Hamiltonian can be written in terms of the local frame defined in equation 5.21 by decomposing into a sum over the $\tilde{A}$ and $\tilde{B}$ sublattices [21–24]

$$\hat{H}_D = D_3^z \sum_{i\in\tilde{A}} \sum_{\boldsymbol{\delta}\in\boldsymbol{\delta}_{3A}} \left(\hat{S}_i^{\tilde{A}\tilde{x}} \hat{S}_{i+\boldsymbol{\delta}}^{\tilde{A}\tilde{y}} - \hat{S}_i^{\tilde{A}\tilde{y}} \hat{S}_{i+\boldsymbol{\delta}}^{\tilde{A}\tilde{x}}\right) + D_3^z \sum_{i\in\tilde{B}} \sum_{\boldsymbol{\delta}\in\boldsymbol{\delta}_{3B}} \left(\hat{S}_i^{\tilde{B}\tilde{x}} \hat{S}_{i+\boldsymbol{\delta}}^{\tilde{B}\tilde{y}} - \hat{S}_i^{\tilde{B}\tilde{y}} \hat{S}_{i+\boldsymbol{\delta}}^{\tilde{B}\tilde{x}}\right). \tag{5.34}$$

Once again, the Holstein-Primakoff and Fourier transformations in equations 4.12 and 4.13 can be applied to find the bilinear term in boson operators. The Hamiltonian in equation 5.33 can be written in the form

$$\hat{H}_D = D_3^z S \sum_{\mathbf{k}} \Gamma_{3\mathbf{k}} \left(\hat{a}_{\mathbf{k}}^\dagger \hat{a}_{\mathbf{k}} - \hat{b}_{\mathbf{k}}^\dagger \hat{b}_{\mathbf{k}}\right), \tag{5.35}$$

where the term $\Gamma_{3\mathbf{k}}$ is defined by

$$\Gamma_{3\mathbf{k}} = 2 \sum_{\boldsymbol{\delta}\in\boldsymbol{\delta}_{3A}} \sin \mathbf{k}\cdot\boldsymbol{\delta}. \tag{5.36}$$

The DM interaction will then adjust the dynamical matrix in equation 5.23 to be of the form

$$\mathcal{D}(\mathbf{k}) = \begin{pmatrix} A+E & B & C & D^* \\ B^* & A-E & D & C \\ C^* & D^* & A+E & B \\ D & C^* & B^* & A-E \end{pmatrix}, \tag{5.37}$$

where the matrix element E is given by

$$E = D_3^z S\Gamma_{3\mathbf{k}}. \tag{5.38}$$

The eigenvalues of $g\mathcal{D}$ are $+\omega_\pm$ and $-\omega_\pm$ where

$$\begin{aligned}\omega_\pm^2(\mathbf{k}) = A^2 + |B|^2 - |C|^2 - |D|^2 + E^2 \pm \\ \sqrt{(2AB - CD^* - C^*D^*)(2AB^* - CD - C^*D) + (BD - B^*D^*)^2 + 4(A^2 - |D|^2)E^2},\end{aligned} \tag{5.39}$$

and the eigenvectors of $g\mathcal{D}$ have components

$$\begin{aligned} W(\omega) =& -(A+E+\omega)\left[(A-E)^2 + |B|^2 - |C|^2 - |D|^2 - \omega^2\right] \\ &+ 2A|B|^2 - 2|D|^2E - BDC^* - B^*D^*C, \\ X(\omega) =& \left[(A-E)^2C^* + |B|^2C^* - |C|^2C^* + |D|^2C - C^*\omega^2\right] \\ &- (A-E)(BD + B^*D^*) + \omega(BD - B^*D^*), \\ Y(\omega) =& B^*\left[(A+\omega)^2 - |B|^2 + |C|^2 - E^2\right] \\ &- (A+\omega)(C+C^*)D + BD^2 - (C-C^*)DE, \\ Z(\omega) =& D\left[A^2 + C^{*2} - |D|^2 - (E+\omega)^2\right] + B^{*2}D^* - 2AB^*C^*. \end{aligned} \tag{5.40}$$

These expressions can be substituted into equation 5.31 to obtain the dispersion and INS intensity of the magnon modes for ordered moments interacting through Heisenberg exchange

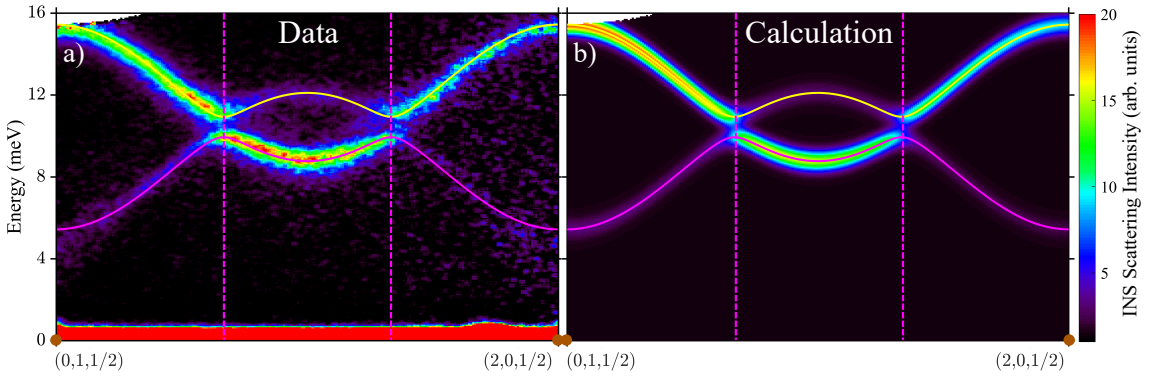

Figure 5.11: a) Slice taken through K points in zero field INS data in $FeTiO_3$ compared to b) modelled dispersions from a model including Heisenberg exchange, single-ion easy-axis anisotropy, and a Dzyaloshinskii–Moriya interaction. The exchange parameters used to fit the dispersions are the same as those used for figure 5.10, with an additional DM interaction parametrised by $|D_3^z| = 0.054$ meV. Magnetic Bragg peak positions are indicated by brown circles on the elastic line, and dashed magenta lines denote the positions of the high-symmetry K points.

with an easy-axis single-ion anisotropy, and DM interaction between third nearest neighbours along $\hat{\mathbf{z}}$. Simulating a slice through the K points - denoted by the dashed magenta lines in figure 5.11 - shows that the avoided crossing at the K points, denoted by dashed vertical magenta lines, is captured. The gap at the K point is given by $\omega_+(\mathbf{K}) - \omega_-(\mathbf{K}) = 3\sqrt{3}|D_3^z|S$. Consequently the sign of the DM vector cannot be determined, only the magnitude.

In order to check that the intensity modulation due to buckling and the corrections to the dispersion and scattering intensity of the magnon modes are implemented correctly, the dispersions and dynamical correlations computed via the analytic expressions are compared to those calculated using the same parameters in SpinW [19]. These quantities are plotted in figure 5.12, and show that the analytic expressions have been derived and implemented correctly.

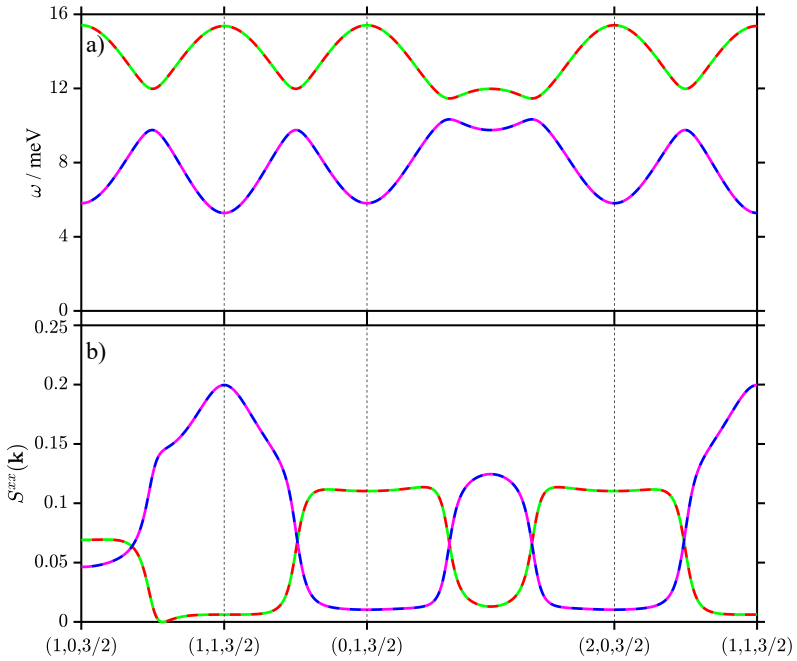

Figure 5.12: Comparison of a) dispersions and b) dynamical correlations of the analytical expressions from the Heisenberg exchange model, including an easy-axis single-ion anisotropy, and a Dzyaloshinskii–Moriya on an easy-axis ordered, buckled honeycomb lattice (plotted with green and magenta dashed lines) with the numerical values calculated from a SpinW model (plotted with red and blue dashed lines).

5.4.2 Spin Wave Model in Intermediate Field

Now consider the ABC stacked honeycomb lattice where an external magnetic field has been applied along the hexagonal **c** axis, but is not strong enough to polarise the magnetic structure. Here, the magnetic ground state of the system will remain antiferromagnetic with spins aligned alternately parallel and antiparallel to the hexagonal **c** axis between adjacent layers. The Hamiltonian for the interaction of the magnetic moments of each lattice site with the external magnetic field of strength B is given by

$$\hat{H}_{\text{ext}} = -g\mu_B B \sum_i \hat{S}_i^z. \tag{5.41}$$

This Zeeman Hamiltonian for an externally applied magnetic field will not mix the eigenstates of the exchange Hamiltonian, but only shift their energies. Consequently, each degenerate magnon mode ω_I will be split into two distinct modes $\omega_I + g\mu_B B$ and $\omega_I - g\mu_B B$, and with each of the split modes having the same dynamical correlations as in zero field.

An intermediate field model can be constructed from the zero field model by adding only an additional parameter - g - denoting the energy splitting of the magnon modes upon applying an external magnetic field. In order to obtain the correct splitting for the experimental values of the applied magnetic field, a cut in energy through the $(\frac{1}{2}, 1, 0)$ position can be taken through the zero field data set and both intermediate field data sets, and each peak fitted with a Lorentzian lineshape.

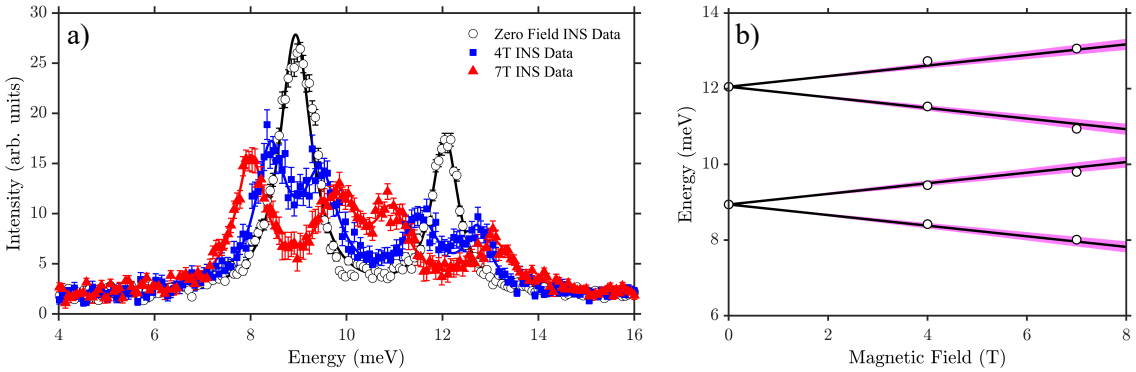

Figure 5.13: a) Cut through the $(\frac{1}{2}, 1, 0)$ position taken through the zero field (open circles), 4 T (blue squares), and 7 T (red triangles) data sets to show the splitting of the magnon modes under an applied magnetic field. Each cut is fitted with two - for the zero field cut - or four - for the 4 T and 7 T cuts - Lorentzian peaks (denoted by solid lines). b) Plotting the energies of the fitted peaks (open circles) shows a linear dependence of the splitting on the applied magnetic field. The error bars are smaller than the size of the symbols. Upon applying an external magnetic field B, the peaks shift by $\pm g\mu_B B$ where $g = 2.42 \pm 0.32$. The black lines are fits of the form $E = E_0 \pm g\mu_B B$, and the magenta shaded regions denote the range of values of energy splitting if g were to vary within ± 0.32.

As shown in figure 5.13a, the cut through the zero field data has two peaks: one at 8.94(1) meV and another at 12.05(1) meV. In the dataset with an externally applied field of 4 T, the cut has four peaks at 8.42(2), 9.45(3), 11.53(3), and 12.73(3) meV. For an externally applied field of 7 T, the cut will again show four peaks at 8.01(1), 9.80(3), 10.94(3), and 13.06(2). Each of the 7 T peaks has shifted by 0.98 ± 0.13 meV compared to 0 T, so the g-factor can be estimated as 2.42 ± 0.32 - shown by the solid lines in figure 5.13b.

In order to check the consistency of the zero field model parameters to the intermediate field data, dispersion points were fitted to the observed modes in the 7 T data and compared to the calculated dispersions in the model. By simultaneously fitting the single-ion anisotropy, first nearest neighbour Heisenberg exchange, DM interaction strength, and the

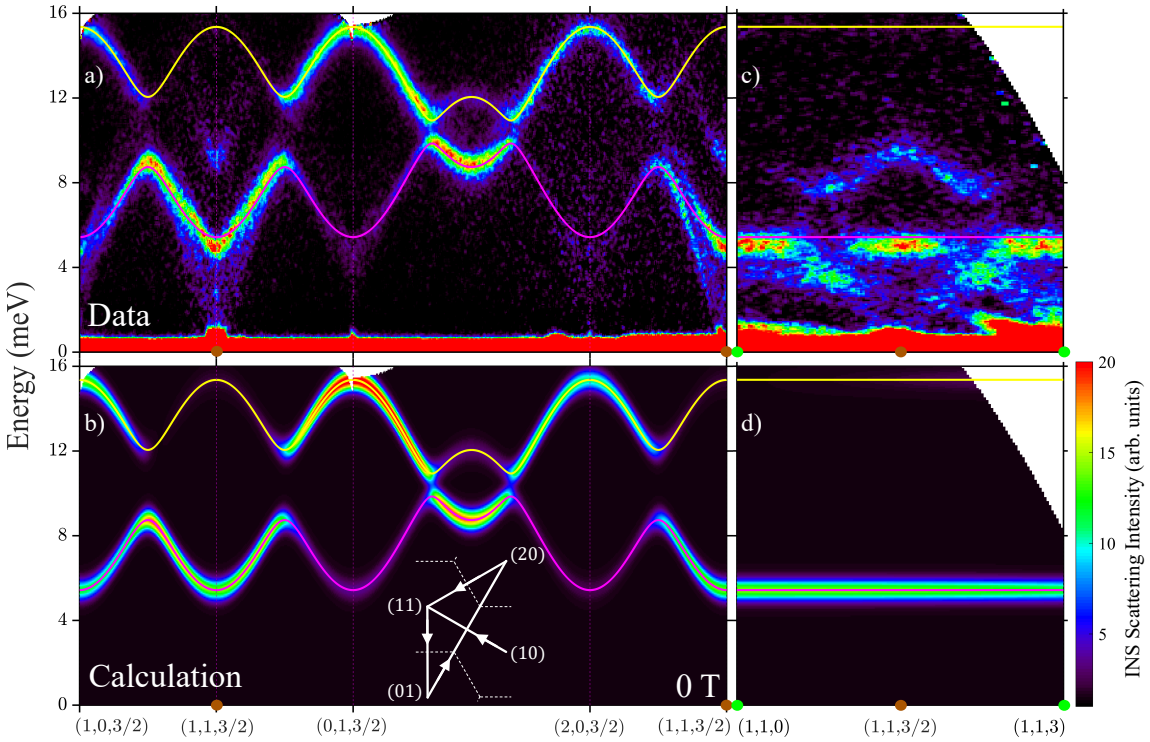

Figure 5.14: INS data comparing the a,c) observed zero field magnon dispersions against b,d) dispersions of the model including Heisenberg exchange, single-ion easy-axis anisotropy, and a Dzyaloshinskii–Moriya interaction. The modelled dispersions - with fitted parameters $J_1 = -0.827$ meV, $D = 1.358$ meV, and $D_3^z = 0.054$ meV - are plotted over each figure in magenta and yellow curves. Structural/antiferromagnetic Bragg peaks are denoted by green/brown circles on the elastic line, at zero energy transfer.

g factor parameters to the zero field and intermediate field data sets, calculations can be made of the zero field data set (shown in figure 5.14), and both intermediate field data sets for externally applied fields of 4 T and 7 T (shown in figure 5.15 and 5.16, respectively) using the same set of parameters - $J_1 = -0.827$ meV, $D = 1.358$ meV, $D_3^z = 0.054$ meV, and $g = 2.549$.

This intermediate field model can reproduce the gapped modes at the K points via a Dzyaloshinskii-Moriya interaction on the third nearest neighbour bond, and has allowed the splitting of the magnon modes to be reproduced via the addition of a Zeeman term in applied field. However, similarly to the exchange model in zero field, there are also two additional signals observed above the magnetic Bragg peak positions in the experimental data that are not captured.

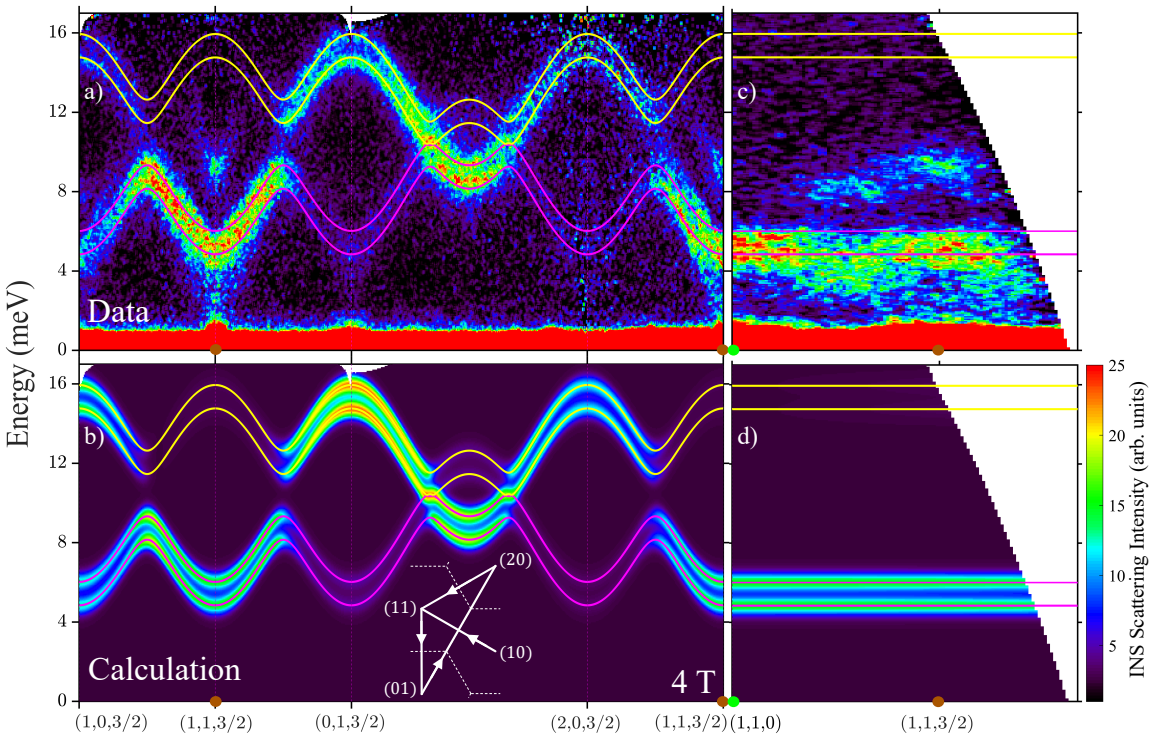

Figure 5.15: Same as figure 5.14, but for 4 T.

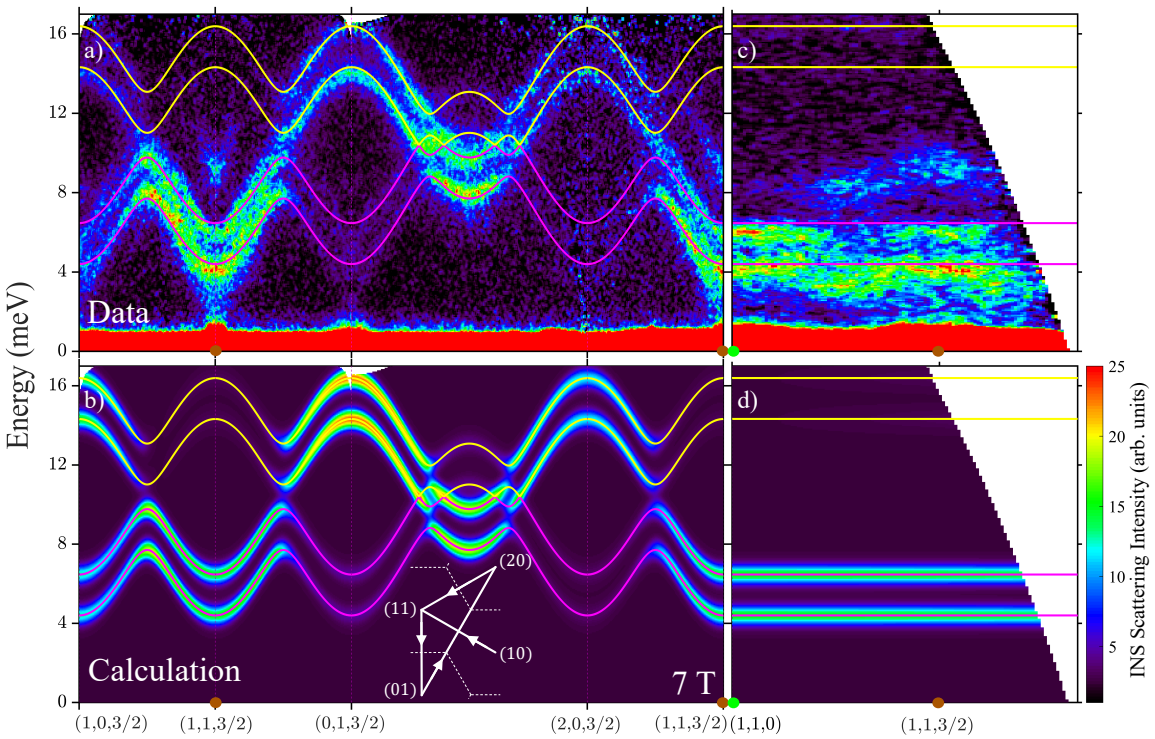

Figure 5.16: Same as figure 5.14, but for 7 T.

5.4.3 Spin Wave Model in the Polarised Phase

Finally consider the ABC stacked honeycomb lattice where the external field applied along the hexagonal **c** axis is sufficiently strong as to polarise the magnetic ground state such that all spins are aligned along the magnetic field direction. The model includes Heisenberg exchanges up to sixth nearest neighbour, a single ion anisotropy D, and a DM interaction $D_3^z\hat{\mathbf{z}}$ between third nearest neighbouring spins. The Hamiltonian describing this system is given by

$$\hat{H} = \sum_{n=1}^{6}\sum_{\langle i,j\rangle_n} J_n \hat{\mathbf{S}}_i \cdot \hat{\mathbf{S}}_j - \sum_i D\left(\hat{S}_i^z\right)^2 + D_3^z \sum_{\langle i,j\rangle_3}\left(\hat{S}_i^x\hat{S}_j^y - \hat{S}_i^y\hat{S}_j^x\right) - g\mu_B B\sum_i \hat{S}_i^z, \quad (5.42)$$

where B is the magnitude of the applied magnetic field along **c**. Competition between easy-axis single ion anisotropy, interlayer Heisenberg exchange, and the external magnetic field can stabilise different magnetic phases. Assuming that the J_1 Heisenberg interaction is larger than the other Heisenberg exchanges so that the spins in a single honeycomb layer are ferromagnetically aligned, three distinct magnetic phases can be considered. The antiferromagnetic phase, with spins aligned alternately parallel and antiparallel to the hexagonal **c** axis between adjacent layers; the polarised phase, with spins aligned along the direction of the external magnetic field; and a spin-flop phase where the spins in each honeycomb layer are ferromagnetically aligned and subtend an angle θ alternately clockwise and anticlockwise from the hexagonal **c** axis between adjacent layers. The ground state energy of each state is given by

$$\begin{aligned}
E_{\mathrm{AFM}}/\left(NS^2\right) &= \frac{1}{2}\left(3J_1 + 6J_3 + 3J_5\right) - \frac{1}{2}\left(J_2 + 6J_4 + 3J_6\right) - D,\\
E_{\mathrm{Pol.}}/\left(NS^2\right) &= \frac{1}{2}\left(3J_1 + 6J_3 + 3J_5\right) + \frac{1}{2}\left(J_2 + 6J_4 + 3J_6\right) - D - g\mu_B B/S,\\
E_{\mathrm{SF}}/\left(NS^2\right) &= \frac{1}{2}\left(3J_1 + 6J_3 + 3J_5\right) + \frac{1}{2}\left(J_2 + 6J_4 + 3J_6\right)\cos 2\theta - D\cos^2\theta - g\mu_B B\cos\theta/S.
\end{aligned} \quad (5.43)$$

By defining the dimensionless parameters

$$x = \frac{D}{J_2 + 6J_4 + 3J_6},$$
$$y = \frac{g\mu_B B}{(J_2 + 6J_4 + 3J_6)S}, \tag{5.44}$$

a phase diagram showing the lowest energy magnetic ground state is plotted in figure 5.17. For $x > 1/2$, there is a first order phase transition at $y = 1$ between the antiferromagnetic phase and the spin-polarised phase, where the spectral gap has a minimum - but does not close - at the spin-flip transition; whereas for $x < 1/2$, there is a first order transition from the antiferromagnetic to the spin-flop phase, followed by a second order transition to the spin-polarised phase as y increases.

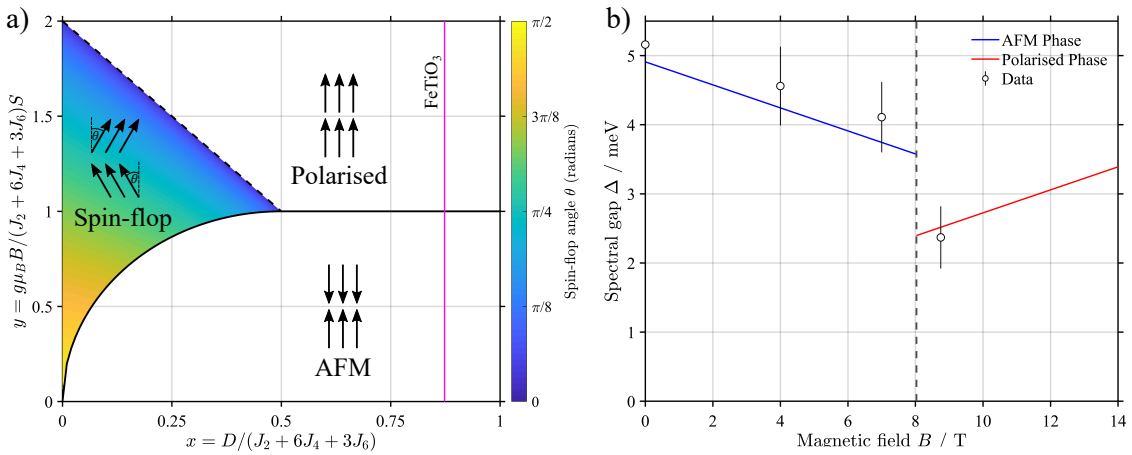

Figure 5.17: a) Phase diagram depicting antiferromagnetic, spin-flop, and polarised magnetic ground states that are stabilised by competition between single-ion anisotropy and the external magnetic field in the presence of interlayer Heisenberg exchange couplings. The solid black lines denote first-order transitions, whereas the dashed line denotes a second order transition. The shaded region depicts the spin-flop phase with the colour of the shading indicating the spin-flop angle θ from the hexagonal **c** axis. The magenta line denotes the value of x calculated from the fitted parameters in table 5.6.1, and indicates that applying a magnetic field along the hexagonal **c** axis drives a first order spin-flop transition from the antiferromagnetic phase to the polarised phase. b) Plot of the spectral gap at the $(1, 1, 3/2)$ position within the Heisenberg exchange model with single-ion anisotropy in the antiferromagnetic (blue line) and polarised (red line) phases. Data points (open circles) correspond to the centres of cuts taken through the $(1, 1, 3/2)$ position in the 0 T, 4 T, 7 T, and 8.75 T data sets. The grey dotted line at 8 T denotes the critical field for the spin-flip transition. Note that the spectral gap does not completely close at the transition field.

Since a first order transition between the antiferromagnetic and the polarised phase is

observed at $B_C = 8.03$ T, as shown by the jump in magnetisation in figure 5.2, it is necessary to include interlayer Heisenberg exchanges J_2, J_4, and J_6 subject to the following constraints

$$D > \frac{J_2 + 6J_4 + 3J_6}{2}, \tag{5.45}$$

$$B_C = \frac{(J_2 + 6J_4 + 3J_6)S}{g\mu_B} = 8.03 \text{ T}. \tag{5.46}$$

In the spin-polarised phase, the term proportional to B is the dominant term in the Hamiltonian and stabilises the magnetic ground state for spins along $\hat{\mathbf{z}}$. In this magnetic ground state, the primitive magnetic unit cell is the same as the primitive structural unit cell with only two magnetic sublattices, denoted by A and B. Since all spins are coaligned, the Holstein-Primakoff transformation can be performed in the global frame with

$$\begin{aligned}
\hat{S}_i^{Az} &= S - \hat{a}_i^\dagger \hat{a}_i, \\
\hat{S}_i^{Ax} &= \sqrt{S/2}(\hat{a}_i^\dagger + \hat{a}_i), \\
\hat{S}_i^{Ay} &= i\sqrt{S/2}(\hat{a}_i^\dagger - \hat{a}_i), \\
\hat{S}_i^{Bz} &= S - \hat{b}_i^\dagger \hat{b}_i, \\
\hat{S}_i^{Bx} &= \sqrt{S/2}(\hat{b}_i^\dagger + \hat{b}_i), \\
\hat{S}_i^{By} &= i\sqrt{S/2}(\hat{b}_i^\dagger - \hat{b}_i).
\end{aligned} \tag{5.47}$$

The Fourier transformation and commutation relations in equations 4.13 and 4.14 can be used to write the Hamiltonian in 5.42 as a bilinear term of the form

$$\hat{H} = \sum_{\mathbf{k}} \begin{pmatrix} \hat{a}_{\mathbf{k}}^\dagger & \hat{b}_{\mathbf{k}}^\dagger \end{pmatrix} \mathcal{D}(\mathbf{k}) \begin{pmatrix} \hat{a}_{\mathbf{k}} \\ \\ \hat{b}_{\mathbf{k}} \end{pmatrix}, \tag{5.48}$$

where the dynamical matrix $\mathcal{D}(\mathbf{k})$ is of the form

$$\mathcal{D}(\mathbf{k}) = \begin{pmatrix} A+E & B \\ B^* & A-E \end{pmatrix}, \tag{5.49}$$

where the matrix elements are given by

$$\begin{aligned} A &= \left[-3J_1 - J_2 - 6J_3 + J_3\gamma_{3\mathbf{k}} - 6J_4 + J_4\gamma_{4\mathbf{k}} - 3J_5 - 3J_6 + 2D\right] S + g\mu_B B, \\ B &= \left[J_1\gamma_{1\mathbf{k}} + J_2\gamma_{2\mathbf{k}} + J_5\gamma_{5\mathbf{k}} + J_6\gamma_{6\mathbf{k}}\right] S, \\ E &= D_3^z S\Gamma_{3\mathbf{k}}. \end{aligned} \tag{5.50}$$

The normalised eigenvectors of $\mathcal{D}(\mathbf{k})$ are

$$\begin{pmatrix} \bar{X}(\mathbf{k},\omega) \\ \bar{Y}(\mathbf{k},\omega) \end{pmatrix} \tag{5.51}$$

where $X(\mathbf{k},\omega) = \omega - A + E$, $Y(\mathbf{k},\omega) = B^*$, and these factors are normalised by $\bar{X} = X/\sqrt{\mathcal{N}}$ where $\mathcal{N} = |X|^2 + |Y|^2$. The eigenvalues are given by

$$\omega_\pm(\mathbf{k}) = A \pm \sqrt{|B|^2 + E^2}. \tag{5.52}$$

There are two non-degenerate magnon modes in this model with dispersions $\omega_\pm(\mathbf{k})$. The dynamical matrix element B vanishes at the K point, and so the gap at the K points is given by $2|E|$, the same as in zero field. The magnon dynamical structure factor is

$$S^{xx}(\mathbf{k},\omega) = S^{yy}(\mathbf{k},\omega) = \sum_{\eta=\pm} \frac{S}{4\mathcal{N}} |X+Y|^2_{\mathbf{k}}\, \delta(\omega - \omega_\eta(\mathbf{k})), \tag{5.53}$$

where the sum η is over the upper and lower magnon modes. The magnon dispersions and INS intensities for the high-field spin polarised phase where moments interact via Heisenberg exchange and DM interactions can be modelled using the expressions in equations 5.52 and 5.53 - as shown in figure 5.19. Dispersion points for 0 T, 7 T, and 8.75 T were simultaneously

fitted to the same Hamiltonian parameters with the agreement between data and calculation shown in figure 5.18d, and fitted parameters listed in table 5.6.1.

J_1	-0.806(3) meV	J_2	0.000(2) meV
J_3	-0.024(2) meV	J_4	0.045(3) meV
J_5	-0.024(3) meV	J_6	0.134(7) meV
D	0.938(9) meV	D_3^z	0.054(4) meV
g	2.876(38)		

Table 5.3: Fitted exchange parameters for the Heisenberg exchange model, with easy-axis single-ion anisotropy, a Dzyaloshinskii-Moriya interaction along the third nearest neighbour bond, and a Zeeman interaction.

For a given set of parameters for the models defined in this section, the energy of each mode can be calculated and compared to the empirical dispersion points. A χ^2 value can be assigned to a given parameter set by calculating $\sum_i (\omega_{\text{obs},i} - \omega_{\text{calc},i})^2$ where the sum is over all empirical dispersion points, $\omega_{\text{obs},i}$ denotes the energy of the ith fitted dispersion point, $\omega_{\text{calc},i}$ denotes the energy of the ith dispersion point calculated in the model. By minimising the value of χ^2 via steepest descent, the model parameters can be fitted to the zero field, intermediate field, and high field data sets simultaneously. The fitted dispersion points can be visualised by plotting them over a slice through the corresponding data set - as shown in figure 5.18a-c. All dispersion data points are first reduced to the first Brillouin zone and then copies of all points are made using the symmetry operations of the $\bar{3}m$ point group, then this set is translated in reciprocal space to all Brillouin zones, then are overplotted over these slices from data in reciprocal space in order to check the consistency of the agreement between the extracted experimental dispersion points and the data.

The fitting procedure kept the critical field B_C fixed to 8.03 T by fitting the parameters J_2, J_4, and g while adjusting the J_6 parameter according to equation 5.46. Since the J_4 and J_6 parameters - corresponding to Heisenberg exchange along the fourth and sixth nearest neighbour bonds, respectively - were included in the fit, it is reasonable to also include Heisenberg exchange parameters along the third and fifth nearest neighbour bonds, J_3 and J_5. Including these additional interactions captured the in-plane dispersions of

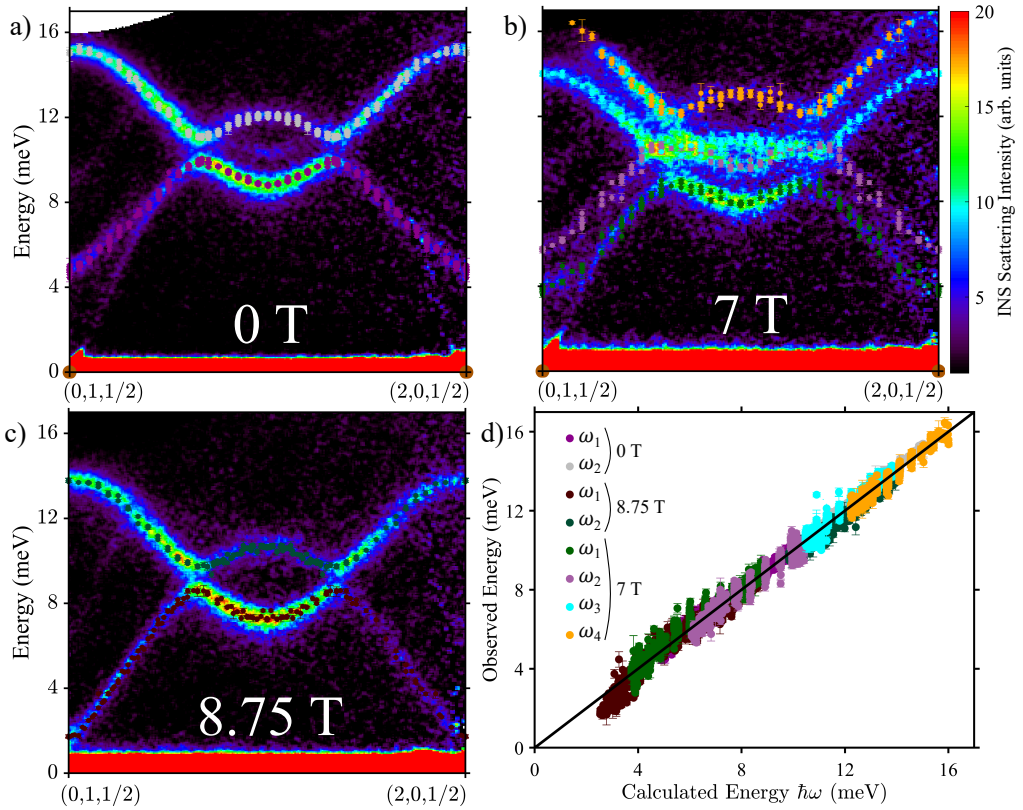

Figure 5.18: Slices through the 0 T (a), 7 T (b) and 8.75 T (c) INS data sets with dispersion points mapped from symmetry equivalent (hkl) values overplotted. Magnetic Bragg peak positions are denoted by brown circles on the elastic lines of a and b. d) Scatter plot showing the energy of over 7500 experimentally observed dispersion points for the 0 T, 8.75 T, and 7 T data sets plotted against their calculated values using the easy-axis ordered Heisenberg exchange model including an easy-axis single-ion anisotropy, a Dzyaloshinskii–Moriya interaction, and a Zeeman interaction with parameters in table 5.6.1. The black line is a 1 : 1 plot to show the agreement between the observed and modelled dispersions.

the magnon modes more accurately. The fitted value of D - 0.938 meV - exceeds the combination $(J_2+6J_4+3J_6)/2$ which takes a value of 0.537 meV calculated using the fitted parameters. Consequently, the inequality in equation 5.45 is satisfied and the magnetic phase transition between the antiferromagnetic and polarised phases is first order without going via a spin-flop phase, consistent with the magnetisation data presented in figure 5.2. The fitted parameter set has $J_2 = 0$. As shown subsequently in section 5.5, a non-zero J_2 coupling would lead to an in-plane shifting of the position of the magnon gap between the acoustic and optical magnons in the spin-polarised phase away from the two-dimensional K-points. However, as shown in figure 5.26b, there is no evidence for such a shift at the

K points in the high-field magnon dispersions. The magnon dispersions in 8.75 T, 7 T, 4 T, and zero field are calculated using parameter set in table 5.6.1 and plotted in figures 5.19-5.21 and compared to the INS data.

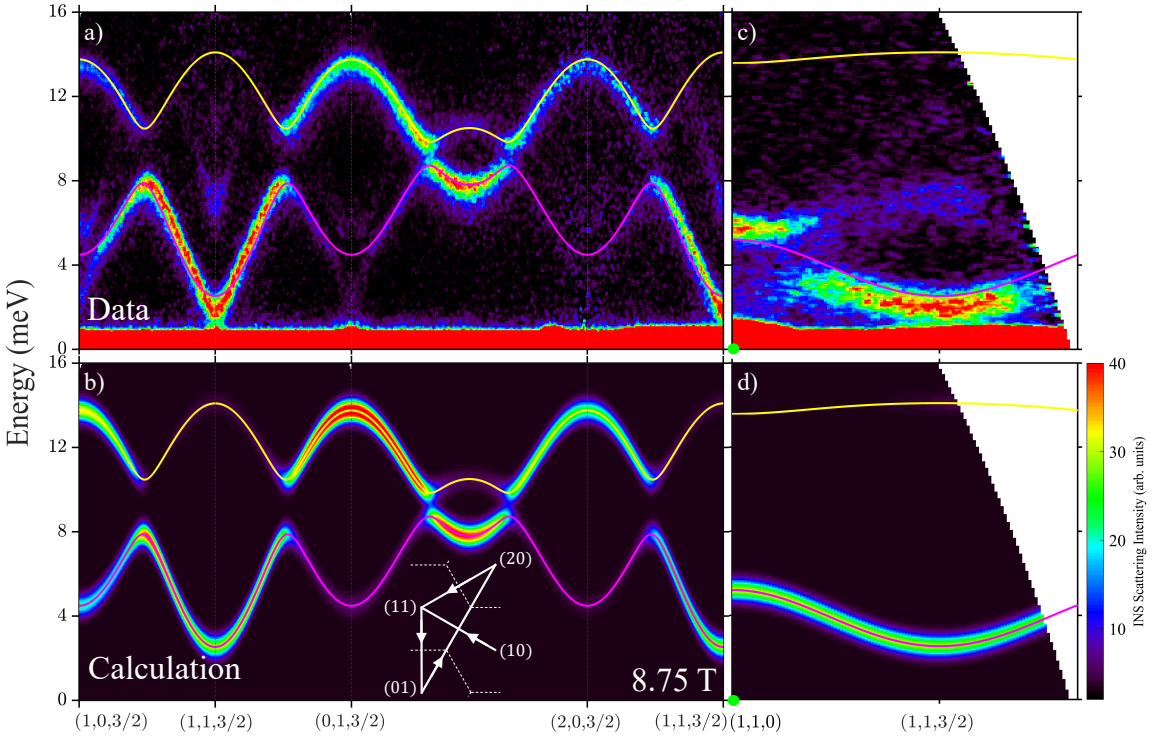

Figure 5.19: INS data comparing the a,c) observed 8.75 T magnon dispersions against b,d) dispersions of easy-axis ordered moments calculated using LSWT. The modelled dispersions - with parameters listed in table 5.6.1 - are plotted over each figure in magenta and yellow curves. Structural Bragg peaks are denoted by green circles on the elastic line.

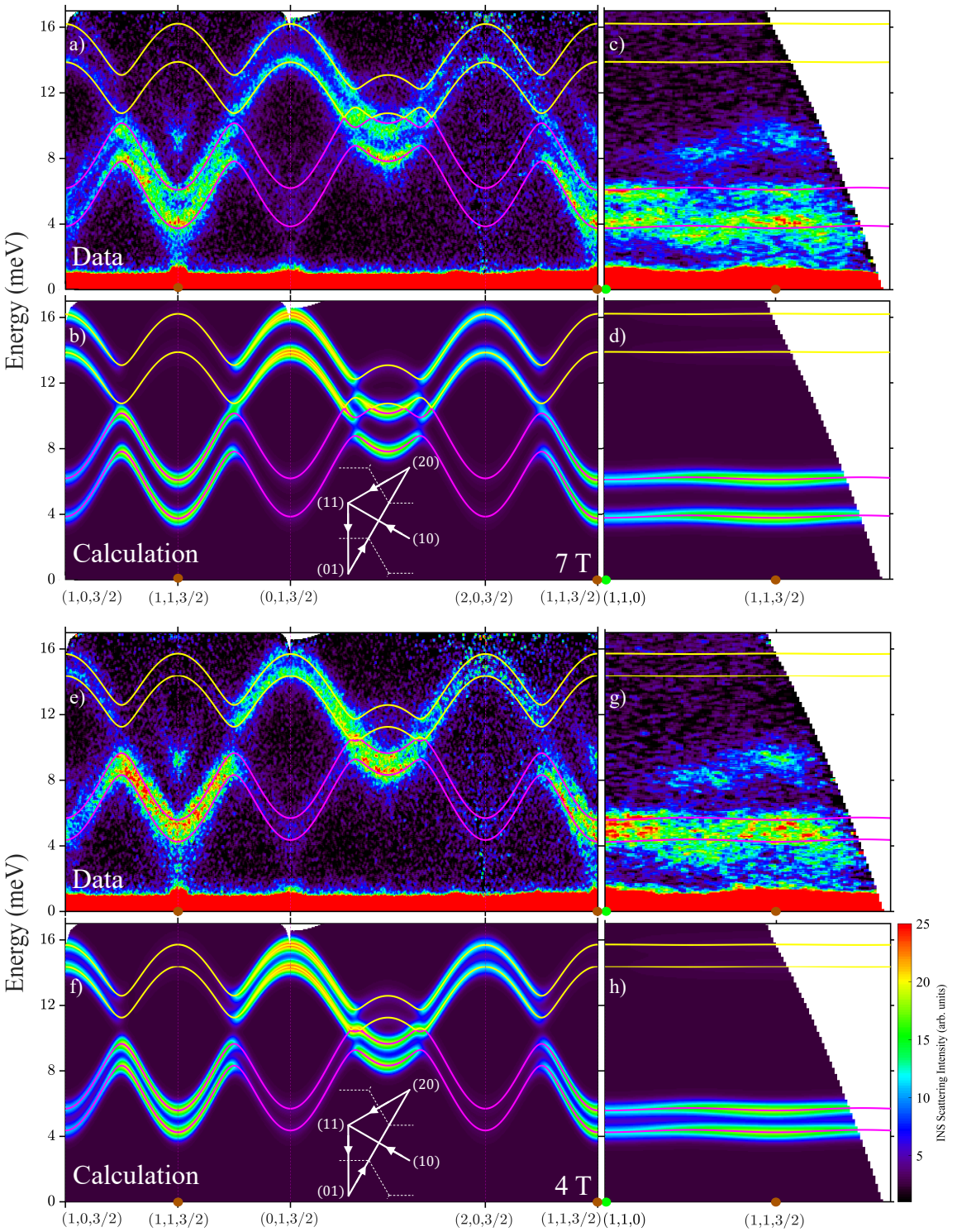

Figure 5.20: INS data comparing the a,c) observed 7 T and e,g) observed 4 T magnon dispersions against b,d,f,h) dispersions in the antiferromagnetic phase calculated using LSWT. The modelled dispersions - with parameters listed in table 5.6.1 - are plotted over each figure in magenta and yellow curves. Structural/antiferromagnetic Bragg peaks are denoted by green/brown circles on the elastic line.

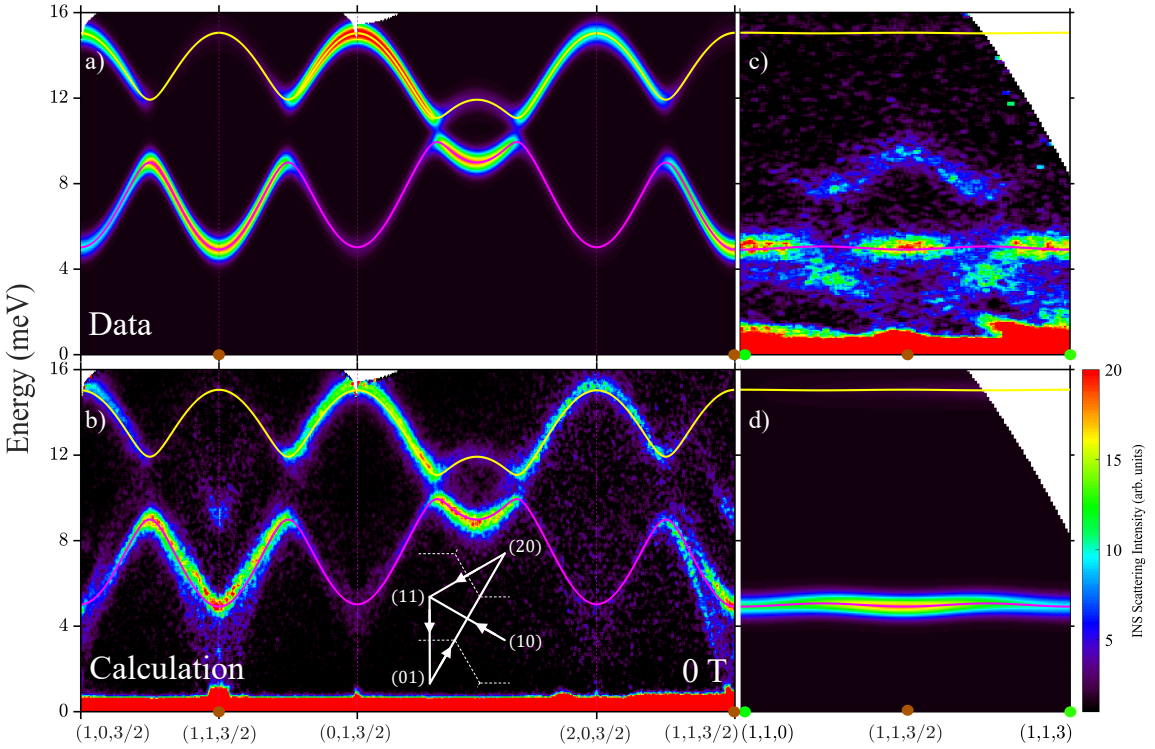

Figure 5.21: INS data comparing the a,c) observed magnon dispersions in zero field against b,d) dispersions in the antiferromagnetic phase calculated using LSWT. The modelled dispersions - with parameters listed in table 5.6.1 - are plotted over each figure in magenta and yellow curves. Structural/antiferromagnetic Bragg peaks are denoted by green/brown circles on the elastic line.

5.5 Gapped Nodal Lines and Isospin Winding

In this section, the features of the magnon dispersions around the K points of the Brillouin zone as observed in INS will be investigated for the zero field antiferromagnetic ground state and the high field spin-polarised magnetic ground state.

5.5.1 Zero Field Nodal Lines

As demonstrated in subsection 5.4.1, the magnon dispersions in the vicinity of the K points in zero field are captured by linear spin wave theory incorporating exchange couplings up to sixth nearest neighbour, local easy-axis anisotropy, and a DM interaction on the third nearest neighbour bond. In the absence of DM interactions, the dispersions take the form $\omega_{\pm}(\mathbf{k})$ and $\omega_{\pm}(\mathbf{k}+\mathbf{Q})$ where

$$\begin{aligned}\omega_{\pm}^2(\mathbf{k}) = A^2 + |B|^2 - |C|^2 - |D|^2 \pm \\ \sqrt{(2AB - CD^* - C^*D^*)(2AB^* - CD - C^*D) + (BD - B^*D^*)^2},\end{aligned} \tag{5.54}$$

$\mathbf{Q}$ is the magnetic ordering wavevector, and the modes are doubly degenerate, so $\omega_{\pm}(\mathbf{k}) = \omega_{\pm}(\mathbf{k}+\mathbf{Q})$. The terms A, B, C, and D are elements of the dynamical matrix and are given by

$$\begin{aligned}A &= \left[-3J_1 + J_2 - 6J_3 + J_3\gamma_{3\mathbf{k}} + 6J_4 - 3J_5 + 3J_6 - 2D\right] S, \\ B &= \left[J_1\gamma_{1\mathbf{k}} + J_5\gamma_{5\mathbf{k}}\right] S, \\ C &= J_4\gamma_{4\mathbf{k}} S, \\ D &= \left[J_2\gamma_{2\mathbf{k}}^* + J_6\gamma_{6\mathbf{k}}^*\right] S.\end{aligned} \tag{5.55}$$

A nodal line is the locus of points $\mathbf{k}$ where $\omega_+(\mathbf{k}) = \omega_-(\mathbf{k})$ which in this case holds when

$$(2AB - CD^* - C^*D^*)(2AB^* - CD - C^*D) + (BD - B^*D^*)^2 = 0.$$

At the K points, the terms $\gamma_{n\mathbf{k}}$ vanish for $n = 1, 4, 5,$ and 6, and so B and C are both

equal to zero and the nodal line condition is satisfied. Hence, in the absence of the DM interactions D_3^z, the model will have straight nodal lines along L that project in the hk plane at the K points of the two-dimensional Brillouin zone.

Now consider the case where the DM interaction on the third nearest neighbour bond is non-zero. Here the nodal line condition becomes

$$(2AB - CD^* - C^*D^*)(2AB^* - CD - C^*D) + (BD - B^*D^*)^2 + (2AE)^2 - |2D^*E|^2 = 0.$$

where $E = D_3^z S\Gamma_{3\mathbf{k}}$, as presented in equation 5.38. At the K points, the nodal line condition will reduced to $A^2 = |D|^2$ which will have no solutions for any set of exchange parameters J that stabilise the easy axis antiferromagnetic ground state. The cut through the zero field INS data in energy through the $(2/3, 2/3)$ K point shown in figure 5.22 shows two peaks separated by 1.2 meV, and is fitted by adjusting the magnitude of the DM interaction to be 0.050(3) meV. Such a peak separation is only reproduced in the zero field model by the inclusion of a DM interaction, which will gap out the nodal line for all L values. The gap between the magnon modes at the K points is given by $2|E| = 6\sqrt{3}|D_3^z|S$. The calculated dispersions in the vicinity of the K point are shown in figure 5.23 - and show that the magnon modes become gapped at the K point for a non-zero DM interaction.

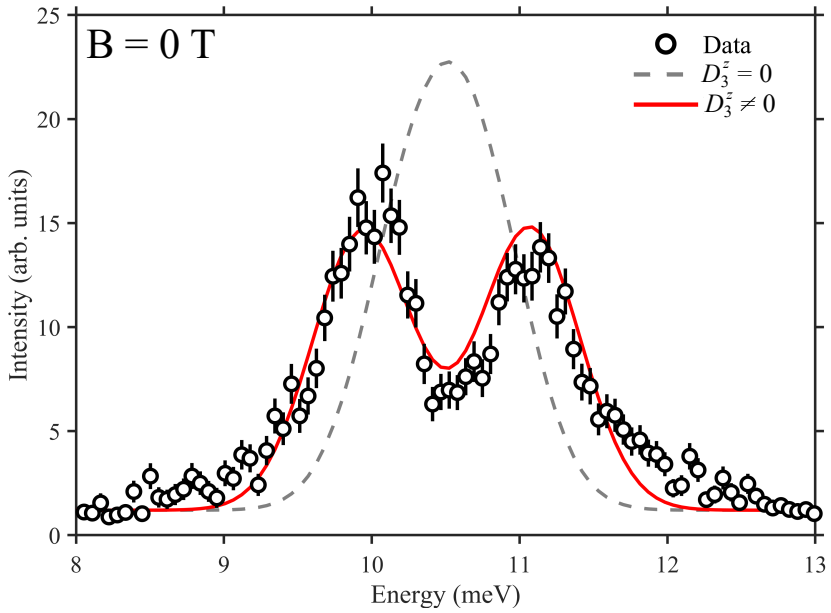

Figure 5.22: Energy scan through the $(2/3, 2/3)$ K point of the zero field INS data for $FeTiO_3$. The integration range for each energy point is a cylinder centred at the K point with a radius of 0.05 $Å^{-1}$ in the hk plane, and for l values in the range $[1, 2]$. The energy scan (white circles) has a two peak profile that is accounted for by the inclusion of a Dzyaloshinskii-Moriya interaction $D_3^z = 0.050$ meV to the LSWT model for the magnon dispersions (red solid line). Removing the Dzyaloshinskii-Moriya interaction will remove the gap at the K point, centring the scattering weight at the crossing point, resulting in a single peak (grey dashed line).

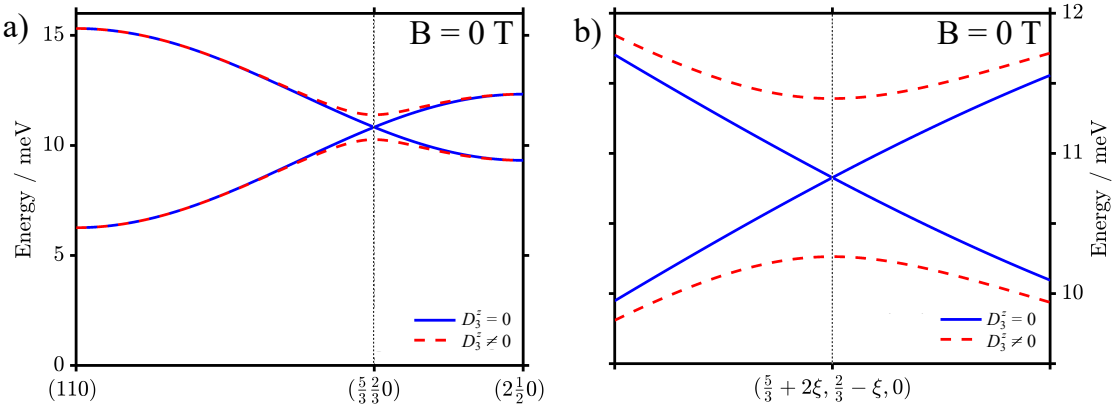

Figure 5.23: Calculated magnon dispersions in zero field in the vicinity of a K point - dashed vertical black line. The blue solid curves shows the dispersions for Heisenberg exchange and single-ion anisotropy terms only; the red dashed curves show the dispersions when a non-zero Dzyaloshinskii-Moriya exchange interaction is included, in which case there is a gap between the two modes at the K point. b) is a zoomed-in version of a) near the K-point at (5/3,2/3,0).

5.5.2 High Field Nodal Lines

Now consider the high field INS data, taken with the sample in an applied field where the magnetic structure has undergone a phase transition to a spin polarised phase. As seen in figure 5.5, the magnon band structure - as for the zero field case - has a gap between the two modes at the K point. As seen in section 5.4.3, the modes in the vicinity of the K point can be described by the Heisenberg exchange with single-ion anisotropy and DM interactions between the spin polarised moments. In the absence of DM interactions, the dispersions of the magnon modes are given by

$$\omega_{\pm}(\mathbf{k}) = A \pm |B|,$$

where A and B are the dynamical matrix elements given in equation 5.50:

$$\begin{aligned} A &= \left[-3J_1 - J_2 - 6J_3 + J_3\gamma_{3\mathbf{k}} - 6J_4 + J_4\gamma_{4\mathbf{k}} - 3J_5 - 3J_6 - 2D\right] S + g\mu_B B, \\ B &= \left[J_1\gamma_{1\mathbf{k}} + J_2\gamma_{2\mathbf{k}} + J_5\gamma_{5\mathbf{k}} + J_6\gamma_{6\mathbf{k}}\right] S. \end{aligned}$$

Nodal lines - the locus of points where the acoustic and optical magnons cross - will occur when the dynamical matrix element $|B| = 0$. At any given K point, the terms $\gamma_{n\mathbf{k}}$ will equal zero for $n = 1, 4, 5,$ and 6. Consequently, for $J_2 = 0$, the nodal line condition is satisfied and so in the absence of DM interactions, the nodal lines will be straight and vertical along L with an in-plane projection at the two-dimensional K points.

In order to determine the effect of J_2 on the nodal line structure, consider the case where J_1 and J_2 are the only non-zero Heisenberg exchange interactions. In the vicinity of the $(2/3, 5/3)$ and $(4/3, 1/3)$ K points, the wavevector may be written as $\mathbf{k} = \mathbf{K} + \delta\mathbf{k}$ for $\delta k_x = |\delta k| \cos\alpha$ and $\delta k_y = |\delta k| \sin\alpha$. In this case, terms $\gamma_{1\mathbf{k}}$ and $\gamma_{2\mathbf{k}}$ to leading order in $|\delta k|$ are given by

$$\begin{aligned} \gamma_{1\mathbf{k}} &= \frac{\sqrt{3}a}{2}|\delta k| e^{\pm i\alpha} e^{2\pi i\epsilon L}, \\ \gamma_{2\mathbf{k}} &= e^{-2\pi i L/3} e^{2\pi i\epsilon L}, \end{aligned} \tag{5.56}$$

where the upper sign holds in the vicinity of $(2/3, 5/3)$, and the lower sign holds in the vicinity of $(4/3, 1/3)$. Hence, the nodal line condition is satisfied for

$$\begin{aligned} |\delta\mathbf{k}| &= \frac{2}{\sqrt{3}a}\frac{J_2}{|J_1|}, \\ \alpha &= \mp 2\pi L/3. \end{aligned} \tag{5.57}$$

Consequently, the effect of the J_2 exchange term will be to shift the nodal lines away from the K point by $|\delta\mathbf{k}|$ which will then wind around the K point with constant radius with a period of $L = 3$. Since there are only a single pair of magnon modes - rather than the two pairs in the zero field case - there will only be a single winding nodal line around each K point. The nodal lines are illustrated in figure 5.24.

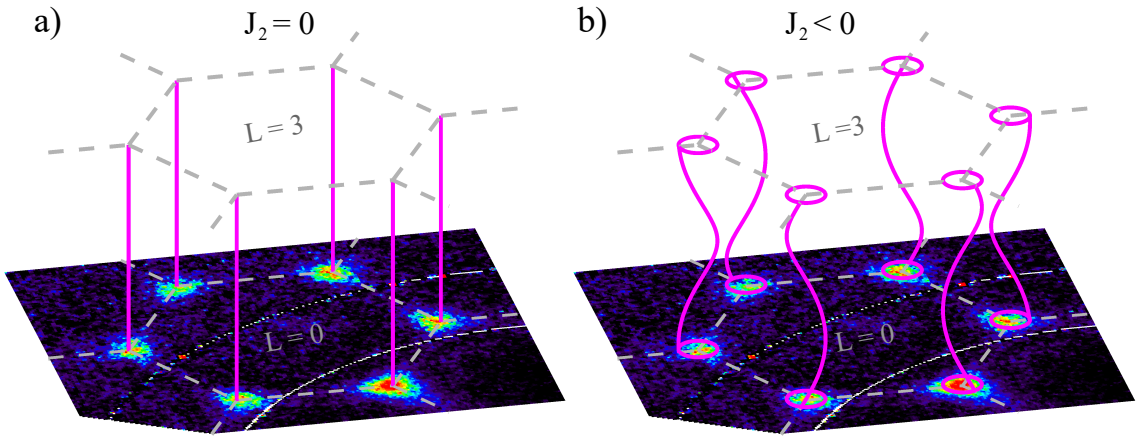

Figure 5.24: Nodal lines along L in the high field exchange model a) for $J_2 = 0$ and b) for $J_2 < 0$.

In the presence of DM interaction, the dispersion of the magnon modes is given by

$$\omega_{\pm}(\mathbf{k}) = A \pm \sqrt{|B|^2 + E^2},$$

where $E = D_3^z S\Gamma_{3\mathbf{k}}$ as defined in equation 5.50. The inclusion of a DM interaction gaps out the nodal line for all L values, and the effect of the J_2 and D_3^z terms on the high field magnon dispersions near the K points are illustrated in figure 5.25.

At the K points, E takes the value $-3\sqrt{3}D_3^z S$, and so for $J_2 = 0$, the optical and

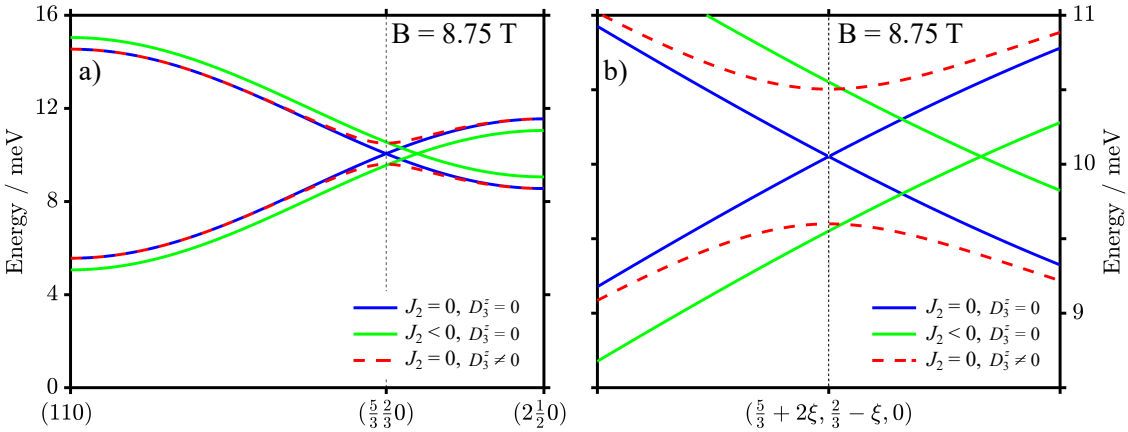

Figure 5.25: Calculated magnon dispersions in the high field phase in the vicinity of the K point. In the absence of J_2 exchange or DM couplings (blue solid curves), the magnon dispersions cross at the K points - there is a nodal line at the K points. The J_2 term does not open a gap but shifts the nodal line position away from the K point (green solid curves), whereas the Dzyaloshinskii-Moriya interaction gaps out the nodal line (red dashed curves). b) is a zoomed in version of a) near the K point $(5/3, 2/3)$

acoustic magnons will obtain a gap $\omega_+(\mathbf{K}) - \omega_-(\mathbf{K}) = 6\sqrt{3}D_3^z S$, and the nodal lines will be gapped out for all values of L. The cut through the high field INS data in energy through the $(2/3, 2/3)$ K point shown in figure 5.26 shows two peaks, which can only be explained with a non-zero DM interaction, with the same interaction strength as for the zero field case, 0.050(3) meV. The two peaks seen in figures 5.22 in zero field and 5.26a) in high field have essentially the same separation - 1.16(6) meV and 1.10(8) meV, respectively. Simply equating these gaps to $6\sqrt{3}S|D_3^z|$ will give an overestimation of the magnitude of the DM interaction $|D_3^z|$ consistent with the value listed in table 5.6.1. This overestimation of the DM interaction occurs since any cut or slice through the K point will have a finite integration range and will include scattering weight contributions in such a fashion as to overestimate the gap, consequently the previously fitted value of $D_3^z = 0.055$ meV can be revised down to 0.050 meV. The same azimuthal scan can be taken and compared to the calculated intensity including the non-zero DM interaction and varying the second nearest neighbour J_2 from the fitted value $J_2 = 0$ meV. Although the DM interaction opens a gap between the optical and acoustic magnons at the K points, leading to two peaks of equal intensity in figure 5.26, the further inclusion of a non-zero J_2 interaction will shift this gap away from the K point and lead to a difference of intensity between the two peaks as shown

in figure 5.26b). By calculating the intensity in the azimuthal scan for $J_2 = 0$ meV and $J_2 = \pm 0.1$ meV and comparing to the azimuthal scan through the 8.75 T INS data, it can be concluded that the value of $J_2 = 0$ meV, within experimental uncertainty, captures the intensity profile of the two peaks better than a non-zero J_2 interaction.

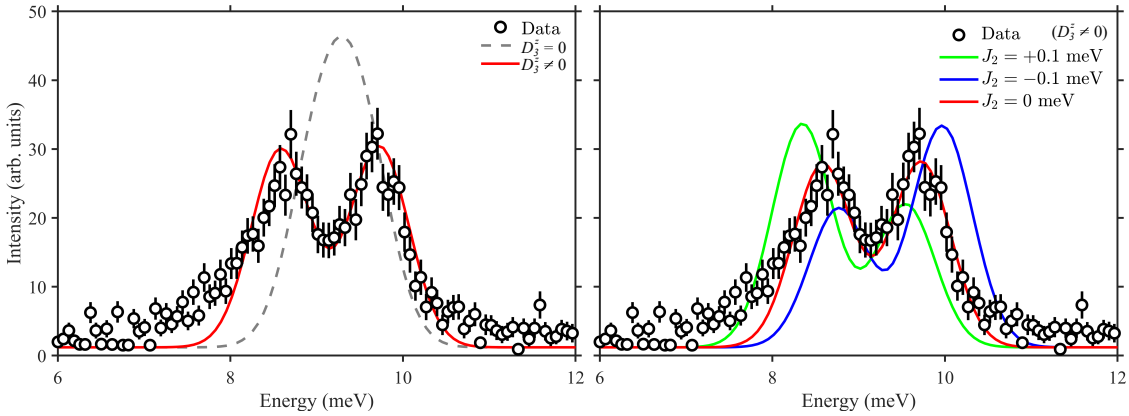

Figure 5.26: Energy scan through the $(2/3, 2/3)$ K point of the high field INS data for $FeTiO_3$. The integration range for each energy point is a cylinder centred at the K point with a radius of 0.05 $Å^{-1}$ in the hk plane, and for L values in a range $L \in [1, 2]$. a) The energy scan (open circles) has a two peak profile that is accounted for by the inclusion of a Dzyaloshinskii-Moriya interaction $D_3^z = 0.050(5)$ meV to the LSWT model for the magnon dispersions (red solid line). Removing the Dzyaloshinskii-Moriya interaction will remove the gap at the K point, centring the scattering weight at the crossing point, resulting in a single peak (grey dashed line). b) The two peaks of the intensity profile in the energy scan (open circles) are of equal intensity, which is captured by setting the second nearest neighbour Heisenberg coupling to 0 meV. Including a non-zero J_2 interaction of $+0.1$ meV (green solid line) and -0.1 meV (blue solid line) gives a difference in intensity between the two peaks in the scan.

5.5.3 Isospin Winding

Despite the nodal lines being gapped out, the twofold azimuthal intensity profile around the K points - as observed in $CoTiO_3$ - remains a feature of the magnon band structure of $FeTiO_3$ in both the zero and high field cases. This is attributed to the relative close proximity of the system in parameter space to a Hamiltonian that possesses nodal lines, specifically the DM interaction D_3^z is relatively very small in comparison to the nearest neighbour exchange J_1. To investigate the nature of the magnon dispersions at the corners of the hexagonal Brillouin zone, it is useful to find an expression of the Hamiltonian for

momentum points in the vicinity of the K/K' points. In the Brillouin zone centred at the (1,1,0) Γ point, the points $(4/3, 1/3)$, $(1/3, 4/3)$, and $(4/3, 4/3)$ can be denoted by K, and the points $(2/3, 2/3)$, $(5/3, 2/3)$, and $(2/3, 5/3)$ can be denoted by K'.

For wavevectors projected into the hk plane displaced by $\delta\mathbf{k} = |\delta\mathbf{k}|(\cos\alpha, \sin\alpha)$ away from a K/K' point, the $\gamma_{1\mathbf{k}}$ term takes the following form to leading order in $|\delta\mathbf{k}|$

$$\gamma_{1\mathbf{k}} = \frac{\sqrt{3}a}{2}|\delta\mathbf{k}|e^{-i\tau(\alpha-\alpha_0)}e^{2\pi i\epsilon L}, \tag{5.58}$$

where α_0 is the angle subtended by a unit vector $\hat{\mathbf{n}}$ that connects Γ with K/K' relative to a reference direction along the $\hat{\mathbf{x}}$ axis. The valley index τ takes the value $+1$ at K points and -1 at K' points. For J_1 coupling with a single-ion anisotropy D, and Dzyaloshinskii-Moriya interaction D_3^z, both the zero field and high field spinwave Hamiltonians (detailed in subsections 5.4.1 and 5.4.3) take the form of an effective Dirac Hamiltonian in the vicinity of K/K' points:

$$\hat{H}_{\text{eff}} = \hat{\psi}^\dagger \left(E_0\hat{I} + v_D|\delta\mathbf{k}| \left(\cos\delta\alpha_\tau(L)\hat{\sigma}_x + \sin\delta\alpha_\tau(L)\hat{\tau}_z\hat{\sigma}_y\right) + \Delta\hat{\tau}_z\hat{\sigma}_z \right)\hat{\psi}, \tag{5.59}$$

where E_0 is a constant dependent on J_1, D, and $g\mu_B B$ and which physically represents a uniform energy shift. $\Delta = |-3\sqrt{3}D_3^z S|$ will open a gap in the spectrum and can be considered as a Dirac mass term. The Dirac velocity v_D is given by $J_1 S\sqrt{3}a/2$. The angular term is $\delta\alpha_\tau(L) = \alpha - (\alpha_0 + 2\pi\epsilon L\tau)$. The operators $\hat{\boldsymbol{\sigma}}$ are Pauli matrices which act on the pseudospin index of the honeycomb lattice. The $\hat{\psi}^\dagger$ term is given by $(\hat{a}_{\mathbf{k}}^\dagger, \hat{b}_{\mathbf{k}}^\dagger)$ - which is a vector of creation operators of excitations on the A and B sublattice with a momentum near the corners of the Brillouin zone. This Hamiltonian has eigenvalues $\lambda_\pm = E_0 \pm \sqrt{v_D^2\delta k^2 + \Delta^2}$ and normalised eigenvectors

$$|\psi_{+,\tau}\rangle = \frac{1}{\sqrt{2\omega(\omega+\Delta)}} \begin{pmatrix} \Delta\tau_z + \sqrt{v_D^2\delta k^2 + \Delta^2} \\ v_D|\delta\mathbf{k}|e^{i\tau_z\delta\alpha_\tau(L)} \end{pmatrix},$$
$$|\psi_{-,\tau}\rangle = \frac{1}{\sqrt{2\omega(\omega+\Delta)}} \begin{pmatrix} -v_D|\delta\mathbf{k}|e^{-i\tau_z\delta\alpha_\tau(L)} \\ \Delta\tau_z + \sqrt{v_D^2\delta k^2 + \Delta^2} \end{pmatrix}, \tag{5.60}$$

where $\omega = \sqrt{v_D^2\delta k^2 + \Delta^2}$. The INS intensity corresponding to these two modes is given by

$$I_{\pm,\tau}(\omega, \delta\mathbf{k}) = \frac{1}{2}\left|\langle\psi_{\pm,\tau}|\hat{a}_{\mathbf{k}}^\dagger + \hat{b}_{\mathbf{k}}^\dagger|0\rangle\right|^2 = \frac{1}{2}\left(1 \pm \frac{v_D|\delta\mathbf{k}|}{\omega}\cos\delta\alpha_\tau(L)\right), \tag{5.61}$$

where $\pm$ corresponds to the upper and lower magnon bands, respectively. Consequently, for ordered spins on the honeycomb lattice with a dominant nearest neighbour exchange and a small Dzyaloshinskii-Moriya interaction D_3^z, the high symmetry points at K and K' will have a magnon spectrum consisting of two cones with a gap of 2Δ. The effective Hamiltonian in the vicinity of these points - as shown in equation 5.59 - takes the form of the Dirac Hamiltonian and the angular dependence of the INS intensity will have a cosinusoidal dependence with the upper and lower bands exactly 180° out of phase, and the extremal points of intensity given by $\alpha = \alpha_0 + 2\pi\epsilon L\tau$.

As shown in figure 5.27, azimuthal intensity scans over an annular region of an in-plane radius in the range $[0.15, 0.2]\text{Å}^{-1}$ around the $(2/3, 2/3)$ K' point were taken for L integrated over three ranges: $[-3, 0]$, $[-1.5, 1.5]$, and $[0, 3]$ in the zero field INS data set for both the upper band (in an energy range $[10.5, 12.5]$ meV), and the lower band (in an energy range $[8.5, 10.5]$ meV). These scans were also taken in the high field INS data set in energy ranges $[9, 11]$ meV to capture the upper band, and $[7, 9]$ meV to capture the lower band. Each scan was fitted with the cosinusoidal form $\mathcal{A}_\pm \pm \mathcal{B}_\pm\cos(\alpha - \alpha_0)$, with $\pm$ for top and bottom bands, respectively, with period 360° for each band, and the top and bottom bands 180° out of phase. For a flat two-dimensional honeycomb layer (i.e. for $\epsilon = 0$), the extremal points of intensity are expected to lie along the direction of the unit vector $\hat{\mathbf{n}}$ connecting

the centre of the Brillouin zone to each K point.

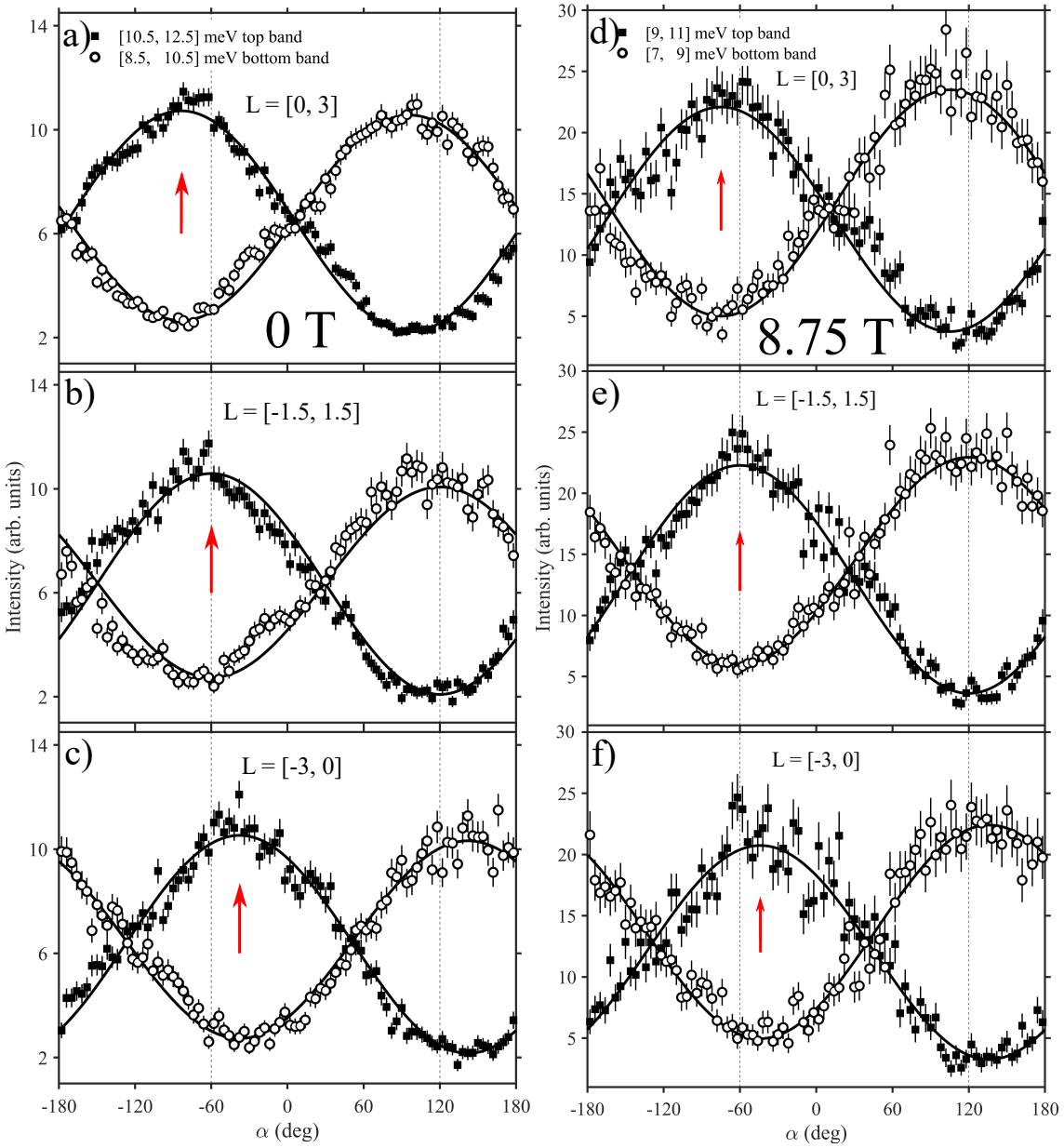

Figure 5.27: Azimuthal intensity dependence in the zero field INS data of $FeTiO_3$ around the $(2/3, 2/3)$ K point for various L-ranges in zero field a-c), and in high field d-f). Black squares/white circles denote the intensity profile at energies above/below the nominal Dirac mode energy at $(2/3, 2/3)$. The dashed vertical lines at $\alpha = -60°$ and $120°$ denote the expected points of extremal intensity for flat, planar honeycomb layers, and the red arrows denote the expected point of extremal INS intensity including the buckling of the layers. Solid black lines are fits to the cosinusoidal form described in the text.

By using the zero field model parameters to calculate the INS intensity of each pixel in

the azimuthal scans, azimuthal scans taken through the experimental data can be compared to their calculated counterparts. For the azimuthal scan centred at $L = 0$, the fitted values of α_0 were $-61(1)^\circ$ in the experimental data compared to $-60(1)^\circ$ in the calculation. The effect of the buckling of the honeycomb layers is to introduce an intensity modulation of $e^{2\pi i \epsilon L}$ due to interference scattering between the sites in the honeycomb layers offset along the vertical **c** axis. The extremal points of intensity in the azimuthal scans wind clockwise about the K' point for increasing L. For the scans over positive values of L, α_0 was fitted to a value of $-85(4)^\circ$, compared to the expected value of $-84(4)^\circ$. For the scans over negative values of L, the experimental value of α_0 was $-37(4)^\circ$ compared to the expected value of $-34(4)^\circ$. The high field azimuthal scans were similarly calculated and the L dependent shift in α_0 for each scan determined: for the $L > 0$ integration range, the experimental value of α_0 was fitted to be $-74(6)^\circ$ compared to the modelled value of $-78(2)^\circ$; for the $L < 0$ integration range, the experimental value of α_0 was fitted to be $-44(2)^\circ$ compared to the modelled value of $-43(2)^\circ$.

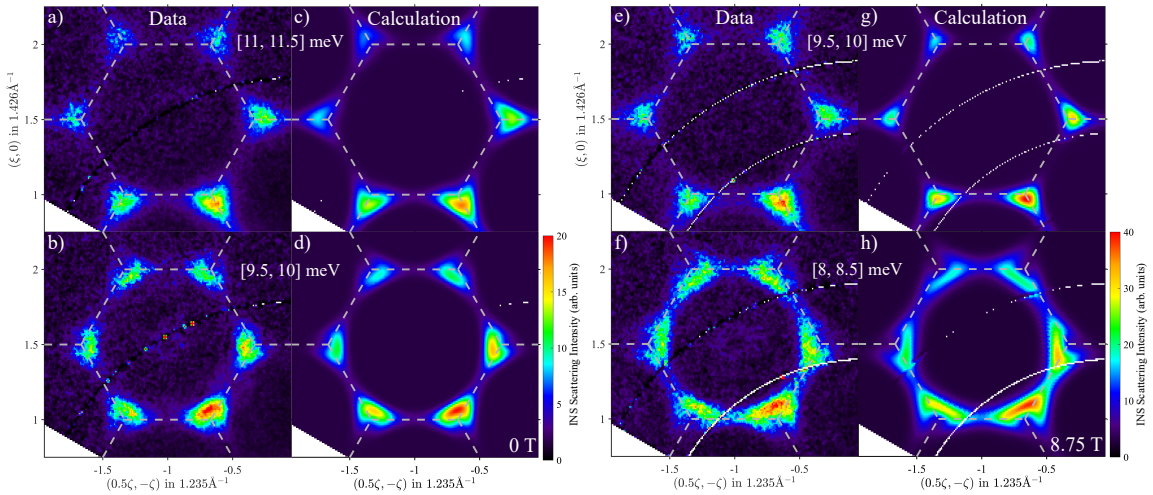

Figure 5.28: Momentum intensity maps above and below the nominal Dirac node energy a-d) in zero field, and e-h) in a field of 8.75 T. Left/right panels are the intensity profiles from INS data/modelling, upper/lower panels are above/below the magnon gap at the high symmetry K/K' points.

The L dependent rotation of the INS intensity about the K point can also be captured in constant energy slices above the avoided crossing point for the zero field data set in an energy range $[11, 11.5]$ meV to capture the upper mode, and an energy range $[9.5, 10]$ meV

to capture the lower mode. Similar slices can be taken through the high field INS data set in energy ranges of $[9.5, 10]$ meV and $[8, 8.5]$ meV in order to separately capture the intensity profile of the upper and lower modes. As for the azimuthal scans, the INS intensity of the pixels in each slice can be calculated using the exchange model, and the scattering intensity around the Brillouin zone boundary is reproduced very well in all cases. As seen in figure 5.28, the scattering intensity is concentrated inside the Brillouin zone for the lower modes, and concentrated outside the Brillouin zone for the upper modes. The intensity profiles are captured well at both zero and high field phases by the same Hamiltonian.

5.6 Further Refinement of the Modelling of Magnon Dispersions

The model presented thus far has used linear spin wave theory to describe the key features of the magnetic excitations. Specifically, the model is able to reproduce acoustic and optical magnon modes, but the experimental data show additional features at low and intermediate energies which cannot be captured by this model. To parametrise these features, additional modes with the correct periodicity will be hypothesised and added with no intrinsic scattering intensity, but with a coupling term with the acoustic magnon, providing a mechanism for an avoided crossing and allow these additional modes to obtain scattering intensity in a narrow region of reciprocal space similar in many respects to the observed inelastic neutron spectrum.

5.6.1 Dispersions in the Polarised Phase

The excitations observed in the polarised phase have three dispersive modes. The first two modes can be considered as magnons, excitations of the high field spin polarised magnetic structure - as modelled in section 5.4.3. The third mode appears to intersect the elastic line at the structural Bragg peak positions and has an avoided crossing with the acoustic magnon mode. This can be seen most clearly in figure reference 5.30a) near the (110), where there are two modes with an avoided crossing in the energy range $4 - 7$ meV, and with scattering weight extending all the way down to the elastic line. In order to capture

these features of the spectrum, consider the presence of a gapless mode with the periodicity of the structural Brillouin zone. Such a dispersion can be mathematically constructed from the LSWT description of XY magnons with ferromagnetically coupled spins in the hexagonal *ab* plane. Although this hypothetical mode may be non-magnetic in nature, this constructed dispersion can be used to parametrise a hypothetical mode with the correct periodicity and may be fit to the experimentally measured dispersions.

First consider the XY Hamiltonian for first and second nearest neighbouring coupling - remembering that this treatment is only used to obtain a parametrisation of the dispersive mode - defined with a Cartesian basis denoted by xyz such that $\mathbf{x}$ is parallel to the hexagonal $\mathbf{a}$ axis, $\mathbf{z}$ is parallel to the hexagonal $\mathbf{c}$ axis, and the frame is defined to be right handed so $\mathbf{y} = \mathbf{z} \times \mathbf{x}$

$$\hat{H}_{\mathrm{XY}} = \sum_{n=1}^{2} \sum_{\langle i,j \rangle_n} j_n^{\perp} \left(\hat{S}_i^x \hat{S}_j^x + \hat{S}_i^y \hat{S}_j^y \right), \tag{5.62}$$

where $j_n^{\perp}$ denotes the in-plane exchange parameter of the nth nearest neighbour coupling. In order to obtain a gapless dispersive mode, the spins can be taken to align in the hexagonal *ab* plane, and a coordinate transformation from the xyz frame to a new $x'y'z'$ frame defined such that the z' axis is along the ordered moment direction

$$\mathbf{x} = \mathbf{z}', \quad \mathbf{y} = \mathbf{x}', \quad \mathbf{z} = \mathbf{y}'. \tag{5.63}$$

This XXZ Hamiltonian then takes the form

$$\hat{H} = \sum_{n=1}^{2} \sum_{\langle i,j \rangle_n} j_n^{\perp} \left(\hat{S}_i^{z'} \hat{S}_j^{z'} + \hat{S}_i^{y'} \hat{S}_j^{y'} \right), \tag{5.64}$$

which can be written in terms of raising and lowering operators via the transformation

$$\begin{aligned}
\hat{S}_i^{Az'} &= S - \hat{a}_i^\dagger \hat{a}_i, & \hat{S}_i^{Bz'} &= S - \hat{b}_i^\dagger \hat{b}_i, \\
\hat{S}_i^{Ax'} &= \sqrt{S/2}(\hat{a}_i^\dagger + \hat{a}_i), & \hat{S}_i^{Bx'} &= \sqrt{S/2}(\hat{b}_i^\dagger + \hat{b}_i), \\
\hat{S}_i^{Ay'} &= i\sqrt{S/2}(\hat{a}_i^\dagger - \hat{a}_i), & \hat{S}_i^{By'} &= i\sqrt{S/2}(\hat{b}_i^\dagger - \hat{b}_i).
\end{aligned} \tag{5.65}$$

Upon applying the Fourier transformation of equation 4.13, the Hamiltonian can be written in the form

$$\hat{H} = \frac{1}{2}\sum_{\mathbf{k}} \left(\hat{a}_{\mathbf{k}}^\dagger, \hat{b}_{\mathbf{k}}^\dagger, \hat{a}_{-\mathbf{k}}, \hat{b}_{-\mathbf{k}}\right) \begin{pmatrix} A & B & 0 & D^* \\ B^* & A & D & 0 \\ 0 & D^* & A & B \\ D & 0 & B^* & A \end{pmatrix} \begin{pmatrix} \hat{a}_{\mathbf{k}} \\ \hat{b}_{\mathbf{k}} \\ \hat{a}_{-\mathbf{k}}^\dagger \\ \hat{b}_{-\mathbf{k}}^\dagger \end{pmatrix}, \tag{5.66}$$

where the dynamical matrix elements are given by

$$\begin{aligned}
A &= -\left(3j_1^\perp + j_2^\perp\right) S, \\
B &= \frac{1}{2}\left[j_1^\perp \gamma_{1\mathbf{k}} + j_2^\perp \gamma_{2\mathbf{k}}\right] S, \\
D &= \frac{1}{2}\left[j_1^\perp \gamma_{1\mathbf{k}}^* + j_2^\perp \gamma_{2\mathbf{k}}^*\right] S,
\end{aligned} \tag{5.67}$$

where $S = 1/2$ is assigned. This Hamiltonian has two modes with dispersions $\omega_{XY\pm}(\mathbf{k})$ given by the eigenvalues of $g\mathcal{D}$ for $g = \mathrm{diag}(1, 1, -1, -1)$

$$\omega_{XY\pm}^2(\mathbf{k}) = A^2 + |B|^2 - |D|^2 \pm \sqrt{4A^2|B|^2 + (BD - B^*D^*)^2}. \tag{5.68}$$

Since only one additional mode is observed in the high field INS data, it is assumed that only the lowest energy $\tilde{\omega} = \omega_{XY-}(\mathbf{k})$ mode interacts with the magnon modes introduced in section 5.4.3 to create a three-mode model:

$$\hat{H}_{comb.} = \sum_{\mathbf{k}} \omega_+(\mathbf{k})\hat{\alpha}^\dagger_{\mathbf{k}}\hat{\alpha}_{\mathbf{k}} + \omega_-(\mathbf{k})\hat{\beta}^\dagger_{\mathbf{k}}\hat{\beta}_{\mathbf{k}} + \tilde{\omega}(\mathbf{k})\hat{x}^\dagger_{\mathbf{k}}\hat{x}_{\mathbf{k}} + g_0\left(\hat{\beta}^\dagger_{\mathbf{k}}\hat{x}_{\mathbf{k}} + \hat{x}^\dagger_{\mathbf{k}}\hat{\beta}_{\mathbf{k}}\right) \tag{5.69}$$

where $\omega_\pm(\mathbf{k})$ are given by the expressions in equation 5.52, g_0 is a coupling constant denoting interconversion between the $\tilde{\omega}$ mode and acoustic magnon ω_- [25]. Here it is assumed that the two magnon modes carry INS intensity, whereas the $\tilde{\omega}$ mode carries no intensity, and for simplicity the $\omega_{XY+}(\mathbf{k})$ mode is omitted. This combined empirical Hamiltonian can be written in a matrix form

$$\hat{H}_{comb.} = \sum_{\mathbf{k}} \left(\hat{a}^\dagger_{\mathbf{k}}, \hat{b}^\dagger_{\mathbf{k}}, \hat{x}^\dagger_{\mathbf{k}}\right) \begin{pmatrix} \omega_{I+} & 0 & 0 \\ 0 & \omega_{I-} & g_0 \\ 0 & g_0 & \tilde{\omega} \end{pmatrix} \begin{pmatrix} \hat{a}_{\mathbf{k}} \\ \hat{b}_{\mathbf{k}} \\ \hat{x}_{\mathbf{k}} \end{pmatrix}. \tag{5.70}$$

The $\hat{b}_{\mathbf{k}}$ and $\hat{x}_{\mathbf{k}}$ subspace of this Hamiltonian can be diagonalised to give two hybridised modes - plotted in figure 5.29 - with dispersions given by the eigenvalues

$$\lambda_\pm(\mathbf{k}) = \frac{\omega_-(\mathbf{k}) + \tilde{\omega}}{2} \pm \sqrt{\left(\frac{\omega_-(\mathbf{k}) - \tilde{\omega}}{2}\right)^2 + g_0^2}. \tag{5.71}$$

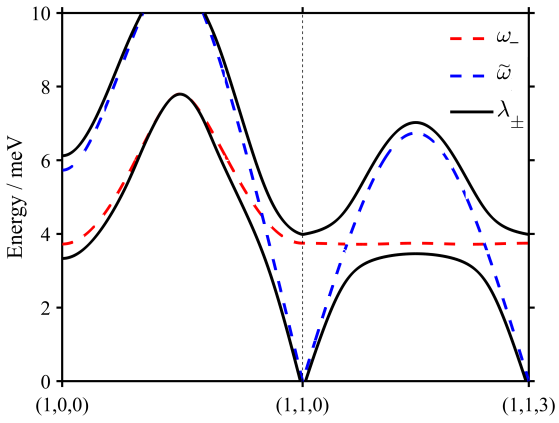

Figure 5.29: Modelled dispersions of an acoustic magnon (red dashed curve), acoustic XY mode (blue dashed curve), and the two modes - $\lambda_\pm$ in equation 5.71 - resulting from their hybridisation (solid black curves).

Since only the magnon modes carry scattering weight in the $g_0 = 0$ case, the dynamical correlator of the diagonalised modes will be proportional to the square of the $\hat{b}_{\mathbf{k}}$ component of the normalised eigenvectors - this is a measure of the magnon character of each of the hybridised modes. Consequently the dynamical correlations for the lowest two modes in the combined model is given by

$$S_{\pm}^{\alpha\beta}(\mathbf{k},\omega) = \frac{(\lambda_{\pm} - \tilde{\omega})^2}{(\lambda_{\pm} - \tilde{\omega})^2 + g_0^2} S_{-}^{\alpha\beta}(\mathbf{k},\omega), \tag{5.72}$$

where $S_{-}^{\alpha\beta}$ is given by the $\eta = -$ term in equation 5.53, and so the interaction term in the Hamiltonian will provide a mechanism for both modes to carry scattering weight in inelastic neutron scattering measurements. For some momentum point $\mathbf{k}$ where the non-interacting acoustic magnon mode and the $\tilde{\omega}$ mode were to intersect at some energy ω, then the effect of the interaction term will be to separate the two modes to $\omega + g_0$ and $\omega - g_0$. Assuming that the dispersion of the modes are smooth and continuous functions of $\mathbf{k}$, the interaction term will provide a mechanism for avoided crossings between the acoustic ω_{-} magnon and $\tilde{\omega}$ mode throughout the Brillouin zone and at such avoided crossing points, the modes will be separated in energy by $2|g_0|$.

This model can be fitted to the high field INS data, and has Heisenberg exchange parameters J_n for $n = 1$ to $n = 6$, an easy-axis anisotropy $-DS_z^2$, a DM interaction along the third nearest neighbour bond and along the $\mathbf{z}$ axis D_3^z, an external magnetic field B, $\tilde{\omega}$ mode parameters $j_1^{\perp}$ and $j_2^{\perp}$, which fix velocities of the in-plane and out-of-plane dispersions, respectively; and a coupling constant g_0 between the acoustic magnon ω_{-} and $\tilde{\omega}$ modes. Before attempting a fit, it is important to recognise the effect of the parameters on the overall shape of the dispersions. The coupling constant g_0 will introduce avoided crossing points between the acoustic magnon and $\tilde{\omega}$ mode with a gap of $2|g_0|$. The Heisenberg exchange, single-ion anisotropy, DM interaction, and g factor parameters previously fitted to the magnon dispersions and listed in table are fixed in the fitting of the dispersions in this hybridised model. The mixing mode parameters $j_1^{\perp}$ and $j_2^{\perp}$ and the coupling parameter g_0 will be allowed to vary in the fit. The fitted model parameters - in units of meV - are listed in table 5.4 with a comparison between the experimentally observed dispersions and those

modelled by this parametrisation given in figures 5.30. While three modes are produced with good agreement between the experimentally observed and modelled dispersions, the low energy 'V' shaped modes observed above the $(1,0,0)$, $(0,1,0)$, and $(2,0,0)$ positions are not reproduced and instead are modelled to have a 'U' shape at these positions. A plot comparing the observed and modelled energies at fitted dispersion points in given in figure 5.32a.

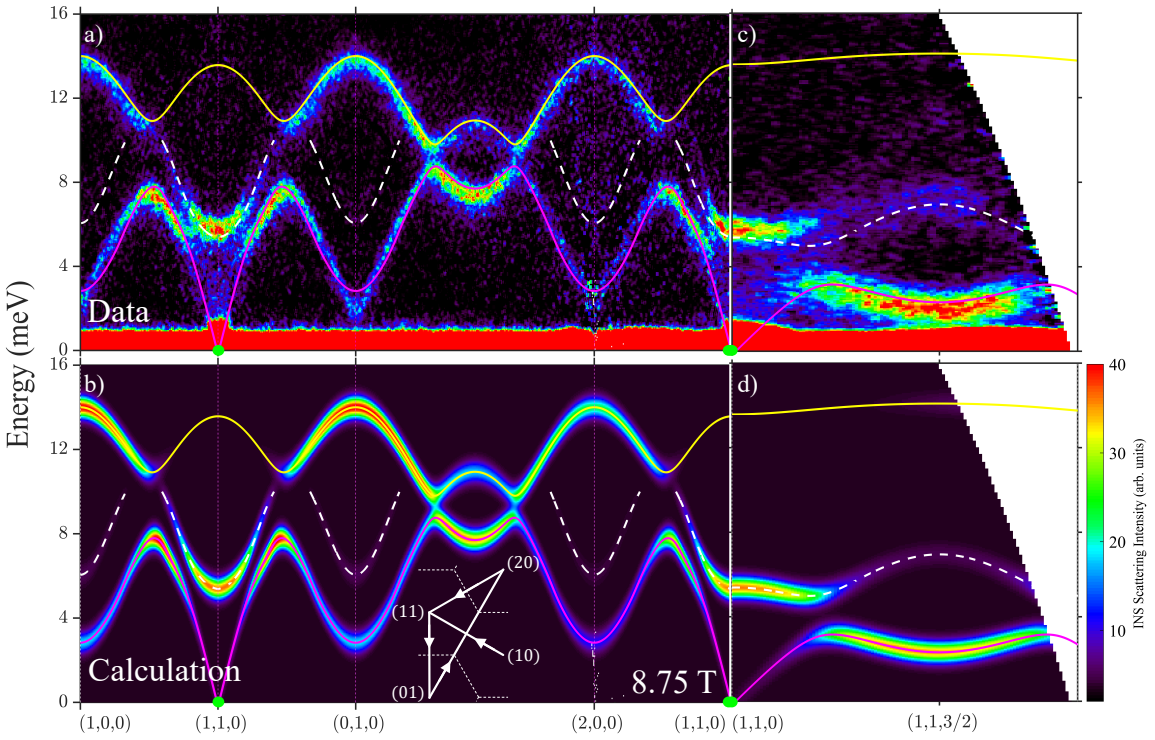

Figure 5.30: Comparison of a,c) slices through the high field INS data against b,d) the same slices modelled with easy-axis ordered moments coupled with an acoustic $\tilde{\omega}$ mode. The modelled dispersions - with parameters listed in table 5.4 - are plotted over each figure in solid magenta, solid yellow, and dashed white curves. The λ_+ dispersion is shown only up to the cutoff energy $\Lambda = 10$ meV. Structural Bragg peaks are denoted by green circles on the elastic line. The in-plane dispersion path for the slice in figures a,c) is shown in the inset of panel b).

This model assumed that the coupling parameter between the acoustic magnon ω_- and $\tilde{\omega}$ mode - g_0 - is independent of $\mathbf{k}$. This raises two problems with the model. The first problem is that the $\tilde{\omega}$ mode would still be visible above the magnon dispersions at the M point (between the two K points) in the calculated slices. The second problem is that at the structural Bragg peak positions (Γ point), the acoustic mode will have some non-zero

dispersion and the $\tilde{\omega}$ mode will be equal to zero. Plugging these values into equation 5.71 will give modes at energies $\omega_- + g_0^2/\omega_-$ and $-g_0^2/\omega_-$ (to leading order in g_0/ω_-), and the lowest most mode will have a negative energy. In order to fix the first of these issues, the coupling parameter must vary throughout the Brillouin zone, and can be taken to be a function of $\tilde{\omega}$, for vanishing g_0 above a threshold energy. The second issue is not as much of a problem as the first issue, the lowermost mixing mode will have vanishing intensity as it approaches the elastic line, so there will be no scattering weight appearing at negative energies. The coupling parameter g_0 was replaced by the function

$$g(\tilde{\omega}) = \frac{g_0}{e^{\frac{\tilde{\omega}-\Lambda}{\delta\omega}} + 1}, \tag{5.73}$$

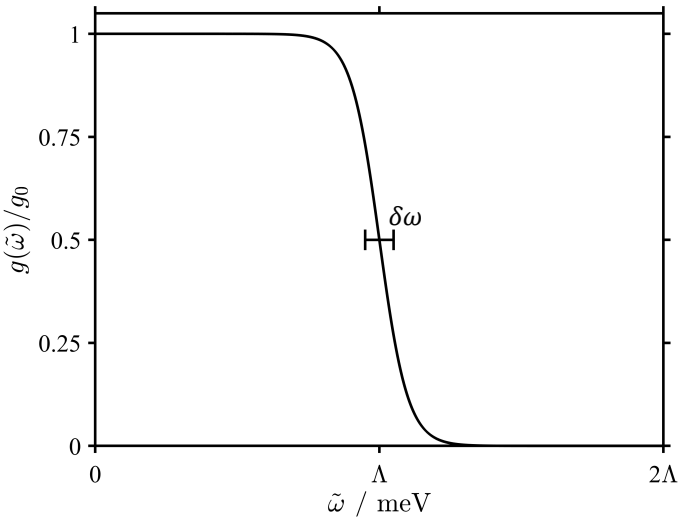

Figure 5.31: Plot of the energy dependence of the mixing mode coupling constant $g(\tilde{\omega})$, as defined in equation 5.73.

where the fitted values of the parameters Λ and $\delta\omega$ are 10 meV and 0.5 meV, respectively. This functional form, plotted in figure 5.31, satisfies both constraints listed above. The plots in figure 5.30b show the dynamical correlations for this assumed form of the coupling parameter g_0. The interconversion of INS intensity between the ω_- and $\tilde{\omega}$ modes is well captured.

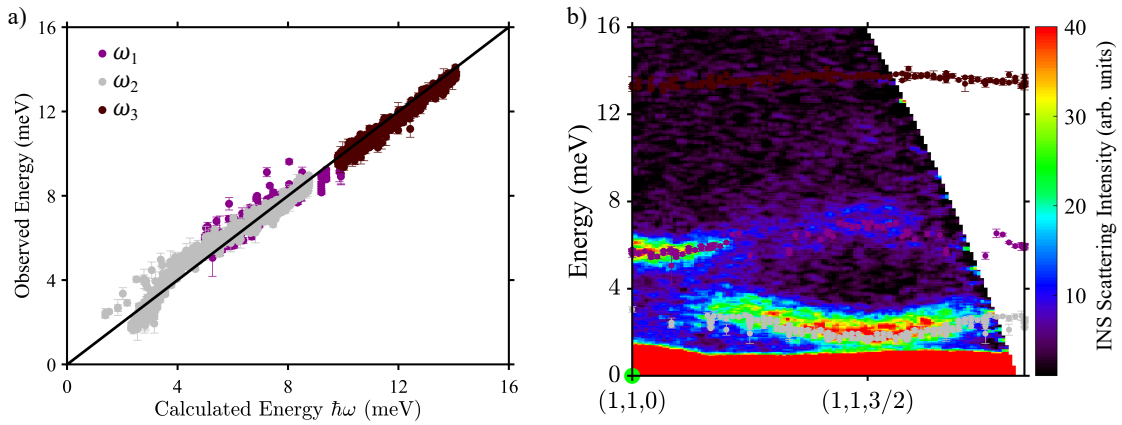

Figure 5.32: a) Scatter plot showing the energy of over 3900 experimentally observed dispersion points - magenta, grey, and red points - ordered in increasing energy in the high field data set compared to the energy of the same points as calculated in the high field model in equation 5.70. The black line is a 1 : 1 plot to show the agreement between the observed and modelled dispersions. b) A slice through the high field data set with dispersion points mapped from symmetry equivalent (hkl) values overplotted. The same colour scheme used for the dispersion points is used in both figures a) and b) to demonstrate the order in which modes were labelled.

5.6.2 Dispersions in Zero Field

As shown in section 5.4.1, the zero-field AFM structure supports a pair of doubly degenerate magnon modes, but there are additional dispersive modes - a faint scattering signal between $8 - 10$ meV and a 'V' shaped signal above the magnetic Bragg peak positions, consequently the additional mixing modes in the spectrum are acoustic and have the periodicity of the antiferromagnetic magnetic Brillouin zone. Following the previous treatment of the high field data, a functional form of the dispersions with the appropriate periodicity can be constructed. Then a combined Hamiltonian can be written to contain the magnon modes, additional mixing modes, with a set of coupling parameters. Finally, the combined Hamiltonian can be diagonalised to provide a set of modes with avoided crossing points and scattering weight shared between all modes. This model has a set of parameters that can be fitted to the observed modes in the zero field data set. In the polarised phase, the additional mode has the periodicity of the structural Brillouin zone and is likely to be an acoustic phonon. However, the origin of the additional modes in the anitferromagnetic phase remains unclear, but can be described using the dispersions for an easy plane model as described below.

The dispersions for an easy plane ordered magnetic structure with the periodicity of the magnetic unit cell have already been derived in section 4.4 for the spin wave model of $CoTiO_3$ with $S = 1/2$. The lowest most dispersions are $\omega_{XY-}(\mathbf{k})$ and $\omega_{XY-}(\mathbf{k}+\mathbf{Q})$, both with the periodicity of the antiferromagnetic Brillouin zone, where

$$\omega^2_{XY-}(\mathbf{k}) = A^2 + |B|^2 - |D|^2 - \sqrt{4A^2|B|^2 + (BD - B^*D^*)^2} \tag{5.74}$$

where in-plane exchange parameters - $j_n^{\perp}$ - couple the components of spins perpendicular to the z axis for the first and second nearest neighbours. The expressions for A, B, and D are

$$\begin{aligned} A &= \left(-3j_1^{\perp} + j_2^{\perp}\right) S, \\ B &= \left[\frac{1}{2}j_1^{\perp}\gamma_{1\mathbf{k}} - \frac{1}{2}j_2^{\perp}\gamma_{2\mathbf{k}}\right] S, \\ D &= \left[\frac{1}{2}j_1^{\perp}\gamma^*_{1\mathbf{k}} - \frac{1}{2}j_2^{\perp}\gamma^*_{2\mathbf{k}}\right] S. \end{aligned} \tag{5.75}$$

Now let the two ω_{XY-} modes be labelled in order of increasing energy - $\tilde{\omega}_1$ and $\tilde{\omega}_2$, with creation operators $\hat{x}_{\mathbf{k}}$ and $\hat{y}_{\mathbf{k}}$, respectively. The dispersions of the magnon modes - as presented in section 5.4.1 - are given by the distinct modes in equation 5.26. The Hamiltonian combining the magnon modes, and the two mixing modes $\tilde{\omega}_{1,2}$, with coupling parameters g_1 and g_2 is given by

$$\hat{H}_{comb.} = \sum_{\mathbf{k}} \left(\hat{a}^{\dagger}_{\mathbf{k}}, \hat{b}^{\dagger}_{\mathbf{k}}, \hat{x}^{\dagger}_{\mathbf{k}}, \hat{y}^{\dagger}_{\mathbf{k}}\right) \begin{pmatrix} \omega_+ & 0 & 0 & 0 \\ 0 & \omega_- & g_1 & g_2 \\ 0 & g_1 & \tilde{\omega}_1 & 0 \\ 0 & g_2 & 0 & \tilde{\omega}_2 \end{pmatrix} \begin{pmatrix} \hat{a}_{\mathbf{k}} \\ \hat{b}_{\mathbf{k}} \\ \hat{x}_{\mathbf{k}} \\ \hat{y}_{\mathbf{k}} \end{pmatrix}. \tag{5.76}$$

Once again, the optical 'XY-like' modes are not included, they are not observed and are hence excluded from the model for simplicity. The subspace of the Hamiltonian describing

the dynamics of the $\hat{b}^\dagger_{\mathbf{k}}$, $\hat{x}^\dagger_{\mathbf{k}}$, and $\hat{y}^\dagger_{\mathbf{k}}$ modes can be diagonalised, with eigenvalues - λ_1, λ_2, λ_3 - giving the three low energy modes in order of increasing energy. The modes have dynamical correlations inherited from the ω_- mode, the fraction of which is the square of the $\hat{b}_{\mathbf{k}}$ component of the corresponding eigenvector. In order to simulate slices of the zero field data, the dispersion of the magnon and mixing modes and the intensity of the magnon modes are calculated analytically. For each $\mathbf{k}$ point the Hamiltonian $\hat{H}_{comb.}$ is diagonalised numerically to obtain the lowest modes λ_1, λ_2, and λ_3 (ω_+ is unaffected).

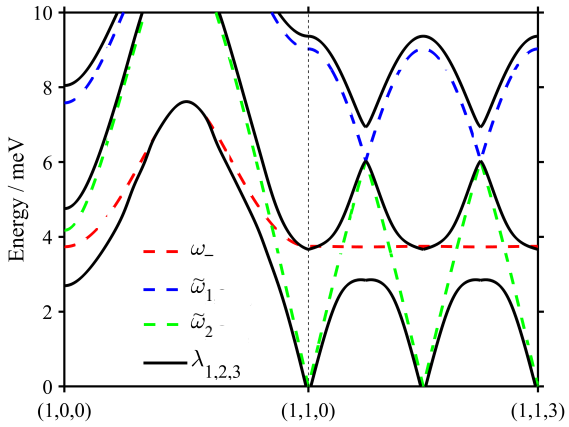

Figure 5.33: Modelled dispersions of an acoustic magnon mode (dashed red curve), a pair of mixing modes $\tilde{\omega}_1$ and $\tilde{\omega}_2$ (dashed blue and green curves), and the three modes λ_n resulting from their hybridisation (solid black curves).

The zero field model will therefore be parametrised by Heisenberg exchange parameters J_n for $n = 1 - 6$, an easy-axis anisotropy $-DS_z^2$, a DM interaction along the third nearest neighbour bond and along the hexagonal $\mathbf{c}$ axis D_3^z, mixing mode parameters $j_m^\perp$ for $m = 1, 2$, and coupling constants g_1 and g_2. In order to reproduce the periodicity of the antiferromagnetic Brillouin zone, the mixing mode parameters must also satisfy the constraints $j_1^\perp < 0$ and $j_2^\perp > 0$. The DM interaction will introduce a gap at the K points. The coupling parameters $g_1(\omega)$ and $g_2(\omega)$ are assumed to have the same functional form $g(\omega)$ as in equation 5.73, except with a higher cutoff $\Lambda = 10.5$ meV. By comparing the calculated slice along $(11L)$ against the observed dispersions, the avoided crossing gaps between the acoustic magnon and the two mixing modes can be used to fit values for the coupling parameters - g_1 and g_2. The magnetic exchange parameters J_1 to J_6, easy axis anisotropy D, and g-factor g have values fixed to those listed in table 5.6.1, with DM coupling D_3^z fixed at

0.050 meV. The data set collected with neutrons of incident energy 7.48 meV was used to fit the lower energy mixing mode parameters $j_1^{\perp}$ and $j_2^{\perp}$, which parametrise the velocity of the mixing mode along the in-plane and out-of-plane directions, respectively. The fitted model parameters are given in table 5.4, with a comparison between the observed and modelled dispersion relations given in figure 5.34.

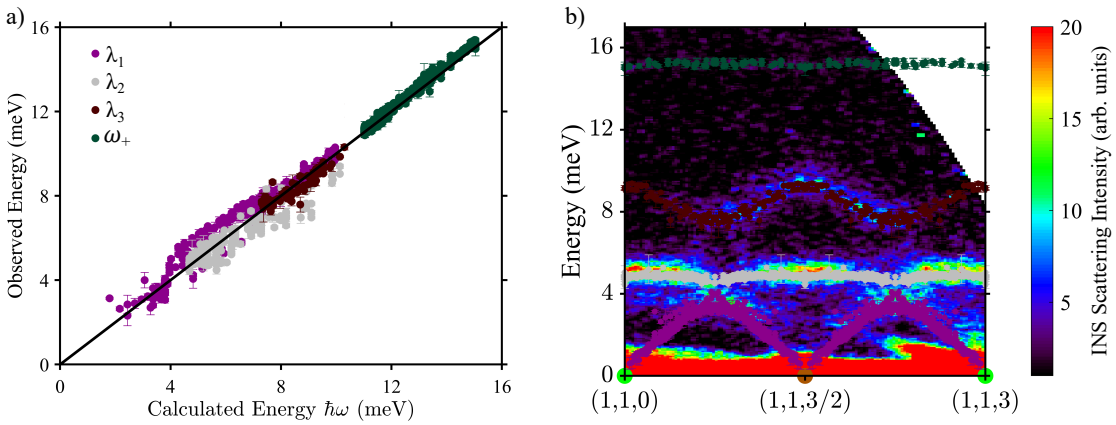

Figure 5.34: a) Scatter plot showing the energy of over 7000 experimentally observed dispersion points in zero field - magenta, grey, green, and red points - labelled 1 to 4 in order of increasing energy compared to the energy of the dispersions of the mixing Hamiltonian in equation 5.76. The black line is a 1 : 1 plot to show the agreement between the observed and modelled dispersion points. b) A slice through the zero field data set with dispersion points mapped from symmetry equivalent (hkl) values overplotted to demonstrate the consistency of the set of empirical dispersion points.

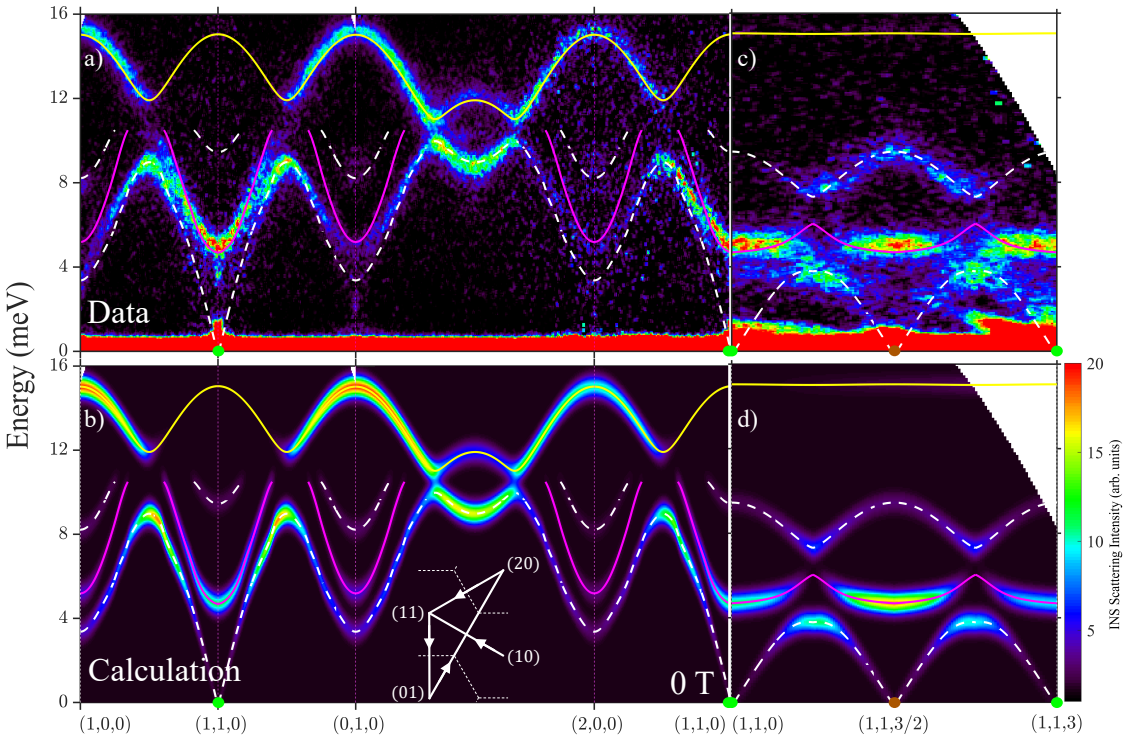

Figure 5.35: Comparison of a,c) slices through the zero field INS data against b,d) the same slices modelled with easy-axis ordered moments coupled with acoustic mixing modes. The modelled dispersions - with parameters listed in table 5.4 - are plotted over each figure in solid magenta, solid yellow, and dashed white curves. The $\lambda_{1,2}$ dispersions are shown only up to the cutoff energy $\Lambda = 10.5$ meV. Structural/antiferromagnetic Bragg peaks are denoted by green/brown circles, on the elastic line. The in-plane dispersion path for the slice in figures a,b) is shown in the inset to panel b).

J_1	-0.806 meV	$j^{\perp}_{1(A)}$	-8.367 meV
J_2	0.000 meV	$j^{\perp}_{2(A)}$	5.350 meV
J_3	-0.024 meV	g_1	0.987 meV
J_4	0.045 meV	g_2	1.372 meV
J_5	-0.024 meV		
J_6	0.134 meV	$j^{\perp}_{1(P)}$	-8.128 meV
D	0.937 meV	$j^{\perp}_{2(P)}$	-3.283 meV
D^z_3	0.050 meV	g_0	0.969 meV
g	2.876 meV		

Table 5.4: Fitted parameters for the Heisenberg exchange model including single-ion anisotropy, Dzyaloshinskii-Moriya interaction, and a Zeeman interaction term, with additional mixing modes, and interactions between the acoustic magnon and mixing modes. The mixing parameters are denoted by the subscript (A) for the zero field, 4 T, and 7 T data sets, and by the subscript (P) for the spin-polarised 8.75 T data set.

5.6.3 Dispersions in Intermediate Field

The mixing modes in the intermediate field data sets remain to be modelled. The Zeeman term arising from an externally applied magnetic field does not mix the magnon modes, only shifts their energies. Consequently, each degenerate magnon mode ω will be split into two distinct modes $\omega + g\mu_B B$ and $\omega - g\mu_B B$, with the fitted g-factor taken as 2.876. The two mixing modes will intersect the acoustic magnon modes split by the external magnetic field. Consequently, the zero-field case can be repeated twice - once for the $\omega_- + g\mu_B B$ branch, and once for the $\omega_- - g\mu_B B$ branch, to obtain eight modes in total. The combined Hamiltonian in each case is given by:

$$\begin{aligned}\hat{H}_{comb.} = \sum_{\mathbf{k}} \left(\hat{a}_{\mathbf{k}}^{+\dagger}, \hat{b}_{\mathbf{k}}^{+\dagger}, \hat{x}_{\mathbf{k}}^{+\dagger}, \hat{y}_{\mathbf{k}}^{+\dagger}\right) \begin{pmatrix} \omega_{I+} + g\mu_B B & 0 & 0 & 0 \\ 0 & \omega_{I-} + g\mu_B B & g_1 & g_2 \\ 0 & g_1 & \tilde{\omega}_1 & 0 \\ 0 & g_2 & 0 & \tilde{\omega}_2 \end{pmatrix} \begin{pmatrix} \hat{a}_{\mathbf{k}}^{+} \\ \hat{b}_{\mathbf{k}}^{+} \\ \hat{x}_{\mathbf{k}}^{+} \\ \hat{y}_{\mathbf{k}}^{+} \end{pmatrix} + \\ \left(\hat{a}_{\mathbf{k}}^{-\dagger}, \hat{b}_{\mathbf{k}}^{-\dagger}, \hat{x}_{\mathbf{k}}^{-\dagger}, \hat{y}_{\mathbf{k}}^{-\dagger}\right) \begin{pmatrix} \omega_{I+} - g\mu_B B & 0 & 0 & 0 \\ 0 & \omega_{I-} - g\mu_B B & g_1 & g_2 \\ 0 & g_1 & \tilde{\omega}_1 & 0 \\ 0 & g_2 & 0 & \tilde{\omega}_2 \end{pmatrix} \begin{pmatrix} \hat{a}_{\mathbf{k}}^{-} \\ \hat{b}_{\mathbf{k}}^{-} \\ \hat{x}_{\mathbf{k}}^{-} \\ \hat{y}_{\mathbf{k}}^{-} \end{pmatrix}.\end{aligned} \tag{5.77}$$

The dispersions and intensities of each mode are constructed using the same method for each of the $\pm$ branches as for the zero field case. The two subspaces ($\hat{b}_{\mathbf{k}}^{+}$, $\hat{x}_{\mathbf{k}}^{+}$, and $\hat{y}_{\mathbf{k}}^{+}$) and ($\hat{b}_{\mathbf{k}}^{-}$, $\hat{x}_{\mathbf{k}}^{-}$, and $\hat{y}_{\mathbf{k}}^{-}$) can each be diagonalised separately, each giving three modes with dispersions (λ_1^{+}, λ_2^{+}, and λ_3^{+}) and (λ_1^{-}, λ_2^{-}, and λ_3^{-}), respectively - shown in figure 5.36.

The dispersions of the intermediate field case can be modelled and compared to the dispersions observed in the intermediate field INS data for both 4 T and 7 T. In order to

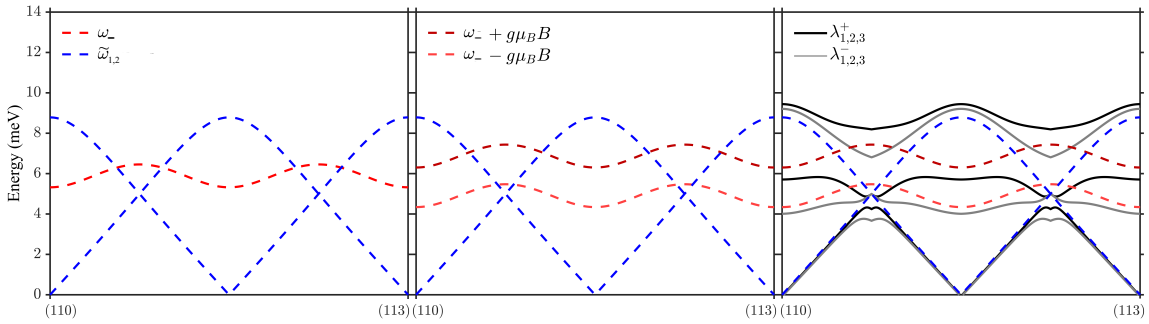

Figure 5.36: Modelled dispersions of a) an acoustic magnon mode (red dashed line) and a pair of acoustic mixing modes (dashed blue lines), b) the acoustic magnon mode is split by an applied magnetic field (dashed dark and light red lines), c) and the six modes - $\lambda^{\pm}_n$ for $n = 1, 2, 3$ - resulting from their hybridisation (black and grey solid lines).

check the consistency of the zero field model parameters for the intermediate field data, dispersion points were fitted to the observed modes in the 7 T data and compared to the calculated dispersions in the model. The scatter plot in figure 5.37 shows the observed dispersion plotted against the experimental dispersion and the straight line is a 1 : 1 plot in order to show the goodness of fit. Indeed, the zero field parameters in table 5.4 are appropriate to model the intermediate field data for both data sets with an externally applied field of 4 T and 7 T, as shown in figure 5.38.

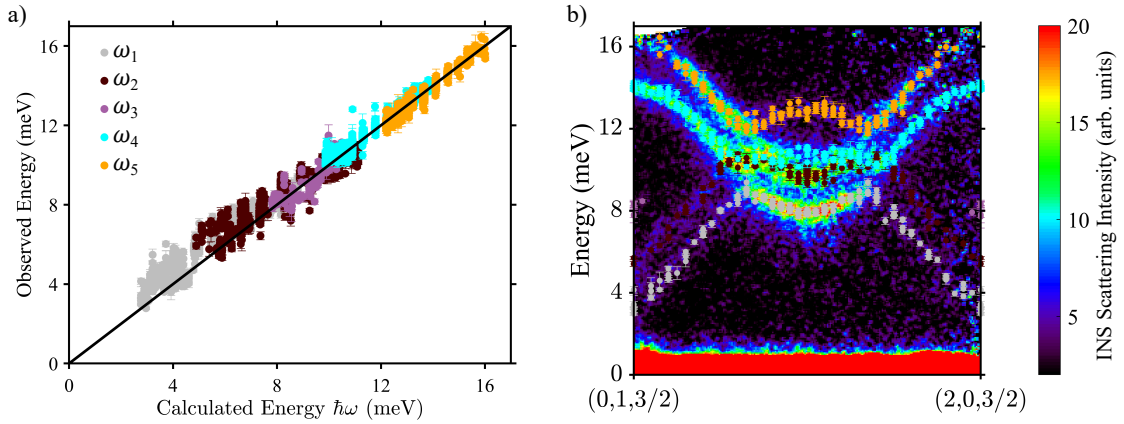

Figure 5.37: a) Scatter plot showing the energy of over 2500 experimentally extracted dispersion points in the 7 T data set compared to the energy of the same points as calculated in the model. ω_1, ω_2, and ω_3 in this plot denote the three most intense acoustic modes at a given K point in order of increasing energy, ω_4 and ω_5 denote the two optical magnon modes. The black line is a 1 : 1 plot to show the goodness of fit. b) A slice through the 7 T data set with dispersion points mapped from symmetry equivalent (hkl) values overplotted to illustrate the modes labelled from 1 to 5 in order of increasing energy at a given value of $\mathbf{k}$.

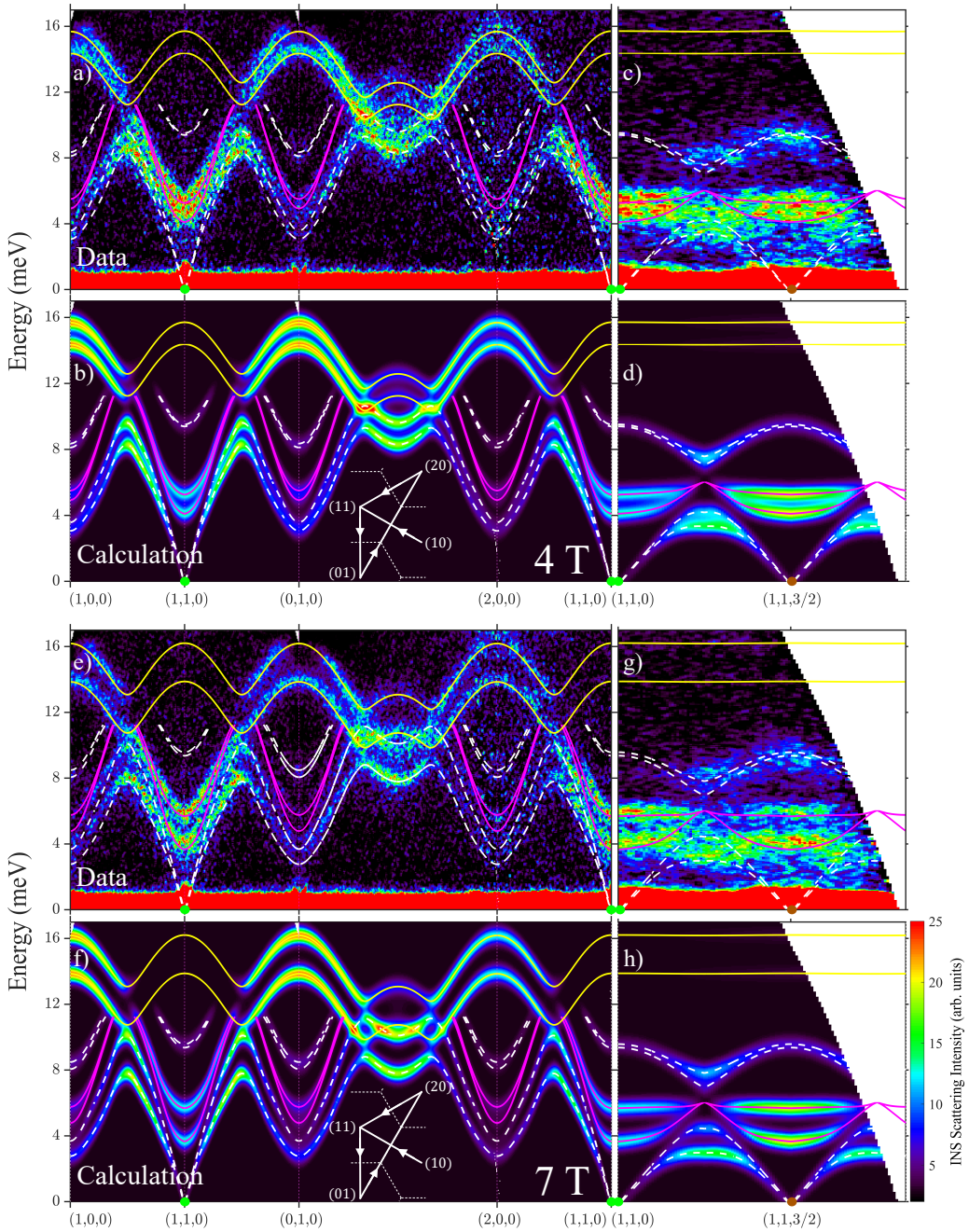

Figure 5.38: Comparison of a,c) slices through the 4 T field INS data, and e,g) slices through the 7 T field INS data against b,d,f,h) the same slices modelled with magnons coupled to acoustic $\tilde{\omega}_{1,2}$ modes. The modelled dispersions - with parameters listed in table 5.4 - are plotted over each figure in solid magenta, solid yellow, and dashed white curves. The $\lambda^{\pm}_{2,3}$ dispersions are shown only up to the cutoff energy $\Lambda = 10.5$ meV. Structural/antiferromagnetic Bragg peaks are denoted by green/brown circles, on the elastic line. The in-plane dispersion path for the slices in figures a,b,e,f) is inset in figures b) and f).

5.7 Conclusions

In summary, INS measurements of the magnetic excitations of the easy-axis stacked honeycomb $FeTiO_3$ were performed under an external magnetic field along the hexagonal **c** axis of strengths 0, 4, 7, and 8.75 T. These measurements revealed the presence of hybridised modes and gapped Dirac nodal lines. A minimal model compatible with the experimental data has been proposed, which includes the coupling of magnon modes with an additional acoustic mode. Although the linear band crossing between the optical and acoustic magnon modes is gapped out, attributed to the presence of a Dzyaloshinskii-Moriya interaction, key signatures of proximity to Dirac magnon physics have been observed via a two-fold intensity periodicity in azimuthal scans attributed to isospin winding around the nominal Dirac node. These features were observed in both the zero field antiferromagnetic phase and the high-field spin-polarised phases.

References

1. Do, S.-H. *et al. Gaps in Topological Magnon Spectra: Intrinsic vs. Extrinsic Effects* 2022. `https://arxiv.org/abs/2204.03720`.
2. Nikitin, S. E. *et al. Thermal Evolution of Dirac Magnons in the Honeycomb Ferromagnet $CrBr_3$* 2022. `https://arxiv.org/abs/2204.11355`.
3. Chen, L. *et al.* Topological Spin Excitations in Honeycomb Ferromagnet CrI_3. *Phys. Rev. X* **8,** 041028 (4 Nov. 2018).
4. Yuan, B. *et al.* Dirac Magnons in a Honeycomb Lattice Quantum XY Magnet $CoTiO_3$. *Phys. Rev. X* **10,** 011062 (2020).

5. Elliot, M. *et al.* Order-by-disorder from bond-dependent exchange and intensity signature of nodal quasiparticles in a honeycomb cobaltate. *Nat. Commun.* **12,** 3936 (2021).

6. Ohgaki, K., Ohgaki, M., Tanaka, K., Marumo, F. & Takei, H. Electron-density distribution in ilmenite-type crystals, IV. Iron (II) titanium (IV) trioxide, $FeTiO_3$. *Mineralogical Journal* **14,** 179–190 (1989).

7. Kato, H. *et al.* Metamagnetic Phase Transitions in FeTiO3. *Journal of the Physical Society of Japan* **51,** 1769–1777 (1982).

8. Shirane, G., E. Cox, D., J. Takei, W. & L. Ruby, S. A Study of the Magnetic Properties of the FeTiO3-αFe2O3 System by Neutron Diffraction and the Mössbauer Effect. *Journal of the Physical Society of Japan* **17,** 1598–1611 (1962).

9. Charilaou, M., Sheptyakov, D., Löffler, J. F. & Gehring, A. U. Large spontaneous magnetostriction in $FeTiO_3$ and adjustable magnetic configuration in Fe(III)-doped $FeTiO_3$. *Phys. Rev. B* **86,** 024439 (2012).

10. Kato, H. *et al.* On the obliqueness of the easy axis in collinear antiferromagnetic FeTiO3. *Solid State Communications* **45,** 669–672. ISSN: 0038-1098 (1983).

11. Yamaguchi, Y., Kato, H., Takei, H., Goldman, A. & Shirane, G. Re-examination of the magnetic structure of FeTiO3. *Solid State Communications* **59,** 865–868 (1986).

12. Rodriguez-Carvajal, J. Recent advances in magnetic structure determination by neutron powder diffraction. *Physica B* **192,** 55 (1993).

13. Bewley, R., Taylor, J. & Bennington., S. LET, a cold neutron multi-disk chopper spectrometer at ISIS. *Nuclear Instruments and Methods in Physics Research Section A: Accelerators, Spectrometers, Detectors and Associated Equipment* **637,** 128–134 (2011).

14. Arnold, O. *et al.* Mantid—Data analysis and visualization package for neutron scattering and μSR experiments. *Nucl. Instruments Methods Phys. Res. Sect. A Accel. Spectrometers, Detect. Assoc. Equip.* **764,** 156–166 (2014).

15. Ewings, R. *et al.* Horace: Software for the analysis of data from single crystal spectroscopy experiments at time-of-flight neutron instruments. *Nucl. Instruments Methods Phys. Res. Sect. A* **834,** 132–142 (2016).

16. Bewley, R. *et al.* MERLIN, a new high count rate spectrometer at ISIS. *Phys. B Condens. Matter* **385-386,** 1029–1031 (2006).

17. Sarte, P. M. *et al.* Spin-orbit excitons in CoO. *Phys. Rev. B* **100,** 075143 (2019).

18. White, R. M., Sparks, M. & Ortenburger, I. Diagonalization of the Antiferromagnetic Magnon-Phonon Interaction. *Phys. Rev.* **139,** A450–A454.

19. Toth, S. & Lake, B. Linear spin wave theory for single-Q incommensurate magnetic structures. *Journal of Physics: Condensed Matter* **27** (2015).

20. Coldea, R. *spinwave_dispersions MATLAB code* 2011.

21. Kawano, M. & Hotta, C. Discovering momentum-dependent magnon spin texture in insulating antiferromagnets: Role of the Kitaev interaction. *Phys. Rev. B* **100,** 174402 (2019).

22. Kawano, M., Onose, Y. & Hotta, C. Designing Rashba–Dresselhaus effect in magnetic insulators. *Commun. Phys.* **2,** 27 (2019).

23. Benyoussef, A., Boubekri, A. & Ez-Zahraouy, H. Spin-wave analysis of the XXZ Heisenberg model with Dzyaloshinskii–Moriya interaction. *Physica B: Condensed Matter* **266,** 382–390 (1999).

24. Gao, Y. H., Hickey, C., Xiang, T., Trebst, S. & Chen, G. Thermal Hall signatures of non-Kitaev spin liquids in honeycomb Kitaev materials. *Phys. Rev. Research* **1,** 013014 (2019).

25. Streib, S., Vidal-Silva, N., Shen, K. & Bauer, G. E. W. Magnon-phonon interactions in magnetic insulators. *Phys. Rev. B* **99,** 184442 (2019).

Chapter 6

Zigzag Magnetic Structure in Isoelectronically Doped $(Na_{1-x}Li_x)_2IrO_3$

The honeycomb iridate materials Na_2IrO_3 and $\alpha - Li_2IrO_3$ have been experimentally shown to exhibit magnetic ordering stabilised by bond-dependent anisotropic interactions on the honeycomb lattice. It has been previously proposed that isoelectronic doping between these two materials may produce a material proximate to a quantum spin-liquid phase. In this chapter, the structural and magnetic properties of Li-doped Na_2IrO_3 are studied using X-ray scattering techniques. It is demonstrated that isoelectronically doped samples of Na_2IrO_3 are prone to stacking faults and rotational twins, with common twinning axes and angles characterised. Furthermore, resonant elastic X-ray scattering measurements of 5% Li-doped material reveal a zigzag ordered magnetic phase similar to the parent Na_2IrO_3 compound, albeit with a suppressed Néel temperature.

6.1 Structual Analysis of Honeycomb Iridate Samples

The crystal structure of Na_2IrO_3 consists of honeycomb layers of Ir^{4+} ions, where each ion is surrounded by an octahedron of O^{2-} ions. The neighbouring octahedra share an edge, which is an important microscopic feature for bond dependent anisotropic exchange

to be present [1]. Each honeycomb layer of iridium ions is interspersed with Na^+ ions such that each sodium ion is surrounded by six iridium ions. Furthermore, a hexagonal layer of Na^+ ions is stacked in-between adjacent honeycomb layers of iridium ions. The unit cell is monoclinic with space group C2/m [2]. Upon cooling below 15.3 K, the magnetic moments of the Ir ions order in a zig-zag pattern as per figure 2.4d. $\alpha{-}Li_2IrO_3$ is isostructural to Na_2IrO_3, where Na^+ ions are replaced by Li^+ ions, however the volume of the structural unit cell for $\alpha{-}Li_2IrO_3$ is slightly smaller than that of Na_2IrO_3 - this is to be expected since the Li^+ have a smaller ionic radius than Na^+ ions [3]. Below 15 K, the magnetic moments of the Ir ions transition into an incommensurate spiral ordered state [4]. The lattice parameters of both structures are summarised in Table 6.1.

Cell parameters
Space group: $C2/m$ ($\alpha = \gamma = 90°$)

	a (Å)	b (Å)	c (Å)	β (°)
Na_2IrO_3 [2]	5.427(1)	9.395(1)	5.614(1)	109.037(18)
$\alpha{-}Li_2IrO_3$ [3]	5.169(7)	8.938(2)	5.121(7)	109.75(6)

Table 6.1: Structural unit cell parameters of Na_2IrO_3 and α-Li_2IrO_3

Since Na_2IrO_3 and $\alpha - Li_2IrO_3$ are isostructural, one may potentially synthesise a solid solution $(Na_{1-x}Li_x)_2IrO_3$ in a compositional range from $x = 0$ to $x = 1$. In this case, a quantum phase transition at some intermediate value of x may be expected between the two very different magnetic orders of the end members. However in practice, it has been found that the solid solution can only be stabilised in the range $0 < x < 0.25$, and the synthesis of nominally higher values of x was found to lead to phase separation between an $x = 0.25$ stable state and $\alpha - Li_2IrO_3$ [5]. For $x < 0.25$ it has been established experimentally via diffraction and supported by band strucutre calculations that the doped Li^+ ions replace Na^+ ions inside the honeycomb layers, at $x = 0.25$ all Na^+ ions in the honeycomb layers have been replaced. As seen in table 6.1, the bond lengths and angles in the honeycomb iridate structure vary between the $x = 0$ (pure Na_2IrO_3) and $x = 1$ (pure $\alpha{-}Li_2IrO_3$) endpoints and so the values of the exchange couplings in the Hamiltonian - and hence the magnetic ground state and transition temperature - are sensitive to replacing the Na^+ with Li^+ ions.

This chapter reports scattering studies of samples with $0 < x < 0.25$ synthesised by the Philipp Gegenwart group at Augsburg. One method of measuring the magnetic structure is to perform magnetic resonant x-ray diffraction on single crystal samples of these doped honeycomb iridates. In order to undertake such measurements, a high quality lab grown sample must be obtained, and as such it is important to perform prior characterisation of the structural quality of these crystalline samples. X-ray diffraction measurements were performed at room temperature using an Mo-source Supernova diffractometer on a number of $(Na_{1-x}Li_x)_2IrO_3$ samples of 5%, 6%, 10%, 13%, and 25% Li^+ doping, in addition to samples of Na_2IrO_3. The fitted unit cell parameters are listed in table 6.1.

Cell parameters for $(Na_{1-x}Li_x)_2IrO_3$

Space group: $C2/m$ ($\alpha = \gamma = 90°$)

	a (Å)	b (Å)	c (Å)	β (°)	N_x
$x = 0$ (Na_2IrO_3)	5.427(6)	9.401(21)	5.621(16)	108.85(21)	25
$x = 0.05$	5.385(10)	9.322(21)	5.609(9)	108.73(9)	12
$x = 0.06$	5.390(6)	9.337(15)	5.608(12)	108.71(13)	26
$x = 0.1$	5.378(2)	9.312(2)	5.605(2)	108.72(3)	1
$x = 0.13$	5.353(8)	9.266(16)	5.600(6)	108.53(12)	12
$x = 0.25$	5.318(8)	9.207(16)	5.577(15)	108.55(6)	12

Table 6.2: Structural unit cell parameters of $(Na_{1-x}Li_x)_2IrO_3$ measured at $T = 300$ K using the Supernova diffractometer for $x = 0, 0.05, 0.06, 0.13, 0.25$. Values are obtained by averaging over the fitted unit cells of N_x measured samples.

Upon substituting the Na^+ with Li^+ ions, the a and b lattice parameters were found to decrease with the ratio a/b constant to within 0.1%. This is indicative of the Ir^{4+} honeycomb lattice contracting uniformly as large Na^+ ions are replaced by smaller radius Li^+ ions. Furthermore, the c lattice parameter was found to decrease uniformly upon Li substitution and was fitted to $c(x) = c_0 - \delta x$ for $c_0 = 5.619(4)$Å and $\delta = 0.168(29)$Å. The space group of the Na_2IrO_3 parent material - C2/m - remains a good fit to crystals in the low doping regime, consistent with previous studies [5].

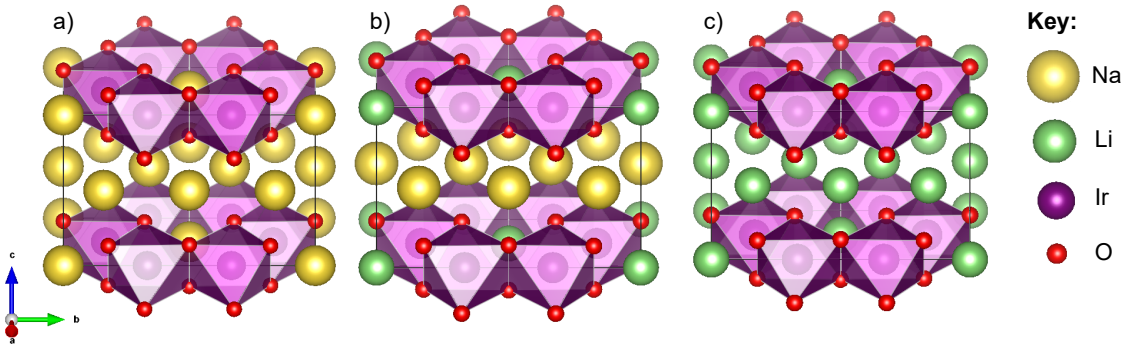

Figure 6.1: a) Structural unit cell of Na_2IrO_3. Honeycomb layers of Ir^{4+} ions are interspersed with Na^+ ions, and these layers are interleaved with hexagonal layers of Na^+ ions. b) Structural unit cell of $Na_3LiIr_2O_6$. Upon doping Na_2IrO_3 with Li^+ ions, the Na^+ ions in the honeycomb layer of Ir^{4+} ions are replaced by Li^+ ions. For 25% doping, all Na^+ ions in the honeycomb planes of Ir^{4+} ions are completely substituted by Li^+ ions. c) The structural unit cell of $\alpha - Li_2IrO_3$ is isostructural to that of Na_2IrO_3 with all Na^+ ions replaced by Li^+ ions.

In the C2/m space group, the diffraction pattern has the selection rule $h + k = 2n$ from C-centring. Crystalline samples of a material may be twinned, that is, they may consist of separate crystals that share the same lattice parameters, but have differing spatial orientations. As a result, the diffraction patterns will contain Bragg peaks that cannot be indexed by the diffraction pattern of a single grain, but indexed by Miller indices related to a main grain and additional grains, with the additional grains rotated away from the main grain. Three common twins found in α-Li_2IrO_3 have been previously identified [5]:

- 'Type A': Rotation by 180° about the (101) axis. This will exchange the crystallographic **a** and **c** axes.
- 'Type $B^{\pm}$': Rotation by $\pm 90°$ about the $(\bar{1}01)$ axis. This will rotate the **b** axis onto the $\pm(101)$ axis.
- 'Type $C^{\pm}$': Rotation by $\pm 120°$ about the (001) axis.

Stacking faults have also been found to occur readily in both Na_2IrO_3 and α-Li_2IrO_3, manifested in the X-ray diffraction patterns as rods along l with selection rule $k = 3n + 1$ or $k = 3n + 2$, and $h + k$ even. The occurrence of these stacking faults can be explained by a small energy cost in having a honeycomb layer displaced by $\pm\mathbf{b}/3$. In order to determine twinning schemes in a crystalline honeycomb iridate sample, X-ray diffraction patterns of

the hk, hl, and kl planes can be collected and compared to calculated patterns. Almost all samples were found to have twins corresponding to a rotation about the (001) axis.

Since the honeycomb arrangement in the ab plane is near ideal with almost 3-fold rotational symmetry, i.e with b/a almost equal to $\sqrt{3}$, it is useful to define an idealised hexagonal metric with basis vectors $\mathbf{a}_h$, $\mathbf{b}_h$, $\mathbf{c}_h$ in terms of the monoclinic metric with basis vectors $\mathbf{a}_m$, $\mathbf{b}_m$, $\mathbf{c}_m$ used to define the crystal structure in Figure 6.1. The hexagonal metric is exact if $a_m = b_m/\sqrt{3} = c_m$ and $\cos\beta_m = -1/3$, which has honeycomb layers stacking in a manner that repeats every three honeycomb layers. The structural parameters as listed in Table 6.1 are consistent with these ideal conditions to within 3.5%. Assuming an idealised monoclinic lattice, the basis transformation can be written as a matrix equation:

$$\begin{pmatrix} \mathbf{a}_h \\ \mathbf{b}_h \\ \mathbf{c}_h \end{pmatrix} = \begin{pmatrix} 1 & 0 & 0 \\ -1/2 & 1/2 & 0 \\ 1 & 0 & 3 \end{pmatrix} \begin{pmatrix} \mathbf{a}_m \\ \mathbf{b}_m \\ \mathbf{c}_m \end{pmatrix}. \tag{6.1}$$

The benefits of labeling Bragg peaks in the hexagonal metric is that the (001) axis is normal to the hk plane. In both settings, the $\mathbf{c}^*$ axis is normal to the plane of the honeycomb layers, but the $\mathbf{c}^*$ axis of the hexagonal metric is normal to the hk plane. If the peaks observed in diffraction are labelled in the hexagonal metric, rotational twins about the $\mathbf{c}^*$ axis can be identified easily. Furthermore, it is useful to define a Cartesian frame with unit vectors $\hat{\mathbf{x}}$, $\hat{\mathbf{y}}$, and $\hat{\mathbf{z}}$ in which the real and reciprocal lattice vectors can be defined in both the monoclinic and hexagonal settings

$$\begin{pmatrix} \mathbf{a}_m \\ \mathbf{b}_m \\ \mathbf{c}_m \end{pmatrix} = \begin{pmatrix} a_m & 0 & 0 \\ 0 & b_m & 0 \\ c_m\cos\beta & 0 & c_m\sin\beta \end{pmatrix} \begin{pmatrix} \hat{\mathbf{x}} \\ \hat{\mathbf{y}} \\ \hat{\mathbf{z}} \end{pmatrix}, \tag{6.2}$$

and

$$\begin{pmatrix} \mathbf{a}_m^* \\ \mathbf{b}_m^* \\ \mathbf{c}_m^* \end{pmatrix} = 2\pi \begin{pmatrix} 1/a_m & 0 & -\cot\beta/a_m \\ 0 & 1/b_m & 0 \\ 0 & 0 & 1/c_m \sin\beta \end{pmatrix} \begin{pmatrix} \hat{\mathbf{x}} \\ \hat{\mathbf{y}} \\ \hat{\mathbf{z}} \end{pmatrix}. \tag{6.3}$$

The lattice vectors for the hexagonal metric are defined in the idealised case where $a_m = b_m/\sqrt{3} = c_m$ and $\cos\beta_m = -1/3$ as

$$\begin{pmatrix} \mathbf{a}_h \\ \mathbf{b}_h \\ \mathbf{c}_h \end{pmatrix} = a_m \begin{pmatrix} 1 & 0 & 0 \\ -1/2 & \sqrt{3}/2 & 0 \\ 0 & 0 & 2\sqrt{2} \end{pmatrix} \begin{pmatrix} \hat{\mathbf{x}} \\ \hat{\mathbf{y}} \\ \hat{\mathbf{z}} \end{pmatrix}, \tag{6.4}$$

and

$$\begin{pmatrix} \mathbf{a}_h^* \\ \mathbf{b}_h^* \\ \mathbf{c}_h^* \end{pmatrix} = \frac{2\pi}{a_m} \begin{pmatrix} 1 & 1/\sqrt{3} & 0 \\ 0 & 2/\sqrt{3} & 0 \\ 0 & 0 & 1/2\sqrt{2} \end{pmatrix} \begin{pmatrix} \hat{\mathbf{x}} \\ \hat{\mathbf{y}} \\ \hat{\mathbf{z}} \end{pmatrix}. \tag{6.5}$$

'Type C' twinning was found to be a ubiquitous feature of the measured samples. In addition to rotations of $\pm 120^\circ$ about $\mathbf{c}^*$, some samples were found to have an additional twin corresponding to a rotation of some angle θ about $\mathbf{c}^*$. Such samples were also found to exhibit composite twins - corresponding to rotations of $\theta \pm 120^\circ$ about $\mathbf{c}^*$, giving six twins overall. As a shorthand notation, let this set of six twins be denoted by $C_\theta^\pm$. For example, one sample of 6% doping had a diffraction pattern that can be indexed by grains belonging to $C_\theta^\pm$ for $\theta = -5.5^\circ$; one sample of 13% doping had a diffraction pattern that can be indexed by grains belonging to $C_\theta^\pm$ for $\theta = +5^\circ$. There was only one sample of 10% doping that was measured in x-ray diffraction, and the sample was a thin plate around 4mm in diameter, whereas other measured samples were typically between $200\mu m$ to 1mm

in diameter. X-ray diffraction measurements were taken by aligning the beam onto the centre of the sample, and later measurements were taken by aligning the beam onto the edges of the sample. All diffraction data from this sample could be characterised by a main grain, two twins rotated by $-13°$ and $-52°$ about $\mathbf{c}^*$, and for each of these three grains, an extra pair of twins rotated by an additional angle of $\pm 120°$. As shown in figure 6.2, rotational twins about the $\mathbf{c}^*$ axis can be visually identified from the $hk0$ planes labelled in the hexagonal metric.

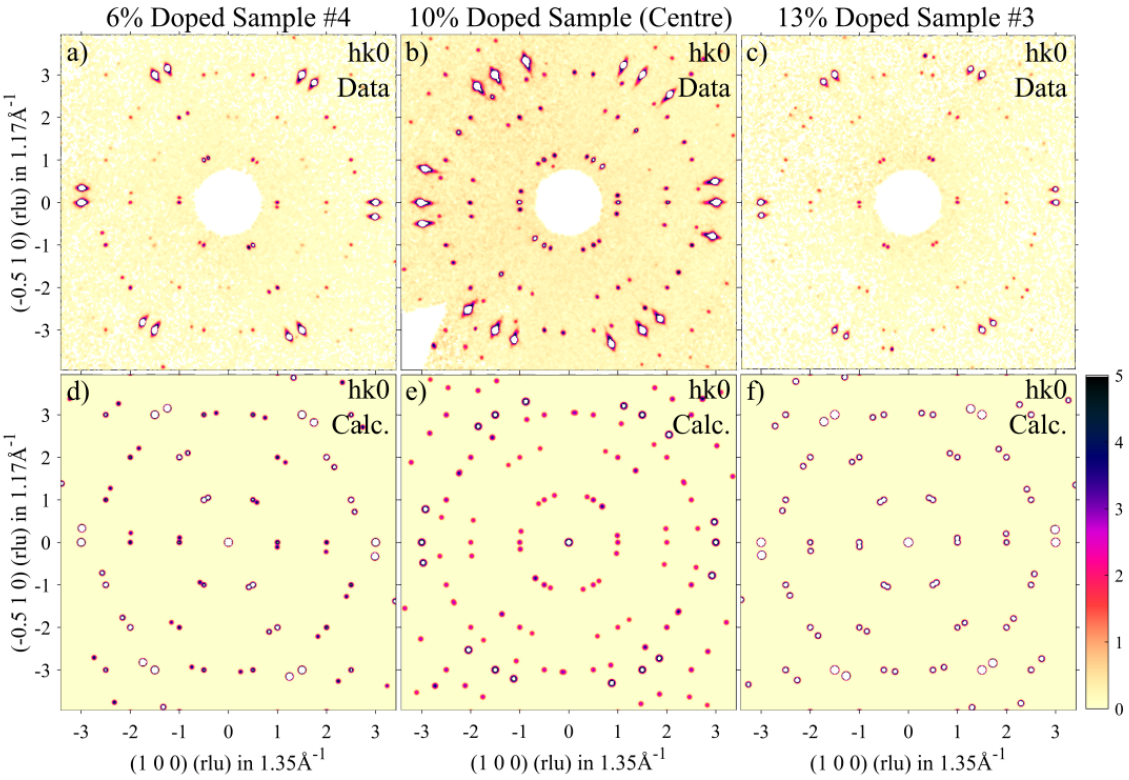

Figure 6.2: Comparison of the diffraction pattern in the $hk0$ hexagonal plane data (top row) versus calculations (bottom row) including rotational twins about the $\mathbf{c}^*$ axis. a-c) Diffraction data for a 6% doped sample (top left), a 10% doped sample (top centre), and a 13% doped sample (top right).

While 'type C' twinning was readily observed in nearly all samples, 'type A' twinning was rarely found - and only three samples were characterised with this twinning scheme. By comparing equations 6.3 and 6.5, the $\mathbf{a}_m^* + \mathbf{c}_m^*$ axis is parallel to $\mathbf{a}_h^* - \mathbf{b}_h^*/2 + 4\mathbf{c}_h^*$. When indexed in the hexagonal metric, one of the samples (5% sample #12 - seen in figure 6.3) has diffraction planes $0kl$, $hk1$, and $hk\bar{1}$ that can be indexed by a main grain with a type A twin, and a pair of type C$^{\pm}$ twins.

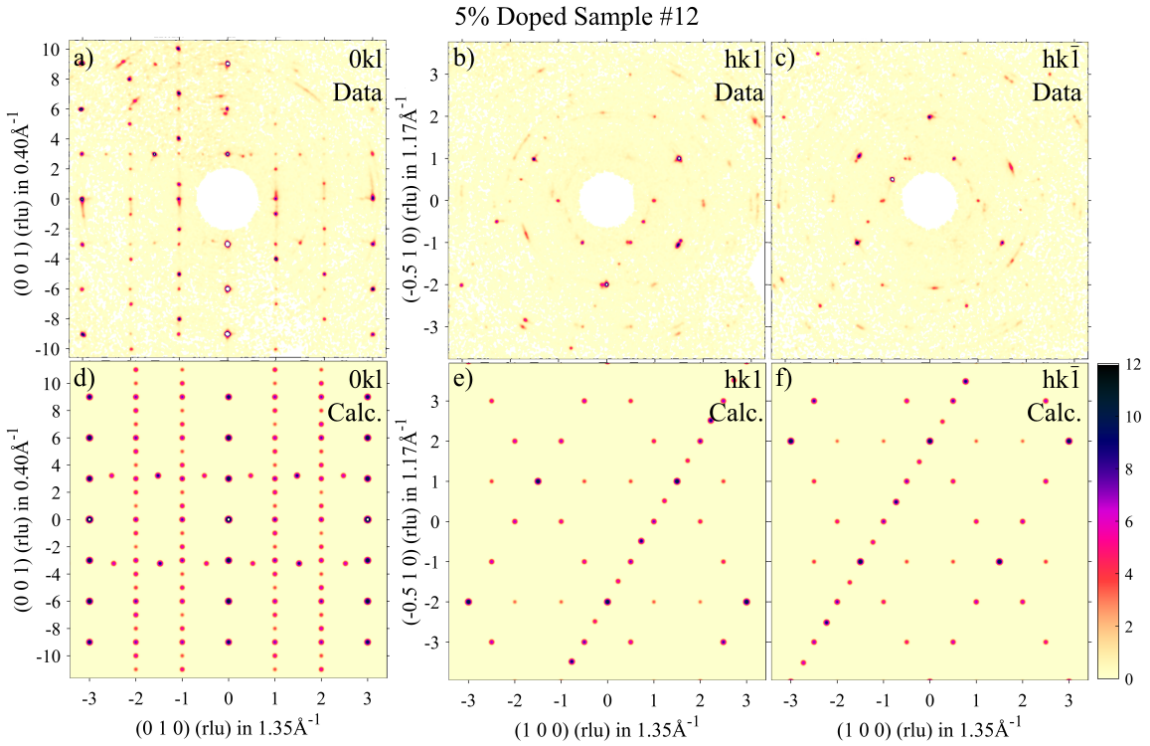

Figure 6.3: Comparison of the $0kl$ (left), $hk1$ (centre), and $hk\bar{1}$ (right) planes in diffraction data (top) versus calculated planes (below) displaying rotational twins about the $\mathbf{c}^*$ axis, and a rotational twin about the monoclinic $\mathbf{a}$ axis in a 5% doped sample. The rotational twin about the monoclinic $\mathbf{a}$ axis provides additional peaks along the $(0k1)$ and $(0k\bar{1})$ axis in a) and d), along the $(1k1)$ axis in b) and e), and along the $(\bar{1}k\bar{1})$ axis in c) and f).

On the other hand, another sample (5% sample #16 - seen in figure 6.4) was indexed in the hexagonal metric with a main grain, a twin rotated 180° about the $(1, \frac{\bar{1}}{2}, 4)_h$ axis (type A), a pair of twins rotated $\pm 120°$ about the $(0, 0, 1)_h$ axis (type $C^{\pm}$), a twin rotated $-90°$ about the $(1, 1, 4)_h$ axis, and a twin rotated $+90°$ about the $(1, \bar{2}, 4)_h$ axis. These final two twins were found by considering a composition of A followed by C^+ type twinning, and A followed by C^- type twinning, respectively. This can be seen as follows: a Cartesian basis $\hat{\mathbf{x}}\hat{\mathbf{y}}\hat{\mathbf{z}}$ can be assigned to the main grain using the same convention used in equations 6.2-6.5. Another Cartesian basis $\hat{\mathbf{x}}'\hat{\mathbf{y}}'\hat{\mathbf{z}}'$ can be assigned to a twin rotated with respect to the main grain. Let R be the rotation matrix relating the two bases by

$$\begin{pmatrix} \hat{\mathbf{x}}' & \hat{\mathbf{y}}' & \hat{\mathbf{z}}' \end{pmatrix} = R \begin{pmatrix} \hat{\mathbf{x}} & \hat{\mathbf{y}} & \hat{\mathbf{z}} \end{pmatrix}. \tag{6.6}$$

The rotation matrices for A and $C^{\pm}$ type twins are given by

$$R_A = \begin{pmatrix} -1/3 & 0 & 2\sqrt{2}/3 \\ 0 & -1 & 0 \\ 2\sqrt{2}/3 & 0 & 1/3 \end{pmatrix}, \quad R_{C^\pm} = \begin{pmatrix} -1/2 & \mp\sqrt{3}/2 & 0 \\ \pm\sqrt{3}/2 & -1/2 & 0 \\ 0 & 0 & 1 \end{pmatrix}, \tag{6.7}$$

and the composite transformation is given by $R_\pm = R_{C^\pm} R_A$

$$R_\pm = \begin{pmatrix} 1/6 & \pm\sqrt{3}/2 & -\sqrt{2}/3 \\ \mp\sqrt{3}/6 & 1/2 & \pm\sqrt{6}/3 \\ 2\sqrt{2}/3 & 0 & 1/3 \end{pmatrix}. \tag{6.8}$$

The axis of rotation $\hat{\mathbf{e}}_\pm$ is given by the normalised eigenvector of $R_\pm$ with eigenvalue 1; the angle of rotation is given by $\cos\theta_\pm = [\mathrm{tr}(R_\pm) - 1]/2$, where in this case $\cos\theta_\pm = 0$ and so $|\theta_\pm| = \pi/2$. In order to determine the sign of the angle, a column vector $\mathbf{v}$ that is normal to both axes of rotation $\hat{\mathbf{e}}_\pm$ can be constructed. This column vector will then transform under $R_\pm$ as $R_\pm \mathbf{v} = \cos\theta_\pm \mathbf{v} + \sin\theta_\pm (\hat{\mathbf{e}}_\pm \times \mathbf{v})$. Since $\sin\theta$ is an odd function of θ, this expression will allow the sign of $\theta_\pm$ to be determined. In this case, the axis of rotation is given by $\hat{\mathbf{e}}_\pm = \left(1/\sqrt{6}, \pm 1/\sqrt{2}, 1/\sqrt{3}\right)^T$, which is parallel to the $(1,1,4)_h$ and $(1,-2,4)_h$ axes, respectively. The vector $\mathbf{v}$ may be taken to be $\left(1/\sqrt{3}, 0, -1/\sqrt{6}\right)$ and transforms as $R_\pm \mathbf{v} = \cos\left(\frac{\pi}{2}\right)\mathbf{v} \mp \sin\left(\frac{\pi}{2}\right)(\hat{\mathbf{e}}_\pm \times \mathbf{v})$, indicating that the angle of rotation is $-\pi/2$ for R_+ and $+\pi/2$ for R_-. As shown in figures 6.3 and 6.4, type A twins, appearing with a main grain on its own or in composition with a type $C^\pm$ twin, can be visually identified from the $0kl$, $hk1$, and $hk\bar{1}$ planes labelled in the hexagonal metric.

In all of the samples measured in x-ray diffraction, none were characterised by a type B twinning scheme. This is likely to be more common for samples closer to the $\alpha-Li_2IrO_3$ endpoint than the Na_2IrO_3 endpoint since the percentage difference between the a and c lattice parameters in the monoclinic setting is around 3.3% for Na_2IrO_3, but is $> 1\%$ for $\alpha-Li_2IrO_3$.

In addition to these previously identified A and $C^\pm$ type twins, many samples were identified to have twins corresponding to rotations of multiples of 15° about the $\mathbf{c}^*$ axis.

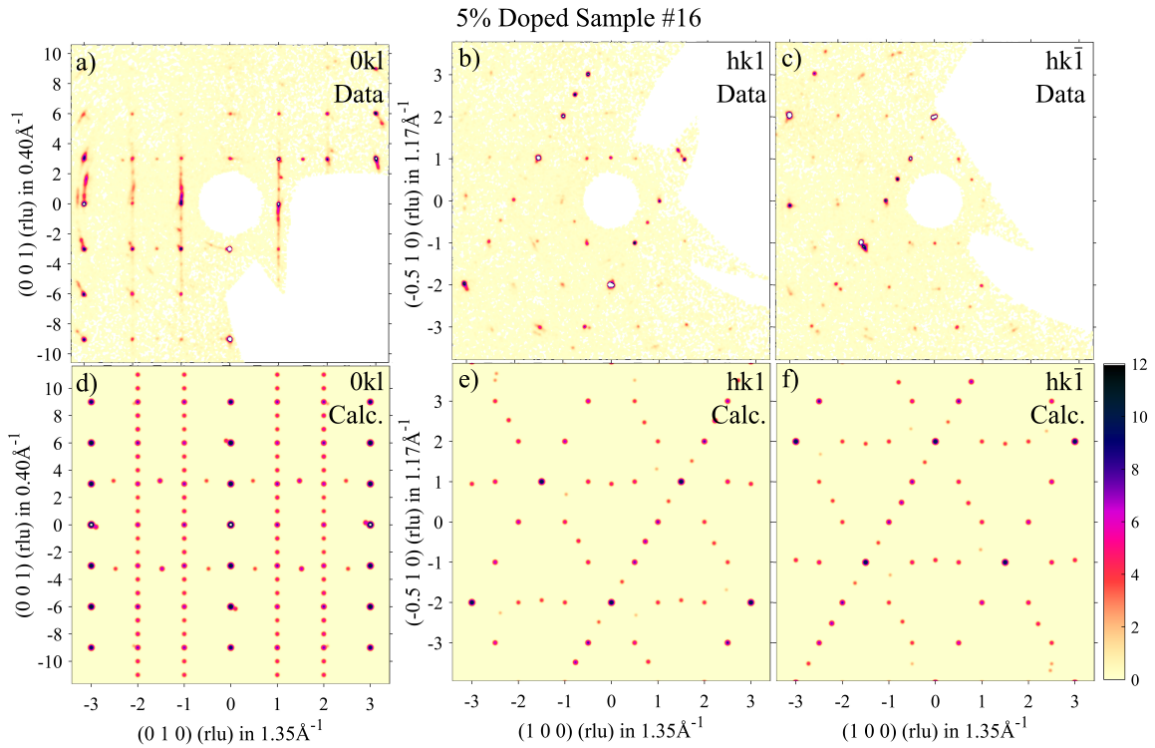

Figure 6.4: Comparison of the diffraction pattern in the $0kl$, $hk1$, and $hk\bar{1}$ hexagonal planes (top row) versus calculations (bottom row), including rotational twins about the $\mathbf{c}^*$ axis, a rotational twin about the monoclinic $\mathbf{a}$ axis, and twins resulting from composite rotations about both the $\mathbf{a}$ and $\mathbf{c}^*$ axis in a 5% doped sample. The rotational twin about the monoclinic $\mathbf{a}$ axis provides additional peaks along the $(0k1)$ and $(0k\bar{1})$ axis in a) and d). The additional peaks along the $(1k1)$ axis in b) and e), and along the $(\bar{1}k\bar{1})$ axis in c) and f), are rotated about the $\mathbf{c}^*$ axis normal to the plane giving a tessellating triangular pattern with a number of peaks along each triangular edge.

To diagnose these twins, the diffraction pattern in the $hk0$ plane labelled in the hexagonal metric was considered. Here, peaks can be readily identified as corresponding to either the main grain of the crystal, or by a rotation of θ about the $\mathbf{c}^*$ axis. From this plane, a set of all possible trial values of θ and $180° - \theta$ can be constructed as a candidate twinning scheme. Calculating the $hk2$, $hk\bar{2}$, $2kl$, $\bar{2}kl$, $h2l$, and $h\bar{2}l$ planes in the hexagonal setting and comparing to the experimentally measured diffraction planes allows some trial values of θ to be ruled out and provides an accurate characterisation of the diffraction pattern. Samples analysed using the techniques outlined above were deemed to have good structural quality provided that only $C^{\pm}$ twinning was observed, and the peaks along the hexagonal $(00l)$ direction were well localised and distinguishable from any streaks arising from stacking faults.

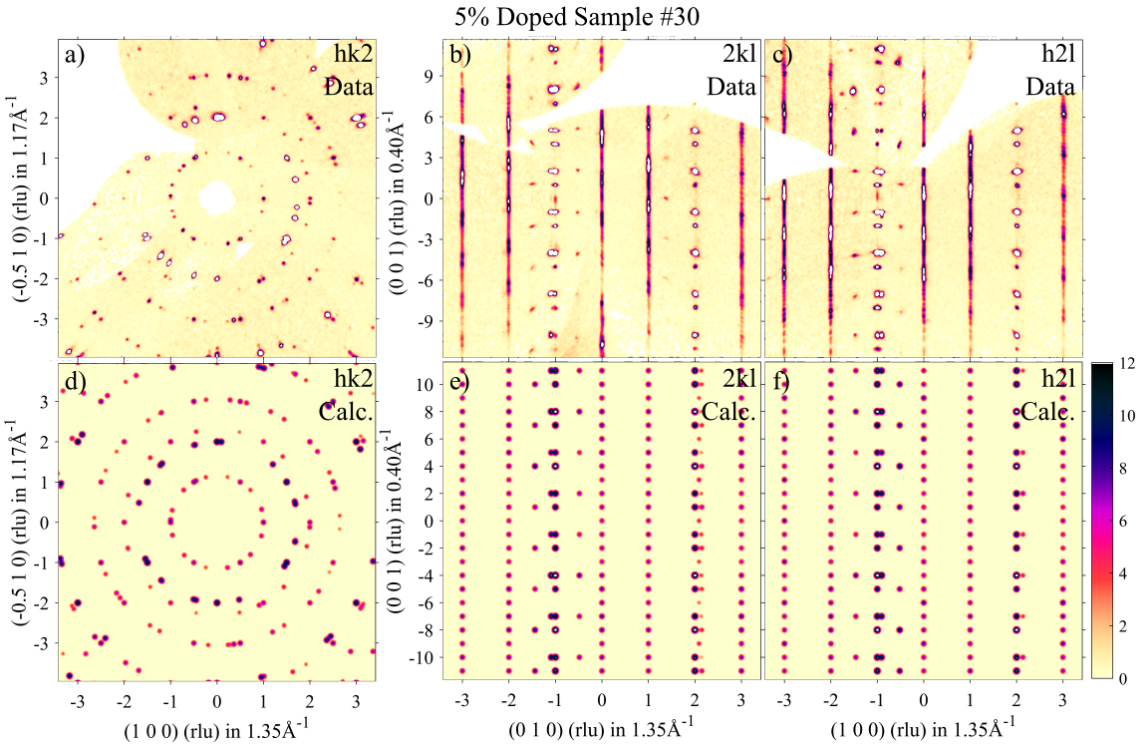

Figure 6.5: Comparison of the diffraction pattern in the $hk2$ (left), $2kl$ (centre), and $h2l$ (right) planes in diffraction (top) versus calculations (bottom), displaying many rotational twins about the $\mathbf{c}^*$ axis and - in b) and c) - stacking faults in streaks along the $(0, 0, L)$ direction. Rotational twins rotated at $-165°$, $-120°$, $-103°$, $-75°$, $-60°$, $-3°$, $15°$, $45°$, $60°$, $120°$, $135°$, and $163°$ about the $\mathbf{c}^*$ axes were characterised for this sample. Candidate twins were be identified from the $hk2$ plane, and were used to reproduce features in the $2kl$ and $h2l$ planes including most notably additional peaks in the region bounded by the $(20l)$ and $(22l)$ axes in b) and e), and in the region bounded by the $(02l)$ and $(\bar{2}2l)$ axes in c) and f).

The best quality samples were identified as candidates for resonant elastic x-ray scattering (REXS) experiments, and mounted onto brass pucks. These brass pucks could be loaded onto a custom made brass mount which was designed to match the specifications of the P09 beamline at PETRA III [6], or onto a copper drum designed to match the specifications of the I16 beamline at Diamond Light Source [7]. Separately, a cradle was created to allow the brass mount to be loaded into a Rigaku SmartLab x-ray diffractometer. X-ray diffraction experiments were performed on this instrument using a Cu $K\alpha$ source. An initial $2\theta/\omega$ scan confirmed that the (001) axis is normal to the surface of the plate-like samples. A $\theta/2\theta$ scan on a 5% doped sample showed two peaks - corresponding to the splitting of the lines of the Cu $K\alpha$ radiation - confirming that the samples consisted of only a single phase.

The sample was tilted so that a φ scan of 360° would move the (202) Bragg peak into the scattering plane. This scan showed three peaks of equal scattering intensity offset by 120° - providing direct evidence that the sample has a main grain and $C^{\pm}$ twins. Furthermore, an ω rocking curve scan about the (004) Bragg peak was performed for a Na_2IrO_3 sample, a 5% Li-substituted sample, and a 25% Li-substituted samples. While the Na_2IrO_3 sample had a single peak in the ω scan with a Lorentzian lineshape of width 0.24°, the doped samples were fitted with broader lineshapes consisting of two Lorentzian peaks. This indicates that the doped samples - even those identified as having the best structural quality in their respective batches - exhibit a large mosacitiy and the samples consists of multiple misaligned crystallites.

Rietveld refinement of the structural parameters of a 5% Li-substituted sample of $(Na_{1-x}Li_x)_2IrO_3$ was performed using X-ray diffraction data taken using the Rigaku SuperNova diffractometer at 300 K with FullProf [8], with the results tabulated in table 6.3. The analysis was performed using 718 reflections which were indexed from a single grain in the diffraction pattern. Due to the rotational twinning about the $\mathbf{c}^*$ axis all grains will contribute to the scattering intensity of the $(00L)$ peaks, but only one grain will contribute to the scattering intensity of all peaks away from the $\mathbf{c}^*$ axis. As a result, the measured scattering intensities of the $(00L)$ type peaks were anomalously high and consequently such peaks were ignored in the Rietveld analysis.

Cell parameters

Space group: $C2/m$ (#12)

a, b, c (Å)	5.36374(14)	9.2888(2)	5.59878(19)
α, β, γ (°)	90	108.755(4)	90

Volume (Å^3) 264.13(2)

Atomic fractional coordinates

Atom	Site	x	y	z	Occ.
Ir	$4g$	0.5	0.16682(9)	0	1
Na1	$2a$	0	0	0	1
Na2	$2d$	0.5	0	0.5	14/15
Li2	$2d$	0.5	0	0.5	1/15
Na3	$4h$	0.5	0.34104(161)	0.5	14/15
Li3	$4h$	0.5	0.34104(161)	0.5	1/15
O1	$8j$	0.75741(529)	0.17879(286)	0.80281(633)	1
O2	$4i$	0.71461(409)	0	0.19812(492)	1

Table 6.3: Refined 300 K crystal structure parameters of $(Na_{1-x}Li_x)_2IrO_3$ for $x = 0.05$

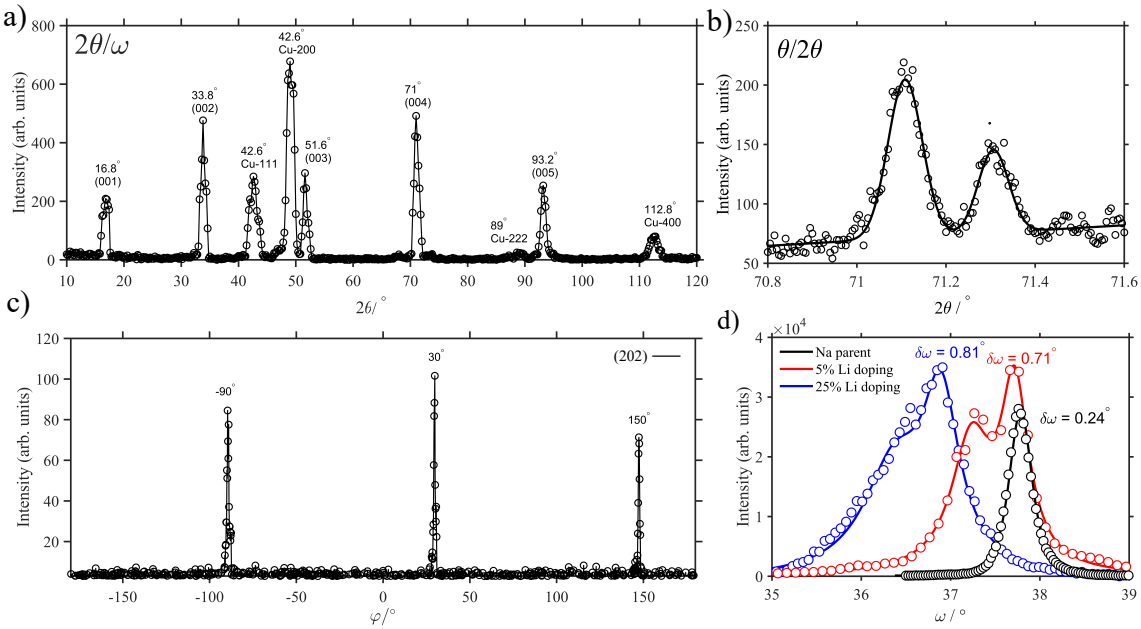

Figure 6.6: X-ray diffraction measurements using a point source detector showing a) a $2\theta/\omega$ scan - showing the surface normal is parallel to the (001) axis. Powder lines are also observed from the copper and brass materials of the sample holder. b) A $\theta/2\theta$ scan showing two peaks fitted to a Gaussian lineshape and a sloping background. The peaks have centres of 71.11° and 71.31° with widths 0.041° and 0.036°, respectively. The splitting of the peaks can be attributed to the splitting of the Cu $K\alpha$ line used as a source of x-rays. The appearance of only two single peaks suggests that the sample is single phase. c) A φ scan shows three peaks at $-90°$, 30°, and 150°. These can be attributed to three different (202) peaks from the presence of $\pm 120°$ rotational twins about the (001) axis. The scans in a-c were taken on a sample of $(Na_{1-x}Li_x)_2IrO_3$ for $x = 0.05$. d) ω scans of the (004) peak taken on a sample of Na_2IrO_3(black), and 5% (red) and 25% (blue) Li-substituted samples of $(Na_{1-x}Li_x)_2IrO_3$. The narrow and single peak line shape of the Na_2IrO_3 sample is contrasted to the broadened lineshapes consisting of multiple peaks - indicative of a broader mosaicity and poorer structural quality - for the 5% and 25% Li-substituted samples.

6.2 Resonant X-Ray Scattering Experimental Details

Of all samples characterised by x-ray diffraction, two 25% Li-substituted samples were selected for resonant elastic x-ray diffraction experiments using the P09 beamline at PETRA III [6, 9]. The samples were mounted with the (001) surface normal and cooled to a base temperature of 2 K. An extensive search of the high symmetry points and directions of the Brillouin zone was performed with an incident x-ray beam energy tuned to $E = 11.217$ keV, close to the Ir L_3 absorption edge. The search was performed using a Pilatus two-dimensional x-ray detector [10] and using an avalanche photodiode (APD) point

detector using a (333) aligned Au crystal as a polarisation analyser. In order to search for magnetic Bragg peaks corresponding to magnetic order with the ordering wavevector $\mathbf{q} = (0, 1, 1/2)_m$ of the parent Na_2IrO_3 compound, the magnetic resonant diffraction intensity was collected in scans along high symmetry directions in the monoclinic $0kl$ scattering plane. Additionally, magnetic Bragg peaks were searched for along high symmetry directions in the $h0l$ plane in order to test for incommensurate spiral order with magnetic ordering wavevector $\mathbf{q} = (h, 0, 0)_m$, as found in $\alpha - Li_2IrO_3$. However, no magnetic Bragg peaks were observed in either of these planes. This experiment may have failed to observe long range magnetic order for a number of reasons. First, the magnetic ordered moment of this material may be too small for magnetic Bragg peaks to have been observed within the sensitivity of the experimental setup. Moreover, the sample quality may have 'smeared' the usually sharp magnetic Bragg peaks into diffuse rods in reciprocal space. Furthermore, the $x = 0.25$ samples - with a proposed $T_N = 6$ K - may not have magnetically ordered at the achieved base temperature of the cryostat $T = 2.7$ K, with the sample also potentially unable to thermalise to the base temperature of the cryostat due to heating from the intense incident beam.

Additional resonant x-ray scattering (REXS) experiments were performed using the I16 beamline at the Diamond Light Source [7]. A $(Na_{1-x}Li_x)_2IrO_3$ sample of 5% Li doping and a diameter of 1 mm was selected and mounted with the (001) axis normal. The sample was cooled using a closed cycle refrigerator with concentric Be domes to a base CCR temperature of 5 K and the x-ray energy tuned to 11.217 keV, close to the Ir L_3 absorption edge. An initial search using a Pilatus two-dimensional detector [10] could not reliably detect magnetic peaks within the sensitivity of the instrument. However, the more sensitive APD detector was used and provided clear evidence for magnetic diffraction reflections.

Structural diffraction peaks were observed at $\boldsymbol{\tau} = (h, k, l)_m$ for $h+k =$ even. Additional peaks - shown in figure 6.7a-c - were observed at $\boldsymbol{\tau} \pm \mathbf{q}$ with the propagation vector given by $\mathbf{q} = (0, 1, 0.5)_m$. Notwithstanding the sample mosaicity, the peaks are relatively sharp and indicate long range magnetic order. The temperature dependence of the intensity of these peaks is shown in figure 6.7d, indicating a transition temperature $T_N = 12$ K. Furthermore,

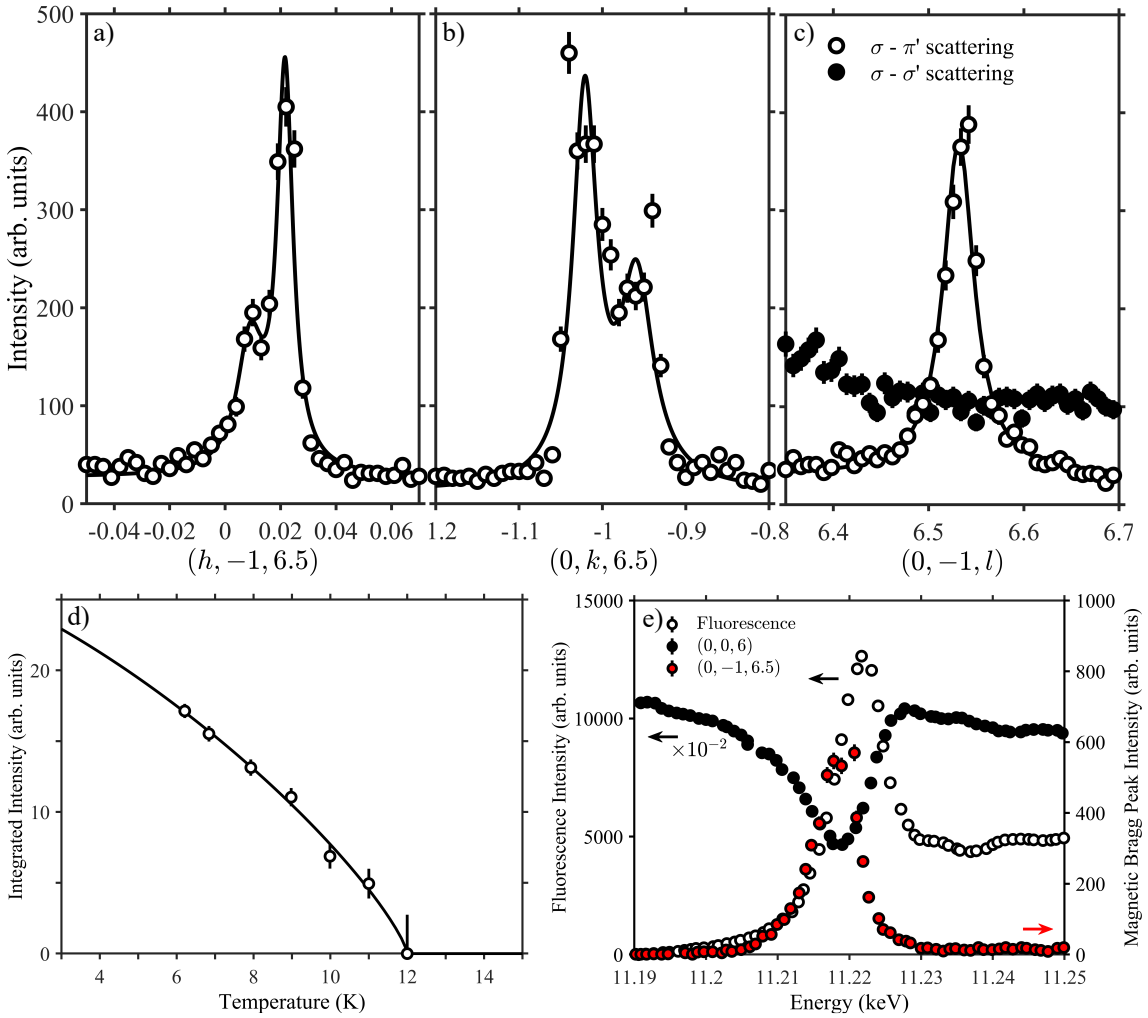

Figure 6.7: Resonant elastic x-ray scans for the magnetic peak at $(0, -1, 6.5)_m$. Open circles in scans a-c) along the $(h00)$, $(0k0)$, and $(00l)$ directions respectively show the scattering intensity in the $\sigma - \pi'$ channel using polarisation analysis. The filled circles in scan c) show the scattering intensity in the $\sigma - \sigma'$ channel, where the peak is no longer observed, but the background signal is far higher. The curves in a-c) show fits to a Lorentzian lineshape - where two Lorentzian peaks have been used in a) and b) - these additional features can be attributed to the sample mosaicity. d) Temperature dependence of the integrated intensity of the magnetic Bragg peak. The black line is a guide to the eye to highlight the onset of magnetic Bragg peak intensity below 12 K. e) Energy scan through the magnetic resonance energy for the magnetic $(0, -1, 6.5)_m$ Bragg peak (red circles), the structural $(0, 0, 6)$ Bragg peak (filled circles), and the fluoresence signal (open circles). The magnetic signal has a resonant enhancement of scattering intensity upon the onset of fluorescence, whereas the structural signal has a minimum of scattering intensity at the resonant energy, due to enhanced beam absorption near resonance.

the energy dependence of the peak intensity is plotted in figure 6.7e. The peaks at $\boldsymbol{\tau} \pm \mathbf{q}$ have a resonant enhancement of intensity, in contrast to the peaks at $\boldsymbol{\tau}$ which have a reduction

in scattering intensity around the Ir L_3 absorption edge. The temperature and energy dependence of the scattering intensity of the $\boldsymbol{\tau} \pm \mathbf{q}$ peaks indicate that they are indeed magnetic in origin.

A further indication of the magnetic nature of the $\boldsymbol{\tau} \pm \mathbf{q}$ peaks can be seen from polarisation analysis of the scattered x-rays. For an incident beam with a polarisation normal to the scattering plane, charge scattering will be seen in the $\sigma - \sigma'$ channel where the direction of the polarisation is unchanged by scattering, and remains normal to the scattering plane. Conversely, magnetic scattering will be seen in the $\sigma - \pi'$ channel where the polarisation is rotated 90° to lie in the scattering plane. In this experiment, polarisation analysis was performed using the (333) reflection from an Au crystal. As can be seen in figure 6.7c, the peaks at $\boldsymbol{\tau} \pm \mathbf{q}$ were only observed in $\sigma - \pi'$ scattering, but were absent in $\sigma - \sigma'$ scattering.

In addition to investigating the magnetic structure via measurements of the magnetic Bragg peaks, the structural quality of the sample was investigated by translating the sample in the plane normal to the sample surface normal and performing a rocking curve scan - denoted by the angle η - about the structural $(0, 0, 6)$ Bragg peak. The rocking curve angle η is equivalent to the angle ω in the scans in figure 6.6d. The maximum intensity in each rocking curve scan can be plotted as a function of the two translational displacements s_x and s_y to form a raster map. In this measurement, a 10-by-10 grid of points with a step size of 0.1 mm was used. This can be contrasted with the size of the beam footprint which is approximately 20 μm in diameter. The raster map in figure 6.8a reveals three 'hotspot' regions of high scattering, and the rocking curve scans at each hotspot are peaked at different values in η - with the third brightest point exhibiting multiple peaks in the η scan. This range in the number of peaks can be attributed to the mosaicity of the crystalline sample. Magnetic Bragg peaks were searched for, but could not be found, with the beam centred on the brightest 'hotspot' - labelled 2 in figure 6.8a; magnetic Bragg peaks could be found, however, in the second brightest 'hotspot' - labelled 1 in figure 6.8a.

With the structural quality of the sample surveyed with a raster map and confirmation of the magnetic nature of the $\boldsymbol{\tau} \pm \mathbf{q}$ magnetic Bragg peaks with the ordering wavevector $\mathbf{q} = (0, 1, 0.5)$, an azimuthal scan was performed by placing the sample in the scattering condition to scatter from the $(0, -1, 6.5)$ magnetic Bragg peak, and rotating the polarisation

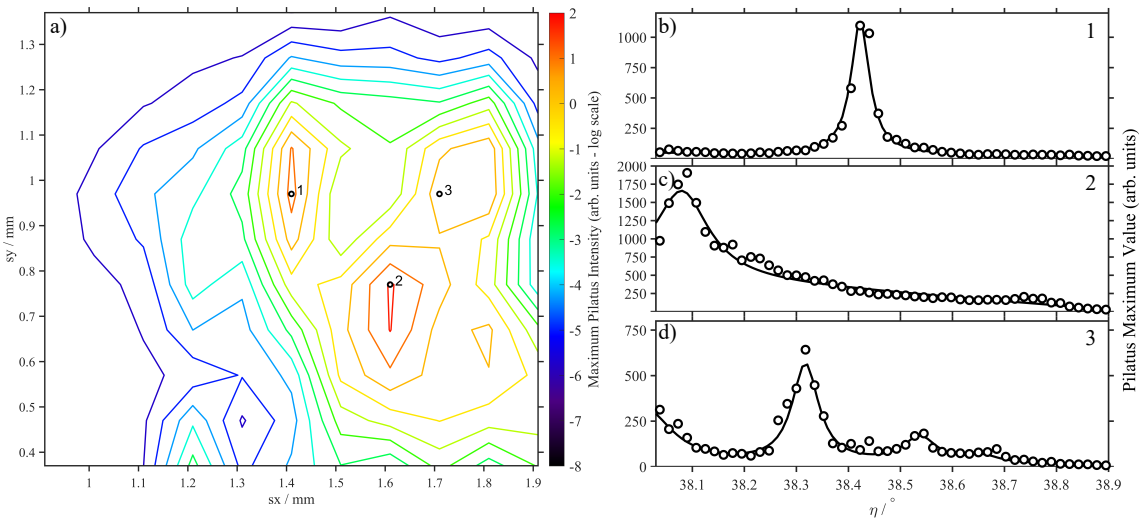

Figure 6.8: a) Raster map showing the intensity of the $(0, 0, 6)$ structural Bragg peak scanned across the surface sample. The three brightest regions are denoted by a small circle and numbered. b-d) Rocking curve - η - scans at the corresponding brightest 'hotspot' points showing different peak positions in η - indicating that the sample has a $0.5(1)^\circ$ mosaicity.

analyser to measure magnetic scattering in the $\sigma - \pi'$ channel. The sample can be rotated around the wavevector transfer $\mathbf{Q}$ with the azimuthal angle parametrised by ψ, with the convention that $\psi = 0^\circ$ places $\mathbf{a}_m^*$ in the scattering plane, and ψ increases as the sample is rotated anti-clockwise about $\mathbf{Q}$. The selected values of ψ range from 20° to -180° and from -180° to 80°, incremented in steps of 12.5°. A scan through the $(0, -1, 6.5)$ magnetic Bragg peak along the $(0, 0, 1)$ direction was taken for each ψ value.

Some scans appeared to consist of multiple peaks: all scans had a peak at a fixed value of L and with fixed width δL (see figure 6.9b), however some scans included an additional peak increasing the total scattering intensity (see figure 6.9c). Plotting the total scattering intensity as a function of the azimuthal angle ψ gives an asymmetrical shape, whereas plotting the scattering intensity of the peak of fixed centre and width produces a symmetrical shape - with two anomalous points where the two peaks in the L scan could not be resolved - at $\psi = -30^\circ$ and -17.5°. The additional scattering intensity may be understood as the beam moving across the surface of the sample upon rotating ψ. For a range of angles of ψ from -42.5° to 7.5°, the beam may strike a region of the sample with a misaligned - yet still magnetically ordered - grain that contributes additional scattering intensity to the

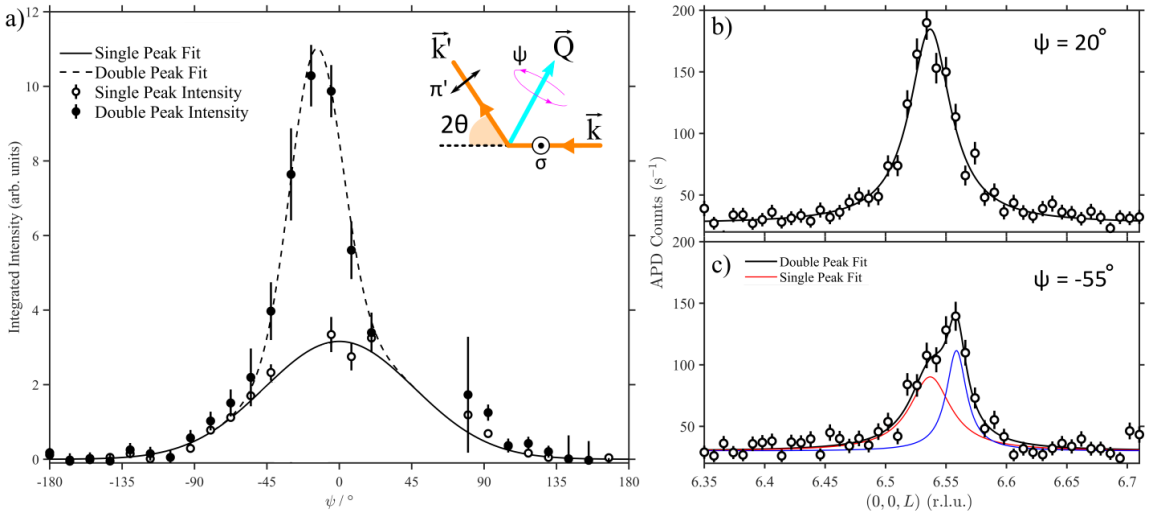

Figure 6.9: a) Integrated intensity of the $(0, -1, 6.5)_m$ magnetic Bragg peak as a function of the azimuthal angle ψ. Each point in the ψ scan is found by scanning along the $(0, 0, L)$ direction and attempting to fit a peak profile. The solid line is a Gaussian fit to the open points - the dashed line has an additional Gaussian added fitted to the filled points; the dotted line has an additional Gaussian subtracted to fit the single peak intensity. The L scan for b) $\psi = 20°$ is fitted with a single Lorentzian lineshape; the scan for c) $\psi = -55°$ is fitted with two Lorentzian lineshapes (red and blue lines). The lineshape shown in red has the same centre and width as the single peak in (b), the solid line in (c) is the sum of the lineshapes shown in red and blue. The single peak intensity points in (a) (open points) are found from the area of the peaks fitted with the same centre and width as the red peak in (c), whereas the double peak intensity points in (a) (filled points) are found from the area of the scattering signal - i.e. the black lines in (b) and (c). The scattering geometry is shown in the inset to (a).

L scans. The scattering intensity for the single peak fit is consistent with previous REXS experiments on Na_2IrO_3 [11].

6.3 Structure Factor Analysis

The observation of magnetic Bragg peaks with a magnetic ordering wavevector of $\mathbf{q} = (0, 1, 0.5)_m$ reveals information about the magnetic structure. The component of $\mathbf{q}$ along $\mathbf{c}^*$ reveals that the honeycomb layers are stacked antiferromagnetically, and the components of $\mathbf{q}$ in the hk plane can be used to attempt to reconstruct the arrangement of spins in a single honeycomb layer. The two Ir ions have fractional coordinates $(0, \pm y_{Ir}, 0)$ with $y_{Ir} = 0.332$ and can be labelled as Ir1 and Ir2, respectively. Due to the C-centring there are an additional pair of Ir ions, labelled as Ir3 and Ir4, with positions $(1/2, 1/2 \pm y_{Ir}, 0)$.

For any given arrangement of the magnetic moments of the Ir1 and Ir2 ions, the magnetic ordering wavevector fixes the moment orientation of the Ir3 and Ir4 to be anti-parallel to their corresponding ions related by C-centring.

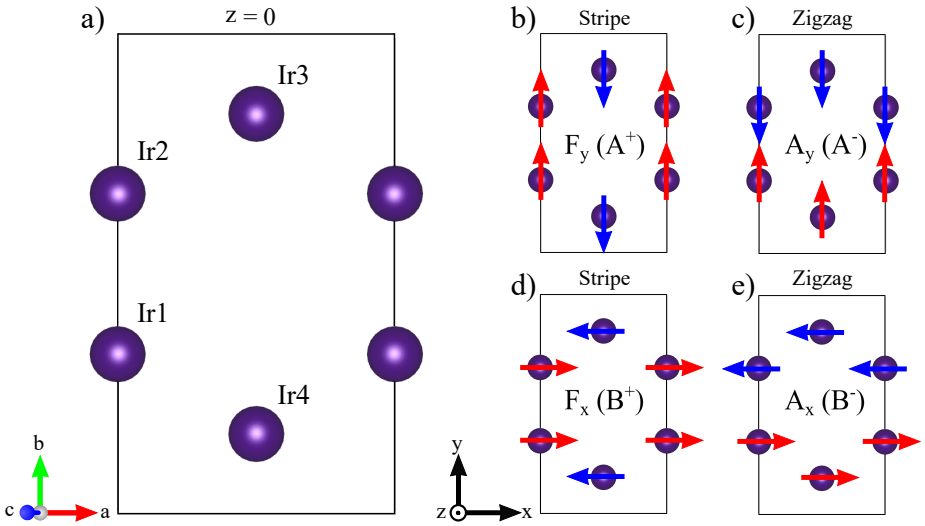

Figure 6.10: a) $z = 0$ layer of the magnetic iridium ions with b-e) magnetic structures that transform according to single irreducible representations. The Ir3, 4 sites are related to the Ir1, 2 sites by a translation of $(1/2, 1/2, 0)$. Moments related by this translation will have anti-parallel spins. The degrees of freedom of the orientation of the magnetic moments of the Ir1, 2 sites can be described by basis vectors. The F/A basis vector denotes a parallel/anti-parallel arrangement of the moments on the Ir1, 2 sites, and the subscript denotes the component of the moment described by the basis vector.

The real space orientation of the moments on the Ir1 and Ir2 sites remain unfixed and may be decomposed into basis vectors in the following form

$$\mathbf{M}_n = \sum_{\alpha} (a_\alpha A^n_\alpha + f_\alpha F^n_\alpha)\hat{\boldsymbol{\alpha}}, \tag{6.9}$$

where n can take the value 1 or 2 and denotes the Ir1 and Ir2 ion, the sum is over the Cartesian coordinates $\alpha = x, y, z$ as defined in equation 6.2, and the basis vectors F^n_α and A^n_α denote parallel and anti-parallel arrangement of the α component of the Ir1 and Ir2 moments. These basis vectors will transform according to different irreducible representations of the $2/m$ point group symmetry of the crystal structure, as tabulated in table 6.4 [12].

The F basis vectors transform under the elements of the symmetry group as gerade irreducible representations, and as depicted in figure 6.10b,d form a magnetic ground state with stripe ordering. On the other hand, the A basis vectors depicted in figure 6.10c,e

Irrep	E	C_2	i	iC_2	Basis vector
A_g	1	1	1	1	F_y
B_g	1	-1	1	-1	F_x, F_z
A_u	1	1	-1	-1	A_y
B_u	1	-1	-1	1	A_x, A_z

Table 6.4: Character table of the $2/m$ (C_{2h}) point group.

transform as ungerade irreducible representations and give a magnetic ground state with zigzag ordering. The structure factors corresponding to the F and A basis vectors - and hence the stripe and zigzag magnetic ground states depicted in figure 6.10- for magnetic scattering at the wavevector $\mathbf{Q} = (h, k, l) \pm \mathbf{q}$ are proportional to

$$\begin{aligned} S^F_{\mathbf{Q}} &= 2 f_C \cos\left[2\pi(k \pm 1)y\right], \\ S^A_{\mathbf{Q}} &= 2 f_C i \sin\left[2\pi(k \pm 1)y\right], \end{aligned} \tag{6.10}$$

where $f_C = 1 + e^{i\pi(h+k)}$ enforces the $h + k =$ even selection rule imposed by the C-centring of the lattice. In the case where $y_{Ir} = 1/3$, the F basis vectors contribute to the magnetic scattering for all allowed magnetic Bragg peak positions. Conversely, the A basis vectors contribute to magnetic scattering only for magnetic Bragg peaks that are the $\pm\mathbf{q}$ satellites of the (h, k, l) structural Bragg peaks for $k \pm 1 \neq 3n$, for integer n. Since no magnetic scattering intensity was observed for $\mathbf{Q} = (1, 0, 6.5)$, the F basis vectors can be ruled out and the magnetic structure taken to be zig-zag ordered, with an A basis vector corresponding to the A_u and B_u irreducible representations in table 6.4.

The real space components of the magnetic moments can be written in terms of Fourier components in the following form

$$\mathbf{M}_n(\mathbf{r}) = \sum_{\mathbf{k}=\pm\mathbf{q}} \mathbf{M}_{\mathbf{k},n} e^{-i\mathbf{k}\cdot\mathbf{r}}. \tag{6.11}$$

For the A basis vector, the Fourier components satisfy $\mathbf{M}_{\mathbf{q},1} = -\mathbf{M}_{\mathbf{q},2}$ and sites related by C-centring translations have the same Fourier components. Additionally, $\mathbf{M}_{\mathbf{q},n} = \mathbf{M}^*_{-\mathbf{q},n}$

ensures that the real space moments are real. The magnetic structure factor is then given by

$$\begin{aligned}\boldsymbol{\mathcal{F}}(\mathbf{Q}) &= \sum_n \mathbf{M}_{\pm\mathbf{q},n} e^{i\mathbf{Q}\cdot\mathbf{r}_n} \\ &= \sum_\alpha M^\alpha_{\pm\mathbf{q},n} S^A_{\mathbf{Q}} \hat{\boldsymbol{\alpha}},\end{aligned} \tag{6.12}$$

where α denotes Cartesian coordinates x, y, and z.

6.4 Azimuthal Dependence of Scattering Intensity

In a resonant x-ray scattering experiment, the incoming beam of wavevector $\mathbf{k}$ and polarisation $\boldsymbol{\epsilon}$ is scattered from the sample into an outgoing beam of wavevector $\mathbf{k}'$ and polarisation $\boldsymbol{\epsilon}'$. The intensity at a scattering wavevector $\mathbf{Q} = \mathbf{k}' - \mathbf{k}$ is proportional to [13]

$$\left|(\hat{\boldsymbol{\epsilon}'} \times \hat{\boldsymbol{\epsilon}}) \cdot \boldsymbol{\mathcal{F}}(\mathbf{Q})\right|^2. \tag{6.13}$$

For a σ-polarised incident beam, the magnetic scattering intensity will appear only in the $\sigma - \pi'$ channel. In this case, the cross product of the polarisation vectors of the incident and scattered beams will be parallel to the wavevector of the scattered beam: $\hat{\boldsymbol{\epsilon}'} \times \hat{\boldsymbol{\epsilon}} = \hat{\mathbf{k}}'$. Consequently, the magnetic scattering intensity will depend only upon the component of the magnetic structure factor parallel to the scattered beam wavevector - $\mathcal{F}_\parallel$. In the case of a magnetic structure described by a single irreducible representation, the magnetic basis vector may be of the form of $(A_x, 0, A_z)$ corresponding to the B_u irreducible representation and moments constrained to the ac plane, or the basis vector may be of the form $(0, A_y, 0)$ corresponding to the A_u irreducible representation with moments constrained to the monoclinic $\mathbf{b}$ axis. An azimuthal scan can be performed by keeping the sample in the scattering condition and rotating the sample around the scattering wavevector $\mathbf{Q}$. The projection of the structure factor onto the direction of the scattered beam will depend on the azimuthal angle ψ, where $\psi = 0^\circ$ corresponds to the condition that the monoclinic $\mathbf{a}^*$ axis lies in the scattering plane, and the sample rotates counter-clockwise with increasing ψ. By perform-

ing an azimuthal scan by rotating about $\mathbf{Q} = (0, -1, 6.5)_m$ - approximately parallel to the $\mathbf{c}^*$ axis - the scan is peaked around $\psi = 0°$ which corresponds to the monoclinic ac plane lying almost parallel to the scattering plane. Therefore, by assuming a magnetic structure that transforms under a single irreducible representation, the magnetic basis vectors can be taken to be $(A_x, 0, A_z)$ with magnetic moments lying in the monoclinic ac plane. Further analysis of the azimuthal ψ dependence of the magnetic x-ray scattering intensity allows the moment orientation within the ac plane to be estimated; the absolute magnitude of the magnetic moments, however, cannot be determined from the resonant x-ray scattering experiment.

In order to evaluate the magnetic scattering intensity as a function of the azimuthal angle ψ, it is useful to define two separate Cartesian frames. The first is a 'crystallographic' frame denoted by xyz, defined in equations 6.2-6.5 such that the monoclinic $\mathbf{a}$ axis lies along the $\hat{\mathbf{x}}$ axis, the $\mathbf{b}$ axis lies along the $\hat{\mathbf{y}}$ axis, and $\mathbf{c}^*$ axis lies along the $\hat{\mathbf{z}}$ axis. In this case, the scattering vector $\mathbf{Q} = (0, -1, 6.5)_m$ lies entirely within the yz plane and makes an angle λ with the $\hat{\mathbf{z}}$ axis where $\tan\lambda = kc_m \sin\beta/(lb_m)$. It is important to note that the above choice of $\mathbf{Q}$ gives a negative value of λ, see figure 6.11. The second frame is a 'laboratory' frame with an orthonormal basis $\hat{\mathbf{u}}_1$, $\hat{\mathbf{u}}_2$, and $\hat{\mathbf{u}}_3$: where $\hat{\mathbf{u}}_3$ is parallel to $\mathbf{Q}$, $\hat{\mathbf{u}}_2$ is parallel to $\mathbf{k} \times \mathbf{k}'$ and is normal to the scattering plane, and $\hat{\mathbf{u}}_1 = \hat{\mathbf{u}}_2 \times \hat{\mathbf{u}}_3$. For $\psi = 0°$, $\mathbf{a}^*$ is in the scattering plane and the scattered beam direction is most readily defined in the laboratory frame where $\hat{\mathbf{k}}' = \cos\theta\hat{\mathbf{u}}_1 + \sin\theta\hat{\mathbf{u}}_3$. On the other hand, the moment direction is most readily defined in the crystallographic axes. As a result, it is useful to define a transformation between the crystallographic and laboratory frames.

The magnetic structure factor can be written with components $(\mathcal{F}_x, \mathcal{F}_y, \mathcal{F}_z)$ in the crystallographic frame or with components $(\mathcal{F}_1, \mathcal{F}_2, \mathcal{F}_3)$ in the laboratory frame. These two coordinate systems can be related by the transformation

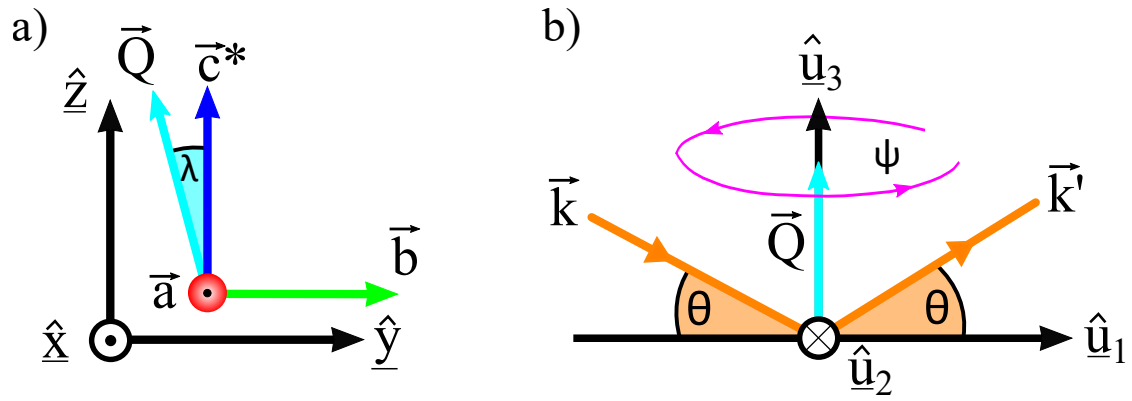

Figure 6.11: Illustration of a) the xyz coordinate system defined in terms of the crystallographic lattice vectors, and b) the $u_1u_2u_3$ coordinate system defined in terms of the scattering geometry. The cyan arrow denotes $\mathbf{Q}$, the scattering wavevector, which is along the $\hat{\mathbf{u}}_3$ axis, and is in the yz plane - subtending an angle λ from the $\hat{\mathbf{z}}$ axis towards $\hat{\mathbf{y}}$. The orange arrows denote the incoming and scattered beam, labelled $\mathbf{k}$ and $\mathbf{k}'$, respectively. The scattering angle is 2θ, with $\hat{\mathbf{u}}_2$ normal to the scattering plane, and $\hat{\mathbf{u}}_1$ subtending an angle θ from $\mathbf{k}'$. The magenta arrow denotes the azimuthal angle ψ which is a right handed rotation about $\mathbf{Q}$.

$$\begin{pmatrix} \mathcal{F}_1 \\ \mathcal{F}_2 \\ \mathcal{F}_3 \end{pmatrix} = T(\psi = 0) \begin{pmatrix} \mathcal{F}_x \\ \mathcal{F}_y \\ \mathcal{F}_z \end{pmatrix}, \tag{6.14}$$

where the transformation $T(\psi = 0)$ maps coordinates in the xyz crystallographic frame to coordinates in the $u_1u_2u_3$ laboratory frame when the azimuthal angle $\psi = 0$, in which case the $\mathbf{a}^*$ axis lies in the scattering plane. This matrix form of this transformation is

$$T(\psi = 0) = \begin{pmatrix} \sin\beta/N & \sin\lambda\cos\lambda\cos\beta/N & -\sin^2\lambda\cos\beta/N \\ -\sin\lambda\cos\beta/N & \cos\lambda\sin\beta/N & -\sin\lambda\sin\beta/N \\ 0 & \sin\lambda & \cos\lambda \end{pmatrix}, \tag{6.15}$$

where N is a normalising factor given by $\sqrt{\sin^2\lambda\cos^2\beta + \sin^2\beta}$. For any general azimuthal angle ψ, the system is rotated about the $\hat{\mathbf{u}}_3$ axis. Let $T(\psi)$ be the transformation between

coordinates in the xyz frame to coordinates in the $u_1u_2u_3$ frame for any azimuthal angle ψ. This matrix form of this transformation is given by

$$T(\psi) = R(\psi)T(\psi = 0) = \begin{pmatrix} \cos\psi & -\sin\psi & 0 \\ \sin\psi & \cos\psi & 0 \\ 0 & 0 & 1 \end{pmatrix} T(\psi = 0). \tag{6.16}$$

Now, the projection of the magnetic structure factor onto the scattered beam direction is given by $\boldsymbol{\mathcal{F}} \cdot \hat{\mathbf{k}}' = \mathcal{F}_1 \cos\theta + \mathcal{F}_3 \sin\theta$. Using the transformation of $T(\psi)$, this expression can be written in terms of the components of the moment in the xyz frame. Explicitly, $\boldsymbol{\mathcal{F}} \cdot \hat{\mathbf{k}}' = \sum_{\alpha=x,y,z} g_\alpha \mathcal{F}_\alpha$, where the geometric factors g_α are given by:

$$\begin{aligned} g_x &= \cos\theta \cos\psi', \\ g_y &= -\cos\theta \sin\psi' \cos\lambda + \sin\theta \sin\lambda, \\ g_z &= \cos\theta \sin\psi' \sin\lambda + \sin\theta \cos\lambda, \end{aligned} \tag{6.17}$$

where the angle ψ' is defined by $\psi - \arctan(\sin\lambda/\tan\beta)$ in order to simply the expressions of the geometric factors. The angular shift $\arctan(\sin\lambda/\tan\beta)$ arises since $\psi = 0$ corresponds to the $\mathbf{a}^*$ axis lying in the plane, yet due to the monoclinic crystal structure $\mathbf{a}$ and $\mathbf{a}^*$ are not parallel, and so there is a small offset of the $\mathbf{a}$ axis from the scattering plane for $\psi = 0$. In this case, the angular shift $\arctan(\sin\lambda/\tan\beta)$ takes the value $1.56°$. For magnetic moments constrained to the ac plane with an angle μ from the $\mathbf{a}$ axis, the components of the magnetic moment written in terms of the crystallographic axes is given by $M(\cos\mu, 0, \sin\mu)$ and the projection of the magnetic structure factor to the scattered beam direction is proportional to

$$\begin{aligned} \boldsymbol{\mathcal{F}} \cdot \hat{\mathbf{k}}' &\propto (g_x \cos\mu + g_z \sin\mu) \\ &= \left(\cos\mu\cos\theta\cos\psi' + \sin\mu\sin\lambda\cos\theta\sin\psi' + \sin\mu\cos\lambda\sin\theta\right). \end{aligned} \tag{6.18}$$

The intensity profile can be modelled for the moment orientation angle μ by finding the square of equation 6.18. As a result, the moment orientation angle was fitted to $\mu = 38.1° \pm 3.2°$. The same magnetic structure has been proposed for pure Na_2IrO_3 with a moment orientation angle of $44.3° \pm 1.2°$ [14].

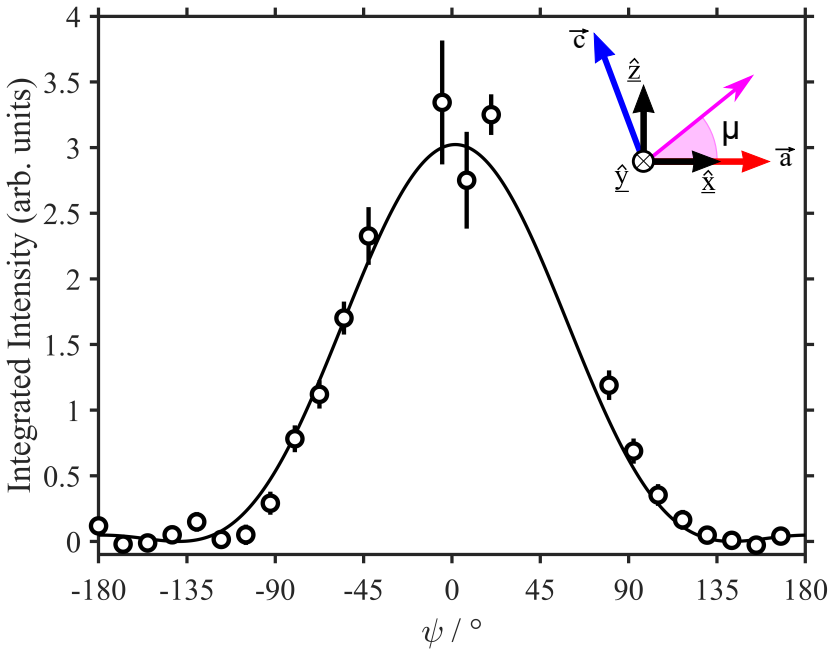

Figure 6.12: Azimuthal scan about the $(0, -1, 6.5)_m$ magnetic Bragg peak (open circles, from figure 6.9) with a fitted profile for magnetic moments constrained to the crystallographic ac plane and the moment direction subtending an angle μ - fitted to be $38.1° \pm 3.2°$ - from the **a** axis. It is assumed that the moments are constrained to the ac plane - shown in the inset diagram - with the magenta arrow denoting the direction of the magnetic moment.

Relaxing the assumption of a magnetic structure with a single irreducible representation allows for a tilting of the Ir moments out of the ac plane described by the A_y basis vector. In this case, the real space moment orientation is given by $M(\sin\zeta\cos\mu, \cos\zeta, \sin\zeta\sin\mu)$ with components written in terms of the crystallographic axes. Here, $\zeta = \pi/2$ constrains the magnetic moments to the ac plane and the previous magnetic structure is recovered; a small tilt out of the plane can be parametrised by $\delta\zeta$ such that $\zeta = \pi/2 + \delta\zeta$. The A_y basis vector will have a relative phase φ with respect to the A_x and A_z basis vectors, and using equation 6.12 gives a magnetic structure factor of

$$\boldsymbol{\mathcal{F}}(\mathbf{Q}) = S^A_{\mathbf{Q}} \left(\cos\mu\hat{\mathbf{x}} - \delta\zeta e^{i\varphi}\hat{\mathbf{y}} + \sin\mu\hat{\mathbf{z}}\right) + \mathcal{O}\left((\delta\zeta)^2\right). \tag{6.19}$$

The effect of the out-of-plane tilt of the magnetic moment can be seen by first noting that the offset angle λ is small. Then by combining the geometric factors in equation 6.17 for $\lambda = 0^\circ$ - in which case $\psi' = \psi$ - and the expression for the magnetic form factor in equation 6.19, the component of the magnetic form factor along the scattered beam direction for spins canted at a small angle $\delta\zeta$ out of the ac plane will be approximately

$$\mathcal{F}_{\parallel} \approx S^A_{\mathbf{Q}} \left[(\cos\mu\cos\theta\cos\psi + \sin\mu\sin\theta) + \delta\zeta e^{i\varphi}\cos\theta\sin\psi + \mathcal{O}\left((\delta\zeta)^2\right)\right]. \tag{6.20}$$

Consequently, the resonant magnetic scattering intensity can be written as a power series of the tilt angle $\delta\zeta$. Specifically, $I(\delta\zeta) = I^{(0)} + I^{(1)}\delta\zeta + \mathcal{O}\left((\delta\zeta)^2\right)$, where $I^{(0)}$ is proportional to the square of the expression in equation 6.18 and $I^{(1)}$ is approximate to

$$I^{(1)} \approx \left|S^A_{\mathbf{Q}}\right|^2 \cos\varphi \left[\cos\mu\cos^2\theta\sin 2\psi + \sin\mu\sin 2\theta\sin\psi\right]. \tag{6.21}$$

As a result, it may be concluded that the leading order correction to the resonant magnetic scattering intensity for a small tilt of the magnetic moments out of the ac plane is an odd function of the azimuthal angle ψ. Additionally, the effect of the out-of-plane tilt is maximal when the phase between the magnetic basis vectors - φ - is an integer multiple of π. By fitting the exact form of the magnetic resonant scattering intensity for $\varphi = 0^\circ$, the out-of-plane tilt was fitted to be $\delta\zeta = 2.5^\circ \pm 4.6^\circ$ - and so it may be concluded that the best fit for the magnetic structure is that the magnetic moments are constrained to the monoclinic ac plane.

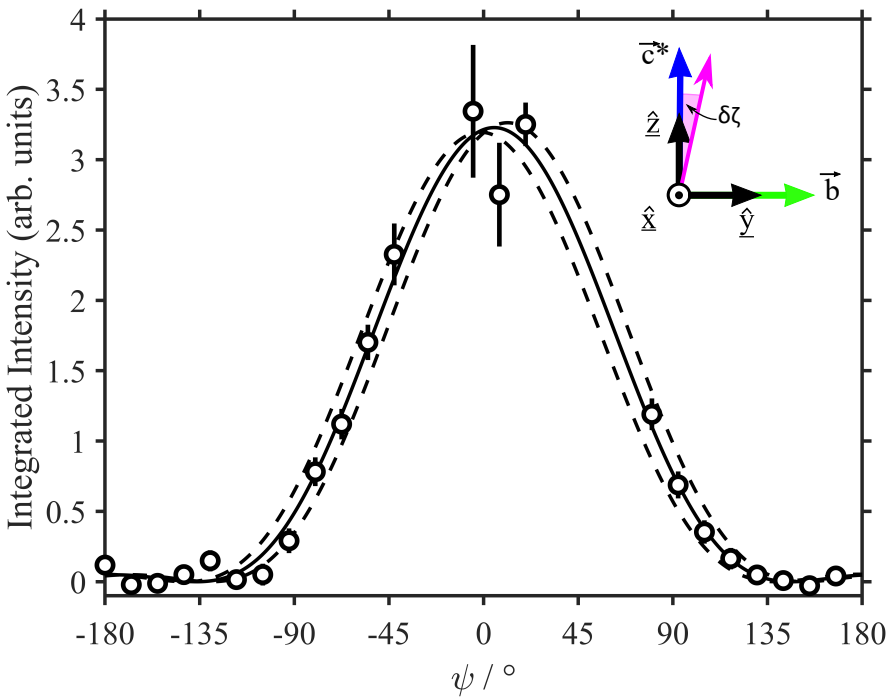

Figure 6.13: Azimuthal scan about the $(0, -1, 6.5)_m$ magnetic Bragg peak with a fitted profile for magnetic moments tilted out of the *ac* plane and the moment direction subtending an angle $\delta\zeta$ - fitted to be $2.5° \pm 4.6°$ - from the $\mathbf{c}^*$ axis. The solid line shows the fitted profile for $\delta\zeta = 2.5°$, with the dotted lines showing the two fitted profiles for $\delta\zeta = 2.5° \pm 4.6°$. The angle $\delta\zeta$ parametrises the tilting of the moments out of the *ac* plane - shown in the inset diagram - with the magenta arrow denoting the direction of the magnetic moment.

6.5 Fitted Magnetic Structure

The previous analysis of REXS experimental data has determined that the magnetic ordering wavevector of a 5% Li-doped sample of $(Na_{1-x}Li_x)_2IrO_3$ is $(0, 1, 1/2)_m$ with a zig-zag magnetic structure described by the A_x and A_z basis vectors, which transform as the B_u irreducible representation of the point group $2/m$. These basis vectors reproduce the absence of magnetic scattering at $(1, 0, 6.5)_m$ and the intensity profile of the azimuthal scan at $(0, -1, 6.5)_m$, and give one free parameter - μ - which parametrises the orientation of the moment in the *ac* plane, fitted - as shown in figure 6.12 - with a value $38.1° \pm 3.2°$. The amplitude of the magnetic moment, however, cannot be measured by REXS yet may be measured in further studies using neutron powder diffraction, as done in similar studies of Na_2IrO_3 [15]. Relaxing the assumption of a magnetic structure described by a single irreducible representation allows for the tilting of the magnetic moments out of the *ac* plane.

The fitted value of this tilt is small - $\delta\zeta = 2.5^\circ \pm 4.6^\circ$ - and the special case of moments confined to the *ac* plane ($\delta\zeta = 0^\circ$) is within the error bars of this fitted value. Consequently, the best fit magnetic structure is zig-zag ordering with spins confined to the *ac* plane - consistent with the magnetic structure of Na_2IrO_3[2]. Such a magnetic structure is in the neighbourhood of the Kitaev limit in the Heisenberg-Kitaev model [16, 17], and further studies, such as inelastic resonant x-ray scattering [14] or inelastic neutron scattering [2] may allow the exchange parameters stabilising the ground state to be constrained to within an experimentally determined range of values.

The Fourier component $\mathbf{M}_{\mathbf{q},n}$ of the site with index n has the following properties

1. The magnetic structure is described by the A basis vectors: $\mathbf{M}_{\mathbf{q},1} = -\mathbf{M}_{\mathbf{q},2}$,
2. The moments are constrained to the *ac* plane: $M_x = M\cos\mu$, $M_y = 0$, $M_z = M\sin\mu$,
3. The real space orientation of the moments must be a real number: $\mathbf{M}_{\mathbf{q},n} = \mathbf{M}^*_{-\mathbf{q},n}$,

the Fourier components are given by

$$\mathbf{M}_{\mathbf{q},n} = (-1)^{n+1}\frac{M}{2}\left[\hat{\mathbf{x}}\cos\mu + \hat{\mathbf{z}}\sin\mu\right]e^{i\mathbf{q}\cdot(\mathbf{r}_n - \mathbf{r}_1)}. \tag{6.22}$$

The Fourier components of the moments can be used to construct the real space orientation of the magnetic moments using equation 6.11 - and is given by

$$\mathbf{M}_n(\mathbf{r}) = (-1)^{n+1}M\left[\hat{\mathbf{x}}\cos\mu + \hat{\mathbf{z}}\sin\mu\right]\cos\mathbf{q}\cdot\mathbf{r}_n. \tag{6.23}$$

Where $\mathbf{M}_n(\mathbf{r})$ denotes the magnetic moment at position $\mathbf{r}$ with site index $n = 1, 2$ corresponding to the sites Irn of figure 6.10. Translating by the C-centring vector $(1/2, 1/2, 0)$, or by translating by the crystallographic $\mathbf{c}$ lattice vector will reverse the direction of the magnetic moment. The proposed magnetic structure for 5% Li-substituted $(Na_{1-x}Li_x)_2IrO_3$ is plotted in figure 6.14.

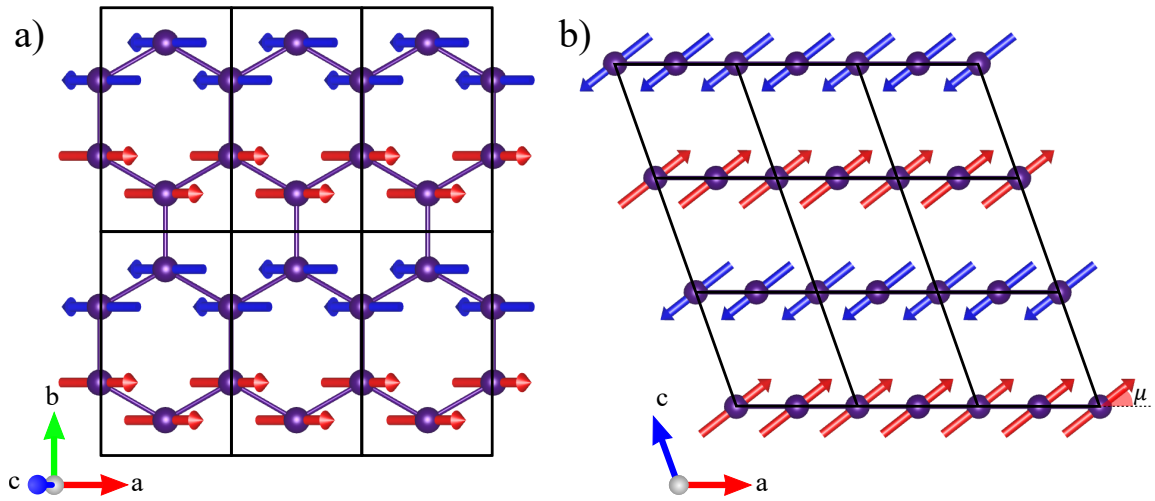

Figure 6.14: Magnetic structure of 5% Li-doped $(Na_{1-x}Li_x)_2IrO_3$ viewed a) in the *ab* plane of the honeycomb layers, and b) in the *ac* plane perpendicular to the plane of the honeycomb layers. The iridium ions are denoted by purple spheres, with nearest neighbour bonds also denoted in purple. The boundaries of the structural unit cell are denoted by the solid black lines. The magnetic structure is antiferromagnetic and consists of antiparallel spins of equal magnitude, shown in red and blue respectively. The magnetic structure has zig-zag ordering with anti-parallel moments for sites related by a centring translation. The honeycomb layers stack antiferromagnetically, and moments corresponding to sites related by a translation of the structural lattice parameter **c** are anti-parallel.

6.6 Conclusions

In summary, the structural quality of isoelectronically doped honeycomb iridate crystalline samples were measured using x-ray diffraction, and stacking faults and rotational twins were found to be ubiquitous features of such samples. The structural quality of these samples proved to be a limiting factor in the ability to employ resonant elastic x-ray scattering techniques in order to determine the magnetic structure of honeycomb iridates. Despite these limitations, the magnetic structure of a single 5% Li-substituted sample was measured, and found to exhibit zig-zag ordering with moments constrained to the *ac*-plane. Such ordering has previously been measured on the parent material Na_2IrO_3, however, isoelectronic doping appears to change the spin orientation angle in the *ac*-plane, in addition to suppressing

the Néel temperature.

References

1. Jackeli, G. & Khaliullin, G. Mott Insulators in the Strong Spin-Orbit Coupling Limit: From Heisenberg to a Quantum Compass and Kitaev Models. *Phys. Rev. Lett.* **102,** 017205 (2009).

2. Choi, S. K. *et al.* Spin Waves and Revised Crystal Structure of Honeycomb Iridate Na_2IrO_3. *Phys. Rev. Lett.* **108,** 127204 (2012).

3. Freund, F. *et al.* Single crystal growth from separated educts and its application to lithium transition-metal oxides. *Sci Rep* **6,** 35362 (2016).

4. Williams, S. C. *et al.* Incommensurate counterrotating magnetic order stabilized by Kitaev interactions in the layered honeycomb $\alpha-Li_2IrO_3$. *Phys. Rev. B* **93,** 195158 (2016).

5. Manni, S. *et al.* Effect of isoelectronic doping on the honeycomb-lattice iridate A_2IrO_3. *Phys. Rev. B* **89,** 245113 (2014).

6. Strempfer, J. *et al.* Resonant scattering and diffraction beamline P09 at PETRA III. *Journal of Synchrotron Radiation* **20,** 541–549 (2013).

7. Collins, S. P. *et al.* Diamond Beamline I16 (Materials & Magnetism). *AIP Conference Proceedings* **1234,** 303–306 (2010).

8. Rodriguez-Carvajal, J. Recent advances in magnetic structure determination by neutron powder diffraction. *Physica B* **192,** 55 (1993).

9. Francoual, S. *et al.* Single-crystal X-ray diffraction and resonant X-ray magnetic scattering at helium-3 temperatures in high magnetic fields at beamline P09 at PETRA III. *Journal of Synchrotron Radiation* **22,** 1207–1214 (2015).

10. Brönnimann, C. & Trüb, P. in *Synchrotron Light Sources and Free-Electron Lasers: Accelerator Physics, Instrumentation and Science Applications* (eds Jaeschke, E. J., Khan, S., Schneider, J. R. & Hastings, J. B.) 995–1027 (Springer International Publishing, Cham, 2016).

11. Liu, X. *et al.* Long-range magnetic ordering in Na_2IrO_3. *Phys. Rev. B* **83,** 220403 (2011).

12. Dresselhaus, M. S., Dresselhaus, G. & Jorio, A. *Group Theory: Application to the Physics of Condensed Matter* (Springer, 2008).

13. Hill, J. P. & McMorrow, D. F. Resonant Exchange Scattering: Polarization Dependence and Correlation Function. *Acta Crystallographica Section A* **52,** 236–244 (1996).

14. Hwan Chun, S. *et al.* Direct evidence for dominant bond-directional interactions in a honeycomb lattice iridate Na_2IrO_3. *Nat. Commun.* **12,** 3936 (2021).

15. Ye, F. *et al.* Direct evidence of a zigzag spin-chain structure in the honeycomb lattice: A neutron and x-ray diffraction investigation of single-crystal Na_2IrO_3. *Phys. Rev. B* **85,** 180403 (2012).

16. Chaloupka, J., Jackeli, G. & Khaliullin, G. Kitaev-Heisenberg Model on a Honeycomb Lattice: Possible Exotic Phases in Iridium Oxides A_2IrO_3. *Phys. Rev. Lett.* **105,** 027204 (2010).

17. Rau, J. G., Lee, E. K.-H. & Kee, H.-Y. Generic Spin Model for the Honeycomb Iridates beyond the Kitaev Limit. *Phys. Rev. Lett.* **112,** 077204 (2014).

Chapter 7

Concluding Remarks

Two of the systems researched for this thesis were single crystal samples of the ilmenite structure, namely $CoTiO_3$ and $FeTiO_3$. The inelastic neutron scattering (INS) measurements performed on $CoTiO_3$ revealed pairs of nodal lines that wind around the corners of the two-dimensional Brillouin zone. $CoTiO_3$ was the first material in which such a gapless Dirac magnons were experimentally observed, and the azimuthal dependence of the INS intensity in the vicinity of the magnon crossing points, as presented in figure 5.27 now forms a benchmark measurement for confirming the presence of topological magnons in neutron scattering measurements. Since the publication of results of INS experiments on $CoTiO_3$ [1, 2], similar work was undertaken on the materials $CrCl_3$ [3], $CrBr_3$ [4], and elemental Gd [5]. $CrCl_3$ and $CrBr_3$ are isostructural materials that consist of van der Waals layers of two dimensional honeycomb lattices of Cr^{3+} ions, and INS measurements reveal a spectrum of gapless Dirac magnons with a two-fold azimuthal intensity profile around the crossing points [6]. INS measurements performed on a single crystal sample of 99.99% enriched ^{160}Gd, which has a hexagonal close packed crystal structure, also revealed Dirac nodal lines with a two-fold azimuthal intensity profile. Furthermore, a 'nodal plane' was observed where the two magnon modes are degenerate across the entire hk plane for half-integer values of l [5]. In addition to providing an experimental realisation of Dirac nodal lines, $CoTiO_3$ also provided an experimental realisation of a quantum order-by-disorder mechanism arising to bond-dependent exchange. Evidence for a quantum order-by-disorder mechanism was provided by the presence of a spectral gap above the magnetic Bragg peak

positions, and the presence of bond dependent exchange provides an accurate description of both the magnon dispersions along the boundary of the Brillouin zone and the two-peak profile of an energy scan with a cylindrical integration range centred at the corners of the two-dimensional Brillouin zone. In addition to the topological effects observed in magnon band structures, the two-fold azimuthal intensity profile is also observed in spin-orbit excitons in $CoTiO_3$, illustrating that Dirac nodal lines and azimuthal intensity profile are universal features observed in bosonic excitations supported by the honeycomb lattice. The azimuthal intensity scans were made for $FeTiO_3$, where a Dzyaloshinskii-Moriya interaction gaps out the optical and acoustic magnon bands. Such a gap gives rise to Chern bands stacked in 3D [7], and consequently $FeTiO_3$ provides an experimental realisation of a magnon Chern insulator. Furthermore, the magnon dispersions can be described by a Heisenberg model with up to sixth nearest neighbour coupling, with an easy-axis single-ion anisotropy which arises due to the crystal field effects and spin-orbit coupling. In zero field, there are four magnon modes, coming in doubly degenerate pairs. This degeneracy is lifted under the application of a magnetic field along the hexagonal **c** axis. Once this field exceeds a critical value of 8 T, the system undergoes a metamagnetic transition to a spin-polarised phase, and there are only two Ising magnon modes. In the spin-polarised phase, there is an additional low energy mode with the periodicity of the structural unit cell, and this additional mode hybridises with the acoustic magnon mode via magnon-phonon coupling. In the antiferromagnetic phase, there are a pair of additional low energy modes that have the periodicity of the magnetic unit cell and undergo a coupling with the acoustic magnon mode. These additional modes have been described by a phenomenological model, but the microscopic origin of these modes remains unclear. The final system researched as part of this thesis is Li-doped Na_2IrO_3, which was found to have myriad structural faults such as stacking faults and rotational twins. Such structural issues render the observation of magnetic ordering via REXS difficult. Despite such challenges, evidence for zig-zag ordering in a 5% Li-doped sample was found. Such a magnetic structure is similar to the parent structure of Na_2IrO_3, but the Néel temperature is suppressed upon substitution of the Na^+ ions with Li^+ ions. In order to investigate the effect of further Li substitution upon the magnetic structure, crystal growth techniques may have to be refined in order to allow for the

growth of crystalline samples with fewer structural defects. Additionally, the development of complimentary techniques to observe magnetic ordering in layered honeycomb materials, such as torque magnetometry, could enable the further exploration of the magnetic phase diagram of Li-doped Na_2IrO_3.

References

1. Elliot, M. *et al.* Order-by-disorder from bond-dependent exchange and intensity signature of nodal quasiparticles in a honeycomb cobaltate. *Nat. Commun.* **12,** 3936 (2021).
2. Yuan, B. *et al.* Dirac Magnons in a Honeycomb Lattice Quantum XY Magnet $CoTiO_3$. *Phys. Rev. X* **10,** 011062 (2020).
3. Do, S.-H. *et al. Gaps in Topological Magnon Spectra: Intrinsic vs. Extrinsic Effects* 2022. `https://arxiv.org/abs/2204.03720`.
4. Nikitin, S. E. *et al. Thermal Evolution of Dirac Magnons in the Honeycomb Ferromagnet $CrBr_3$* 2022. `https://arxiv.org/abs/2204.11355`.
5. Scheie, A. *et al.* Dirac Magnons, Nodal Lines, and Nodal Plane in Elemental Gadolinium. *Phys. Rev. Lett.* **128,** 097201 (2022).
6. Schneeloch, J. *et al.* Gapless Dirac magnons in $CrCl_3$. *npj Quantum Materials* **7** (2022).
7. McClarty, P. A. Topological Magnons: A Review. *arXiv:2106.01430* (2021).